Non-Adiabatic Multi-Dimensional Quantum Dynamics of Br_2 in Solid Argon

INAUGURAL – DISSERTATION

zur Erlangung des Doktorgrades
der Freien Universität Berlin
Fachbereich Biologie, Chemie, Pharmazie

vorgelegt von
Alexander Borowski
aus Ebersdorf

2008

Diese Arbeit wurde in der Zeit von April 2004 bis Dezember 2007 unter der Betreuung durch Herrn Priv.-Doz. Dr. Oliver Kühn am Fachbereich Chemie, Biologie, Pharmazie der Freien Universität Berlin in der Arbeitsgruppe von Herrn Prof. Dr. Jörn Manz durchgeführt.

Erst-Gutachter:	Prof. Dr. Oliver Kühn
Zweit-Gutachter:	Prof. Dr. Jörn Manz

Tag der Disputation:	18.07.2008

Publications

Interaction potentials: The diatomics-in-molecules approach
A. Borowski, A. Cohen, R.B. Gerber and O. Kühn
ch. 4.6, pp. 318-324 in:
"Analysis and Control of Ultrafast Photoinduced Reactions"
O. Kühn and L. Wöste (eds.)
Springer Series in Chemical Physics Vol. 87, Springer, Heidelberg, 2007

Tailoring model Hamiltonians for dihalogen – rare gas matrix problems
A. Borowski and O. Kühn
Theoretical Chemistry Accounts, Vol. 117, pp. 521-533 (2007)

Towards a quantum mechanical description of the photochemistry of dihalogens in rare gas matrices
A. Borowski and O. Kühn
Journal of Photochemistry and Photobiology A, Vol. 190, pp. 169-176 (2007)
special issue on:
"Theoretical Aspects of Photoinduced Processes in Complex Systems"
Irene Burghardt (ed.)

Nonadiabatic quantum dynamics of Br_2 in solid Ar: A four-dimensional study of the B to C state predissociation
Chemical Physics, Vol. 347, pp. 523-530 (2008)
special issue on:
"Ultrafast Photoinduced Processes in Polyatomic Molecules - Electronic Structure, Dynamics and Spectroscopy"
M. Thoss, G. Stock and T.J. Martinez (eds.)

Abstract

This work investigates the matrix-induced predissociation of the electronically excited B-state of Br_2 molecules in solid Ar. Using the multi-configuration time-dependent Hartree (MCTDH) method wave packet simulations are performed on multi-dimensional, non-adiabatically coupled B- and C-state potential energy surfaces (PES) upon laser pulse excitation from the electronic ground (X-) state. The quantum models required are developed in the framework of a combined Cartesian reaction surface (CRS) – vibronic coupling Hamiltonian (VCH) approach. For calculating the necessary excited state potential energy surfaces and coupling matrix elements a specific implementation of the semi-empirical Diatomics-in-Molecules (DIM) is introduced and extended to calculate analytical gradients and Hessian.

The models investigated comprise two anharmonic reaction coordinates, two vibronic coupling modes and up to 17 harmonic matrix modes. Expressed in these coordinates the potential energy surfaces of the B- and C-states form a crossing seam, which connects individual conical intersections (CI).

The numerical results of the wave packet simulations are analyzed in terms of electronic populations, one- and two-dimensional nuclear densities, as well as position and energy expectation values. With respect to the predissociation it is shown, that both, asymmetric and symmetric matrix motions are important for triggering nonadiabatic transitions between the B- and C-states. These transitions occur after about 500 fs for each second round trip of the Br_2 molecule and require the elongation of the matrix. In addition, the effect of vibrational preexcitation of individual nuclear degrees of freedom on the dynamics in the excited state is investigated. Here, depending on whether a reaction coordinate or vibronic coupling mode is preexcited one either observes dynamics in a different Franck-Condon region of the B-state or a doubling of the effective non-adiabatic coupling.

In the last part of the work a full-dimensional, simplified model (2096 harmonic + 1 anharmonic nuclear degree of freedom) is developed to simulate the B-state absorption spectrum. The zero-phonon line (ZPL) and phonon sideband (PSB) contributions of the calculated spectrum are found in reasonable agreement with experimental results. In particular, the specific double peak structure of the phonon sideband contributions is reproduced and resolved in terms of individual normal modes.

Kurzfassung

In dieser Arbeit wird die matrix-induzierte Prädissoziation des elektronisch angeregten B-Zustandes von Br_2-Molekülen in Ar-Festkörpern untersucht. Unter Anwendung der Vielkonfigurations- zeitabhängigen Hartree-Methode (multi-configuration time-dependent Hartree, MCTDH) werden dazu Wellenpaketsimulationen auf mehrdimensionalen, nicht-adiabatisch gekoppelten B- und C-Zustandspotentialflächen (potential energy surfaces, PES) nach Laserpulsanregung aus dem elektronischen (X-) Grundzustand durchgeführt. Die dafür benötigten Quantenmodelle werden im Rahmen eines kombinierten, kartesischen Reaktionsflächen (Cartesian reaction surface, CRS) – vibronischen Kopplungsoperator-Ansatzes (vibronic coupling Hamiltonian, VCH) entwickelt. Zur Berechnung der Potentialenergieflächen und Kopplungsmatrixelemente wird die semiempirische Diatomics-in-Molecules (DIM) Methode problemspezifisch implementiert und um die Berechnung analytischer Gradienten und Hessematrixelemente erweitert.

Die untersuchten Modelle berücksichtigen zwei anharmonische Reaktionskoordinaten, zwei vibronische Kopplungsmoden und bis zu 17 harmonische Matrixmoden. In der Darstellung durch diese Koordinaten zeigen die Potentialenergieflächen des B- und C-Zustandes einen Kreuzungssaum (crossing seam), der einzelne konische Durchschneidungen (conical intersections, CI) miteinander verbindet.

Die numerischen Resultate der Wellenpaketsimulationen werden anhand elektronischer Populationen, ein- und zwei-dimensionaler Aufenthaltswahrscheinlichkeiten der Kerne, sowie Orts- und Energieerwartungswerten untersucht. In Bezug auf die Prädissoziation wird gezeigt, dass sowohl asymmetrische als auch symmetrische Matrixbewegungen notwendig sind, um nicht-adiabatische Übergänge zwischen dem B- und C-Zustand auszulösen. Diese Übergänge finden nach ca. 500 fs etwa jede zweite Umlaufperiode des Br_2-Moleküls statt und erfordern eine Auslenkung der Matrix. Zusätzlich wird der Einfluss der Schwingungsvoranregung einzelner Freiheitsgrade im elektronischen Grundzustand auf die Dynamik im angeregten Zustand untersucht. Hierbei beobachtet man, je nach dem, ob eine Reaktionskoordinate oder eine vibronische Kopplungsmode vorangeregt wird, entweder die Dynamik in einem anderen Franck-Condon Bereich des B-Zustandes oder eine Erhöhung der effektiven nicht-adiabatischen Kopplung um das Doppelte.

Im letzten Teil der Arbeit wird ein volldimensionales, vereinfachtes Modell (2096 harmonische + 1 anharmonischer Kernfreiheitsgrad) zur Simulation des B-Zustandsabsorptionsspektrums entwickelt. Die Nullphononenlinien (zero-phonon lines, ZPL) und Phononenseitenbanden (phonon sidebands, PSB) des berechneten Spektrums stimmen weitgehend mit dem Experiment überein. Insbesondere wird die spezifische Doppelpeakstruktur der Phononenseitenbanden reproduziert und anhand einzelner Normalmoden aufgelöst.

Contents

1 Introduction

1.1 Overview

Based upon their simple composition dihalogen and interhalogen molecules in cryogenic rare gas matrices have drawn attention as prototypical condensed phase systems. Their constituent parts are among the experimentally and theoretically best characterized systems known in gas phase spectroscopy [1–3] and solid state physics [4–7]. The coupling between the chromophore and its host shows up in spectra, which consist of zero-phonon lines (ZPL) and phonon sidebands (PSB) [8–10]. The crystalline, inert and transparent host provided by the rare gas matrix enables a detailed spectroscopic investigation of the dihalogen molecule under well-defined, spatially fixed conditions, for a review see Refs. [11–13]. In particular Schwentner and coworkers unraveled a host of phenomena such as ultrafast spin-flip [14–16] for ClF molecules in Ar matrices, further specific matrix motions accompanying the electronic and vibrational excitation of Cl_2 in Ar [17], as well as effective chromophore potentials and vibrational energy relaxation effects [18], coherent collisional energy transfer processes [19], displacive excitation of zone-boundary phonons [20] and coherent phonon dynamics [21] in case of Br_2 in solid Ar. The various effects related to the issue of coherence versus decoherence effects have also been illuminated by Apkarian and coworkers for the system I_2 in Ar [22–24] and Kr [25–27].

The presence of coherence lasting for hundreds of femtoseconds observed in the mere of these experiments triggered the question of coherently controlling these systems by means of shaped laser pulses. Here, for instance, chirped pulse experiments, which compensate for the effect of wave packet dispersion, have been applied in order to differentiate between those effects originating from the anharmonicity of the bare dihalogen molecular potential and those resulting from its interaction with the matrix. This way the control of wave packet revivals as well as the extraction of dephasing time scales could be realized [28]. Further, using wave packet interferometry experiments in terms of phase-locked pulse pairs applied to the $B \leftarrow X$ transition of Cl_2 in Ar, excited state wave packets with well-defined chromophore-matrix interactions, that is which mostly consist of either zero-phonon or phonon side band contributions, could be prepared providing a proof that the electronic coherence is preserved on a time scale of about 600 fs [29] .

The theoretical treatment of the long lasting electronic and vibrational coherence effects observed requires a quantum approach to these systems. For the latter the evaluation of potential energy surfaces (PES) is a necessary prerequisite and a key issue, which is challenged by the manifold of dihalogen valence states and the large number of nuclear degrees of freedom. This situation is further complicated by the mixing of the various electronic

states due to the coupling to nuclear motions giving rise to non-adiabatic transitions.
Much effort has been devoted especially to the description of these non-adiabatic electronic transitions in classical trajectory simulations for the nuclei using Tully's surface hopping approach [30–32] in combination with the semi-empirical diatomics-in-molecules (DIM) method for the efficient on-the-fly calculation of the PES. Originally introduced by Ellison in 1963 [33,34] this method was refined later on by Tully [35,36] for application to molecular collision dynamics simulations. In particular for halogen - rare gas systems the success of the DIM method, and closely related approaches, can be illustrated by a number of publications starting from the early 1990s. For instance, Gersonde and Gabriel [37,38] have studied the photo-dissociation of HCl and Cl_2 in Xe crystals, Lawrence and Apkarian [39] the spin-orbit transitions of I atoms caged in crystalline Xe and Kr, Batista and Coker [40–42] the photo-dissociation and recombination dynamics of I_2 in liquid and solid Xe and Ar as well as the defragmentation of anionic $I_2^-Ar_n$ clusters. At about the same time Gerber et al. [43–46] investigated the non-adiabatic dissociation dynamics of HCl and F_2 in solid Ar, Grigorenko et al. [47–49] analyzed the PES and stability of He-Cl_2 and Ar-Cl_2 van der Waals clusters, next to the photo-dissociation simulations of Cl_2 in Ne matrices. Similarly, Buchachenko et al. [50–53] studied triatomic X-Rg species such as Ne-I_2, Ar-I_2, Kr-I_2, He-Cl_2, Ar-Cl_2, and He-Br_2 using DIM. Methodically, the DIM method has been extended to treat flexible molecules like I_3 [54–57] in condensed phase environment, and generalized to calculate the PES for quasi-stationary states of polyatomic anions [58]. Altogether, in these applications the DIM method has proven as reasonable compromise between accuracy and numerical feasibility.
Although the classically nuclear dynamics on non-adiabatically coupled electronic potential energy surfaces can be treated in full dimensionality, all the above examples miss the phase information responsible for quantum effects in the nuclear motion. Such effects, however, are fundamental for the description of the coherence effects observed in the related experiments mentioned above. Here, semi-classical approximations have been pursued which retain phase information along classical trajectories [59–64]. Alternatively, quantum-classical hybrid methods [65,66] and mean-field type approaches such as the classically separable potential method [67–69] have been applied. Originally developed for one-dimensional quantum propagations only, the latter method has been extended to include also quantum correlations between pairs of nuclear coordinates [70].
Strict quantum approaches, on the other hand, are restricted to the description of a few nuclear degrees only as these approaches require the calculation of a multi-dimensional PES in advance. Focusing on the laser excitation process and restricting the dynamics to short times, reduced dimensionality models on the basis of DIM-generated PES for one and two effective nuclear degrees of freedom have provided valuable insight into the coherent nature of the photo-dissociation, as well as into the inter-system crossing dynamics mediated by spin-orbit coupling, for the molecules F_2 [71–73], ClF [15,16,74,75] and Cl_2 [76,77] in Ar matrices.
Whereas in these simulations the weak and moderate spin-orbit constants (SOC) of the

light halogen species F and Cl could be applied as coupling parameters for controlling the spin-flip between the excited molecular singlet and triplet states, the large spin-orbit coupling constants of the heavy halogen atoms Br and I lead to an enhanced energy splitting of the molecular dissociation limits. In its consequence, the lower bound and repulsive excited molecular states cross one another. For symmetry reasons, the various spin-obit coupled states are orthogonal in the bare Br_2 and I_2 molecules, such that non-adiabatic transitions between the crossing states can only occur due to the coupling to the molecular rotation. In condensed phase environment, however, they are coupled by nuclear motions of the surrounding. Here, in particular symmetry-breaking plays an important role as demonstrated experimentally [78–80] and theoretically [40, 81] for the predissociation of I_2. This effect is also reflected when comparing the rather low predissociation yield observed for Br_2 in the gas phase [82] with its increase in matrix environment [83]. The quantum description of this phenomenon provides a challenge for theory as illustrated in the following.

1.2 Objective

The objective of this thesis is the theoretical description and investigation of the quantum dynamics of Br_2 molecules in Ar matrices. Mainly, the theoretical interests in this system has been motivated by the recent time-resolved and spectroscopic experiments of the Schwentner group, see Sec. 1.1 and Ref. [84]. Among the phenomena of interest are the wave packet dynamics in the electronically excited B-state, the role of the coupling of the chromophore to individual lattice phonons and the related effect of non-adiabatic transitions (predissociation) to other electronic states. Here it should be noted, that the unique localization of the lowest energy crossing between the excited B- and C-state favors Br_2 over, for instance, I_2 as chromophore for the investigation of predissociation in condensed phase.

Specifically, this work focusses on the scenario of a laser-induced $B \leftarrow X$ transition with subsequent B-state population transfer to the C-state. This specific predissociation channel is shown for a one-dimensional model of Br_2 in Ar in Fig. 1.1, which also illustrates various other non-adiabatic transition pathways in terms of Landau-Zener [85, 86] and Rosen-Zener [87] type crossings. Topologically, these crossings may give rise to, for example, conical intersections [88] in more general, multi-dimensional situations as will be demonstrated below in Sec. 3.3.

As a theoretical tool for the treatment of such conical intersections the vibronic coupling Hamiltonian has played a decisive role, not only for the general appreciation of its symmetry properties and structural peculiarities [88], but also for the development of dynamics methods [89, 90]. Particularly, the latter comprise wave packet [91–93] and density matrix propagations [94, 95] as well as classical trajectory-based approaches [96]. However, in view of the observed nuclear and electronic coherence effects the theoretical description of the dynamics clearly requires a quantum approach for the present system.

This task can be subdivided into an electronic structure problem and a nuclear dynamics

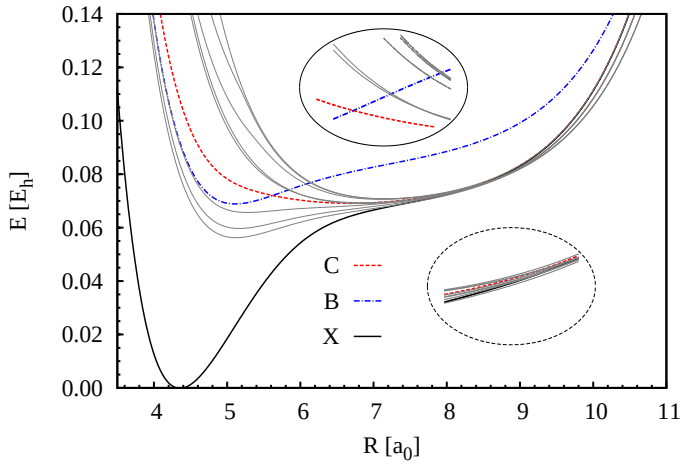

Figure 1.1: 1D effective potential curves for Br_2 in Ar with Landau-Zener (solid ellipse) and Rosen-Zener type crossings (dashed ellipse) leading to non-adiabatic transitions among the B- (dash-dotted line) and C-states (dashed line). The other repulsive (above C-state) and bound excited states (below B-state) contributing during the electronic relaxation to the X-state (solid line) are drawn as grey curves.

problem. In a first step, it requires the solution of the stationary Schrödinger equation to generate potential energy surfaces, which in a second step are utilized to solve the time-dependent Schrödinger equation for the nuclear motion. The solution of both subtasks involves models, which, in application to Br_2 in Ar, require approximations to the electronic structure as well as to the nuclear degrees of freedom.

Specifically, these approximations apply to the semi-empirical description of the spectroscopically relevant electronic states within the framework of DIM theory. Further, they apply to the choice of nuclear degrees of freedom as well as to the PES spanned by these coordinates, which should cover most parts of the anharmonicity and the coupling of the nuclear motion. A promising concept for the definition of such coordinates, particularly in multi-dimensional situations, is provided by the Cartesian reaction surface (CRS) approach [97–100]. This approach is based on the interpolation between reactant and product geometries and has been successfully applied to the description of Hydrogen-transfer reactions proceeding on the PES of a single electronic state, for a review, see Ref. [101].

In order to take into account the non-adiabatic transitions among the PES of different electronic states this approach has to be combined with vibronic coupling theory for specific application to Br_2 in Ar. Particularly, the vibronic coupling approach builds upon the idea of a Taylor expansion of the PES with respect to harmonic nuclear degrees of freedom in the vicinity of the geometry, where the electronic states cross leading to a multi-mode vibronic coupling problem. This approach is well established [89, 102, 103] and has been extensively applied to the simulation of ultrafast quantum dynamics of, for instance, pyrazine [90, 104] or Jahn-Teller systems [105] using the multi-configuration time-dependent Hartree (MCTDH) method. Here, the latter method [106, 107] turned out to be an efficient tool for solving the time-dependent Schrödinger equation in case of multi-dimensional, vibronically coupled systems.

In the following, all these theoretical concepts mentioned, that is the DIM method, the CRS concept, the VCH approach as well as the MCTDH method will be applied to Br_2 in Ar. The necessary steps are outlined below.

1.3 Outline

This work can be sectioned into three main parts: First, the calculation of the electronic states for Br_2 molecules in Ar matrices using the DIM method. Second, the construction of a Cartesian reaction surface Hamiltonian for this system in the framework of vibronic coupling theory. Third, the solution of the time-dependent Schrödinger equation for this Hamiltonian using the MCTDH method.
In more detail, Chap. 2 introduces the formalism of the DIM method putting emphasis on halogen molecules in rare gas matrices. Starting with the basic idea of this method in Sec. 2.1, which is followed by a brief discussion of Hund's coupling case c, a model basis set containing 36 spin-orbit coupled molecular states will be introduced in Sec. 2.2 as fundament for the DIM representation of heavy dihalogen molecules. The details of constructing a dihalogen - rare gas interaction Hamiltonian will be explored in Sec. 2.3 on the basis of various body frame and basis set transformation steps.
Sec. 2.4 is dedicated to the specific application of the DIM method to Br_2 molecules in Ar matrices. After introducing the required pair potentials and setting up a proper simulation box this system will be subject to a geometry relaxation in Sec. 2.4.3, which will be complemented by an investigation of the Br_2 ground state rotational barrier for its double substitutional lattice site within the Ar crystal.
The possibility of reducing the complexity of the electronic DIM Hamiltonian will be explored in Sec. 2.4.4 taking into account two scenarios of different nuclear symmetry. First, electronic symmetry consideration will be utilized to classify different coupling types, which subsequently will be analyzed in terms of a specific block-mask diagonalization technique. Based upon the results of this investigation a DIM-Hamiltonian incorporating only those electronic states relevant for photo-dissociation will be explored in Sec. 2.4.5. Here, particular attention is spent on the B-state crossing region, for which eigenvectors and eigenvalues between full and reduced DIM-Hamiltonian representations will be compared in Sec. 2.4.5.
Chap. 3 is concerned with the construction of a reduced but multi-dimensional quantum model for Br_2 in Ar on the basis of a combined Cartesian reaction surface (CRS) and vibronic coupling Hamiltonian (VCH) concept. The required small and large amplitude approximations to the nuclear motion will be introduced in Sec. 3.1.1 and Sec. 3.1.2 employing each alternative representations of the PES in terms of Cartesian coordinates and normal modes, respectively. Using vibronic coupling theory these introductory considerations applying to the PES of a single electronic state will be extended to the representation of the PES in case of many, vibronically coupled electronic states in Sec. 3.1.3. This leads to the introduction of vibronic coupling and tuning modes. The former provide the linear coupling *between* - and the latter the linear coupling *within* - given electronic states.

The specific application of these concepts will be detailed in Sec. 3.2. Here, in Sec. 3.2.1 heuristic two-dimensional potential energy surfaces for the motion of specific cage fragments will be investigated first, before systematically defining a more general matrix coordinate in Sec. 3.2.2, which will be shown to cover many lattice normal modes. Then, after identifying important coupling modes in Sec. 3.3 a minimum Cartesian reaction surface linear vibronic coupling model for Br_2 in Ar is subject to quantum simulations within the frame of MCTDH theory in Chap. 4.
The basic concepts of the MCTDH approach are briefly reviewed in Sec. 4.1 putting emphasis on the multi-set formulation of the method. This part is followed by details on the grid representation of the reaction surface in Sec. 4.2.
In order to unravel the mechanistic aspects of the B- to C-state predissociation laser-driven wave packet dynamics simulations will then be performed in Sec. 4.3 using a 4D minimal model first. After setting up the Schrödinger equation and defining various quantities necessary for the analysis of this model, the effect of different X-state vibrational conditions onto the B-state wave packet dynamics and the efficiency of the population transfer to the C-state will be investigated. Depending on whether a reaction coordinate or a coupling mode is initially preexcited one either observes wave packet dynamics in a different Franck-Condon regime or an increased effective non-adiabatic coupling. Further, analyzing the numerical results in terms of 1D and 2D reduced densities, as well as the energy exchange between the coordinates, it will be explicitly shown, that the matrix dynamics is essential for triggering the B- to C-state non-adiabatic transitions.
In Sec. 4.4 this minimum model will be expanded by a single tuning mode. Specifically, in a study comparative to the investigations of Sec. 4.3 it will be shown, how this particular phonon mode modulates the energy gap between the B- and C-states. Eventually, by rediscretizing the harmonic bath spectral density of states and replacing this single tuning mode by a manifold of 17 effective oscillators this 5D model will be further expanded towards a 21D model in Sec. 4.5 for taking into account the effect of vibrational relaxation.
Finally, taking up the challenge provided by recent spectroscopic experiments [84], in Sec. 4.6 a simple, but full-dimensional quantum model containing 2096 lattice normal modes, which are linearly coupled to an anharmonic 1D effective Br_2 potential, will be used to calculate the B-state absorption spectrum for a detailed comparison to the experiment. The focus of this model does not lie on the dynamics but on the stationary spectroscopy of the B-state. Its predissociation via the C-state, however, will not be considered in this simple model.
The major investigations and most important results of this work will then be summarized in Chap. 5. Finally, an Appendix, Chap. 5, completes this thesis by illustrating the various techniques and concepts employed in detail, as well as by examples.

2 DIM Method for X_2-Rg Systems

2.1 Basic Concept

The fundamental concept of the DIM method [33–36] is the description of a polyatomic molecule in terms of all possible pair interactions between its atoms. This idea is closely connected to the valence bond (VB) concept of electron pairs forming the chemical bond between each two atoms. Underlying this heuristic idea is a spatial assignment of electrons to either individual two-center bonds in a polyatomic molecule or, consequently, to individual atoms for large inter-nuclear separations. In the latter case the polyatomic electronic wave function can be represented by an antisymmetrized product of atomic basis functions, and the polyatomic energy can be expressed by the sum of atomic energies. At moderate inter-nuclear separations, however, individual atoms share their electrons, which then can be assigned to diatomic groups rather than to single atoms within such product ansatz for the electronic wave function. In the specific case of a single halogen guest molecule (X_2) in a crystalline host matrix of closed shell rare gas atoms (Rg) with $^1S_0$ character the electronic wave function can be written as a product of diatomic basis functions, representing the X_2 molecule, and atomic s-functions, representing the individual Rg atoms. Accordingly, such product ansatz permits the decomposition of the polyatomic Hamiltonian into diatomic and atomic fragments in its matrix representation. In view of the semi-empirical character of the DIM method these matrix elements are parameterized by pair potentials.

2.2 The Molecular X_2 Hamiltonian

2.2.1 Hund's Coupling Cases c

The choice of an appropriate basis for the representation of the diatomic electronic wave function depends on the halogen species under consideration. Common to all halogen atoms is a ^2P term for the atomic ground state with the electronic configuration p^5, in which an electron hole acts like a single electron with the quantum numbers $L = 1$ and $S = \frac{1}{2}$ for its electronic angular momentum $\mathbf{L}$ and its spin $\mathbf{S}$, respectively. Taking into account the spin-orbit interaction according to the Russel-Saunders $(\mathbf{L}, \mathbf{S})$ coupling scheme, the atomic doublet term ^2P is split up into the spin-coupled terms $^2P_{3/2}$ and $^2P_{1/2}$.
In particular for the heavy halogen species bromine and iodine the energies of this atomic term separation (3685 and 7603 cm^{-1} [108]) are comparable to, or even larger than, the molecular dissociation energies of Br_2 and I_2 in the excited B-state (3758 and 4278 cm^{-1} [2, 109]). For such a case the interaction between $\mathbf{L}$ and $\mathbf{S}$ is strong as compared to their

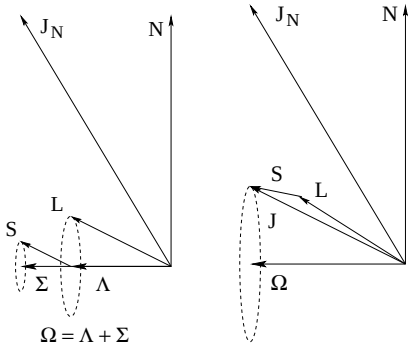

Figure 2.1: Vector coupling scheme and axial quantization of the spin $\sim$ ($\mathbf{S}$), orbital $\sim$ ($\mathbf{L}$), coupled electronic $\sim$ ($\mathbf{J}$), nuclear $\sim$ ($\mathbf{N}$) and total angular momentum ($\mathbf{J_N} = \mathbf{\Omega} + \mathbf{N}$) for Hund's coupling case a (left) and Hund's coupling case c (right).

separate interaction with the axial intra-molecular electric field, which leads to a spatial quantization of the total electronic angular momentum $\mathbf{J}$ with the axial component $\mathbf{\Omega}$, rather than to an independent quantization of $\mathbf{L}$ and $\mathbf{S}$ with the respective axial components $\mathbf{\Lambda}$ and $\mathbf{\Sigma}$ [1]. This situation corresponds to Hund's coupling case c according to the general classification scheme of the interaction between molecular rotation and electronic motion by F. Hund [110]. The different vector coupling schemes of the angular momenta are contrasted in Fig. 2.1 for Hund's case a and Hund's case c, where the spin-orbit coupling is weak for the former.
In the limiting case of strong spin-orbit coupling the quantum number Ω of the axial component $\mathbf{\Omega}$ of the total electronic angular momentum $\mathbf{J}$ is the only "good" quantum number for the designation of a molecular state. For a diatomic molecule with the atoms a and b the resultant molecular electronic angular momentum $\mathbf{J}$ can be obtained by adding the single atomic electronic angular momenta $\mathbf{J}_a$ and $\mathbf{J}_b$:

$$\mathbf{J} = \mathbf{J}_a + \mathbf{J}_b. \tag{2.1}$$

Correspondingly, the molecular quantum number Ω can be obtained by adding the single atomic quantum numbers M_{J_a} and M_{J_b}:

$$\Omega = |M_{J_a} + M_{J_b}|. \tag{2.2}$$

To every combination of two atomic M_J values there corresponds a different molecular state, except that states differing only in the sign of both M_J values form a degenerate pair as long as $\Omega \neq 0$.

2.2.2 Molecular Wave Function

A zero order approximation to the molecular wave function $\psi_\Omega^{(X_2)}$ of a dihalogen $X_a - X_b$ can be represented by a proper linear combination of diatomic products of non-overlapping

spin-coupled atomic states $|J, M\rangle_a$ and $|J, M\rangle_b$:

$$\psi_{\Omega}^{(X_2)} = \sum_{i}^{n_i} c_{\Omega,i} |J, M\rangle_{a,i} |J', M'\rangle_{b,i} \,, \tag{2.3}$$

where n_i denotes the number of distinct products $|J, M\rangle_{a,i}|J', M'\rangle_{b,i}$ for a given molecular state Ω with the expansion coefficients $c_{\Omega,i}$. In Tab. 2.1 these Hund's case c basis functions and term symbols Ω_w^σ for a homonuclear molecule originating from the union of two identical ^2P atoms are listed (see also Refs. [40, 111]) and ordered according to the quantum numbers $\Omega = 0, 1, 2, 3$ for the parity characters $w = g, u$ of the wave function with respect to an inversion of the nuclei. For those states with quantum number $\Omega = 0$ a different reflection symmetry $\sigma = +, -$ of the wave function with respect to a plane containing the molecular axis can be distinguished. In addition, next to the Hund's case a term symbols $^{2\Sigma+1}\Lambda_w^\sigma$ denoting the origin of the Hund's case c terms, also the common spectroscopic trivial names as well as the atomic dissociation limits are given in Tab. 2.1. A general scheme for the construction of these molecular basis functions can be found in the works of Chang [112] and Umanski and Nikitin [113]. Notice, that Buchachenko and Stepanov [50] have discussed alternative expressions with the same symmetry properties for some Hund's case c wave functions.

Since the tabulated wave functions are the *symmetry eigenfunctions* to the irreducible representations of the molecular symmetry point group $D_{\infty h}$, the diatomic Hamiltonian matrix is block diagonal with respect to their symmetries. That is, within the given basis set of 36 diatomic states the molecular Hamiltonian separates into two 4×4 matrices $(0_g^+, 0_u^-)$ and two 1×1 matrices $(0_g^-, 0_u^+)$, each being non-degenerate, and into two 2×2 matrices $(2_g, 2_u)$, one 3×3 matrix (1_g), one 5×5 matrix (1_u), and one 1×1 matrix (3_u), each being doubly degenerate (cf. Tab. 2.1). Moreover, since the tabulated wave functions are the *linearly independent eigenfunctions* to the irreducible representations, the individual block matrices of the diatomic Hamiltonian are diagonal. This circumstance permits the parameterization of its diagonal elements by molecular potential energy curves, e.g. from spectroscopic data or ab initio calculations. Strictly speaking, in the latter case such parameterization is valid only, if the calculated molecular orbitals (MO) significantly overlap with the "model" p-basis employed in the DIM method [114, 115]. As a heuristic argument supporting this overlap criterion one can consider the covalent excited states of a halogen molecule to be formal electron substitutions of its $\sigma_g^2\pi_u^4\pi_g^4\sigma_u^0$ MO orbital ground state configuration with predominant contributions from atomic valence shell p-orbitals.

2.3 The Construction of the X-Rg Interaction Hamiltonian

The fundamental concept for the description of the intrinsic interactions within the given system of N atoms, which in the following are labeled by the index $i = 1, \ldots, N-2$ for the individual rare gas atoms Rg_i, and the index $\alpha = a, b$ for the single halogen atoms X_α, is the representation of all X_α-Rg_i pair interactions in a joint basis of dihalogen molecular

Table 2.1: Molecular Hund's Case c states and their case a origins.

$^{2\Sigma+1}\Lambda_w^\sigma$	Ω_w^σ	$\sum_i c_{\Omega,i}\lvert J,M\rangle_{a,i}\lvert J',M'\rangle_{b,i}$	Dissociation
$X, 1\ ^1\Sigma_g^+$	0_g^+	$\frac{1}{\sqrt{2}}\left\{\lvert\frac{3}{2},\ \frac{1}{2}\rangle_a\lvert\frac{3}{2},-\frac{1}{2}\rangle_b-\lvert\frac{3}{2},-\frac{1}{2}\rangle_a\lvert\frac{3}{2},\ \frac{1}{2}\rangle_b\right\}$	$^2P_{3/2}+{}^2P_{3/2}$
$a', {}^3\Sigma_g^-$	0_g^+	$\frac{1}{\sqrt{2}}\left\{\lvert\frac{3}{2},\ \frac{3}{2}\rangle_a\lvert\frac{3}{2},-\frac{3}{2}\rangle_b-\lvert\frac{3}{2},-\frac{3}{2}\rangle_a\lvert\frac{3}{2},\ \frac{3}{2}\rangle_b\right\}$	$^2P_{3/2}+{}^2P_{3/2}$
$^3\Pi_g$	0_g^+	$\frac{1}{2}\left\{\lvert\frac{3}{2},\ \frac{1}{2}\rangle_a\lvert\frac{1}{2},-\frac{1}{2}\rangle_b-\lvert\frac{1}{2},-\frac{1}{2}\rangle_a\lvert\frac{3}{2},\ \frac{1}{2}\rangle_b+\lvert\frac{3}{2},-\frac{1}{2}\rangle_a\lvert\frac{1}{2},\ \frac{1}{2}\rangle_b-\lvert\frac{1}{2},\ \frac{1}{2}\rangle_a\lvert\frac{3}{2},-\frac{1}{2}\rangle_b\right\}$	$^2P_{3/2}+{}^2P_{1/2}$
$2\ ^1\Sigma_g^+$	0_g^+	$\frac{1}{\sqrt{2}}\left\{\lvert\frac{1}{2},\ \frac{1}{2}\rangle_a\lvert\frac{1}{2},-\frac{1}{2}\rangle_b-\lvert\frac{1}{2},-\frac{1}{2}\rangle_a\lvert\frac{1}{2},\ \frac{1}{2}\rangle_b\right\}$	$^2P_{1/2}+{}^2P_{1/2}$
$^3\Pi_g$	0_g^-	$\frac{1}{2}\left\{\lvert\frac{3}{2},\ \frac{1}{2}\rangle_a\lvert\frac{1}{2},-\frac{1}{2}\rangle_b-\lvert\frac{1}{2},-\frac{1}{2}\rangle_a\lvert\frac{3}{2},\ \frac{1}{2}\rangle_b-\lvert\frac{3}{2},-\frac{1}{2}\rangle_a\lvert\frac{1}{2},\ \frac{1}{2}\rangle_b+\lvert\frac{1}{2},\ \frac{1}{2}\rangle_a\lvert\frac{3}{2},-\frac{1}{2}\rangle_b\right\}$	$^2P_{3/2}+{}^2P_{1/2}$
$a, {}^3\Pi_g$	1_g	$\frac{1}{\sqrt{2}}\left\{\lvert\frac{3}{2},\ \frac{3}{2}\rangle_a\lvert\frac{3}{2},-\frac{1}{2}\rangle_b-\lvert\frac{3}{2},-\frac{1}{2}\rangle_a\lvert\frac{3}{2},\ \frac{3}{2}\rangle_b\right\}$ $\frac{1}{\sqrt{2}}\left\{\lvert\frac{3}{2},-\frac{3}{2}\rangle_a\lvert\frac{3}{2},\ \frac{1}{2}\rangle_b-\lvert\frac{3}{2},\ \frac{1}{2}\rangle_a\lvert\frac{3}{2},-\frac{3}{2}\rangle_b\right\}$	$^2P_{3/2}+{}^2P_{3/2}$
$^1\Pi_g$	1_g	$\frac{1}{\sqrt{2}}\left\{\lvert\frac{3}{2},\ \frac{3}{2}\rangle_a\lvert\frac{1}{2},-\frac{1}{2}\rangle_b-\lvert\frac{1}{2},-\frac{1}{2}\rangle_a\lvert\frac{3}{2},\ \frac{3}{2}\rangle_b\right\}$ $\frac{1}{\sqrt{2}}\left\{\lvert\frac{3}{2},-\frac{3}{2}\rangle_a\lvert\frac{1}{2},\ \frac{1}{2}\rangle_b-\lvert\frac{1}{2},\ \frac{1}{2}\rangle_a\lvert\frac{3}{2},-\frac{3}{2}\rangle_b\right\}$	$^2P_{3/2}+{}^2P_{1/2}$
$^3\Sigma_g^-$	1_g	$\frac{1}{\sqrt{2}}\left\{\lvert\frac{3}{2},\ \frac{1}{2}\rangle_a\lvert\frac{1}{2},\ \frac{1}{2}\rangle_b-\lvert\frac{1}{2},\ \frac{1}{2}\rangle_a\lvert\frac{3}{2},\ \frac{1}{2}\rangle_b\right\}$ $\frac{1}{\sqrt{2}}\left\{\lvert\frac{3}{2},-\frac{1}{2}\rangle_a\lvert\frac{1}{2},-\frac{1}{2}\rangle_b-\lvert\frac{1}{2},-\frac{1}{2}\rangle_a\lvert\frac{3}{2},-\frac{1}{2}\rangle_b\right\}$	$^2P_{3/2}+{}^2P_{1/2}$
$^3\Pi_g$	2_g	$\frac{1}{\sqrt{2}}\left\{\lvert\frac{3}{2},\ \frac{3}{2}\rangle_a\lvert\frac{3}{2},\ \frac{1}{2}\rangle_b-\lvert\frac{3}{2},\ \frac{1}{2}\rangle_a\lvert\frac{3}{2},\ \frac{3}{2}\rangle_b\right\}$ $\frac{1}{\sqrt{2}}\left\{\lvert\frac{3}{2},-\frac{3}{2}\rangle_a\lvert\frac{3}{2},-\frac{1}{2}\rangle_b-\lvert\frac{3}{2},-\frac{1}{2}\rangle_a\lvert\frac{3}{2},-\frac{3}{2}\rangle_b\right\}$	$^2P_{3/2}+{}^2P_{3/2}$
$^1\Delta_g$	2_g	$\frac{1}{\sqrt{2}}\left\{\lvert\frac{3}{2},\ \frac{3}{2}\rangle_a\lvert\frac{1}{2},\ \frac{1}{2}\rangle_b-\lvert\frac{1}{2},\ \frac{1}{2}\rangle_a\lvert\frac{3}{2},\ \frac{3}{2}\rangle_b\right\}$ $\frac{1}{\sqrt{2}}\left\{\lvert\frac{3}{2},-\frac{3}{2}\rangle_a\lvert\frac{1}{2},-\frac{1}{2}\rangle_b-\lvert\frac{1}{2},-\frac{1}{2}\rangle_a\lvert\frac{3}{2},-\frac{3}{2}\rangle_b\right\}$	$^2P_{3/2}+{}^2P_{1/2}$
$B', {}^3\Pi_u$	0_u^-	$\frac{1}{\sqrt{2}}\left\{\lvert\frac{3}{2},\ \frac{3}{2}\rangle_a\lvert\frac{3}{2},-\frac{3}{2}\rangle_b+\lvert\frac{3}{2},-\frac{3}{2}\rangle_a\lvert\frac{3}{2},\ \frac{3}{2}\rangle_b\right\}$	$^2P_{3/2}+{}^2P_{3/2}$
$1\ ^3\Sigma_u^+$	0_u^-	$\frac{1}{\sqrt{2}}\left\{\lvert\frac{3}{2},\ \frac{1}{2}\rangle_a\lvert\frac{3}{2},-\frac{1}{2}\rangle_b+\lvert\frac{3}{2},-\frac{1}{2}\rangle_a\lvert\frac{3}{2},\ \frac{1}{2}\rangle_b\right\}$	$^2P_{3/2}+{}^2P_{3/2}$
$^1\Sigma_u^-$	0_u^-	$\frac{1}{2}\left\{\lvert\frac{3}{2},\ \frac{1}{2}\rangle_a\lvert\frac{1}{2},-\frac{1}{2}\rangle_b+\lvert\frac{1}{2},-\frac{1}{2}\rangle_a\lvert\frac{3}{2},\ \frac{1}{2}\rangle_b-\lvert\frac{3}{2},-\frac{1}{2}\rangle_a\lvert\frac{1}{2},\ \frac{1}{2}\rangle_b-\lvert\frac{1}{2},\ \frac{1}{2}\rangle_a\lvert\frac{3}{2},-\frac{1}{2}\rangle_b\right\}$	$^2P_{3/2}+{}^2P_{1/2}$
$2\ ^3\Sigma_u^+$	0_u^-	$\frac{1}{\sqrt{2}}\left\{\lvert\frac{1}{2},\ \frac{1}{2}\rangle_a\lvert\frac{1}{2},-\frac{1}{2}\rangle_b+\lvert\frac{1}{2},-\frac{1}{2}\rangle_a\lvert\frac{1}{2},\ \frac{1}{2}\rangle_b\right\}$	$^2P_{1/2}+{}^2P_{1/2}$
$B, {}^3\Pi_u$	0_u^+	$\frac{1}{2}\left\{\lvert\frac{3}{2},\ \frac{1}{2}\rangle_a\lvert\frac{1}{2},-\frac{1}{2}\rangle_b+\lvert\frac{1}{2},-\frac{1}{2}\rangle_a\lvert\frac{3}{2},\ \frac{1}{2}\rangle_b+\lvert\frac{3}{2},-\frac{1}{2}\rangle_a\lvert\frac{1}{2},\ \frac{1}{2}\rangle_b+\lvert\frac{1}{2},\ \frac{1}{2}\rangle_a\lvert\frac{3}{2},-\frac{1}{2}\rangle_b\right\}$	$^2P_{3/2}+{}^2P_{1/2}$
$A, {}^3\Pi_u$	1_u	$\frac{1}{\sqrt{2}}\left\{\lvert\frac{3}{2},\ \frac{3}{2}\rangle_a\lvert\frac{3}{2},-\frac{1}{2}\rangle_b+\lvert\frac{3}{2},-\frac{1}{2}\rangle_a\lvert\frac{3}{2},\ \frac{3}{2}\rangle_b\right\}$ $\frac{1}{\sqrt{2}}\left\{\lvert\frac{3}{2},-\frac{3}{2}\rangle_a\lvert\frac{3}{2},\ \frac{1}{2}\rangle_b+\lvert\frac{3}{2},\ \frac{1}{2}\rangle_a\lvert\frac{3}{2},-\frac{3}{2}\rangle_b\right\}$	$^2P_{3/2}+{}^2P_{3/2}$
$C, {}^1\Pi_u$	1_u	$\lvert\frac{3}{2},\ \frac{1}{2}\rangle_a\lvert\frac{3}{2},\ \frac{1}{2}\rangle_b$ $\lvert\frac{3}{2},-\frac{1}{2}\rangle_a\lvert\frac{3}{2},-\frac{1}{2}\rangle_b$	$^2P_{3/2}+{}^2P_{3/2}$
$1\ ^3\Sigma_u^+$	1_u	$\frac{1}{\sqrt{2}}\left\{\lvert\frac{3}{2},\ \frac{3}{2}\rangle_a\lvert\frac{1}{2},-\frac{1}{2}\rangle_b+\lvert\frac{1}{2},-\frac{1}{2}\rangle_a\lvert\frac{3}{2},\ \frac{3}{2}\rangle_b\right\}$ $\frac{1}{\sqrt{2}}\left\{\lvert\frac{3}{2},-\frac{3}{2}\rangle_a\lvert\frac{1}{2},\ \frac{1}{2}\rangle_b+\lvert\frac{1}{2},\ \frac{1}{2}\rangle_a\lvert\frac{3}{2},-\frac{3}{2}\rangle_b\right\}$	$^2P_{3/2}+{}^2P_{1/2}$
$2\ ^3\Sigma_u^+$	1_u	$\frac{1}{\sqrt{2}}\left\{\lvert\frac{3}{2},\ \frac{1}{2}\rangle_a\lvert\frac{1}{2},-\frac{1}{2}\rangle_b+\lvert\frac{1}{2},\ \frac{1}{2}\rangle_a\lvert\frac{3}{2},\ \frac{1}{2}\rangle_b\right\}$ $\frac{1}{\sqrt{2}}\left\{\lvert\frac{3}{2},-\frac{1}{2}\rangle_a\lvert\frac{1}{2},-\frac{1}{2}\rangle_b+\lvert\frac{1}{2},-\frac{1}{2}\rangle_a\lvert\frac{3}{2},-\frac{1}{2}\rangle_b\right\}$	$^2P_{3/2}+{}^2P_{1/2}$
$^3\Delta_u$	1_u	$\lvert\frac{1}{2},\ \frac{1}{2}\rangle_a\lvert\frac{1}{2},\ \frac{1}{2}\rangle_b$ $\lvert\frac{1}{2},-\frac{1}{2}\rangle_a\lvert\frac{1}{2},-\frac{1}{2}\rangle_b$	$^2P_{1/2}+{}^2P_{1/2}$
$A', {}^3\Pi_u$	2_u	$\frac{1}{\sqrt{2}}\left\{\lvert\frac{3}{2},\ \frac{3}{2}\rangle_a\lvert\frac{3}{2},\ \frac{1}{2}\rangle_b+\lvert\frac{3}{2},\ \frac{1}{2}\rangle_a\lvert\frac{3}{2},\ \frac{3}{2}\rangle_b\right\}$ $\frac{1}{\sqrt{2}}\left\{\lvert\frac{3}{2},-\frac{3}{2}\rangle_a\lvert\frac{3}{2},-\frac{1}{2}\rangle_b+\lvert\frac{3}{2},-\frac{1}{2}\rangle_a\lvert\frac{3}{2},-\frac{3}{2}\rangle_b\right\}$	$^2P_{3/2}+{}^2P_{3/2}$
$b', {}^3\Delta_u$	2_u	$\frac{1}{\sqrt{2}}\left\{\lvert\frac{3}{2},\ \frac{3}{2}\rangle_a\lvert\frac{1}{2},\ \frac{1}{2}\rangle_b+\lvert\frac{1}{2},\ \frac{1}{2}\rangle_a\lvert\frac{3}{2},\ \frac{3}{2}\rangle_b\right\}$ $\frac{1}{\sqrt{2}}\left\{\lvert\frac{3}{2},-\frac{3}{2}\rangle_a\lvert\frac{1}{2},-\frac{1}{2}\rangle_b+\lvert\frac{1}{2},-\frac{1}{2}\rangle_a\lvert\frac{3}{2},-\frac{3}{2}\rangle_b\right\}$	$^2P_{3/2}+{}^2P_{1/2}$
$^3\Delta_u$	3_u	$\lvert\frac{3}{2},\ \frac{3}{2}\rangle_a\lvert\frac{3}{2},\ \frac{3}{2}\rangle_b$ $\lvert\frac{3}{2},-\frac{3}{2}\rangle_a\lvert\frac{3}{2},-\frac{3}{2}\rangle_b$	$^2P_{3/2}+{}^2P_{3/2}$

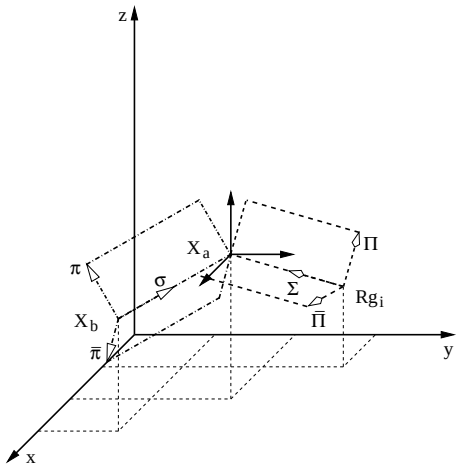

Figure 2.2: Body-frame transformation from the initial molecular reference frame $M = (\Pi, \bar{\Pi}, \Sigma)$ of the X_a-Rg_i van der Waals complex via the laboratory frame $L = (x, y, z)$ to the final reference frame $D = (\pi, \bar{\pi}, \sigma)$ of the X_a-X_b molecule.

states, which are spatially associated with the X_2 molecular axis. This requires a number of transformation steps, which are detailed in the following.

2.3.1 Body-Frame Transformation

A single van der Waals complex X_α-Rg_i can be imagined as a halogen p-radical interacting with a closed shell s^2p^6-atom. Its electronic angular momenta can be classified in terms of Σ- and Π-type interactions. The matrix representation of its interaction Hamiltonian, $\mathbf{V}_M^{X_\alpha - Rg_i}$, is diagonal in the basis set $\{|p_\Pi\rangle, |p_{\bar{\Pi}}\rangle, |p_\Sigma\rangle\}$ of the respective molecular reference frame $M = (\Pi, \bar{\Pi}, \Sigma)$ (see Fig. 2.2):

$$\mathbf{V}_M^{X_\alpha - Rg_i} = \begin{pmatrix} V_\Pi & 0 & 0 \\ 0 & V_{\bar{\Pi}} & 0 \\ 0 & 0 & V_\Sigma \end{pmatrix} . \tag{2.4}$$

In order to express this fragment Hamiltonian with respect to the quantization axis of the dihalogen molecule X_a-X_b a two-step sequence of body-frame transformations is employed (see Ref. [40]) as it is schematically depicted in Fig. 2.2.
At first, an orthogonal matrix $\mathbf{T}_{M,L}$ is applied to $\mathbf{V}_M^{X_\alpha - Rg_i}$ according to the following unitary transformation:

$$\mathbf{V}_L^{X_\alpha - Rg_i} = \mathbf{T}_{M,L}\, \mathbf{V}_M^{X_\alpha - Rg_i}\, \mathbf{T}_{M,L}^{\mathrm{T}} . \tag{2.5}$$

This step carries the diatomic fragment Hamiltonian $\mathbf{V}_M^{X_\alpha - Rg_i}$ into the laboratory frame $L = (x, y, z)$. In the respective basis set $\{|p_x\rangle, |p_y\rangle, |p_z\rangle\}$ of unique orientation the matrix representation $\mathbf{V}_L^{X_\alpha - Rg_i}$ is then no longer diagonal.
The transformation matrix $\mathbf{T}_{M,L}$ in Eq. (2.5) is associated with the *transpose* of the Eulerian rotation matrix Eq. (5.3) in Sec. 5.1 of the Appendix. With reference to Fig. 2.2 its

explicit matrix elements can be expressed by means of Cartesian unit vector components. Skipping the labels α and i for the exemplary characterization of an interaction pair X-Rg by its distance vector $\mathbf{R}$ with the norm R, the axial unit vector components $\mathbf{R}/R$:

$$e_x = \frac{x}{R}, \qquad e_y = \frac{y}{R}, \qquad e_z = \frac{z}{R} \tag{2.6}$$

can be used for conveniently defining the trigonometric functions of the Eulerian azimuthal and polar angles α and β, respectively:

$$\cos\alpha = \frac{e_x}{\sqrt{1-e_z^2}} \qquad \sin\alpha = \frac{e_y}{\sqrt{1-e_z^2}} \tag{2.7}$$

$$\cos\beta = e_z \qquad \sin\beta = \sqrt{1-e_z^2}\,. \tag{2.8}$$

Explicitly, the application of the latter in the unitary transformation Eq. (2.5) results in an all-Cartesian representation of X-Rg Hamiltonian matrix in the laboratory frame L:

$$\mathbf{V}_L^{X_\alpha - Rg_i} = \begin{pmatrix} V_\Pi + (V_\Sigma - V_\Pi)e_x^2 & (V_\Sigma - V_\Pi)e_x e_y & (V_\Sigma - V_\Pi)e_x e_z \\ (V_\Sigma - V_\Pi)e_y e_x & V_\Pi + (V_\Sigma - V_\Pi)e_y^2 & (V_\Sigma - V_\Pi)e_y e_z \\ (V_\Sigma - V_\Pi)e_z e_x & (V_\Sigma - V_\Pi)e_z e_y & V_\Pi + (V_\Sigma - V_\Pi)e_z^2 \end{pmatrix}\,. \tag{2.9}$$

Since this frame is the same for all X-Rg interaction pairs, the individual fragment Hamiltonian matrices $\mathbf{V}_L^{X_\alpha - Rg_i}$ can be summed up separately for each halogen atom X_a and X_b:

$$\mathbf{V}_L^{X_\alpha - Rg} = \sum_{i=1}^{N-2} \mathbf{V}_L^{X_\alpha - Rg_i}\,. \tag{2.10}$$

This direct summation at the first level of transformation steps can considerably save computational effort as compared to a summation at the end of all subsequent transformation steps. It appears that this efficiency aspect has been overlooked in previous works [37,40,46] utilizing the DIM approach.

In a second unitary transformation step, another orthogonal matrix, $\mathbf{T}_{L,D}$, which specifies the mutual orientation of both halogen atoms with respect to the laboratory frame, is applied to the individual partial sums $\mathbf{V}_L^{X_\alpha - Rg}$ from Eq. (2.10):

$$\mathbf{V}_D^{X_\alpha - Rg} = \mathbf{T}_{L,D}\,\mathbf{V}_L^{X_\alpha - Rg}\,\mathbf{T}_{L,D}^{\mathrm{T}}\,, \tag{2.11}$$

resulting in their new representation $\mathbf{V}_D^{X_\alpha - Rg}$ within the reference frame $D = (\pi, \bar{\pi}, \sigma)$ of the dihalogen (cf. Fig. 2.2). The transformation matrix $\mathbf{T}_{L,D}$ now directly corresponds to the Eulerian matrix in Eq. (5.3), so its matrix elements can be obtained in analogy to Eq. (2.7). This second transformation step, however, is necessary only if a reorientation of the X_2 molecule relative to the laboratory frame needs to be taken into account explicitly, e.g. for the description of its restricted and free rotation in solid and liquid rare gases, respectively.

2.3.2 Spin-Orbit Coupled Representation

Being expressed in a basis set $|p_D\rangle$ of real p-orbitals $\{|p_\pi\rangle, |p_{\bar{\pi}}\rangle, |p_\sigma\rangle\}$ with the desired orientation, three more steps are necessary for representing the X-Rg Hamiltonian in a basis of spin-orbit coupled functions $|J, M\rangle$. In order to keep these steps self-contained, the explicit definition of the transformation matrices is given in Sec. 5.2 of the Appendix. First, a transformation matrix $\mathbf{T}_{D,m_l}$ converts the real-valued representation of $\mathbf{V}_D^{X_\alpha-Rg}$ into its hermitian representation $\mathbf{V}_{m_l}^{X_\alpha-Rg}$ within the complementary basis set $|m_l\rangle$ of electronic angular momentum eigenfunctions according to the unitary transformation:

$$\mathbf{V}_{m_l}^{X_\alpha-Rg} = \mathbf{T}_{D,m_l}\, \mathbf{V}_D^{X_\alpha-Rg}\, \mathbf{T}_{D,m_l}^{\mathrm{T}} \ . \tag{2.12}$$

Next, the electronic spin is introduced by a formal product expansion of the respective basis set $|m_l\rangle$ with spin eigenfunctions $|m_s\rangle$. Accordingly, the Hamiltonian matrix $\mathbf{V}_{m_l m_s}^{X_\alpha-Rg}$ in the uncoupled representation $|m_l, m_s\rangle$ can be obtained by the outer product of $\mathbf{V}_{m_l}^{X_\alpha-Rg}$ from Eq. (2.4) with a 2×2 identity matrix $\mathbf{I}_2$:

$$\mathbf{V}_{m_l m_s}^{X_\alpha-Rg} = \mathbf{V}_{m_l}^{X_\alpha-Rg} \otimes \mathbf{I}_2 \ . \tag{2.13}$$

Starting from this representation of the X-Rg fragment Hamiltonian, its spin-coupled representation $\mathbf{V}_{JM}^{X_\alpha-Rg}$ in the basis set $|J, M\rangle$ can then be obtained by a subsequent unitary transformation with a Clebsh-Gordan matrix $\mathbf{T}_{m_l m_s, JM}$:

$$\mathbf{V}_{JM}^{X_\alpha-Rg} = \mathbf{T}_{m_l m_s, JM}\, \mathbf{V}_{m_l m_s}^{X_\alpha-Rg}\, \mathbf{T}_{m_l m_s, JM}^{\mathrm{T}} \ . \tag{2.14}$$

Note, that a complementary approach has been given by Buchachenko et al. [50,51], where, starting from the spin-coupled representation of the X-Rg fragment Hamiltonian and employing a Jacobian coordinate system, a single Wigner transformation is used for the body-frame transformation between the X-Rg and X_2 quantization axis.

2.3.3 Molecular Basis Representation of X-Rg Fragment Hamiltonians

In order to represent the fragment Hamiltonians $\mathbf{V}_{JM}^{X_\alpha-Rg}$ of the individual halogen atoms X_a and X_b in a basis set of the X_2 molecular states (see Tab. 2.1), at first a tensor product with an 6×6 identity matrix $\mathbf{I}_6$ is applied to each of both matrices separately:

$$\mathbf{V}_{JM_a JM_b}^{X_a-Rg} = \mathbf{V}_{JM}^{X_a-Rg} \otimes \mathbf{I}_6 \tag{2.15}$$

$$\mathbf{V}_{JM_a JM_b}^{X_b-Rg} = \mathbf{I}_6 \otimes \mathbf{V}_{JM}^{X_b-Rg} \ . \tag{2.16}$$

This way, the diatomic Hilbert space $\mathcal{H}_{ab} = \mathcal{H}_a \otimes \mathcal{H}_b$ is introduced by the tensor product of the single atomic Hilbert spaces $\mathcal{H}_a$ and $\mathcal{H}_b$. Correspondingly, its eigenfunctions can be represented by products of atomic eigenfunctions.
The final transformation of the fragment Hamiltonians in Eq. (2.15) and Eq. (2.16) to a joint representation within the basis set of Hund's case c eigenfunctions $\psi_\Omega^{(X_2)}$ (cf. Eq. (2.3))

is accomplished by the following unitary transformation:

$$\mathbf{V}_{\Omega}^{X_2-Rg} = \mathbf{T}_{JM,\Omega} \left(\mathbf{V}_{JM_aJM_b}^{X_a-Rg} + \mathbf{V}_{JM_aJM_b}^{X_b-Rg} \right) \mathbf{T}_{JM,\Omega}^{\mathrm{T}} \ . \tag{2.17}$$

Here, the respective transformation matrix $\mathbf{T}_{JM,\Omega}$ contains the molecular expansion coefficient from Tab. 2.1, its concrete representation is given by Eq. (5.6) in the supplementary Sec. 5.2 of the Appendix.
This step permits the consideration of all X_2-Rg interactions as a perturbation to the energies of the isolated halogen molecule, as well as the assignment of individual matrix elements to the symmetry eigenfunctions of the unperturbed system. Thus, the total electronic Hamiltonian can be expressed as a sum of the diagonal matrix $\mathbf{H}_{\Omega}^{X_2}$ for the dihalogen molecule and a non-diagonal matrix $\mathbf{V}_{\Omega}^{X_2-Rg}$ for its interaction with the rare gas matrix. As the interaction among the Rg-atoms is independent of the electronic state of the dihalogen molecule, it contributes with the same value to each diagonal element of the total electronic Hamiltonian, to which it simply can be added after multiplication by a 36×36 identity matrix $\mathbf{I}_{36}$:

$$\mathbf{H}_{\Omega}^{el} = \mathbf{H}_{\Omega}^{X_2} + \mathbf{V}_{\Omega}^{X_2-Rg} + \left(\sum_{i=1}^{N-3} \sum_{j=i+1}^{N-2} V^{Rg_i-Rg_j} \right) \times \mathbf{I}_{36} \ . \tag{2.18}$$

This Hamiltonian parametrically depends on all nuclear coordinates. Further, upon choosing Hund's case c states as a basis, it contains the spin-orbit coupling. In contrast to the more common LCAO ansatz (linear combination of atomic orbitals) for molecular orbitals the DIM wave functions as defined by Eq. (2.3) consist of products of atomic functions, which do not depend on the inter-nuclear separation. In that sense they form a crude diabatic basis of zero-order states, so that the non-diagonal Hamiltonian matrix in Eq. (2.18) can be termed diabatic with respect to the X_2-Rg interaction. Accordingly, the eigenvectors of Eq. (2.18) are adiabatic states, which can be expressed as a superposition of the diabatic ones.

2.4 Application to Br_2 in Ar

2.4.1 Pair Potentials

According to the semi-empirical character of the DIM method the matrix elements of the separate Hamiltonian terms in Eq. (2.18) are parameterized by pair potentials. For parameterizing the matrix elements of the X_2 Hamiltonian (see Sec. 2.2) the Br_2 potential energy curves depicted in Fig. 2.3 have been used. They are based on spin-orbit coupled configuration interaction (SOCI) calculations and have been provided by S. Yabushita [116]. Due to degeneracy effects these 23 potential energy curves give rise to the 36 diagonal elements required for the matrix representation of the molecular Br_2 Hamiltonian.
With reference to Eq. (2.4) in Sec. 2.3 the Br-Ar interaction is characterized by two anisotropic components V_{Σ} and V_{Π} (see Fig. 2.4), which have been determined using the

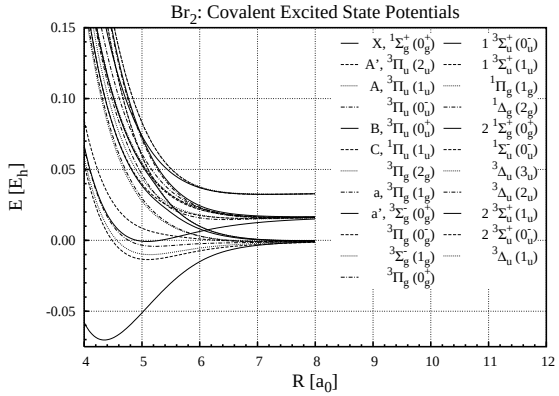

Figure 2.3: Ab initio SOCI potential energy curves for the lower 23 molecular Hund's case c states of Br_2 originating from its $\sigma_g^2\pi_u^4\pi_g^4\sigma_u^0$ MO configuration [116] (see also Ref. [108,117]). Potential energy curves are ordered by increasing Franck-Condon excitation energies from ground state minimum, state labels are explained in Tab. 2.1.

piecewise analytic spin-orbit coupled potentials $V_{3/2,1/2}, V_{3/2,3/2}$ and $V_{1/2,1/2}$ from photoelectron spectroscopic data by Neumark et al. [118, 119], according to the following relations [120]:

$$V_\Sigma = \frac{(\frac{2}{3}\Delta + V_{3/2,1/2})V_{3/2,3/2} - (\Delta + V_{3/2,1/2})V_{3/2,1/2}}{V_{3/2,3/2} - V_{3/2,1/2} - \frac{1}{3}\Delta} \tag{2.19}$$

$$V_\Pi = V_{3/2,1/2}\ . \tag{2.20}$$

In order to enable an analytic evaluation of forces and force constants, the numerical data from Eq. (2.19) and Eq. (2.20) have been refitted to continuous functions of Extended Rydberg (ER) type [121]:

$$V_{ER} = -D_e\left(1 + a_1(R-R_e) + a_2(R-R_e)^2 + a_3(R-R_e)^3\right)e^{-a_1(R-R_e)}\ . \tag{2.21}$$

The corresponding parameters dissociation energy D_e, equilibrium distance R_e as well as the Taylor expansion coefficients a_1, a_2, a_3 are compiled in Tab. 2.2. Note, that the error of the fit is on the order of 1%, but the error of the source data [118, 119] on the order of 10%.

For modelling the Ar-Ar interaction a simple Lennard-Jones (LJ) potential (see Fig. 2.4) has been utilized:

$$V_{LJ} = 4\varepsilon\left(\left(\frac{\sigma}{R}\right)^{12} - \left(\frac{\sigma}{R}\right)^{6}\right)\ , \tag{2.22}$$

which closely resembles the accurate Hartree-Fock-dispersion (HFDID) potential given by Aziz [122, 123]. The particular values for the Lennard-Jones energy ε and the van der Waals radius σ are listed in Tab. 2.2, likewise.

When comparing both interactions in Fig. 2.4 and Tab. 2.2, the binding energy on the order of 10^{-4} E_h clearly underlines their dispersive van der Waals nature. In order to avoid the numerical overhead of long-range contributions in the calculation of pair interactions, the

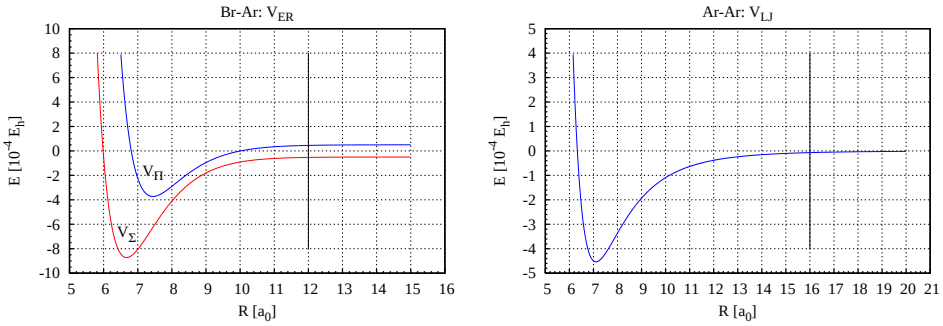

Figure 2.4: Br-Ar interaction (left) with the anisotropic components V_Σ and V_Π and isotropic Ar-Ar interaction (right). The cut-off radii $R_C^{Br-Ar} = 12$ a$_0$ and $R_C^{Ar-Ar} = 16$ a$_0$ are indicated by vertical lines each. For purposes of better visibility the potentials V_Π and V_Σ have been shifted off by $\pm 0.5 \times 10^{-4}$ E$_h$.

cut-off radii $R_C^{Br-Ar} = 12$ a$_0$ and $R_C^{Ar-Ar} = 16$ a$_0$ have been utilized for the Br-Ar and Ar-Ar potentials, respectively.

Table 2.2: Pair Potential Parameters

Br-Ar				Ar-Ar		
Extended Rydberg		V_Σ	V_Π	Lennard-Jones		V_{LJ}
D_e	$[10^{-4}E_h]$	8.223	4.226	ε	$[10^{-4}E_h]$	4.536
R_e	$[a_0]$	6.672	7.446	σ	$[a_0]$	6.331
a_1	$[a_0^{-1}]$	1.773	1.635			
a_2	$[a_0^{-2}]$	0.525	0.242			
a_3	$[a_0^{-3}]$	0.146	0.063			

2.4.2 Choice of the Simulation Box

As it has already been shown in previous works on Cl_2 [124–126] and I_2 [22, 23, 25] in Ar matrices, also in the case of Br_2 [127, 128] the halogen molecule occupies a double substitutional lattice site along the ⟨110⟩ crystallographic direction of a face-centered cubic (fcc) Ar crystal, which is depicted in Fig. 2.5. A lattice cutout along this direction exposes an overall D_{2h} symmetry for the Ar atoms surrounding the chromophore. In the following, the construction of an adequate simulation box, reflecting this particular symmetry, is detailed.

Therefore, at first the unit cell of an Ar fcc lattice as depicted in Fig. 2.6 is considered. It contains $N = 4$ atoms per cube with the lattice constant a, the volume $V = a^3$ and the number density $\rho = \frac{N}{V} = \frac{4}{a^3}$. For a typical reduced density $\rho^* = \rho \cdot \sigma^3 = 1$ in terms of the Lennard-Jones parameter σ (see Tab. 2.2) its lattice constant is determined by $a = \sqrt[3]{4} \cdot \sigma = 10.05$ a$_0$.

Upon bisection by the [110] crystallographic plane, according to Fig. 2.6 the tetra-atomic basis element of the fcc unit cell is cleaved along its diagonal into subunits with the lattice constant $\frac{a}{\sqrt{2}}$. By its two atoms these subunits each define new basis elements for the generic

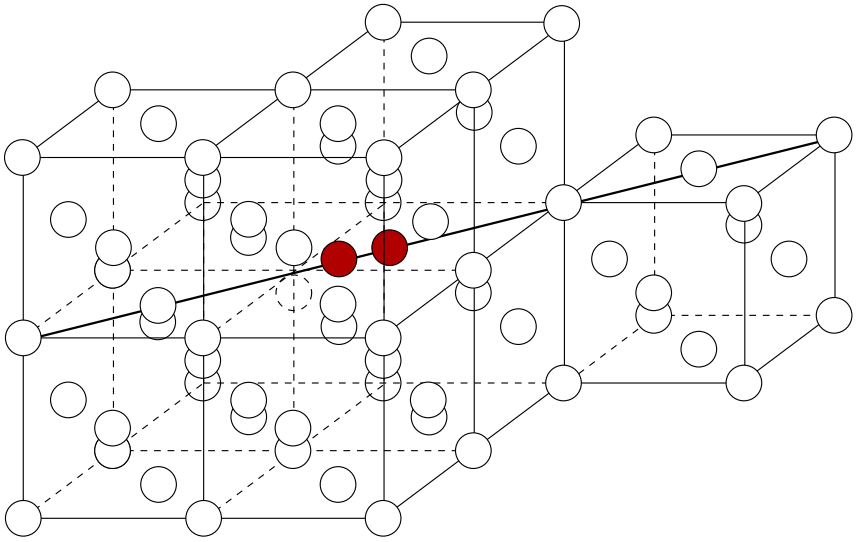

Figure 2.5: Br_2 molecule (filled circles) in a double substitutional site pointing in ⟨110⟩ direction (solid line) of an Ar fcc lattice (empty circles).

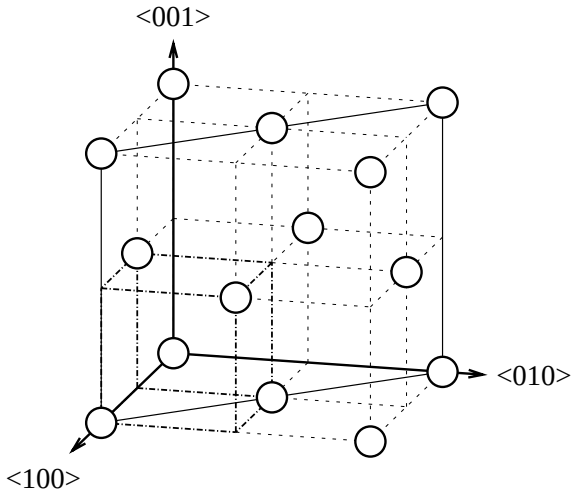

Figure 2.6: Unit cell of the Ar fcc lattice. Upon bisection by the [110] plane (solid frame) its tetra-atomic basis element (dash-dotted sub-cube) forms two new basis elements with each two atoms, whose repetitive translation generates a specific prolongation of the lattice along ⟨110⟩ direction, see Fig. 2.7.

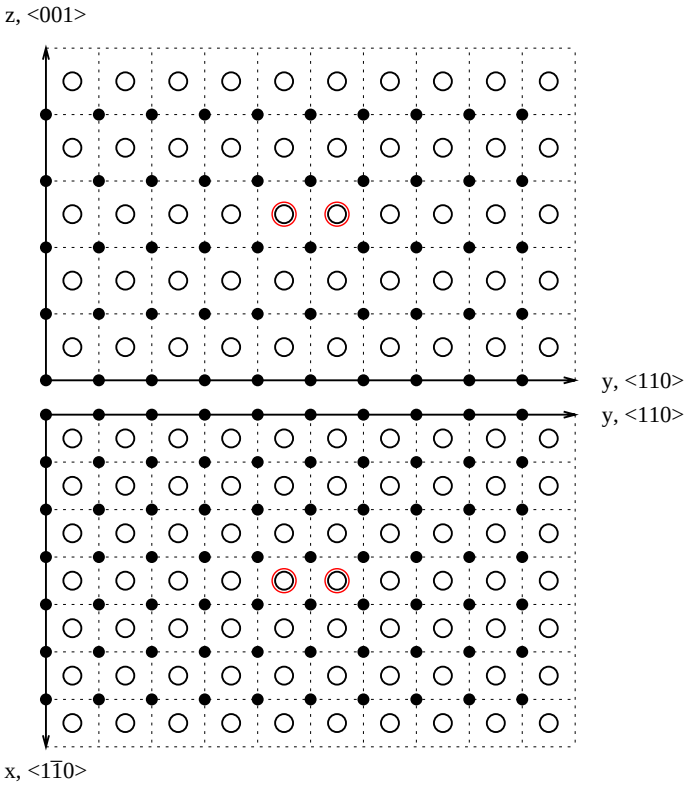

Figure 2.7: Schematic front (yz) and top (xy) view of an orthorhombic simulation box in $\langle 110 \rangle$ direction. It consists of $7 \times 10 \times 5$ primitive cells (dashed) along the directions x,y,z. The two central Br atoms (hidden) are covered by doubly layered arrays of Ar atoms shown in stereographic projection (dots and circles).

translation of the lattice in $\langle 110 \rangle$ direction. The resulting super-cell is depicted in Fig. 2.7. Its particular extension is determined by the sum of the Br-Ar and Ar-Ar cut-off radii, such, that each Ar atom within the cut-off distance R_C^{Br-Ar} being influenced by the linear motion of the Br_2 molecule between its two adjacent Ar neighbors with the separation $2 \times \frac{a}{\sqrt{2}}$, can interact with all other Ar atoms within the radius R_C^{Ar-Ar}. Explicitly, this requirement results in a box dimension of 56 $a_0 \times 70.22$ $a_0 \times 56$ a_0 along the directions x,y and z. This criterion is fulfilled using *either* $7 \times 10 \times 5$ *or* $8 \times 10 \times 6$ primitive cells with $N = 700$ and $N = 960$ atoms in total, respectively. For most of the calculations in this work the smaller simulation box in Fig. 2.7 has been applied obtaining fully converged results as compared to the larger box. This finding can be understood from the pair distribution histogram in Fig. 2.8. Here, the interactions among the N atoms give rise to $\frac{1}{2}N(N-1)$ pairs in total, which are individually distributed over the distance R_{ij}. When considering only the relevant contributions, e.g. among the Ar atoms within the radius $R_{ij} \leq R_C^{Ar-Ar}$, this number can be reduced effectively by more than 90%, such, that it scales linearly with the box size.

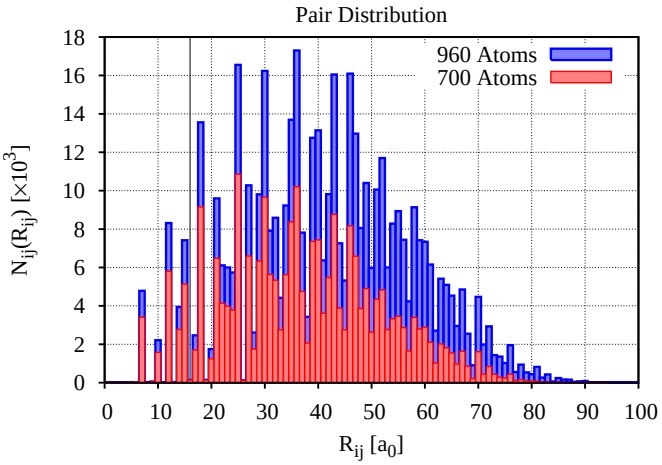

Figure 2.8: Pair distribution histogram showing the number of pairs N_{ij} versus pair distance R_{ij} for two different simulation boxes with $N = 700$ (foreground) and $N = 960$ (background) atoms. The application of the cut-off radius $R_C^{Ar-Ar} = 16$ a$_0$ (solid line) restricts the number of relevant pairs by more than 90%.

2.4.3 Geometry Relaxation

As a prerequisite for the considerations in Sec. 2.4.4 and Sec. 3.2.2 the individual equilibrium geometries of the system from Fig. 2.7 have to be calculated for the electronic X- as well as B-state. Therefore, modified Newtonian equations of motion, Eq. (5.17) and Eq. (5.18) of the Nosé-Hoover Thermostat in the Appendix (see Sec. 5.3), have been solved using the following finite-difference Velocity-Verlet algorithm [129]:

1st half-step:

$$x_i(t+\delta t) = x_i(t) + v_i(t)\delta t + \frac{1}{2}\left[\frac{f_i(t)}{m_i} - \xi(t)v_i(t)\right]\delta t^2 \tag{2.23}$$

$$v_i(t+\frac{\delta t}{2}) = v_i(t) + \left[\frac{f_i(t)}{m_i} - \xi(t)v_i(t)\right]\frac{\delta t}{2} \tag{2.24}$$

$$\xi(t+\delta t) = \xi(t) + \frac{\sum_{i=1}^{3N} m_i v_i^2(t+\frac{\delta t}{2}) - 3Nk_BT_f}{M}\delta t \tag{2.25}$$

2nd half-step:

$$v_i(t+\delta t) = \frac{1}{1+\xi(t+\delta t)\frac{\delta t}{2}}\left[v_i(t+\frac{\delta t}{2}) + \frac{f_i(t+\delta t)}{m_i}\frac{\delta t}{2}\right] . \tag{2.26}$$

In its first step, the atomic positions x_i and the friction coefficient ξ at time $t+\delta t$ are obtained from their values at time t according to Eq. (2.23) and Eq. (2.25). In the second step the velocities v_i at time $t+\delta t$, Eq. (2.26), are updated from their values at time $t+\frac{\delta t}{2}$ of the previous step, Eq. (2.24), after the forces f_i have been recalculated.
As numerical parameters for the integration of these coupled equations of motion a time step $\delta t = 1$ fs, a final simulation temperature $T_f = 10^{-6}$ K and a reservoir coupling parameter $M \equiv m_{Ar}$ have been used. According to Eq.(2.25) the last two parameters continuously adjust the strength of the friction coefficient.

In order to preserve the symmetry of the system in the propagation, the following initial conditions have been applied:

$$v_i(t=0) = 0 \qquad x_i(t=0) = x_i^0$$
$$\xi(t=0) = 0 \qquad f_i(t=0) = f_i^0$$

This way, rather than starting from a random velocity distribution for a given temperature, the forces f_i^0 at the ideal atomic positions x_i^0 have been initiated first. These forces f_i depend on the respective electronic state and can be obtained analytically in the scope of the present DIM approach as detailed in Sec. 5.5 of the Appendix.
In order to explicitly take into account the periodic character of a solid, the simulation box in Fig. 2.7 was subject to periodic boundary conditions and minimum image convention [130,131]. In other words, periodic boundary conditions ensure that each particle exceeding the box boundaries reenters the simulation box from the opposite side. In combination with cut-off radii the minimum image convention guarantees that each particle at the boundary of the box shares the same coordination sphere as in its center.

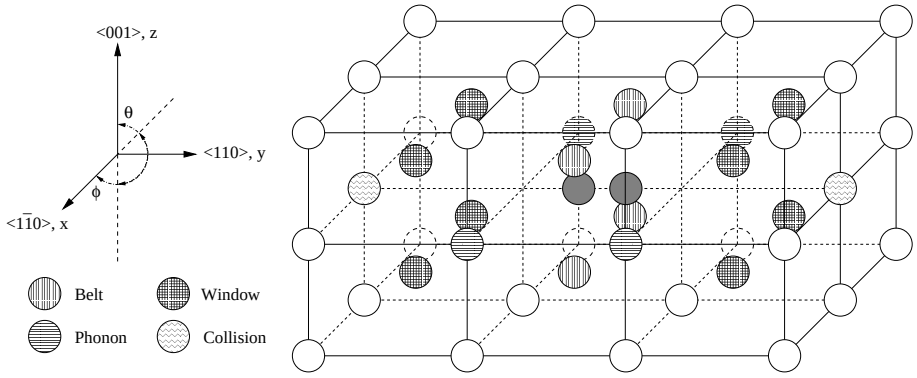

Figure 2.9: Cage of nearest neighbor (Belt, Phonon, Window and Collision) atoms surrounding the Br_2 molecule (filled).

Table 2.3: Absolute (10^{-3} a_0) and relative (%) displacements of nearest neighbor Ar atoms (see Fig. 2.9) with respect to their idealized lattice values for a relaxation of the system in the electronic X- and B states. The direction of the individual displacements is specified by a positive or negative sign.

State	X-State			B-State		
Shift	Δx	Δy	Δz	Δx	Δy	Δz
Belt	+198 (5.6)	0 (0.0)	+467 (9.3)	+193 (5.4)	0 (0.0)	+389 (7.7)
Phonon	+45 (0.6)	−80 (2.2)	0 (0.0)	+62 (0.9)	−64 (1.8)	0 (0.0)
Window	−33 (0.9)	−156 (2.2)	−55 (1.1)	−18 (0.5)	−126 (1.8)	−32 (0.6)
Collision	0 (0.0)	−193 (1.8)	0 (0.0)	0 (0.0)	−214 (2.0)	0 (0.0)

The results of both, the X-state and the B-state relaxation, are listed in Tab. 2.3 showing the absolute and relative displacements of nearest neighbor cage atoms with respect to their idealized lattice positions. Adapting the terminology from Ref. [17] these nearest

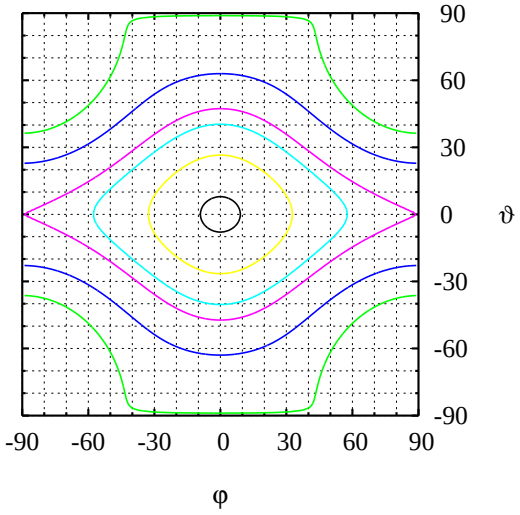

Figure 2.10: Ground round state rotational barrier for Br_2 inside the relaxed cage cavity for fixed $R = 4.35$ a_0 (contour levels 0.0007, 0.0100, 0.0300, 0.0467, 0.1000, 0.1684 E_h).

neighbor atoms depicted in Fig. 2.9 will be labelled Belt, Phonon, Window and Collision atoms (see Fig. 2.9) in the following. Inspecting Tab. 2.3 the overall relaxation effect is seen to be dominant for the Belt atoms, which are pushed outwards due to the repulsion by the chromophore. As consequence of the lowered lattice constant induced by the smaller interatomic separation of the Bromine atoms as compared to the pure Ar lattice the Window atoms are pulled inwards. Likewise, albeit weaker, the Collision atoms are influenced by this shift. The Phonon atoms, on the other hand, which lie in the same plane as the molecule, exhibit only marginal displacements. These findings are in qualitative [17] and quantitative [127, 128] accordance with previous trajectory simulations for Cl_2 and Br_2 in Ar, respectively.

Ground State Rotational Barrier

In addition to the calculated ground state equilibrium geometry also the reorientation of the Br_2 molecule away from the $\langle 110 \rangle$ direction due to its zero-point librational motion has been investigated. Therefore, the ground state barriers for its rotation within the relaxed matrix have been calculated for a fixed Bromine X-state equilibrium bond length $R = 4.35$ a_0 with frozen Ar positions. Starting from the $\langle 110 \rangle$ direction with the coordinates $\varphi = \vartheta = 0°$ the azimuthal and polar angles $-90° \leq \varphi \leq 90°$ and $-90° < \vartheta < 90°$ are defined with respect to the directions $\langle 1\bar{1}0 \rangle$ and $\langle 001 \rangle$ as shown in Fig. 2.9.
According to Fig. 2.10 the energies of the rotational barriers in the directions φ and ϑ can be estimated to 0.047 and 0.168 E_h, respectively. The ratio between these barriers can be understood by a restriction of the rotation by 12 Ar atoms (4 Belt *and* 8 Window atoms) in ϑ-direction versus only 4 Ar atoms (Phonon atoms) in φ-direction. In contrast to the rotational flexible molecules HCl [132–134], HF [135] and ClF [136–140] within the single substitutional site of the Ar lattice, the high ground state barriers for Br_2 indicate that there is no comparable mobility within the double substitutional lattice site. Neglecting

the zero-point librational energy and assuming a ground state vibrational energy of $E_0 \approx 160\ \mathrm{cm}^{-1}$, the librational motion of Br_2 is thus confined to the range $-10° \leq \varphi \leq 10°$ and $-8° \leq \vartheta \leq 8°$. Similar results have been reported for vibrational ground state of Cl_2 in Xe matrices [37].

2.4.4 Classification of Coupling Types

The matrix representation of the electronic DIM-Hamiltonian in the diabatic basis set of 36 dihalogen molecular states makes the detailed investigation of its individual matrix elements, which parametrically depend on all $3N$ nuclear coordinates, a rather complex problem. In particular this holds true for its 630 matrix-induced coupling elements. Thus, this task demands for a problem specific reduction concerning the number of electronic states as well as the number of nuclear degrees of freedom. As a prerequisite it requires the identification and analysis of relevant electronic states and nuclear degrees of freedom. The first step, which is the analysis and subsequent reduction of the electronic Hamiltonian, is considered in this section, the identification of relevant nuclear coordinates is explored in Chap. 3.

Starting from the overall D_{2h} symmetry of Ar atoms around the Br_2 molecule in the relaxed ground state geometry and fixing the Ar atomic positions the two following scenarios are expect to be predominant at low temperatures:

First, a D_{2h} preserving elongation of the Br_2 molecule with respect to its center of mass. Second, a respective elongation along with a tilting of the Br_2 molecular axis about 10° and 8° towards the directions $\langle 1\bar{1}0 \rangle$ and $\langle 001 \rangle$, respectively. This configuration results in a Hamiltonian of C_i symmetry and shall illustrate the effect of symmetry lowering.

The key step in the analysis of the Hamiltonian matrix is its partitioning into individual sub-matrices. With reference to the diagonal structure of the molecular Hamiltonian in the basis set of Hund's case c symmetry eigenfunctions, according to Sec. 2.3.3 the effect of the rare gas atoms can be understood as a perturbation, which induces the coupling among different molecular states. Regardless of its specific structure, this perturbation may be separated into components having the same or a different symmetry as compared to the isolated molecule. Such a projection of the matrix-induced perturbation can be accomplished by imposing the symmetry blocks of the isolated molecule as a mask onto the total Hamiltonian matrix as it is schematically depicted in Fig. 2.11.

According to the partitioning by this mask the off-diagonal elements within the diagonal blocks may be termed *intra-symmetric* couplings, since they couple the diagonal elements (molecular potential energy curves) among each other. In contrast, the matrix elements within the off-diagonal blocks couple sub-matrices of different symmetries and hence may be called *inter-symmetric* couplings. Due to the mixing effects induced by the inter-symmetric coupling type the irreducible representations to the symmetry group $D_{\infty h}$ of the isolated molecule split up into new irreducible representations to the symmetry point groups D_{2h} and C_i of the individual Hamiltonians. This subduction of the irreducible representations is given in Tab. 2.4.

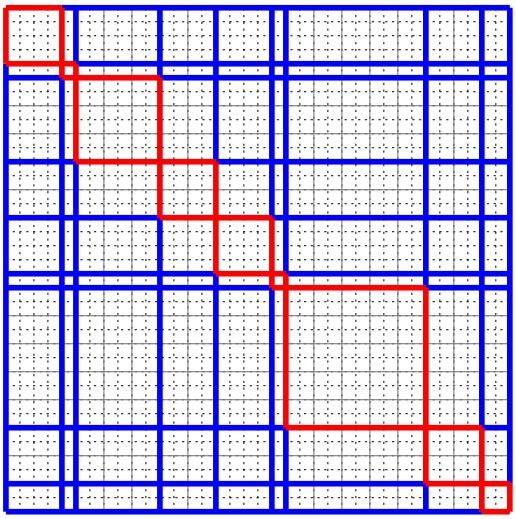

Figure 2.11: Block mask scheme with diagonal blocks containing diagonal and intra-symmetric coupling elements as well as off-diagonal blocks containing inter-symmetric coupling elements. The symmetry blocks are given in the order 0_g^+, 0_g^-, 1_g, 2_g, 0_u^-, 0_u^+, 1_u, 2_u, 3_u top down.

Table 2.4: Subduction of the molecular point group $D_{\infty h}$ into the subgroups D_{2h} and C_i, see [141, 142]. On successive symmetry lowering only the inversions characters g and u are preserved.

$D_{\infty h}$	D_{2h}	C_i
0_g^+	A_g	A_g
0_g^-	B_{1g}	A_g
1_g	$B_{2g} \oplus B_{3g}$	A_g
2_g	$A_g \oplus B_{1g}$	A_g
0_u^-	A_u	A_u
0_u^+	B_{1u}	A_u
1_u	$B_{2u} \oplus B_{3u}$	A_u
2_u	$A_u \oplus B_{1u}$	A_u
3_u	$B_{2u} \oplus B_{3u}$	A_u

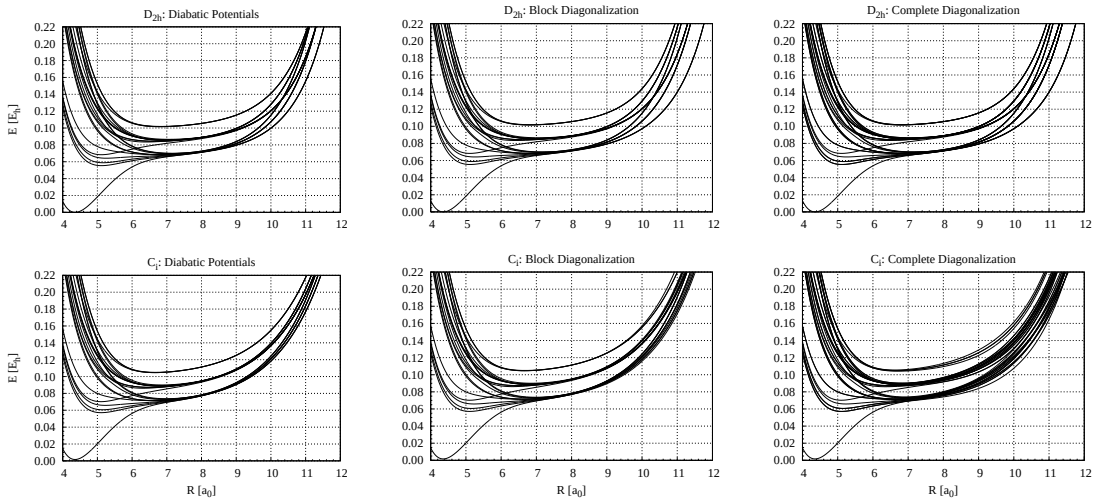

Figure 2.12: Manifold of diabatic potential energy curves (left) compared to those obtained from the first (middle) and second (right) diagonalization step for Br_2 in Ar with D_{2h} (top) and C_i (bottom) symmetry.

The separate role of the two coupling types in this subduction can be unravelled by a two-step diagonalization procedure. This procedure is guided by the symmetry rather than by the strength of the interaction. In its first step, the intra-symmetric couplings are taken into account exclusively, whereas the inter-symmetric couplings are incorporated into the second step. In that sense the second step just completes the *partial* diagonalization of states, which has been achieved in the first step.

This sequence is illustrated in Fig. 2.12 contrasting the manifold of the diabatic versus the adiabatic potential energy curves obtained by the first and second diagonalization steps for the respective Hamiltonians of D_{2h} and C_i symmetry. When comparing the diabatic potential energy curves in matrix environment to the isolated molecule (see Fig. 2.3) they are bent up with increasing bond length due to repulsive on-diagonal contributions of the Ar atoms. Particularly, this matrix-induced confining potential becomes visible for bond lengths $\mathrm{R} \geq 9$ $\mathrm{a_0}$ in case of the D_{2h}-Hamiltonian, as well as for $\mathrm{R} \geq 8$ $\mathrm{a_0}$ in case of the C_i-Hamiltonian. As expected on the basis of Ligand field theory also the three atomic dissociation limits of the free molecule are perturbed by the Rg matrix, which splits them up into six individual branches. This splitting increases with a higher symmetry of the Hamiltonian.

In the next step, which is depicted by the middle part of Fig. 2.12, this splitting is further increased as a general trend when incorporating the intra-symmetric coupling type into the diagonalization. A more detailed view on its concrete effects is provided by Fig. 2.13 exemplary showing the potential energy curves for each individual symmetry block of the D_{2h}-Hamiltonian. Here, the non-degenerate symmetry blocks 0_g^+ and 0_u^- exhibit avoided crossings at the inner ($5 \leq R \leq 6$ $\mathrm{a_0}$, $0.08 \leq E \leq 0.10$ $\mathrm{E_h}$) and outer turning point ($10 \leq R \leq 11$ $\mathrm{a_0}$, $0.12 \leq E \leq 0.14$ $\mathrm{E_h}$) of the potential curves. A similar effect, albeit more subtle, is seen for the degenerate symmetry blocks 1_g, 1_u, 2_u and 3_u, where the avoided

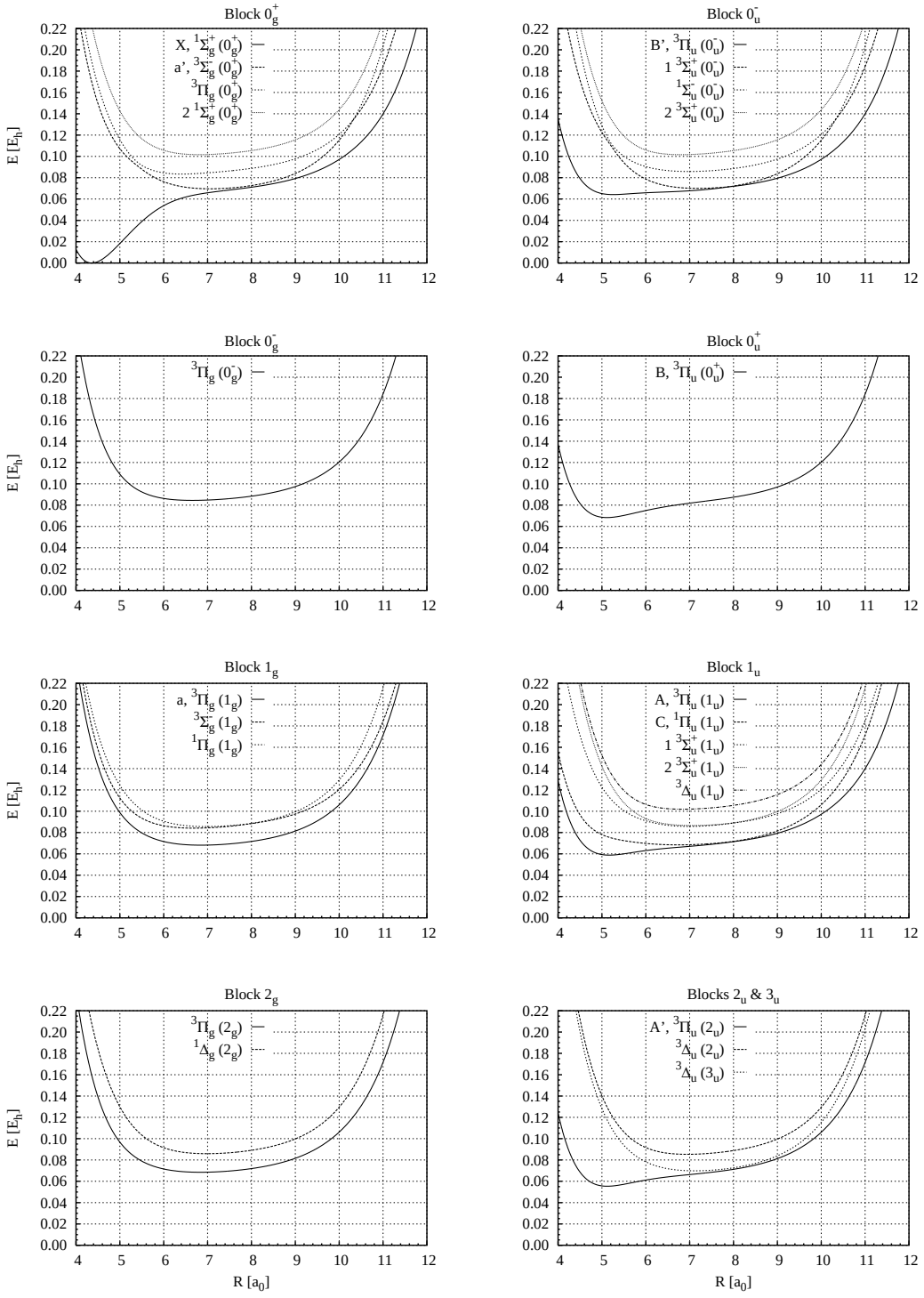

Figure 2.13: Potential energy curves for the DIM valence states along the Br_2 bond distance for fixed Ar positions and D_{2h} symmetry. The data have been obtained by block diagonalization of the Hamiltonian including Ω_w^σ intra-symmetric couplings only. For labeling of the states, compare Tab. 2.1.

crossing is indicated by the increasing energy separation between those potential energy curves, which would share the *same* dissociation limit in the gas phase. Their intrinsic twofold degeneracies, however, are not lifted in this splitting.
The effect of including the inter-symmetric coupling type into the complete diagonalization can be seen when comparing the last two panels in Fig. 2.12 to the preceding block diagonalization step. Inspecting the D_{2h}-Hamiltonian first, one finds almost identical results. Obviously, in the case of an overall D_{2h} symmetry, which can be considered as a subgroup of the $D_{\infty h}$ symmetry group of the isolated molecule, the inter-symmetric coupling type is negligible or even absent here. Thus, in first approximation, one can consider the individual symmetry blocks of the Hamiltonian to be independent. As an important consequence the Hund's case c states of the free molecule retain their meaning, even within the Rg environment. This finding directly justifies the empirical usage of gas phase selection rules in the spectroscopy of dihalogen molecules in cryogenic rare gas matrices.
In contrast to the D_{2h}-Hamiltonian the presence of the inter-symmetric coupling type is explicitly seen for the C_i-Hamiltonian. Starting from bond lengths $R \approx 7$ a_0 this coupling type advances the splitting of the adiabatic potential energy curves towards a complete lifting of all initial degeneracies.
However, in both cases the results suggest, that the interplay of the two coupling types can be considered independently for the three dissociation limits of the free Br_2 molecule, at least as far as moderate bond lengths are concerned. This finding motivates the reduction of the full 36×36 DIM-Hamiltonian matrix towards a smaller sub-matrix, which permits a detailed insight into specific phenomena, such as the predissociation of the electronic B-state.

2.4.5 A Reduced Target-State DIM Hamiltonian

When aiming at a specific reduction of the DIM Hamiltonian the intrinsic energy and coordinate range of the phenomenon investigated provides the main criterion. In application to the B-state excitation of Br_2 in solid Ar this criterion is provided by the Franck-Condon window for the vertical $B \leftarrow X$-transition starting from the ground state equilibrium bond length (see Fig. 2.14).
In order to properly describe the B-state predissociation and the subsequent population of lower lying electronic states a reduced model Hamiltonian should also incorporate the molecular potential curves below to the B-state PES. According to Fig. 2.3 its basis is thus defined by the X (0_g^+)-, A' (2_u)-, A (1_u)-,$^3\Pi_u$ (0_u^-)-, B (0_u^+)-, C (1_u)-, $^3\Pi_g$ (2_g)-, a (1_g)-, a' (0_g^+)-,$^3\Delta_u$ (3_u)- and $1^3\Sigma_u^+$ (0_u^-)-states. Of course, such truncation of the diabatic basis restricts the number of possible linear combinations for the adiabatic states as well as their proportional composition, so that the reduced model has to be checked carefully. This can be accomplished by comparing its eigenvalues and eigenvectors to those obtained from a complete Hamiltonian.
Fig. 2.14 shows the eigenvalues of the reduced D_{2h} and C_i Hamiltonians together with the relative errors with respect to the eigenvalues of the complete Hamiltonians. Comparing

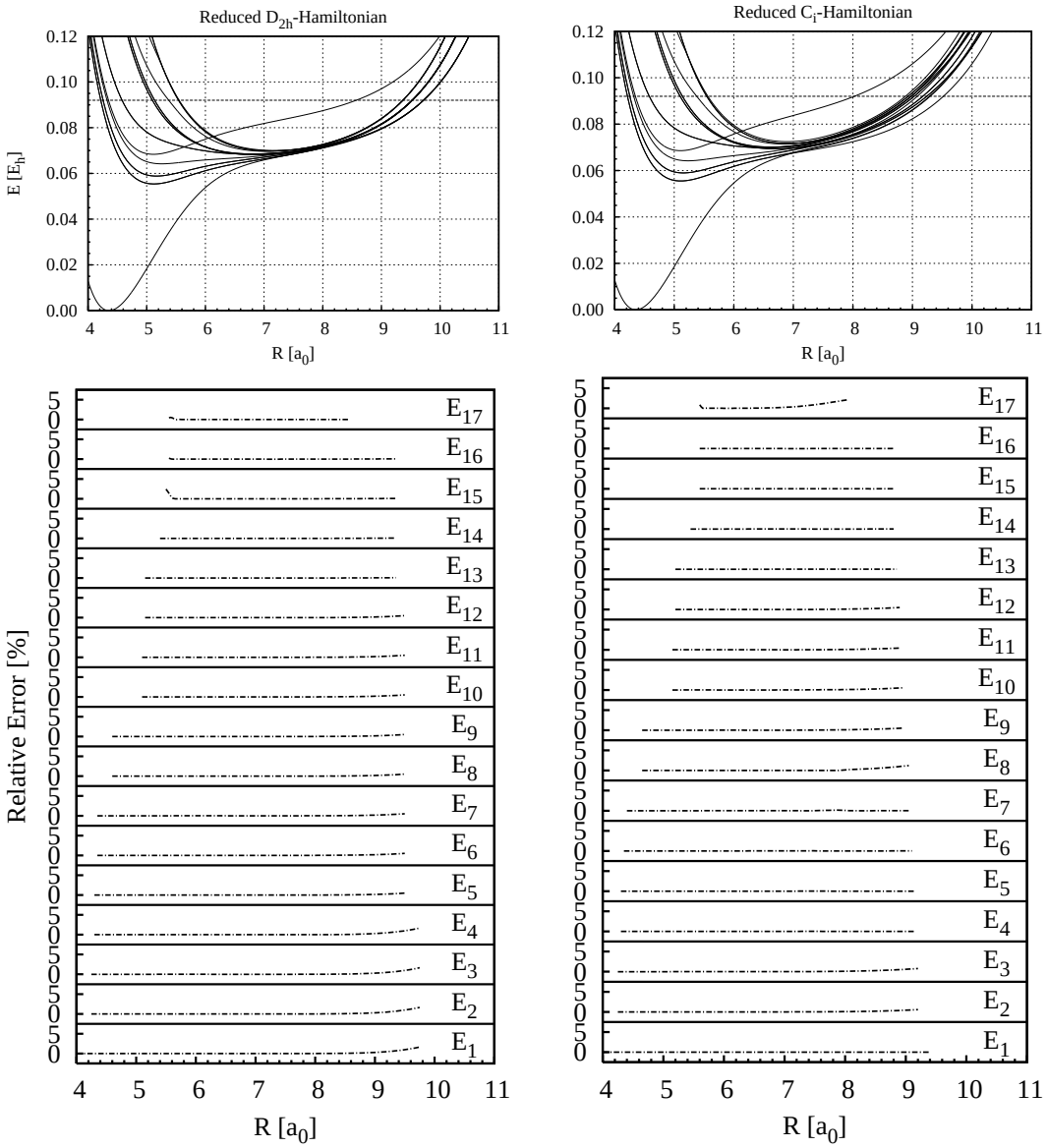

Figure 2.14: Comparison of the 17 adiabatic potential energy curves calculated from reduced Hamiltonians for Br_2 in Ar with D_{2h} and C_i symmetry, the dashed line denotes the Franck-Condon target energy of $E \approx 0.09$ E_h. The lower two panels show the percentage error with respect to the complete Hamiltonian eigenvalues within this target energy interval.

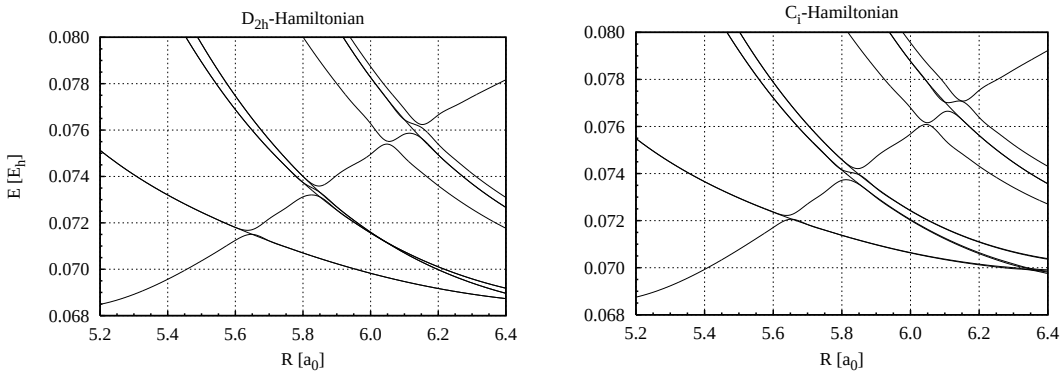

Figure 2.15: Close-up view of the crossing region of the B (0_u^+)-state with the C (1_u)-, $^3\Pi_g$ (2_g)-, a (1_g)-, a' (0_g^+)-, $^3\Delta_u$ (3_u)- and $1^3\Sigma_u^+$ (0_u^-)-state (from left to right) for Br_2 in Ar with D_{2h} (left) and C_i (right) symmetry.

the results for both reduced models, the largest errors occur for the eigenvalue E_{15} and the lower four eigenvalues of the D_{2h}-Hamiltonian, as well as for the eigenvalues E_{17} and E_8 of the C_i-Hamiltonian. However, taking into account that these errors of up to 5% appear only for bond lengths outside the Franck-Condon window of the $B \leftarrow X$ transition, the performance of both reduced Hamiltonians within the target energy interval of $E \approx 0.09\ E_h$ is very good. In other words, the suggested set of potential energy curves is sufficient for reproducing the results of the respective complete Hamiltonians.

B-state Crossing Region

Next, the sensitivity of the reduction within the region shown in Fig. 2.15 is of particular interest, since this region is essential for the predissociation of the B-state. The role of the B-state crossings for predissociation, as well as their dependence on the environmental symmetry, has been investigated by Coker et al. [40, 81] for I_2 in condensed rare gases. Adapting the terminology from Ref. [81] one sees that the overall pattern of quasi-non-avoided (weakly interacting curves) and avoided (strongly interacting curves) B-state crossings is similar for both symmetries investigated. Except for minor differences in the magnitude of the splitting two common characteristics of these crossings can be found on closer examination.

In case the B-state with quantum number $\Omega = 0$ is crossed by a doubly degenerate state $\Omega \neq 0$, there results only *one avoided crossing* whereas *one* of the initially degenerate states follows its original course. In other words a coupling modifies only one of the degenerate states. This circumstance is illustrated by an analytic example of the B, C-state crossing in Sec. 5.4 of the Appendix.

In case that the B-state is crossed by another non-degenerate state with quantum number $\Omega = 0$, there is only avoided crossing and consequently either bound excited state dynamics or predissociative dynamics are to be expected, depending on whether the system follows the upper or the lower part of the adiabatic potential energy curves.

A more detailed view on the quality of the reduction is provided by an analysis of some

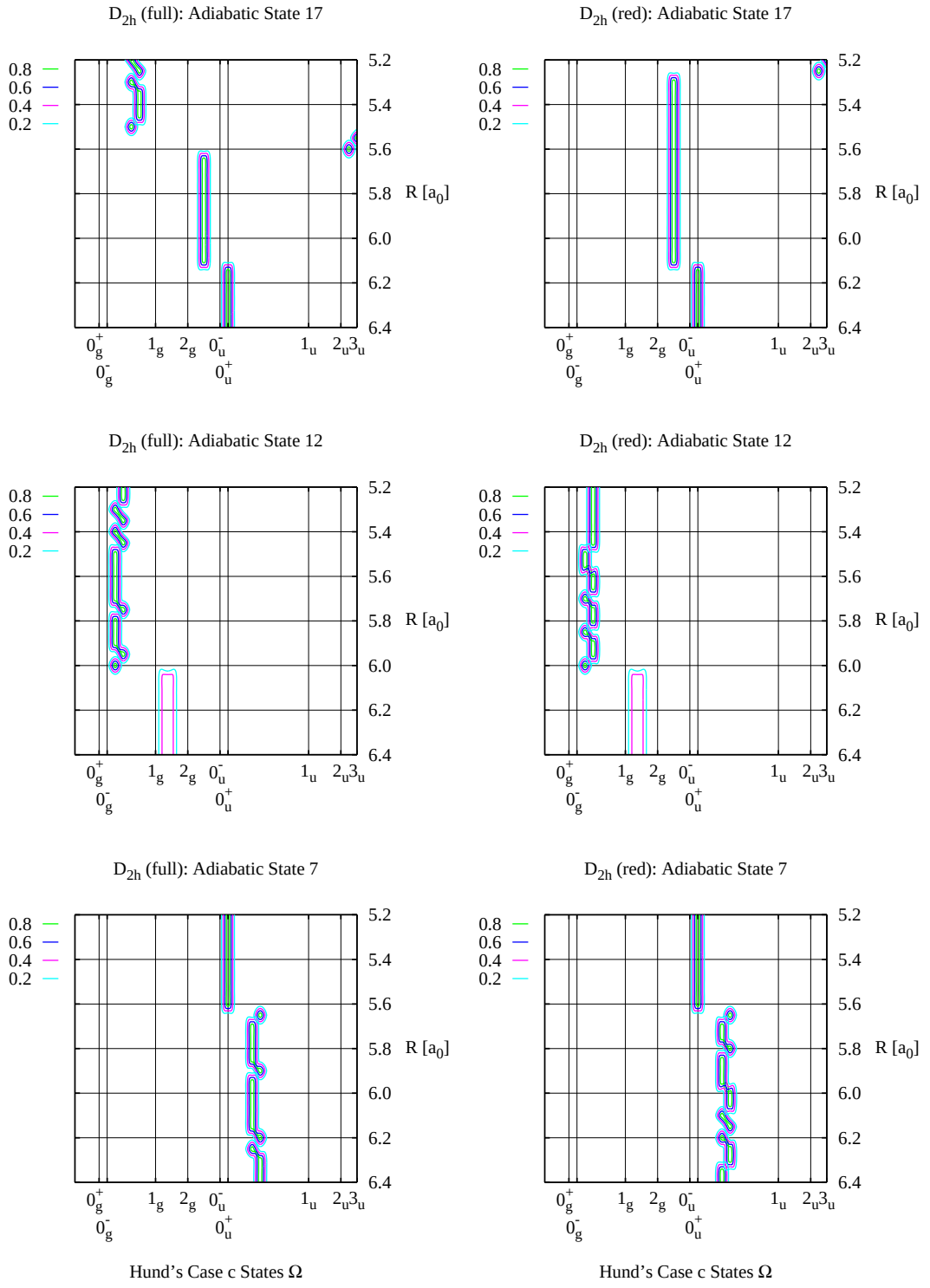

Figure 2.16: Population analysis in 2D projection of the complete (right column) and reduced (left column) D_{2h}-Hamiltonian eigenvectors for the states 17 (upper row), 12 (middle row) and 7 (lower row) corresponding to the highest, an intermediate and the lowest adiabatic potential energy curves in Fig. 2.15.

exemplary eigenvectors out of the B-state crossing region from Fig. 2.15. Therefore, with reference to Fig. 2.14, the eigenvectors to the energy eigenvalues values E_7, E_{12} and E_{17} have been chosen, which correspond to the lowest, a middle one and the highest adiabatic potential curve in Fig. 2.15. Inspired by the overlap criterion of Kuntz et al. [114, 143] the individual populations of the diabatic Hund's case c states have been used as a measure for comparing the composition of adiabatic states between the reduced and full Hamiltonians. The results for the cases D_{2h} and C_i are shown in Fig. 2.16 and Fig. 2.17. In both cases there is an almost quantitative agreement in the composition of the lowest as well as the middle adiabatic states between the reduced and complete Hamiltonians. With respect to the highest adiabatic state, which is energetically close to the set of states discarded from the model, both reduced models deviate in their composition from the complete ones in the range $5.2 \leq R \leq 5.6$ a_0. Here, some of the diabatic states, which are not part of the reduced model, become populated. However, recalling from Fig. 2.14 that the energy of the highest state coincides with the Franck-Condon window only after $R \approx 5.6$ a_0 one can say, that both reduced model Hamiltonians reasonably resemble the complete ones in the relevant regime of B-state crossings.

Next to this quantitative aspects also some qualitative features of the B-state crossings can be explained by means of Fig. 2.16 and Fig. 2.17. As a common characteristic for both cases, a switching between the diabatic states can be found for the lowest and highest adiabatic states. In accordance with Fig. 2.15 these switchings appear at the crossing point $R = 5.6$ a_0 between the B-state (0_u^+ symmetry) and the C-state (1_u symmetry). Further, they appear around $R \approx 6.1$ a_0 between the $1^3\Sigma_u^+$-state of 0_u^- symmetry and the B-state. Such abrupt symmetry switchings hint to a weak diabatic coupling element, but give rise to a strong derivative coupling, as it is exemplary shown for the generic three state model of the B, C-state crossing in Sec. 5.4.

A different character of the symmetry transition can be found for the middle adiabatic state, which corresponds to an avoided crossing between the two repulsive potential energy curves of the a-state (1_g symmetry) and the $^3\Pi_g$-state (2_g symmetry). This avoided crossing appears in the region of coincidence below to the intersection with the B-state potential in Fig. 2.15. Whereas for the D_{2h}-Hamiltonian in Fig. 2.16 one again finds a switching between the respective symmetries 1_g and 2_g around $R \approx 6$ a_0, their gradual transition is seen for the C_i-Hamiltonian in Fig. 2.17, where it extends over a range $5.9 \leq R \leq 6.2$ a_0. As a consequence of the investigations from Sec. 5.4, the diabatic coupling element is expected to be strong in this case and the derivative coupling element weak, in turn.

In essence, the above investigations show, that a reduction of the DIM-Hamiltonian matrix is possible without deteriorating its overall accuracy. Particularly, this finding is relevant for on-the-fly dynamics. In the following the DIM method will be used to calculate Cartesian reaction surfaces and vibronic couplings for quantum simulations. This application, however, requires a further restriction of the DIM-Hamiltonian to the potential energy curves of the X-, B- and C-states only.

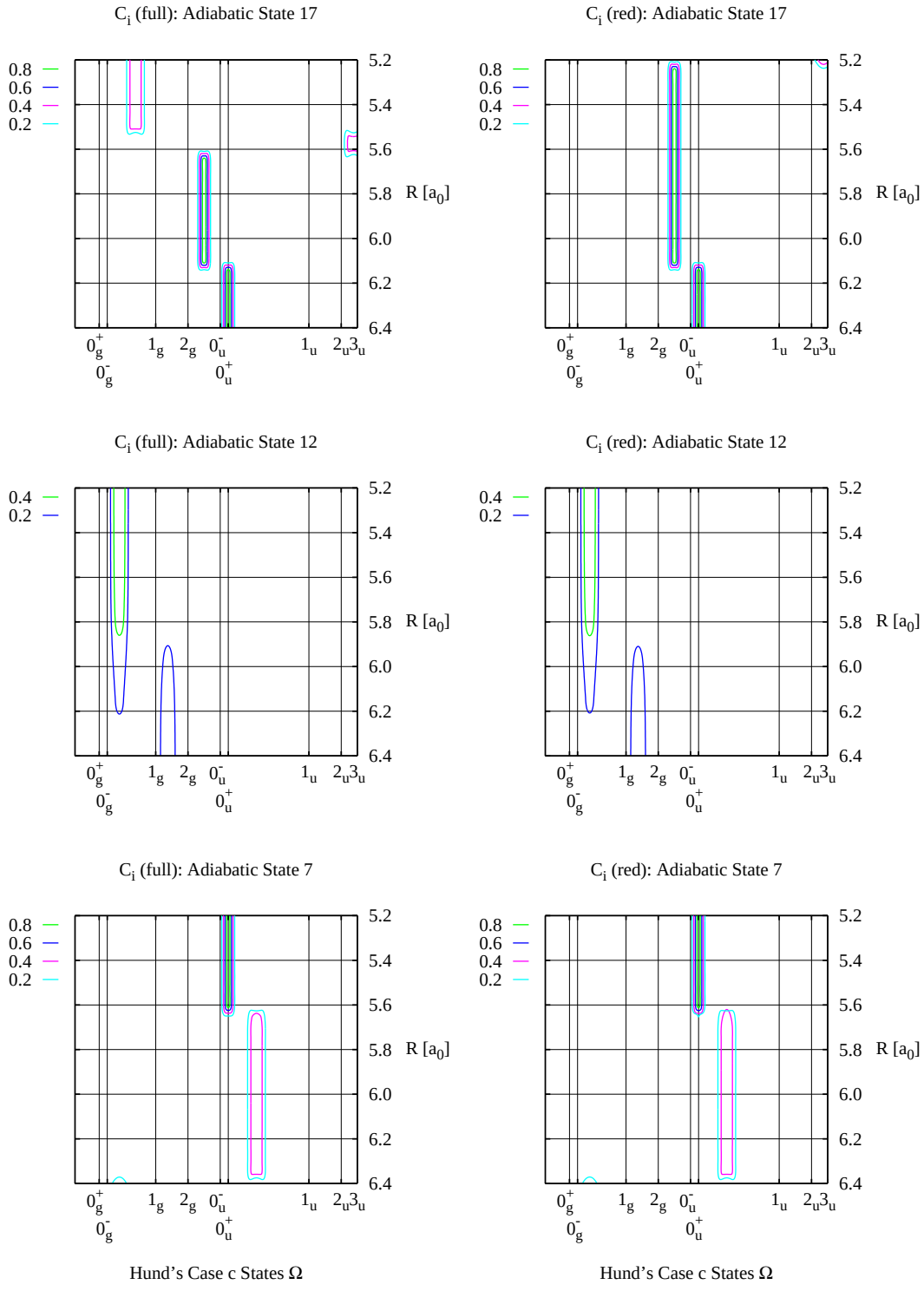

Figure 2.17: Same as Fig. 2.16, but for the full (right column) and the reduced (left column) C_i-Hamiltonians.

3 The Cartesian Reaction Surface Approach and Vibronic Coupling Theory

3.1 Basic Concepts

Whereas the solution of the Newtonian equations of motion (see Sec. 2.4.3 and Sec. 5.3) lead to classical trajectories, which, when knowing the gradients of the potential energy, can be calculated "on the fly", the solution of the time-dependent Schrödinger equation (TDSE) leads to nuclear wave packets and requires the knowledge of the PES as function of the nuclear coordinates. From the technical point of view it is impossible to represent such function globally for systems with many degrees of freedom. Here specific approximations have to be invoked. These approximations either base on a Taylor expansion of the PES or its effective representation within a low-dimensional subspace of nuclear coordinates. The necessary formalism behind these approximations is part of the following sections, for an alternative representation see Refs. [97–100, 144, 145].

3.1.1 Small Amplitude Displacements

Harmonic Approximation

The Cartesian Hamiltonian for an N atomic system, when expressed in the full set of $i = 1, \ldots, 3N$ nuclear coordinates x_i and momenta $p_{x,i}$, is given by the following expression:

$$H = T + V = \sum_{i=1}^{3N} \frac{p_{x,i}^2}{2m_i} + V(\{x_i\}) \ . \tag{3.1}$$

Within the harmonic approximation, which restricts the following considerations to small amplitude displacements (SAD) $\Delta x_i = x_i - x_i^{(0)}$ of the nuclear coordinates for a given electronic state, the $3N$-dimensional PES $V(\{x_i\})$ is expanded into a Taylor series of 2nd order around some reference geometry $\{x_i^{(0)}\}$:

$$V(\{x_i\}) \approx V(\{x_i^{(0)}\}) - \sum_{i=1}^{3N} f_i \Delta x_i + \frac{1}{2} \sum_{i=1}^{3N} \sum_{j=1}^{3N} k_{ij} \Delta x_i \Delta x_j \ . \tag{3.2}$$

The expansion coefficients of this Taylor series are the Cartesian forces f_i and force constants k_{ij} with the definitions:

$$-f_i = \left.\frac{\partial V}{\partial x_i}\right|_{\{x_i^{(0)}\}} , \qquad k_{ij} = \left.\frac{\partial^2 V}{\partial x_i \partial x_j}\right|_{\{x_i^{(0)}\}} , \tag{3.3}$$

where the forces f_i *vanish, if* the reference geometry $\{x_i^{(0)}\}$ of expansion (3.2) corresponds to a stationary point of the $3N$-dimensional PES.
Introducing *mass-weighted* Cartesian coordinates ξ_i and conjugated momenta $p_{\xi,i}$:

$$\xi_i = \sqrt{m_i}\Delta x_i , \qquad p_{\xi,i} = \frac{p_{x,i}}{\sqrt{m_i}} \tag{3.4}$$

the kinetic energy T in Eq. (3.1) takes on a simple form without the explicit requirement of particle masses. As a consequence of the coordinate transformation in Eq. (3.4), also the Taylor expansion coefficients from Eq. (3.3) have to be mass-weighted:

$$\tilde{f}_i = \frac{f_i}{\sqrt{m_i}} , \qquad \tilde{k}_{ij} = \frac{k_{ij}}{\sqrt{m_i m_j}} , \tag{3.5}$$

where the mass-weighted force constants $\tilde{k}_{ij}$, taken at the stationary point $\{x_i^{(0)}\}$, correspond to the matrix elements of a Hessian matrix [62] with the dimension $3N \times 3N$. Substituting the quantities from Eq. (3.5) into Eq. (3.2) and utilizing the variables defined in Eq. (3.4) the Cartesian Hamiltonian from Eq. (3.1) can be rewritten:

$$H \approx \frac{1}{2}\left[\sum_{i=1}^{3N} p_{\xi,i}^2 + \sum_{i=1}^{3N}\sum_{j=1}^{3N} \tilde{k}_{ij}\xi_i\xi_j\right] , \tag{3.6}$$

where the constant energy term $V(\{x_i^{(0)}\})$ to the reference point of the Taylor expansion (3.2) has been omitted, since it just shifts the energy scale of the Hamiltonian. Nevertheless, when comparing Eq. (3.6) with Eq. (3.1) it is seen that the individual degrees of freedom are still coupled in this representation.

Normal Coordinates

In order to eliminate the bilinear coupling terms in Eq. (3.6), first an orthonormal set $\{q_k\}$ of $k = 1, \ldots, 3N$ *normal coordinates* is introduced [146, 147]. These coordinates are related to the set $\{\xi_i\}$ of $i = 1, \ldots, 3N$ SAD coordinates via the following bidirectional linear transform:

$$q_k = \sum_{i=1}^{3N} l_{ki}\xi_i \qquad \longleftrightarrow \qquad \xi_i = \sum_{k=1}^{3N} l_{ik} q_k , \tag{3.7}$$

where the individual linear combination coefficients l_{ki} with $l_{ik} = l_{ki}^{\mathrm{T}}$ correspond to the elements of an orthogonal transformation matrix. Expressed in the set $\{q_k\}$ of normal

coordinates the Hamiltonian from Eq. (3.6) takes on a simple quadratic form:

$$H = \frac{1}{2}\left[\sum_{k=1}^{3N} p_{q,k}^2 + \sum_{k=1}^{3N} \lambda_k q_k^2\right] . \tag{3.8}$$

Here, the $p_{q,k}$ are the conjugated momenta of the normal coordinates q_k, and the $\lambda_k = \omega_k^2$ are the squared normal mode frequencies, which, when comparing Eq. (3.8) to Eq. (3.6), are recognized as eigenvalues of the Hessian matrix Eq. (3.5) according to its *principal axis* transformation. These eigenvalues can be obtained as roots of the eigenvalue problem:

$$|\tilde{k}_{ij} - \lambda\delta_{ij}| = 0 . \tag{3.9}$$

Its eigenvectors contain the linear combination coefficients l_{ki} for the transformation between the mass-weighted Cartesian and the normal coordinates as defined by Eq. (3.7).
In principle, upon initial displacement of the normal coordinates, it is now possible to solve the time-dependent Schrödinger equation for the Hamiltonian Eq. (3.8). Its solutions, however, would be trivial, since the individual normal modes q_k would just harmonically oscillate with their vibrational frequencies ω_k around their equilibrium positions.
When solving the secular equations Eq. (3.9) for a *periodic* system, which is subject to periodic boundary conditions, one obtains $3N-3$ nonzero eigenvalues [62] instead of $3N-6$ as in the general case of a polyatomic molecule. Here, the subset of normal modes $\{q_1, q_2, q_3\}$ with the numerical eigenvalues $\lambda_1, \lambda_2, \lambda_3 \approx 0$ describes the translation of the simulation box as a whole. These normal modes are not required and hence may be projected out. For this purpose, starting from the unity relation of the normal coordinates:

$$\sum_{k=1}^{3N} l_{ik} l_{ki} = 1 \begin{cases} \sum_{k=1}^{3} l_{ik} l_{ki} = \rho_i \\ \sum_{k=4}^{3N} l_{ik} l_{ki} = 1 - \rho_i \end{cases} \tag{3.10}$$

the projectors ρ_i and $1-\rho_i$ are defined. In close analogy to Mulliken's population analysis ρ_i accumulates the squared contributions $|l_{ki}|^2$ of a single DOF ξ_i to the normal modes $k = 1, 2, 3$, which, when carried out over all modes, would give unity, so that $1-\rho_i$ captures its remaining "population" in all other modes $k \neq 1, 2, 3$. The explicit application of the projector $1 - \rho_i$ is demonstrated in Sec. 3.1.2.

3.1.2 Large Amplitude Coordinates

Cartesian Representation

In order to overcome the restrictions of the harmonic approximation to SAD, a new set $\{\zeta_s\}$ of $s = 1, 2, \ldots, N_s \ll 3N$ mass-weighted Cartesian coordinates, which undergo large amplitude displacements and hence may be termed large amplitude coordinates (LAC), is introduced. These coordinates provide a means to account for the full anharmonicity and the full couplings within a relevant subpart of the total system. Without further specification at this point these coordinates may be represented by linear combinations of

the mass-weighted coordinates ξ_i:

$$\zeta_s \;=\; \sum_{i=1}^{3N} u_{si}\xi_i \tag{3.11}$$

with the linear combination coefficients u_{si}, which are chosen to be *orthonormal*. Due to the restriction $N_s \ll 3N$, however, the LACs do not form a *complete* orthonormal set, unlike the normal modes from Eq. (3.7). Depending on the total number $N_s = 1, 2, 3, 4 \ldots$ the set $\{\zeta_s\}$ of LACs spans up a *Cartesian (Reaction) Path, Plane, Surface* or *Hyper-surface* within the $3N$-dimensional PES of the total system. Of course, the subsystem described by such hyper-surface exchanges energy with the remainder part of the total system, the bath. It this context it should be mentioned, that the term "bath" refers to environmental degrees of freedom rather than to a heat bath. The underlying distinction between system and bath can be made explicit by defining another projector ϱ_i:

$$\varrho_i \;=\; \sum_{s=1}^{N_s} u_{is}u_{si} \;, \tag{3.12}$$

which projects the whole set $\{\zeta_s\}$ of LACs onto the individual coordinates ξ_i. According to the interpretation of Eq. (3.10) the projector $1 - \varrho_i$ then fixes all complementary ξ_i contributions which do *not* enter into definition (3.11), and hence are left for the definition of an explicit set $\{[1 - \varrho_i]\xi_i\}$ of bath coordinates.
Whereas the subsystem defined by the LACs can be represented in a rather accurate way, the motions of bath coordinates can only be accounted for in an approximate way. In analogy to Eq. (3.2) this can be accomplished via a Taylor series expansion of the potential energy with respect to the bath degrees of freedom around a *fixed* reference geometry $\{x_i^{(0)}\}$:

$$\begin{aligned} V(\{\zeta_s\}, \{[1 - \varrho_i]\xi_i\}) \;\approx\; & U(\{\zeta_s\}) - \sum_{i=1}^{3N} \tilde{f}_i(\{\zeta_s\})[1 - \varrho_i]\xi_i \\ & + \frac{1}{2}\sum_{i=1}^{3N}\sum_{j=1}^{3N}[1 - \varrho_i]\tilde{k}_{ij}(\{\zeta_s\})[1 - \varrho_j]\xi_i\xi_j \;. \end{aligned} \tag{3.13}$$

Here, the expansion coefficients $U(\{\zeta_s\})$, $\tilde{f}_i(\{\zeta_s\})$ and $\tilde{k}_{ij}(\{\zeta_s\})$ are functions of the LACs. Alternatively to this *frozen bath* [99] version one may think of a modified Taylor expansion, where the *reference* geometry of the bath is not fixed and taken as a function of the system coordinates. This expansion is known as *flexible bath* [99] approach. In contrast to the frozen bath version, the flexible bath approach thus requires the re-optimization of the reference geometry as a function of the system coordinates, which can be seen as a major computational disadvantage of this method.
With the aid of Taylor expansion (3.13) a new Hamiltonian:

$$H \;=\; H_S + H_{SB} \tag{3.14}$$

can be formulated, which is composed of a system Hamiltonian H_S and a mixed Hamiltonian H_{SB}:

$$H_S = \frac{1}{2}\sum_{s=1}^{N_s} p_{\zeta,s}^2 + U(\{\zeta_s\}) \ , \tag{3.15a}$$

$$H_{SB} = \frac{1}{2}\sum_{i=1}^{3N} (p_{\xi,i}[1-\varrho_i])^2 - \sum_{i=1}^{3N} \tilde{f}_i(\{\zeta_s\})[1-\varrho_i]\xi_i + \frac{1}{2}\sum_{i=1}^{3N}\sum_{j=1}^{3N}[1-\varrho_i]\tilde{k}_{ij}(\{\zeta_s\})[1-\varrho_j]\xi_i\xi_j \ , \tag{3.15b}$$

which describes the bath interacting with the system.

Normal Mode Representation

More useful for the interpretation of nuclear motions than the representation of the system-bath Hamiltonian, Eq. (3.15b), in terms of individual, uncoupled coordinates is its formulation in terms of normal modes, as these coordinates already account for a certain degree of coupling. In analogy to the LACs defined by Eq. (3.11) the latter also describe *collective*, but *small* displacements of the mass-weighted Cartesian coordinates. Additionally, the distinction between system and bath by the projector (3.12) is incomplete within the Cartesian representation, since in case $0 < \varrho_i < 1$ it permits the *partial* contribution of the Cartesian coordinates ξ_i to *both*, system and bath. The normal mode representation of the coupled system-bath Hamiltonian from Eq. (3.15b) can be accomplished in two ways.
One way is to successively diagonalize the harmonic potential expansion for the bath degrees of freedom obtaining uncoupled normal modes, whose linear combination coefficients and frequencies change as a function of the system coordinates $\{\zeta_s\}$. This procedure is known as vibrational adiabatic approximation [97,98] and the corresponding normal modes to a given point of the system coordinates are often called *local* or *instantaneous* modes [99].
Alternatively, one may define a fixed set of bath modes at a common reference geometry of the $3N$-dimensional PES, where both, the system and the bath degrees of freedom, are in their equilibrium positions.
Assuming that this reference geometry coincides with $\{x_i^{(0)}\}$ from Sec. 3.1.1, and provided that the respective force constants (3.5) and normal modes (3.7) have already been determined, the projected Hessian matrix with the elements:

$$k'_{ij} = [1-\varrho_i][1-\rho_i]\tilde{k}_{ij}[1-\rho_j][1-\varrho_j] \tag{3.16}$$

is introduced. The interpretation of Eq. (3.16) is straightforward, since it corresponds to two successive projections, where first the set $\{q_1, q_2, q_3\}$ of translational modes and second the set $\{\zeta_s\}$ of LACs are projected out. Upon solving the projected secular problem:

$$|k'_{ij} - \lambda\delta_{ij}| = 0 \tag{3.17}$$

new eigenvalues λ'_k and modes q'_k with linear combination coefficients l'_{ki} are obtained. According to the particular definition of the Hessian matrix, Eq. (3.16), its first $N_s + 3$ eigenvalues λ'_k vanish by construction; the set $\{q'_k\}$ of $k = N_s + 4, \ldots, 3N$ normal modes is then orthogonal to the set $\{\zeta_s\}$. When projecting the forces and force constants of the Taylor expansion (3.13) onto the new set $\{q'_k\}$ of normal modes:

$$f'_k(\{\zeta_s\}) = \sum_{i=1}^{3N} l'_{ki} \tilde{f}_i(\{\zeta_s\}) \qquad k'_{kl}(\{\zeta_s\}) = \sum_{i=1}^{3N}\sum_{j=1}^{3N} l'_{ki} \tilde{k}_{ij}(\{\zeta_s\}) l'_{jl} \tag{3.18}$$

the Cartesian system - bath Hamiltonian from Eq. (3.14) can be rewritten in the following way:

$$H_{SB} = \frac{1}{2} \sum_{k=N_s+4}^{3N} p^2_{q',k} - \sum_{k=N_s+4}^{3N} f'_k(\{\zeta_s\}) q'_k + \frac{1}{2} \sum_{k,l=N_s+4}^{3N}\sum^{3N} q'_k k'_{kl}(\{\zeta_s\}) q'_l \; . \tag{3.19}$$

In contrast to the instantaneous normal modes mentioned before, the fixed bath modes are coupled to the system in their potential energy via linear and bilinear terms, which are functions of the system coordinates.

3.1.3 Vibronic Coupling Theory

When aiming to describe nuclear motions associated with electronic transitions, the considerations from Sec. 3.1.1 and Sec. 3.1.2 have to be extended to multiple electronic states. Additionally, in situations where the potential energy surfaces of two electronic states a and b cross one another the Born-Oppenheimer approximation breaks down and the coupling between nuclear and electronic motion cannot be neglected any longer. Such situations can be described by vibronic coupling theory [89, 91, 102, 103, 148–150]. In contrast to the previous considerations, which have not been restricted to a certain representation, the formulation of the vibronic coupling problem requires a diabatic representation of the electronic Hamiltonian. This criterion is matched by the present DIM approach (see Chap. 2), since the X_2 molecular states (cf. Sec. 2.2.2), which serve as zero-order basis functions of the DIM-Hamiltonian (cf. Sec. 2.3.3), are defined as product functions with constant expansion coefficients, and hence do not depend on the nuclear coordinate.
Conceptionally, the vibronic coupling problem can be formulated in close analogy to Sec. 3.1.1. Assuming that the nuclear dependence of the diagonal as well as off-diagonal matrix elements V_{aa} and V_{ab} of two diabatic states with the labels a and b can be approximated by a Taylor series similar to Eq. (3.2), the respective expansion coefficients are given by the following expressions:

$$-f_i^{(a)} = \left.\frac{\partial V_{aa}}{\partial x_i}\right|_{\{x_i^{(0)}\}} , \qquad k_{ij}^{(a)} = \left.\frac{\partial^2 V_{aa}}{\partial x_i \partial x_j}\right|_{\{x_i^{(0)}\}} , \tag{3.20}$$

$$f_i^{(ab)} = \left.\frac{\partial V_{ab}}{\partial x_i}\right|_{\{x_i^{(c)}\}} , \qquad k_{ij}^{(ab)} = \left.\frac{\partial^2 V_{ab}}{\partial x_i \partial x_j}\right|_{\{x_i^{(c)}\}} . \tag{3.21}$$

Applying the terminology of vibronic coupling theory, the state dependent forces $f_i^{(a)}$ and force constants $k_{ij}^{(a)}$ in Eq. (3.20) are called *intra-state* coupling constants. Accordingly, the expansion coefficients $f_i^{(ab)}$ and $k_{ij}^{(ab)}$ in Eq. (3.21) are termed *inter-state* vibronic coupling constants of 1st and 2nd order. Notice, that the reference geometry in Eq. (3.20) corresponds to $\{x_i^{(0)}\}$, whereas in Eq. (3.21) it corresponds to a crossing point $\{x_i^{(c)}\}$ obeying the condition $V_{aa} = V_{bb}$. Within the present DIM approach, the first and second derivatives of the diabatic potential energy matrix elements from Eq. (3.20) and Eq. (3.21) can be calculated analytically as detailed in Sec. 5.5 of the Appendix. Further, provided that the normal modes from Eq. (3.7) have been calculated for the electronic ground state, and that the quantities from Eq. (3.20) and Eq. (3.21) have been mass-weighted according to Eq. (3.5), the vibronic coupling constants can be mapped onto these normal modes:

$$f_k^{(a)} = \sum_{i=1}^{3N} l_{ki} \tilde{f}_i^{(a)} \ , \qquad k_{kl}^{(a)} = \sum_{i=1}^{3N} \sum_{j=1}^{3N} l_{ki} \tilde{k}_{ij}^{(a)} l_{jl} \ , \tag{3.22}$$

$$f_k^{(ab)} = \sum_{i=1}^{3N} l_{ki} \tilde{f}_i^{(ab)} \ , \qquad k_{kl}^{(ab)} = \sum_{i=1}^{3N} \sum_{j=1}^{3N} l_{ki} \tilde{k}_{ij}^{(ab)} l_{jl} \ . \tag{3.23}$$

Using Eq. (3.22) and Eq. (3.23) the normal mode vibronic coupling Hamiltonian can then be formulated in terms of the following matrix elements:

$$H_{aa} = \frac{1}{2} \sum_k p_{q,k}^2 - \sum_{k \in G_1} f_k^{(a)} q_k + \frac{1}{2} \sum_{k,l \in G_2} \sum q_k k_{kl}^{(a)} q_l \tag{3.24}$$

$$H_{ab} = \sum_{k \in G_3} f_k^{(ab)} q_k + \frac{1}{2} \sum_{k,l \in G_4} \sum q_k k_{kl}^{(ab)} q_l \tag{3.25}$$

Due to symmetry selection rules the single and double sums in Eq. (3.24) and Eq. (3.25) are restricted to certain subsets of modes. The subsets G_1:

$$G_1 \ : \ \Gamma_k \supset \Gamma_A \ ,$$

comprises all normal modes q_k with the irreducible representation Γ_k that transform according to the totally symmetric representation Γ_A of the molecular symmetry group. Since these modes modulate the energy gap between individual diabatic states they are called *tuning modes*. The second subset G_2 covers all pairs of modes:

$$G_2 \ : \ \Gamma_k \times \Gamma_l \supset \Gamma_A \ ,$$

which provide bilinear and quadratic on-diagonal couplings. These modes cause mixing effects and frequency shifts within a given diabatic state. The third subset G_3 of modes accounts for the linear vibronic coupling between two crossing states with the irreducible representations Γ_a and Γ_b:

$$G_3 \ : \ \Gamma_k \times \Gamma_a \times \Gamma_b \supset \Gamma_A \ .$$

These modes are called *coupling modes*. Finally, the set G_4 denotes all pairs of modes which contribute to the off-diagonal elements of the Hamiltonian:

$$G_4 \quad : \quad \Gamma_k \times \Gamma_l \times \Gamma_a \times \Gamma_b \supset \Gamma_A \ .$$

In case that two crossing states have a different parity, that is g and u, the inter-state vibronic coupling must be an odd function of the coupling coordinate. Hence, there exist no constant and quadratic vibronic coupling terms, only linear and bilinear ones are allowed. When taking into account only the linear coupling terms of Eq. (3.24) and Eq. (3.25) one obtains the so-called linear vibronic coupling model. A special case of this model is the Huang-Rhys or shifted oscillator model as described in Sec. 5.7 of the Appendix, which only takes into account the linear intra-state coupling terms.
Following Sec. 3.1.2 the normal mode vibronic coupling Hamiltonian from Eq. (3.24) and Eq. (3.25) can be straightforwardly combined with the Cartesian reaction surface model. Assuming that the set $\{\zeta_s\}$ of LACs defined by Eq. (3.11) contains only totally symmetric coordinates, which do not contribute to vibronic off-diagonal coupling terms, the system Hamiltonian from Eq. (3.15a) is just determined by the respective diagonal matrix elements:

$$H_S^{(aa)} \quad = \quad \frac{1}{2}\sum_{s=1}^{N_s} p_{\zeta,s}^2 + U_{aa}(\{\zeta_s\}) \ , \tag{3.26}$$

where the N_s-dimensional reaction surfaces $U_{aa}(\{\zeta_s\})$ depend on the electronic state considered. Further, when using the set $\{q'_k\}$ of normal modes obtained from Eq. (3.16) and Eq. (3.17), the vibronic coupling Hamiltonian, Eq. (3.24) and Eq. (3.25), can be brought into a form similar to the system-bath Hamiltonian as defined by Eq. (3.14), taking into account, however, that the vibronic coupling quantities from Eq. (3.22) and Eq. (3.23) become functions of the LACs. The vibronically coupled system-bath Hamiltonian is then given by the following matrix elements:

$$H_{SB}^{(a)} \quad = \quad \frac{1}{2}\sum_k p_{q',k}^2 - \sum_{k\in G_1}^{3N} f_k'^{(a)}(\{\zeta_s\})q'_k + \frac{1}{2}\sum_{k,l\in G2}\sum q'_k k_{kl}'^{(a)}(\{\zeta_s\})q'_l \ , \tag{3.27}$$

$$H_{SB}^{(ab)} \quad = \quad \sum_{k\in G_3}^{3N} f_k'^{(ab)}(\{\zeta_s\})q'_k + \frac{1}{2}\sum_{k,l\in G4}\sum q'_k k_{kl}'^{(ab)}(\{\zeta_s\})q'_l \ . \tag{3.28}$$

Together with Eq. (3.26) the both Eqs. (3.27) and (3.28) form the fundament for the description of the vibronically coupled quantum dynamics involving large amplitude motions. However, due to the dependence of the 1st and 2nd order coupling constants on the reaction coordinates, further approximations have to be invoked in the application of Eq. (3.27) and Eq. (3.28), particularly when taking into account, that the number of bath modes may be enormous in case of typical condensed phase situations.

3.2 Two-Dimensional Reaction Surfaces

3.2.1 Analysis of Cage Fragment Displacements

In order to provide an instructive basis for the definition of system coordinates, which have been introduced rather formally in Eq. (3.11) of Sec. 3.1.2, the reduced dimensionality approach as developed for the quantum description of the photo-dissociation dynamics of F_2 [71–73] and ClF [75] molecules in Ar matrices has been adapted to the present system. In this approach the potential energy is taken as a function of the X-X bond distance and a specific matrix coordinate, which describes the motion of a certain cage fragment in the proximity of the dihalogen while keeping all other Rg atoms frozen. For the application of this strategy to Br_2 in Ar the Belt, Phonon, Window and Collision atoms shown in Fig. 2.9 of Sec. 2.4.3 can be considered as prototypic cage fragments. This choice is motivated by their relaxation-induced shifts (see Tab. 2.3) as well as their participation in trajectory simulations of matrix-isolated Br_2 [127, 128] and Cl_2 [17, 62] molecules.
When analyzing the potential energy of the electronic X-, B-, and C-states as function of the Br-Br coordinate versus the centrosymmetric elongation of the Belt, Phonon, Window and Collision atoms one obtains a series of two-dimensional PES shown in Fig. 3.1. Focusing on the X-state surfaces one notices that there is a substantial coupling of the Bromine coordinate to the motion of the Belt, Window and Collision atoms. Whereas the two limiting cases of weak and strong coupling follow from the symmetric and triangular shape of the PES for the Phonon and Collision atoms, its minimum energy path predicts a contraction of the Belt atom frame and an expansion of the Window atom frame with increasing separation of the Br atoms, just as expected on intuitive grounds.
In order to get an impression about the motions of the Bromine and matrix coordinates in the electronically excited states the relief reflection principle [71] can be applied to the B- and C-state surfaces. According to this principle the tangent of the isopotential contour lines at the turning point of the initial motion path determines the subsequent reflection path away from the surface relief. This way, by combining all consecutive reflection path segments a schematic picture of the relative motions onto the excited state PES can be drawn. Such scenarios predict rather large amplitude motions for the Bromine coordinate making its anharmonicity an essential feature for the description of the excited state dynamics. Furthermore, the potential along the individual matrix coordinates is not harmonic, that is in the frame of a system-bath treatment all of these coordinates have to be included into the "system".

3.2.2 Problem-Adapted Reaction Coordinates

Whereas the displacements of the individual cage coordinates have been considered independently in the above approach, a systematic description of their combined motion requires another strategy close to the reaction path method proposed by Miller et al. [99, 100]. For describing the coupled motions of matrix atoms associated with the electronic $B \leftarrow X$ transition, the idea of a reaction path connecting two specific reactant and product geome-

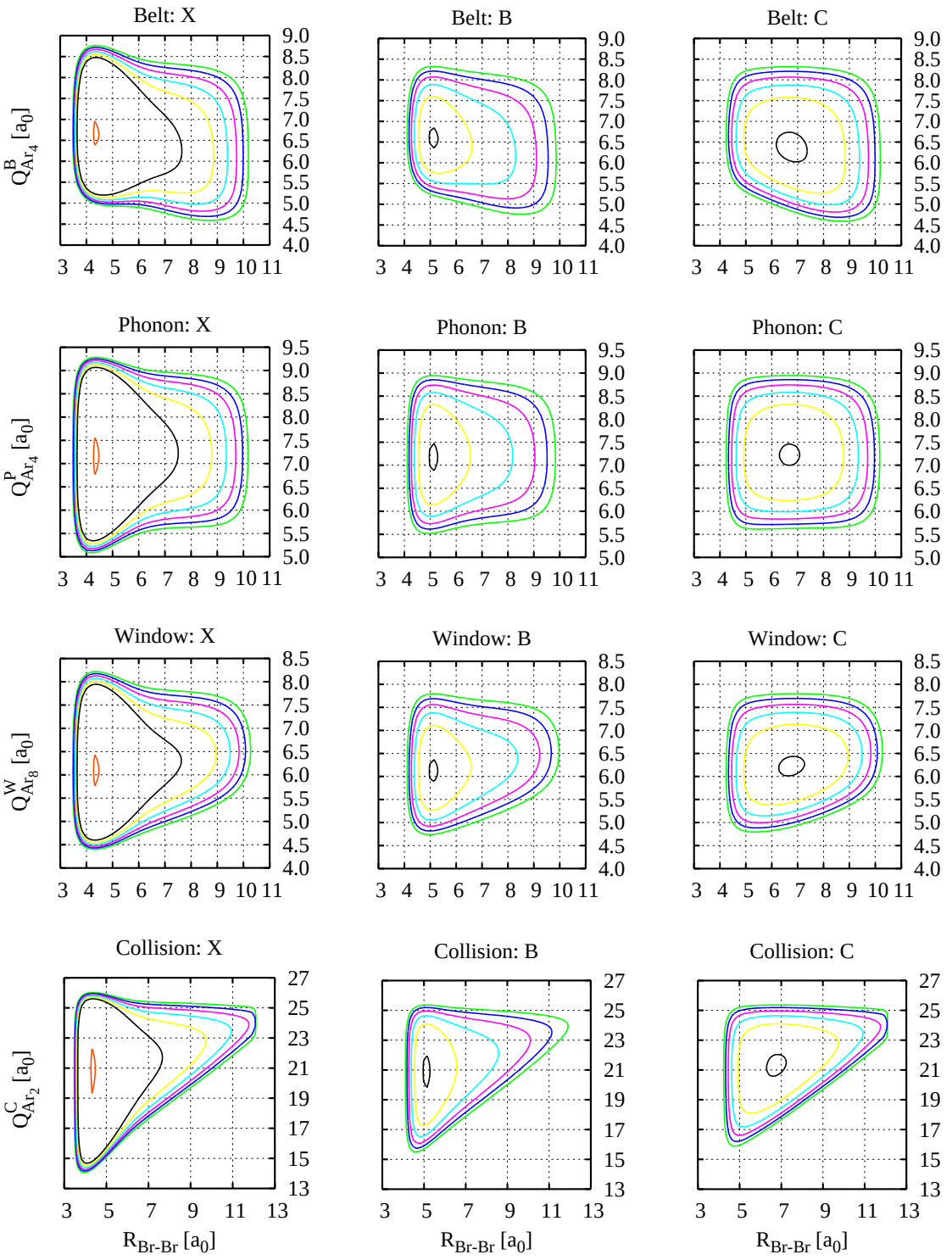

Figure 3.1: Contour plots of 2D-PES showing Bromine coordinate (abscissa) versus Belt (1st row), Phonon (2nd row), Window (3rd row) and Collision (last row) coordinates (ordinates) (cf. Fig. 2.9) for the diabatic X- (left column), B- (middle column) and C-states (right column) with contour levels at 0.001, 0.07, 0.08, 0.09, 0.10, 0.11 and 0.12 E_h.

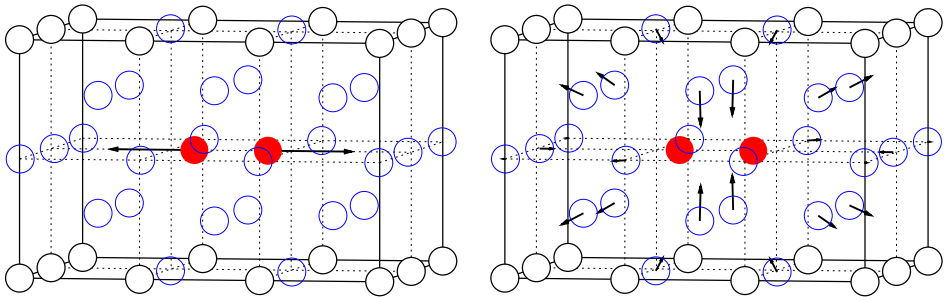

Figure 3.2: Displacement vectors of the mass-weighted Bromine ζ_R (left), Eq. (3.29), and matrix coordinates ζ_{X-B} (right), Eq. (3.30).

tries has to be extended to different electronic states. As opposed to previous applications of the method to Hydrogen-transfer reactions (for a review, see Ref. [101]), which were confined to the electronic ground state, the "product" and "reactant" geometries in the above scenario correspond to minimum energy configurations of the system in *two distinct* electronic states.

For a convenient definition of large amplitude coordinates within the frame of the CRS concept (see Sec. 3.1.2) it is helpful to cast the individual atomic positions of the $i = 1, 2$ Br atoms and the $i = 3, \ldots, N$ Ar atoms into a coordinate vector R of dimension $3N$:

$$\begin{aligned} R &= \{R_{1,x}, \ldots, R_{i,x}, R_{i,y}, R_{i,z}, \ldots, R_{N,z}\} \\ &\widehat{=} \{x_1, \ldots, x_{3i-2}, x_{3i-1}, x_{3i}, \ldots, x_{3N}\} \ . \end{aligned}$$

Using this convention together with the atomic Bromine mass m_{Br} the first LAC can be formulated in terms of the mass-weighted Br-Br distance:

$$\zeta_R = \sqrt{\frac{m_{Br}}{2}}(R_{2,y} - R_{1,y})e_y \ . \tag{3.29}$$

Its displacement vector is shown on the left side of Fig. 3.2, where the coordinate system has been chosen such that the Bromine molecule points along the y-direction indicated by the unit vector e_y in Eq. (3.29). Provided that the equilibrium geometries $R^{(X)}$ and $R^{(B)}$ for the system in the electronic X- and B-states have been determined as described in Sec. 2.4.3, the second reaction coordinate is obtained by the mass-weighted coordinate shift $\Delta = M^{1/2}(R^{(B)} - R^{(X)})$ between the respective minima, where M is a diagonal matrix containing the Br and Ar atomic masses. Projecting out the contributions of the Bromine coordinate $(\Delta, \zeta_R)\zeta_R$ from the matrix coordinate with the aid of a Gram-Schmidt orthogonalization:

$$\zeta_{X-B} = \Delta - (\Delta, \zeta_R)\zeta_R \tag{3.30}$$

followed by normalization, one obtains a "pure" matrix coordinate ζ_{X-B}, which is orthonormal to ζ_R.

The individual atomic displacement vectors of this coordinate ζ_{X-B} with respect to ground state equilibrium geometry $R^{(X)}$ are depicted on the right side of Fig. 3.2. Here it is seen, that the motion along this coordinate involves a collective displacement of the Belt, Phonon, Window and Collision atoms. In this respect ζ_{X-B} resembles the combined effect of the cage fragment coordinates discussed in Sec. 3.2.1.
According to their definitions by Eq. (3.29) and Eq. (3.30) both LACs describe totally symmetric motions, which preserve the $\langle 110 \rangle$ orientation of the Br_2 molecule and the overall D_{2h} symmetry of the matrix cage as well. Furthermore, the definition of ζ_{X-B} in terms of stationary structures predestines this coordinate for the description of matrix motions in the long-time domain, that is after vibrational relaxation in the B-state. Thus it is a priori not clear, whether this coordinate can provide a reasonable description of matrix motions at non-equilibrium distances of the Bromine coordinate. Within the scope of the CRS concept this problem can be addressed by adding another LAC similar to Eq. (3.30) for describing this regime. Test calculations along these lines have been performed using a third relaxed matrix geometry, which corresponds to the outer turning point of the Br-Br motion in the B-state at the Franck-Condon energy ($9\ a_0, 0.09\ E_h$). It turned out that the vector pointing from the B-state minimum geometry to this configuration is nearly parallel to ζ_{X-B}, so the latter should also provide a reasonable description of the matrix motions beyond the Br_2 equilibrium distance in the B-state up to the outer turning point. Finally, it cannot be guaranteed that the intrinsic reaction path from the $B \leftarrow X$ Franck-Condon vertical excitation geometry to the B-state minimum lies in the plane spanned by ζ_R and ζ_{X-B}. This reaction path corresponds to the minimum energy path, which coincides with the path of steepest decent in mass-weighted coordinates when followed downhill from a given transition structure or saddle point [151,152]. However, in view of short-time dynamics this path is likely to be of no relevance. Still this reaction plane model is advantageous over the *individual* cage fragment models of the previous section because it describes their *combined* motion.

Normal Mode Analysis of the Matrix Coordinate

A further analysis of ζ_{X-B} beyond its interpretation in terms of individual cage atom displacements (cf. Fig. 3.2) is provided when projecting this coordinate onto the normal modes of the simulation box from Fig. 2.7. For this purposes, the normal modes $\{q_k\}$ and vibrational frequencies $\{\omega_k\}$ of the X-state PES minimum geometry have been calculated by solving secular problem from Eq. (3.9) as described in Sec. 3.1.1. The respective vibrational density of states $N(\omega)$:

$$N(\omega) \quad = \quad \sum_k \delta(\omega - \omega_k) \tag{3.31}$$

characterizing the normal mode spectrum of the $N = 700$ (2 Br and 698 Ar) atoms in total is shown by the histogram in Fig. 3.3a. Specifically, this histogram has been obtained by counting the number of modes within a finite frequency interval $\Delta\omega = 1\ cm^{-1}$. Its

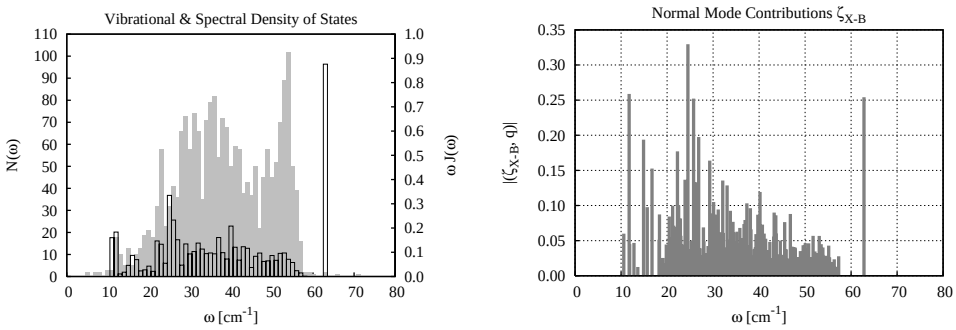

(a) (b)

Figure 3.3: (a) Ground state density of states $N(\omega)$ (grey bars) and spectral density of states $\omega J(\omega)$ to the $B \leftarrow X$ transition (open bars). (b) Projection of matrix coordinate ζ_{X-B} onto the ground state normal modes.

shape is typical for Ar crystals and closely resembles the phonon density of states given in Ref. [7]. Note, that there is an additional peak around $\omega = 320$ cm^{-1} (not shown) for the harmonic X-state vibrational frequency of the Br_2 molecule. Further, the three zero-frequency modes describing the translation of the simulation box have been projected out by means of the projector defined in Eq. (3.10) of Sec. 3.1.1.

The results of the normal mode projection, that is, the individual scalar products (ζ_{X-B}, q_k), are shown in Fig. 3.3b. Inspecting this figure it becomes clear that ζ_{X-B} involves contributions from many (symmetry-preserving) normal modes covering an essential part of the whole phonon spectrum. Hence this coordinate provides a compact description of coupled matrix motions. As a possible drawback of such a description it should be mentioned, that the couplings contained in this coordinate require an additional effort, if an interpretation in terms of individual normal mode couplings is required.

If raising this question of the coupling of individual normal modes to the electronic $B \leftarrow X$ transition, the result of the normal mode projection from Fig. 3.3b may be compared to the spectral density of states $J(\omega)$ shown in Fig. 3.3a. In contrast to the density of states $N(\omega)$ defined by Eq. (3.31) the latter quantity $J(\omega)$:

$$J(\omega) \quad = \quad \sum_k S_k \delta(\omega - \omega_k) \tag{3.32}$$

weights each phonon mode by a dimensionless coupling strength S_k, which reflects its linear response to an electronic transition. According to the Huang-Rhys model given in Sec. 5.7 of the Appendix this coupling (denoted S in Eq. (5.69)) is determined by the force f_k acting on the kth ground state phonon mode q_k in the electronic B-state assuming a vertical transition. Comparing both figures, Fig. 3.3a and Fig. 3.3b, it is seen, that ζ_{X-B} resembles the totally symmetric part of the linear coupling modes in the Franck-Condon region. These intra-state coupling modes (or tuning modes) correspond to the set G_1 of the vibronic coupling Hamiltonian introduced in Eq. (3.24) of Sec. 3.1.3. With respect to the initial aim of modelling a collective coordinate, which reflects the matrix

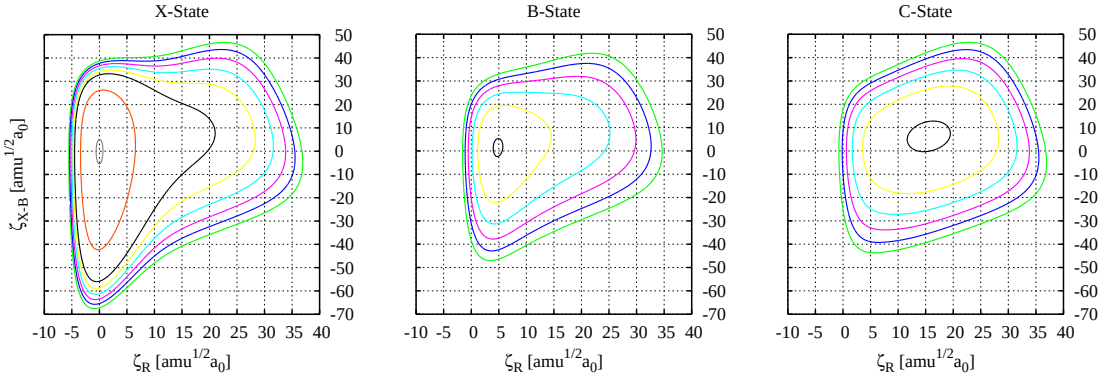

Figure 3.4: 2D plot of the CRS, Eq. (3.13) in Sec. 3.1.2 and Eq. (3.26) in Sec. 3.1.3, as function of the Bromine coordinate ζ_R (abscissa) and the matrix coordinate ζ_{X-B} (ordinate) from Fig. 3.2 in Sec. 3.2.2 for the diabatic X- (left), B- (middle) and C-states (right) with isopotential contour lines at 0.001, 0.035, 0.069, 0.080, 0.090, 0.100, 0.110 and 0.120 E_h.

motions associated to the electronic $B \leftarrow X$ transition, this comparison can be seen as a "self-consistency" check for matching this requirement.

Analysis of Cartesian Reaction Surfaces

After having defined and analyzed the two large amplitude coordinates ζ_R and ζ_{X_B} one can now proceed with the characterization of two-dimensional Cartesian reaction surfaces obtained on the basis of DIM calculations. These Cartesian reaction surface form the fundament for the construction of the system Hamiltonian introduced in Eq. (3.26) of Sec. 3.1.3. The respective diabatic PES for the electronic X-,B- and C-states are shown in Fig. 3.4. Analyzing this figure one notices a characteristic tilting of the PES towards larger ζ_{X-B} with increasing ζ_R for all three states considered. When comparing Fig. 3.4 to Fig. 3.1 this tilting can be attributed to the specific response of the Belt, Window and Collision atoms to the Br-Br bond stretching. In that sense the PES of the X-, B- and C-states in Fig. 3.4 can be understood as a "superposition" of the respective individual potential energy surfaces from Fig. 3.1. Further, as a consequence of the definition from Eq. (3.30) the minimum energy positions of the B- and C-state PES are shifted with respect to the X-state minimum, not only along the Bromine coordinate ζ_R, but also along the matrix coordinate ζ_{X-B}. This positional shift along ζ_{X-B} reflects a different molecule-matrix interaction for different electronic states of the chromophore.
Next to the Br-Ar interactions this shift involves Ar-Ar interactions, which also provide the repulsive potential at rather large elongations of the matrix coordinate making the depicted PES closed shapes. Notice, that the diabatic X- and C- states are essentially degenerate along both coordinates starting from the region of the C-state minimum.

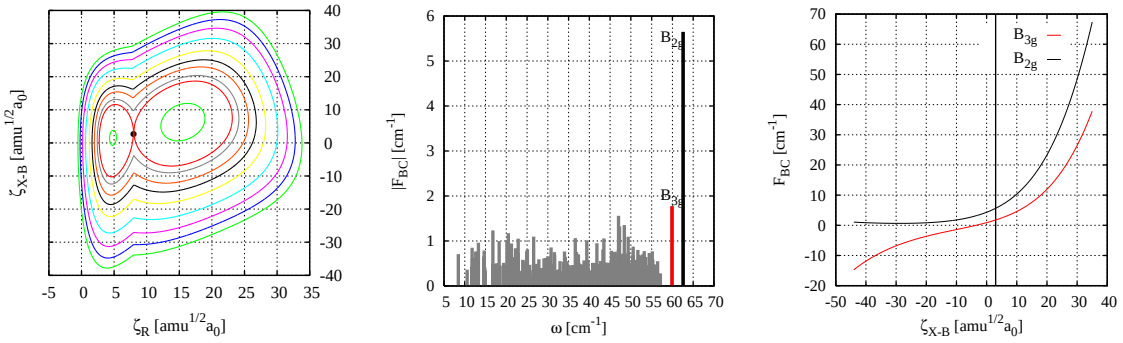

(a) (b) (c)

Figure 3.5: (a) Lower adiabatic $B - C$ surface showing the crossing seam with minimum (dot) at $\zeta_R \approx 8$, $\zeta_{X-B} \approx 3$ amu$^{1/2}$a$_0$. Isopotential contour lines are drawn at 0.069, 0.072, 0.073, 0.075, 0.077, 0.080, 0.085, 0.090, 0.095 and 0.100 E$_h$. (b) Normal mode projection of the BC coupling matrix element at the minimum of crossing seam from (a). (c) Coordinate dependence of the two dominant vibronic coupling modes from (b) with B_{3g} ($\omega_1 \approx 60$ cm^{-1}) and B_{2g} ($\omega_2 \approx 63$ cm^{-1}) symmetry along the crossing seam of (a).

3.3 Identification of Vibronic Coupling Modes

The LAC described in the previous paragraph are constructed such as to capture that part of the molecule-matrix coupling and the anharmonicity of the PES which is related to the symmetric deformation of the matrix cage in the B-state. As it has been pointed out in Sec. 3.2.2 this deformation preserves the overall D_{2h} symmetry of the system, and with it the electronic symmetries of the B- and C-states (cf. Tab. 2.4 in Sec. 2.4.4).
Therefore, in the absence of further matrix couplings, the bare diabatic B- and C-state PES spanned by the LAC intersect and form a crossing seam rather than a conical intersection in adiabatic representation. The topology of this crossing seam can be visualized when following the lowest of the resulting reaction surfaces in the latter representation as shown in Fig. 3.5a. Inspecting this figure one notices that this crossing seam is approximately directed along the matrix coordinate ζ_{X-B}.
That part of matrix motions describing, for instance, asymmetric cage deformations, which are not captured by the LAC, can be coupled to the reaction surface model in terms of harmonic oscillators as described in Sec. 3.1.3. A specific category among this normal modes is denoted by the set G_3 in Eq. (3.28). These normal modes of particular symmetry provide the linear vibronic couplings for the non-adiabatic transition between the B- and C-state PES from Fig. 3.4. In order to identify these coupling modes, first the ground state normal modes from Fig. 3.3a in Sec. 3.2.2 have to be made orthogonal to the plane spanned by the reaction coordinates. Technically, this can be accomplished by diagonalizing the Hessian matrix from Eq. (3.16) in Sec. 3.1.2, where now in addition to the three translational modes the two reaction coordinates ζ_R and ζ_{X-B} have to be projected out by means of the projectors defined in Eq. (3.10) and Eq. (3.12). Following Eq. (3.23) in Sec. 3.1.3 these normal modes can then be utilized for the normal mode representation of the vibronic coupling constants defined by Eq. (3.21). For this purpose the individual gradients $f_i^{(BC)}$

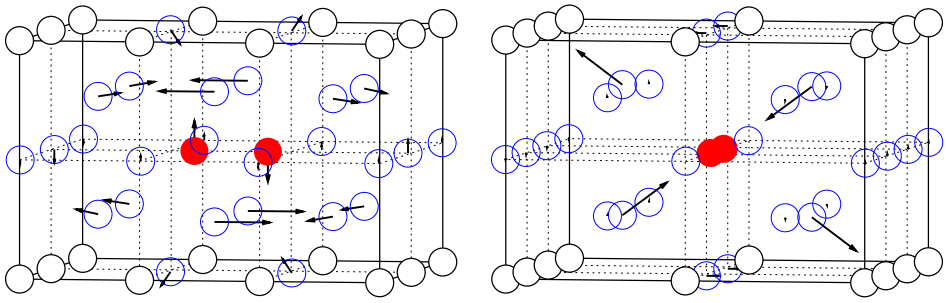

Figure 3.6: Atomic displacement vectors for the vibronic coupling modes q_1 (left) of B_{3g} and q_2 (right) of B_{2g} symmetry from Fig. 3.5.

of the diabatic BC off-diagonal matrix element have been determined at the lowest point of the BC crossing seam, which is marked by a black dot in Fig. 3.5a. The result of the normal mode representation, that is the individual vibronic coupling constants $f_k^{(BC)}$ with $k = 1, \ldots, 3N-5$ are shown in Fig. 3.5b. For a better comparability of the coupling strength to the normal mode frequencies both quantities have been expressed in units of energy. Therefore, the respective gradients have been evaluated in dimensionless oscillator coordinates (for details see Sec. 5.6 and Sec. 5.7 of the Appendix). Analyzing Fig. 3.5b two strongly coupling modes with the normal mode frequencies $\omega_1 = 60$ and $\omega_2 = 63$ cm^{-1} can be readily identified, whereas an almost continuous distribution of modes stretching from 7 to 57 cm^{-1} couples only weakly. As expected on group theoretical grounds the dominant coupling modes, which may be denoted by q_1 (59.9 cm^{-1}) and q_2 (62.6 cm^{-1}), are of B_{3g} and B_{2g} symmetry. The associated atomic displacement vectors are shown in Fig. 3.6. Inspecting this figure one notices that the B_{3g}-mode q_1, next to an antipodal vibration of the Belt and Window atoms, also involves a librational type of motion of the Br_2 molecule while the B_{2g}-mode q_2 corresponds to an asymmetric stretching vibration of the Belt atoms.

When plotting the potential energy of the B- and C- states as a function of the Bromine coordinate ζ_R versus one of the vibronic coupling modes, e.g. the stronger coupling mode q_2 of B_{2g} symmetry, one obtains a conical intersection in adiabatic representation. This conical intersection is visualized in Fig. 3.7, where it is shown, how the motion along q_2 lifts the degeneracy of the resulting PES. Note, that each point of the crossing seam from Fig. 3.5a gives rise to such a conical intersection. In that sense these points topologically concatenate a series of conical intersections along the crossing seam (see, e.g. [153]).

Further, for the construction of a vibronically coupled Cartesian reaction surface in the context of Sec. 3.1.3 it is necessary to have at hand the functional dependencies $f_1^{(BC)}(\zeta_R, \zeta_{X-B})$ and $f_2^{(BC)}(\zeta_R, \zeta_{X-B})$ of the dominant linear vibronic couplings from Fig. 3.5b on the PES. Since ζ_R is approximately constant along the seam (compare Fig. 3.5a) these dependencies are restricted to the matrix coordinate ζ_{X-B}. As it is shown in Fig. 3.5c both vibronic couplings increase upon proceeding elongation of ζ_{X-B} along the crossing seam. This correlation between the matrix coordinate and the vibronic coupling modes q_1 and q_2 immediately becomes plausible when comparing Fig. 3.6 to Fig. 3.2, since both types of

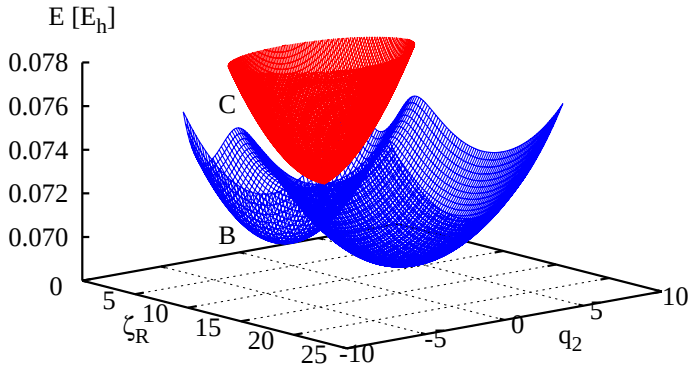

Figure 3.7: Conical intersection between B- and C-states in adiabatic representation when plotting the potential energy as a function of totally symmetric Bromine coordinate ζ_R [amu$^{1/2}$a$_0$] versus the vibronic coupling mode q_2 [dimensionless] of B_{2g} symmetry. For a better visibility of the conical intersection the calculated vibronic coupling constant has been scaled.

coordinates involve the same kind of atoms, that is Window and/or Belt atoms. In addition to these investigations concerning the seam dependence of both dominant vibronic coupling contributions it has been investigated whether the overall coupling pattern of the remainder vibronic coupling modes changes when moving away from the minimum point of the crossing seam. Here it was found that this coupling pattern does not change significantly within the coordinate and energy intervals $-24 \leq \zeta_{X-B} \leq 24$ amu$^{1/2}$a$_0$ and $0.072 \leq E \leq 0.092$ E$_h$.

Comparing Fig. 3.5b to the spectral density in Fig. 3.3a one needs to emphasize that incidentally in both cases there are dominant peaks at frequencies of about 63 cm^{-1}. However, while the 63 cm^{-1} mode in Fig. 3.3a is totally symmetric, it is of B_{2g} symmetry in Fig. 3.6. Furthermore, within the LAC model one still finds a totally symmetric mode with a dominant coupling in the Franck-Condon region. Its character is similar to the full harmonic model described in Fig. 3.3a, but its frequency is shifted to about 61 cm^{-1} upon orthogonalization with the two LAC coordinates.

In essence, a quantum model for describing the B-state predissociation dynamics via the C-state channel should comprise the following nuclear degrees of freedom at minimum: the Bromine and matrix coordinates ζ_R and ζ_{X-B} as well as the vibronic coupling modes q_1 and q_2. This model can be extended by adding tuning modes, that is harmonic normal modes from the $B \leftarrow X$ spectral density of states. These model extensions will be discussed in Sec. 4.4 and Sec. 4.5 on the basis of quantum dynamics simulations for the minimum model in Sec. 4.3 of the following chapter.

4 Quantum Dynamics Simulations

4.1 The Multi-Configuration Time-Dependent Hartree Method

The multi-configuration time-dependent Hartree (MCTDH) method [93,106,107,154–157] has been specifically designed to provide a numerically tractable approach for solving the time-dependent Schrödinger equation:

$$i\hbar\dot{\Psi} \quad = \quad H\Psi \tag{4.1}$$

in case of multi-dimensional systems. Considering a system with f nuclear degrees of freedom k, which may be represented by a set of generalized coordinates $\{Q_k\}$ incorporating the large-amplitude as well as normal mode coordinates ζ and q of the previous sections, the basic concepts behind this method can be illustrated best in contrast to the standard wave packet propagation approach. Establishing the collective index $J = (j_1, \cdots, j_f)$ the standard expansion of the multi-dimensional wave function Ψ into a direct product basis set X_J of time-independent basis functions $\chi_{j_k}^{(k)}(Q_k)$ with the time-dependent expansion coefficients $C_J = C_{j_1 \cdots j_f}(t)$ reads:

$$\Psi(\{Q_k\};t) = \sum_{j_1=1}^{N_1} \cdots \sum_{j_f=1}^{N_f} C_{j_1 \cdots j_f}(t) \prod_{k=1}^{f} \chi_{j_k}^{(k)}(Q_k) \equiv \sum_J C_J X_J \ . \tag{4.2}$$

Here, N_k denotes the number of basis functions $\chi_{j_k}^{(k)}(Q_k)$ required for representing the kth degree of freedom. Practically, for evaluating the action of H onto Ψ, these basis functions are often chosen to be DVR/FBR (grid) functions [158–161]. A comprehensive review of common DVR techniques is given in Ref. [106]. Using expansion Eq. (4.2) and applying the Dirac-Frenkel variational principle to Eq. (4.1):

$$\langle \delta\Psi | H - i\hbar \frac{\partial}{\partial t} | \Psi \rangle \quad = \quad 0 \tag{4.3}$$

the following equations of motions (EOM) for the expansion coefficients C_J can be obtained:

$$i\hbar\dot{C}_J \quad = \quad \sum_L H_{JL} C_L \ , \tag{4.4}$$

where $H_{JL} = \langle X_J | H | X_L \rangle$ denote the matrix elements of the Hamiltonian in the above product basis set. Assuming the same number $N_k = N$ of grid points for all k, the

numerical effort in evaluating Eq. (4.4) becomes proportional to fN^{f+1}. In principle, this exponential scaling restricts the applicability of the direct product expansion, Eq. (4.2), to the quantum description of a few nuclear degrees of freedom only.
Based on the early multi-configurational ideas of Refs. [154, 162] the following ansatz for the wave function Ψ has been proposed [93, 106, 107, 155–157]:

$$\Psi(\{Q_k\};t) = \sum_{j_1=1}^{n_1} \cdots \sum_{j_f=1}^{n_f} A_{j_1 \cdots j_f}(t) \prod_{k=1}^{f} \phi_{j_k}^{(k)}(Q_k;t) \equiv \sum_J A_J \Phi_J \tag{4.5}$$

to overcome these limitations of the numerically exact propagation. Now, the time-dependent expansion coefficients $A_J = A_{j_1 \cdots j_f}(t)$ refer to time-dependent configurations Φ_J, which, in turn, are represented by f-dimensional *Hartree products* of time-dependent *single-particle functions* (SPFs) $\phi_{j_k}^{(k)}(Q_k;t)$. Since these products of one-dimensional wave packets are able to follow the propagation of the system, the individual numbers n_k of single-particle functions required for representing the kth degree of freedom are usually much smaller than the numbers N_k of grid points in the respective time-independent representation Eq. (4.2). Numerically, each SPF $\phi_{j_k}^{(k)}(Q_k;t)$ is represented by a linear combination of time-independent basis (grid) functions $\chi_{i_k}^{(k)}(Q_k)$:

$$\phi_{j_k}^{(k)}(Q_k;t) \quad = \quad \sum_{i_k=1}^{N_k} c_{j_k,i_k}(t) \chi_{i_k}^{(k)}(Q_k) \ . \tag{4.6}$$

Hence, in the limiting case $n_k \rightarrow N_k$ Eq. (4.5) recovers the numerically exact expansion of the wave function Eq. (4.2). However, since both, the expansion coefficients and single-particle functions are time-dependent, Eq. (4.5) also introduces some ambiguities in the representation of the wave function. These redundancies can be lifted when applying additional constraints to the SPFs, e.g. :

$$\langle \phi_j^{(k)} | \phi_l^{(k)} \rangle \quad = \quad \delta_{jl} \ , \tag{4.7}$$

$$\langle \phi_j^{(k)} | \dot{\phi}_l^{(k)} \rangle \quad = \quad 0 \ . \tag{4.8}$$

Further constraints are discussed in Refs. [106, 156, 157]. Specifically, Eq. (4.7) ensures the orthonormality of the SPFs at $t = t_0$, whereas Eq. (4.8) minimizes the motions of the SPFs keeping them orthogonal for all times.
In order to write down the equations of motion for Eq. (4.5) it is helpful to first introduce *single-hole functions*:

$$\Psi_l^{(k)} \quad = \quad \langle \phi_l^{(k)} | \Psi \rangle \ , \tag{4.9}$$

which, in consequence, permit the following alternative expression for Eq. (4.5):

$$\Psi \quad = \quad \sum_l \phi_l^{(k)} \Psi_l^{(k)} \ . \tag{4.10}$$

Based upon these single-hole functions one can then conveniently define *density matrices*:

$$\rho_{jl}^{(k)} = \langle \Psi_k^{(k)} | \Psi_l^{(k)} \rangle \tag{4.11}$$

as well as *mean field* matrix elements acting on the kth degree of freedom only:

$$\langle H \rangle_{jl}^{(k)} = \langle \Psi_k^{(k)} | H | \Psi_l^{(k)} \rangle \ . \tag{4.12}$$

After having defined the *single-particle projector* onto the space of single-particle functions $\{|\phi_{j_k}^{(k)}\rangle\}$:

$$P^{(k)} = \sum_{j_k=1}^{n_k} |\phi_{j_k}^{(k)}\rangle\langle\phi_{j_k}^{(k)}| \tag{4.13}$$

one can employ Eq. (4.11)-Eq. (4.13) for the optimization of the MCTDH coefficients and single-particle functions according to the Dirac-Frenkel variational principle Eq. (4.3). Applying the constraints Eq. (4.7) and Eq. (4.8) the following coupled MCTDH equations of motion can be derived [106, 107]:

$$i\hbar \dot{A}_J = \sum_L \langle \Phi_J | H | \Phi_L \rangle A_L \ , \tag{4.14}$$

$$i\hbar \dot{\boldsymbol{\phi}}^{(k)} = \left(1 - P^{(k)}\right) \left(\boldsymbol{\rho}^{(k)}\right)^{-1} \langle \mathbf{H} \rangle^{(k)} \boldsymbol{\phi}^{(k)} \ . \tag{4.15}$$

Here, $\boldsymbol{\phi}^{(k)} = (\phi_1^{(k)}, \ldots, \phi_{n_k}^{(k)})^T$ refers to a column vector of the individual SPFs $\phi_{j_k}^{(k)}$, and $\boldsymbol{\rho}^{(k)}$ and $\langle \mathbf{H} \rangle^{(k)}$ to the respective density and mean field matrices defined by Eq. (4.11) and Eq. (4.12).

Note, that the eigenvectors and eigenvalues of the density matrix $\boldsymbol{\rho}^{(k)}$, the so-called *natural orbitals* and *natural populations*, are unique quantities with respect to the chosen SPFs, such, that the population of the highest natural orbital provides a measure for the convergence of a MCTDH calculation.

To avoid the direct evaluation of f- and $f-1$-dimensional integrals in the calculation of the Hamilton matrix elements Eq. (4.14) and mean fields Eq. (4.15) the MCTDH package [163] utilizes a separate representation of the Hamiltonian in terms of sums over products of one-dimensional operators, similar to expansion Eq. (4.5). For this purpose any user-supplied PES can be fit into such separable terms using the internal Potfit algorithm [164, 165]. Given s expansion terms and assuming n single-particle functions and N grid points for all f degrees of freedom, the total effort in evaluating Eq. (4.14) and Eq. (4.15) scales proportional to $sfn(N^2 + fn^f)$, which is advantageous over fN^{f+1} from Eq. (4.4) as long as $n \ll N$.

Since the time-dependent Schrödinger Eq. (4.1) is an initial value problem it requires an initial guess $\Psi(t = 0)$, e.g. a simple Hartree product of 1D-eigenfunctions of uncoupled Hamiltonians. Based on this first guess the true ground state wave function Ψ_0 of a coupled Hamiltonian can then be generated by propagating the initial wave packet in imaginary time $t \to -i\tau$. Establishing the time-dependent expectation value $E(\tau)$ of H it follows

from the formal solution of this propagation [106]:

$$\Psi(\tau) \;=\; \exp\left(\int [E(\tau)-E_0]d\tau\right)\exp(-[H-E_0]\tau/\hbar)\Psi(0)\;, \tag{4.16}$$

that $\Psi(\tau)$ relaxes towards the ground state with the energy E_0 while damping out all other eigenstate contributions and preserving the norm of the wave function.
For the specific treatment of non-adiabatic systems a particular MCTDH extension, the so-called *multi-set formalism* has been developed [93,106,107,150,157,166,167] employing different sets of single particle functions for each electronic state. Therefore, the wave function Ψ as well as the Hamiltonian H need to be expanded into the set $\{|a\rangle\}$ of electronic states:

$$|\Psi\rangle \;=\; \sum_a \Psi^{(a)}|a\rangle\;, \tag{4.17}$$

$$H \;=\; \sum_a\sum_b |a\rangle H^{(ab)}\langle b|\;, \tag{4.18}$$

where each wave function $\Psi^{(a)}$ is expanded into MCTDH form (cf. Eq. (4.5)) individually. Labeling the distinct electronic states by additional superscripts a and b the following multi-set equations of motions can be obtained on the basis of Eq. (4.14) and Eq. (4.15) [106,157,167]:

$$i\hbar\dot{A}_J^{(a)} \;=\; \sum_b\sum_L \langle\Phi_J^{(a)}|H^{(ab)}|\Phi_L^{(b)}\rangle A_L^{(b)}\;, \tag{4.19}$$

$$i\hbar\dot{\boldsymbol{\phi}}^{(a,k)} \;=\; \left(1-P^{(a,k)}\right)\left(\boldsymbol{\rho}^{(a,k)}\right)^{-1}\sum_b \langle\mathbf{H}\rangle^{(ab,k)}\boldsymbol{\phi}^{(b,k)}\;. \tag{4.20}$$

Independent of single or multi-set formulation, the MCTDH equations of motion, e.g. Eq. (4.14) and Eq. (4.15) form a system of coupled non-linear differential equations of first order. Alternative to their standard integration in terms of predictor-corrector methods, which is referred to as *variable mean-field* (VMF) [106] integration scheme, the MCTDH package [163] provides another integration scheme specifically developed for the numerically efficient solution of both equations. This so-called *constant mean-field* (CMF) [157] integration scheme utilizes the fact, that the Hamiltonian matrix elements $\langle\Phi_J|H|\Phi_L\rangle$, as well as the products of the inverse density and mean field matrices $\left(\boldsymbol{\rho}^{(k)}\right)^{-1}\langle\mathbf{H}\rangle^{(k)}$, change much slower in time than the MCTDH coefficients and single-particle functions, such that the former matrix elements can be kept constant over some time. In consequence, the differential equation for the A-vector, Eq. (4.14), turns into a set of linear equations with constant coefficients, which can be solved most efficiently using the short iterative Lanczos (SIL) or Lanczos-Arnoldi integrators as implemented in [163]. Similarly, the differential equation for the single-particle functions, Eq. (4.15), splits up into each subsets of uncoupled, but still non-linear equations, which can be integrated using the implemented Bulirsch-Stoer (BS) extrapolation method.

4.2 Grid Representation of the Reaction Surface

For a quantum description of the LAC motions it is necessary to transform the Cartesian reaction surfaces from Fig. 3.4 into a an appropriate discrete variable representation (DVR). This transformation can be accomplished via a finite basis set representation (FBR) of the position operator. Upon diagonalizing its matrix representation one obtains the respective position eigenvalues and eigenfunctions (δ-functions). The matrix elements of the potential energy operator in the discrete variable representation can then be obtained by evaluating the potential energy at these eigenvalues of the position operator. Furthermore, the eigenvector coefficients of the position operator provide the linear combinations for the unitary transformation between the DVR and FBR of the potential energy operator. This way the matrix elements of the potential energy operator in FBR can be calculated efficiently. In particular, the latter representation takes advantage of the fact, that the matrix elements of the kinetic energy operator can be calculated analytically [106].
In order to find an optimal DVR for the representation of the reaction surface it is necessary to estimate the accessible energy and coordinate range of the process under investigation. Focusing, for instance on a Franck-Condon vertical excitation [168,169] from the electronic ground state X to the electronic B-state the reflection principle [1, 169–171] can provide the required information. According to this principle the energy distribution of ground state wave packet in the electronically excited state is determined by its initial width and the gradient of excited state potential at the ground state equilibrium geometry. This principle is exemplified in Fig. 4.1a for a one-dimensional cut of the PES (cf. Fig. 3.4) along the Bromine coordinate ζ_R. It is shown, that the energy distribution of the Br_2 ground state wave packet in the electronic B-state is centered around the $B \leftarrow X$ Franck-Condon excitation energy within a total energy interval of $0.07 \leq E \leq 0.12$, which covers about 124 and 140 vibrational levels on the B- and C-state surfaces, respectively. This energy interval corresponds to a maximum kinetic energy of 0.05 E_h gained by the system upon excitation to the B-state. In mass-weighted coordinates ζ, where the respective momentum operator is defined by $p_\zeta = \frac{\hbar}{i}\frac{\partial}{\partial\zeta}$ this energy value corresponds to a maximum momentum of 13.5 $\hbar/\mathrm{amu}^{1/2}\mathrm{a}_0$.
The number of grid points required for properly representing this momentum value not only depends on the extension of the PES along both LAC, but also on the particular basis set employed. According to Fig. 4.1b the coordinate intervals of all these PES at the respective cutoff energy of 0.12 E_h are given by $\zeta_R \in [-6, 38] \widehat{=} 44$ amu$^{1/2}$a$_0$ and $\zeta_{X-B} \in [-68, 47] \widehat{=} 115$ amu$^{1/2}$a$_0$. In case of a Colbert-Miller DVR [172] or an exponential DVR [159, 173, 174], which is related the fast Fourier transform (FFT) pseudo-spectral method [162, 175], that is when using either particle-in-a-box functions or plane waves as FBR basis sets, one would require 200×500 grid points for a proper DVR representation of the reaction surface. However, in case of a harmonic oscillator (Hermite) DVR [158,160,161] (for details see Sec. 5.6 of the Appendix), only 160×400 are required for describing the accessible energy and coordinate range at the same quality. Thus the harmonic oscillator eigenfunctions provide a more compact representation as compared to one of the former

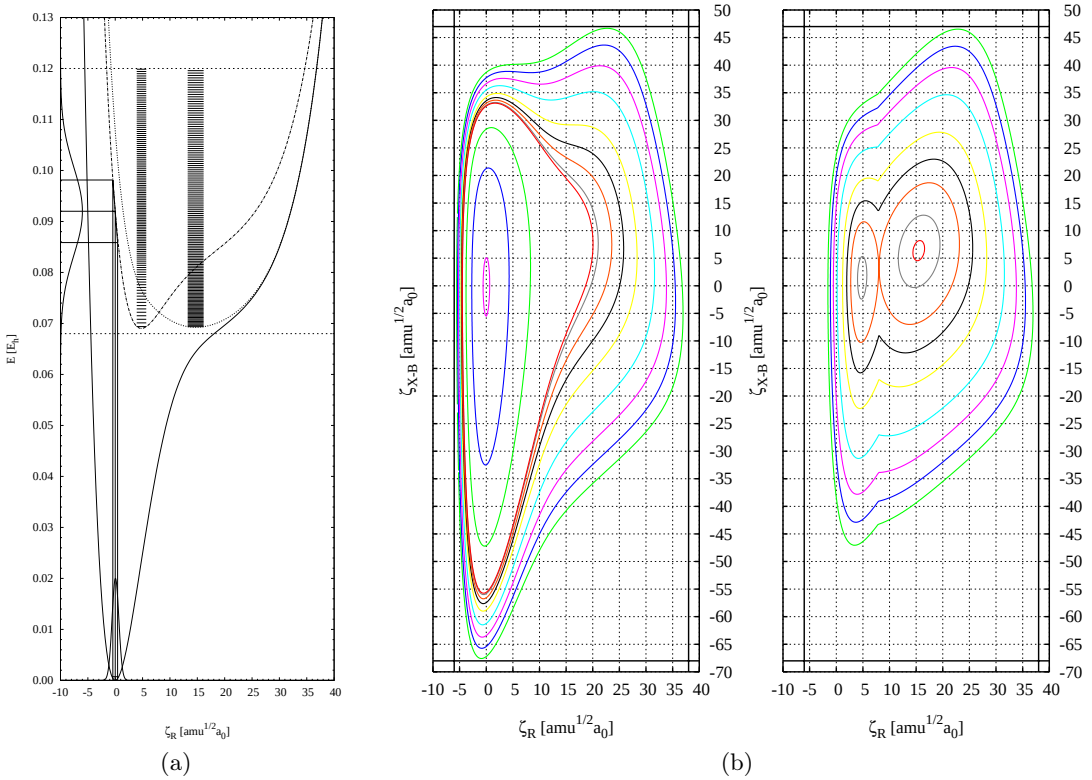

(a) (b)

Figure 4.1: (a) Reflection principle applied to the electronic $B \leftarrow X$ Franck-Condon vertical transition for a one-dimensional cut of the PES from Fig. 3.4 along the Bromine coordinate ζ_R. The corresponding energy distribution of the initial ground state wave packet is shown to approximately cover 124 and 140 vibrational levels in the respective electronic B- (dash-dotted curve) and C-states (dashed curve). (b) Close-up view of the X- and lower adiabatic BC-state surface showing the grid extension along the coordinates ζ_R and ζ_{X-B} for a cutoff-energy of 0.12 E_h (isopotential contour lines are drawn at 0.0007, 0.0200, 0.0450, 0.0685, 0.0693, 0.0719, 0.0750, 0.0800, 0.0900, 0.1000, 0.1100 and 0.1200 E_h).

basis sets, since the respective DVR grid points are not equidistant. This way one can explicitly save 36000 grid points in the DVR representation of the reaction surface, which is particularly relevant for a numerically exact solution of the Schrödinger equation.

4.3 A Four-Dimensional Minimum Model

As it has been detailed in Sec. 3.2.2 and Sec. 3.3 the theoretical description of the vibronically coupled B- and C-state dynamics requires a four-dimensional model at minimum. Specifically, this model incorporates both large amplitude coordinates shown in Fig. 3.2, which span up the Cartesian reaction surfaces from Fig. 3.4, as well as both coupling modes depicted in Fig. 3.6, which provide the linear vibronic B, C-state coupling elements from Fig. 3.5. Explicitly, the matrix representation of time-dependent Schrödinger equation

Eq. (4.1) for this model reads:

$$i\hbar\frac{\partial}{\partial t}\begin{pmatrix}\Psi_X\\ \Psi_B\\ \Psi_C\\ \Psi_{C'}\end{pmatrix} = \begin{pmatrix} T+V_X & -\mu_{XB}\mathcal{E}(t) & 0 & 0\\ -\mu_{BX}\mathcal{E}(t) & T+V_B & -V^*_{BC} & V_{BC'}\\ 0 & -V_{BC} & T+V_C & 0\\ 0 & V^*_{BC'} & 0 & T+V_{C'}\end{pmatrix}\begin{pmatrix}\Psi_X\\ \Psi_B\\ \Psi_C\\ \Psi_{C'}\end{pmatrix} . \quad (4.21)$$

Employing the mass-weighted large-amplitude coordinates ζ_R and ζ_{X-B} as defined by Eq. (3.29) and Eq. (3.30) in Sec. 3.2.2 and the dimensionless oscillator coordinates q_1 and q_2 together with respective frequencies ω_1 and ω_2 from Sec. 3.3 the kinetic energy operator T is given by:

$$T = -\frac{\hbar^2}{2}\left(\frac{\partial^2}{\partial\zeta_R^2}+\frac{\partial^2}{\partial\zeta_{X-B}^2}\right)-\frac{\hbar}{2}\left(\omega_1\frac{\partial^2}{\partial q_1^2}+\omega_2\frac{\partial^2}{\partial q_2^2}\right) . \quad (4.22)$$

Particularly, the usage of orthogonal coordinates has the advantage that there appear no kinetic couplings in Eq. (4.22), at least as long as one does not explicitly consider the effect of librational motion, which, however, was found to be small in Sec. 2.4.3.
Focusing on the potential energy operator representation in Eq. (4.21) its diagonal matrix elements are given by:

$$V_a = U_a(\zeta_R,\zeta_{X-B})+\frac{\hbar}{2}\left(\omega_1 q_1^2+\omega_2 q_2^2\right) \quad (4.23)$$

as a sum of the harmonic potential energy contributions of the coupling modes q_1 and q_2 and the potential energy surfaces $U_a(\zeta_R,\zeta_{X-B})$ with $(a = X, B, C, C')$ from Fig. 3.4. Note, that the diabatic C-states are degenerate, that is $U_C = U_{C'}$.
Its off-diagonal elements, in turn, are determined by the linear vibronic coupling contributions $f^{(1)}_{BC}(\zeta_{X-B})$ and $f^{(2)}_{BC}(\zeta_{X-B})$ of both coupling modes:

$$V_{BC} = V_{BC'} = \hbar f^{(2)}_{BC}(\zeta_{X-B})q_2 + i\cdot\hbar f^{(1)}_{BC}(\zeta_{X-B})q_1 \quad (4.24)$$

as function of the B, C crossing seam shown in Fig. 3.5 of Sec. 3.3. As consequence of the complex valued DIM-Hamiltonian matrix Eq. (2.18), and its derivatives detailed in Sec. 5.2 and Sec. 5.5 of the Appendix, the second term of Eq. (4.24) is purely imaginary (cf. Eq. (4.21)).
In order to describe the laser excitation process a linear approximation to the coordinate dependence of the electronic $B \leftarrow X$ transition moment with the ground state equilibrium geometry serving as a reference has been utilized:

$$\mu_{XB} = \mu^{(0)}_{XB}+\frac{\partial\mu_{XB}}{\partial\zeta_R}\zeta_R \quad (4.25)$$

adapting the respective parameters $\mu^{(0)}_{XB} = 0.15$ ea$_0$ and $\partial\mu_{XB}/\partial\zeta_R = 0.01$ $^e/_{\mathrm{amu}^{1/2}}$ from Refs. [176–178]. Further, employing the semi-classical dipole approximation the laser field

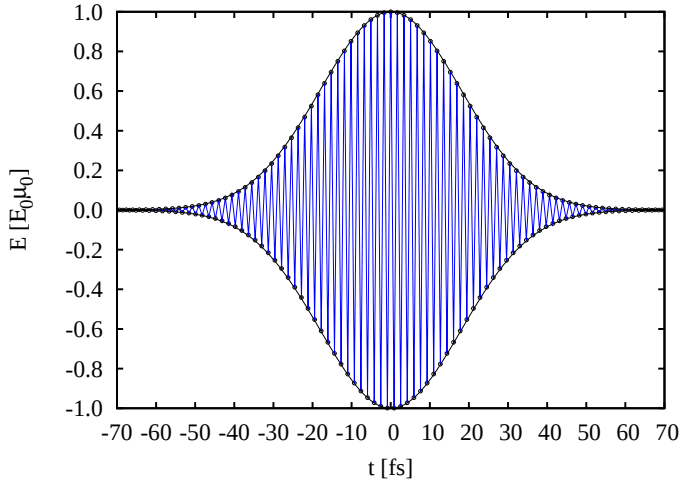

Figure 4.2: Typical laser pulse applied in the simulation of a $B \leftarrow X$ vertical transition with a respective electronic transition moment $\mu^{(0)}_{XB} = 0.15$ ea$_0$ and a resonance frequency $\hbar\omega = 0.09$ E$_\mathrm{h}$ for a pulse duration of $\sigma = 18$ fs and a field strength of $\mathcal{E}_0 = 0.005$ E_h/ea_0, see Eq. (4.26).

itself has been taken into account in the following form:

$$\mathcal{E}(t) \quad = \quad \mathcal{E}_0 \exp(-t^2/2\sigma^2)\cos(\omega t) \ . \tag{4.26}$$

A typical laser pulse applied in the simulations is shown in Fig. 4.2. Its corresponding parameters field strength $\mathcal{E}_0 = 0.005$ E_h/ea_0 and duration $\sigma = 18$ fs refer to an experimental pulse [13] with a full width at half maximum (FWHM) intensity of 30 fs, a laser spot diameter $50 \leq d \leq 100$ μm with a spot area $A = \frac{\pi}{4}d^2$ and a pulse energy of $E = 1$ μJ [1]. For the description of the quantum dynamics on the different electronic states a harmonic oscillator DVR (cf. Sec. 4.2) of Eq. (4.21) has been applied using the multi-set formulation of the MCTDH method (cf. Sec. 4.1). The respective grid parameters for the present 4D minimal model, as well as the models presented in the following sections, are compiled in Tab. 4.1. Using the fact that the dipole operator Eq. (4.25) acts along ζ_R only the constant mean field (CMF) propagation scheme [106] as implemented in the MCTDH package [163] can be applied to the numerical integration of the coupled equations of motion Eq. (4.19)

[1] Switching to the complex representation $2\cos(\omega t) = \exp(i\omega t) + \exp(-i\omega t)$ of the cosine in Eq. (4.26), the field strength $\mathcal{E}_0$ of the laser pulse can be calculated from the relation [145]:

$$E \quad = \quad \frac{A\varepsilon_0 c_0}{\omega}\int [i\dot{\mathcal{E}}^\dagger\mathcal{E} + c.c.]dt \ ,$$

where ε_0 is the vacuum permittivity (electric constant) and c_0 the speed of the light. Using the intermediate result $2\omega\mathcal{E}_0^2\exp(-t^2/\tau^2)$ for the integrand together with the integral $\int_0^\infty \exp(-t^2/\tau^2) = \frac{\sqrt{\pi}}{2}\tau$ the following expression can be obtained:

$$E = A\varepsilon_0 c_0 \mathcal{E}_0^2\sqrt{\pi}\tau \qquad \text{giving} \qquad \mathcal{E}_0 = \frac{2}{d}\sqrt{\frac{E}{\pi^{3/2}\varepsilon_0 c_0 \tau}}$$

after some rearrangement.

Table 4.1: Parameters used for the MCTDH propagation of different models. All coordinates were represented by a harmonic oscillator DVR using N_k grid points; the numbers of SPFs per DOF, n_k, are given in the last columns for the respective electronic states. The numbers in parenthesis refer to reference calculations used to check the convergence of the results.

Mode	N_k	X	B	C	C'
ζ_R	160	2 (3)	10 (15)	10 (15)	10 (15)
ζ_{X-B}	400	2 (3)	10 (15)	10 (15)	10 (15)
q_1	10 (100)	1 (2)	2 (3)	2 (3)	2 (3)
q_2	10 (100)	1 (2)	2 (3)	2 (3)	2 (3)
q_3	65	1 (2)	10 (15)	10 (15)	10 (15)
$\tilde{q}_1$	300	1	1	1	1
$\tilde{q}_2$	100	1	1	1	1
$\tilde{q}_3$	400	1	1	1	1
$\tilde{q}_4$	200	1	1	1	1
$\tilde{q}_5$	200	1	1	1	1
$\tilde{q}_6$	200	1	1	1	1
$\tilde{q}_7$	250	1	1	1	1
$\tilde{q}_8$	150	1	1	1	1
$\tilde{q}_9$	100	1	1	1	1
$\tilde{q}_{10}$	80	1	1	1	1
$\tilde{q}_{11}$	60	1	1	1	1
$\tilde{q}_{12}$	70	1	1	1	1
$\tilde{q}_{13}$	50	1	1	1	1
$\tilde{q}_{14}$	25	1	1	1	1
$\tilde{q}_{15}$	30	1	1	1	1
$\tilde{q}_{16}$	10	1	1	1	1
$\tilde{q}_{17}$	65	1	1	1	1

and Eq. (4.20). Specifically, the A-vector and the SPFs have been integrated applying the complex Lanczos-Arnoldi and Bulirsch-Stoer integrators of the respective maximal orders 15 and 9 with an error tolerance of 10^{-7} atomic units.
For analyzing the wave packet dynamics the following reduced two-dimensional densities along the coordinates ζ_R and ζ_{X-B}:

$$\rho_a(\zeta_R, \zeta_{X-B}; t) \quad = \quad \iint |\Psi_a(\zeta_R, \zeta_{X-B}, q_1, q_2; t)|^2 \, dq_1 dq_2 \ , \tag{4.27}$$

together with the one-dimensional reduced density for ζ_R:

$$\rho_a(\zeta_R; t) \quad = \quad \int \rho_a(\zeta_R, \zeta_{X-B}; t) \, d\zeta_{X-B} \tag{4.28}$$

and, likewise, for ζ_{X-B}, will be used. Furthermore, focusing on the B- to C-state predissociation the relative C-state(s) population defined as:

$$P(t) \quad = \quad \frac{P_C(t) + P_{C'}(t)}{1 - P_X(t)} \ , \tag{4.29}$$

will be monitored, where the individual electronic populations are obtained from:

$$P_a(t) \quad = \quad \int \rho_a(\zeta_R; t) \, d\zeta_R \ . \tag{4.30}$$

In order to unravel the mechanistic aspects of the B- to C-state predissociation laser-driven wave packet simulations have been performed with focus on the dynamics of the relative C-state population, Eq. (4.29), in dependence on different initial conditions, which have been obtained as vibrational eigenstates of one-dimensional X-state PES cuts using the MCTDH package [163]. For this purpose, the following three scenarios have been chosen for a closer examination:

(I) a Franck-Condon vertical excitation starting from the vibrational ground state,

(II) a resonant excitation starting from the first vibrationally excited state along the Bromine coordinate ζ_R, and

(III) a resonant excitation starting from the first vibrationally excited state along the vibronic coupling mode q_2.

The population dynamics for the three different initial conditions is shown in Fig. 4.3. For the given laser parameters the total population transfer to the B-state out of the electronic ground state X amounts to about 8%. One of the first things one notices on inspecting Fig. 4.3 is a step-wise increase of the C-state population during the time intervals 400-550 fs and 1300-1450 fs as a common feature in all three cases considered. In between these two intervals there is approximately a plateau where the population does not change significantly. A similar plateau is observed after 1450 fs. Note, that the overall population

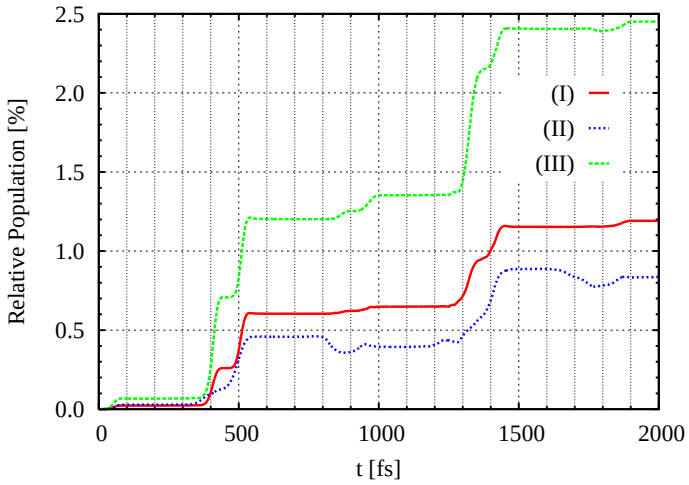

Figure 4.3: Population dynamics (relative C-state population, Eq. (4.29), 4D model) for (I) a Franck-Condon vertical transition, (II) a vibrational preexcitation of the Bromine coordinate ζ_R lowering the excitation energy, and (III) a vibrational preexcitation of the B_{2g}-mode q_2. The scenario of a vibrational preexcitation of the matrix coordinate ζ_{X-B} has been taken out of explicit consideration, since test calculations along these lines have shown almost no effect. Note, that the two C-states are approximately equally populated.

transfer during the first 2 ps amounts to 1-2.5% only, depending on the initial state.
In order to get an impression about the general wave packet dynamics following upon laser pulse excitation to the electronic B-state it is instructive to focus on case (I) as reference first, that is, the Franck-Condon excitation starting from the vibrational ground state. Fig. 4.4 shows the respective time-evolution of the reduced 2D density, Eq. (4.27), on the diabatic B-state PES as series of snapshots taken at characteristic points in time. Around time $t = 0$ fs the wave packet emerges in the Franck-Condon region of the excited B-state surface. At about 50 fs it has reached the crossing seam without significant motion along the matrix coordinate. At $t = 225$ fs the wave packet arrives at the outer turning point of the B-state potential from where it is reflected also in direction of the collective matrix coordinate. The next snapshot shows the wave packet at 400 fs when it passes the crossing seam for the second time, now, however, with its center significantly displaced along the matrix coordinate. After about 450 fs the wave packet hits the inner turning point of the B-state potential completing the first round trip of the Bromine coordinate. The last snapshot shows the wave packet at the end of the propagation interval (2 ps). Altogether the wave packet exhibits a parabolic motion on the B-state surface.
A more specific view onto the non-adiabatically coupled B- and C-state dynamics is provided when analyzing the individual reduced 1D densities, Eq. (4.28), and expectation values of the kinetic energy of the Bromine and matrix coordinates, for case (I) in Fig. 4.5. The respective 1D reduced densities in Fig. 4.5a and Fig. 4.5c reveal an approximate $1 : 2$ ratio for the periods of the Bromine and matrix motions. This ratio can now be correlated with the population dynamics shown in Fig. 4.3. A steep rise in the C-state population occurs whenever the center of the wave packet passes the crossing seem *and* is displaced along the matrix coordinate. Comparing Fig. 4.5a and Fig. 4.5c this condition is matched

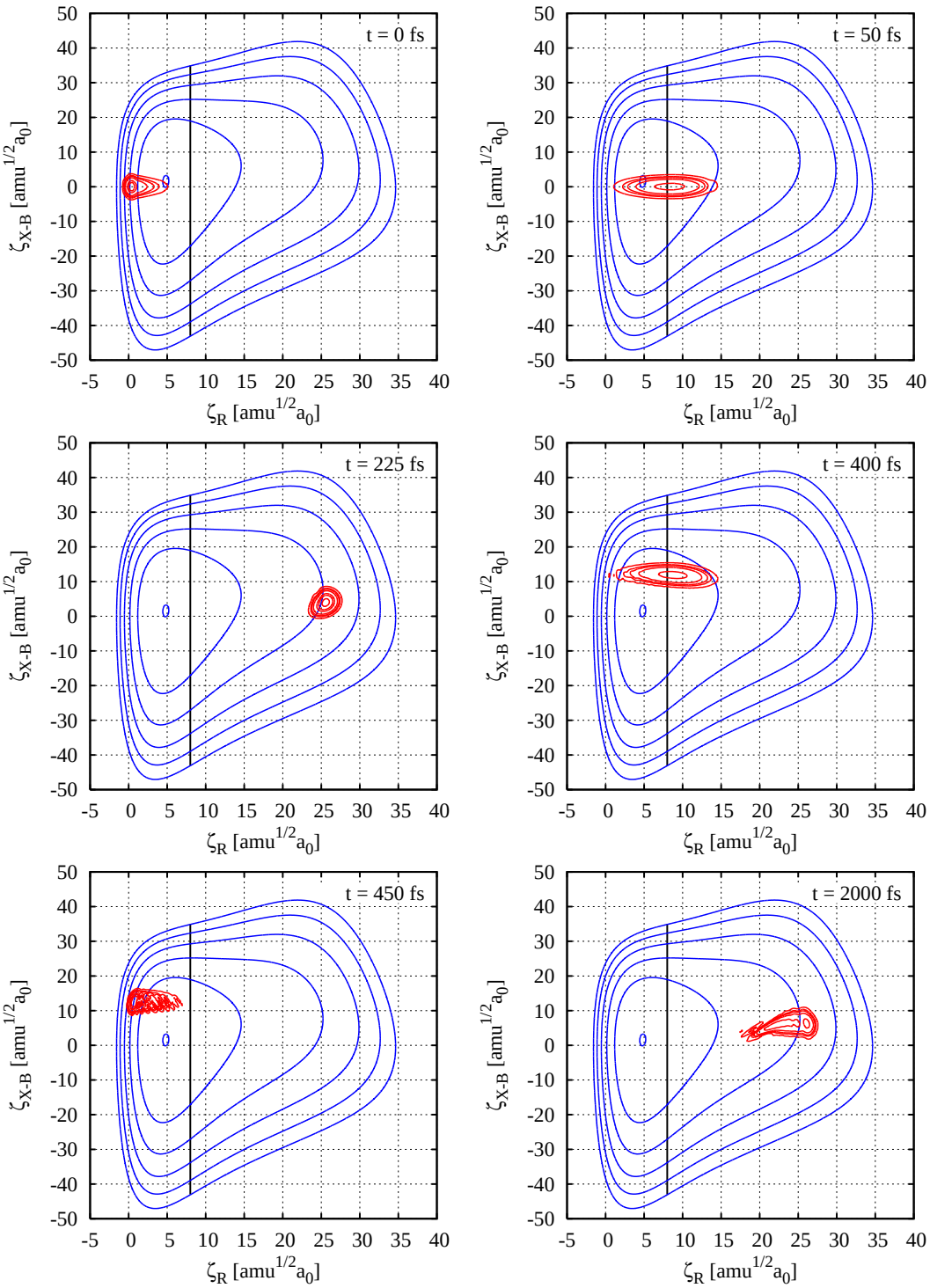

Figure 4.4: Snapshots showing the time-evolution of the 2D reduced density $\rho_B(\zeta_R, \zeta_{X-B})$ (isodensity values 0.0001, 0.0003, 0.0005, 0.001, 0.003, 0.005, 0.01, 0.03) on the diabatic B-state surface (contour levels 0.069, 0.08, 0.09, 0.10, 0.11, 0.12 E_h) after Franck-Condon excitation, case (I). The position of the crossing seam (cf. Fig.3.5a) is indicated by a vertical line.

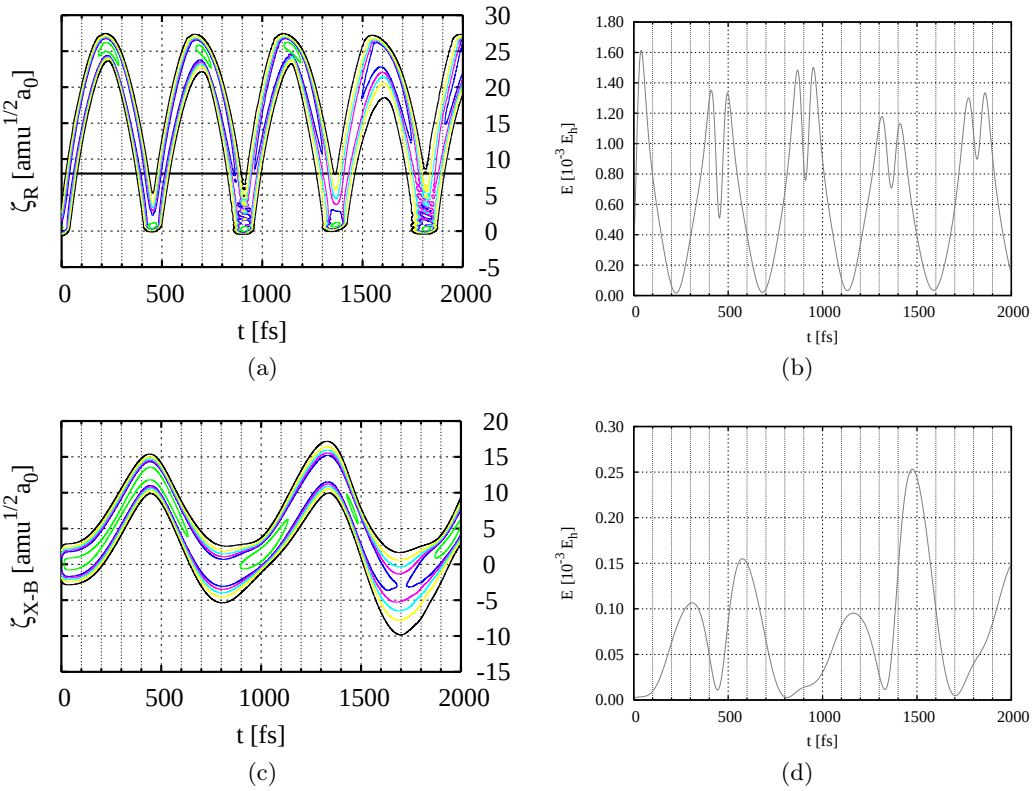

Figure 4.5: Franck-Condon excitation, case (I): Time-dependent reduced 1D B-state densities for (a) the Bromine coordinate $\rho^{(B)}(\zeta_R, t)$ (isodensity values 0.001, 0.003, 0.005, 0.007, 0.01, 0.03) and (c) the matrix coordinate $\rho^{(B)}(\zeta_{X-B}, t)$ (isodensity values 0.002, 0.004, 0.006, 0.008, 0.01, 0.02), together with the time-dependent expectation values of (b) the Bromine kinetic energy and (d) the matrix kinetic energy (in units 10^{-3} $\mathrm{E_h}$). The position of the crossing seam is indicated by a horizontal line in (a).

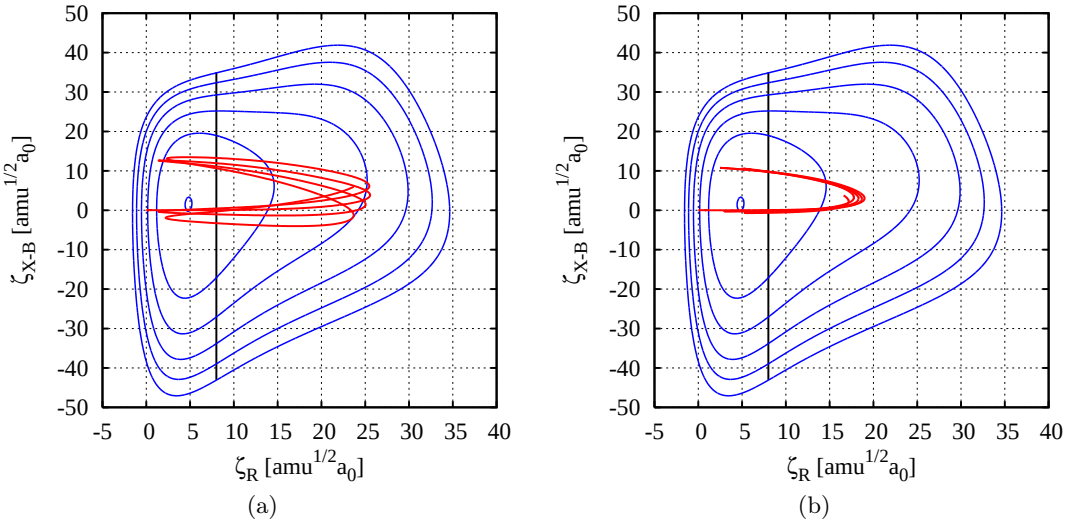

Figure 4.6: Trajectories $(\langle\zeta_R\rangle, \langle\zeta_{X-B}\rangle)$ for the wave packet center of mass motion on the diabatic B-state surface following (a) a Franck-Condon vertical excitation without prior vibrational preexcitation, case (I) (cf. Fig. 4.4), and (b) a resonant excitation of the vibrationally preexcited Bromine coordinate ζ_R, case (II). Potential contours are the same as in Fig. 4.4.

at the times 450 fs and 1350 fs, when the Bromine coordinate is near the inner turning point and the matrix coordinate at the outer turning point. This finding implies that a change of the matrix cage coordinate ζ_{X-B} is essential for triggering the non-adiabatic transition. The reason for this behavior can be found in the dependence of the vibronic coupling strength on the matrix coordinate as shown in Fig. 3.5c of Sec 3.3, i.e. its strong increase upon cage deformation.

A closer look at the population in the rise intervals shows that there is a small plateau which corresponds to the situation that the wave packet has passed the crossing seam and hits the inner turning point. Thus the rise in population originates from a single transfer event per ζ_R round trip, occurring either upon bond elongation or contraction. Note, that the expectation value of the Bromine kinetic energy in Fig. 4.5b exhibits a double peak structure at the inner turning point, where it does not fall off to zero. Its finite value can be explained by the two competing processes of wave packet contraction and dispersion at the inner wall of the B-state PES. Further, when considering the time-evolution of the 1D densities in Fig. 4.5a and Fig. 4.5c, as well as the snapshots of the 2D density in Fig. 4.4, one notices that the wave packet stays relatively compact, which suggests a description of the wave packet motion in terms of time-dependent coordinate expectation values. Such wave packet based trajectories have already been utilized for the analysis of vibronically coupled problems by Domcke and Köppel [91] before. Fig. 4.6a shows the projection of such a wave packet trajectory motion (cf. Fig. 4.4) onto the $(\langle\zeta_R\rangle, \langle\zeta_{X-B}\rangle)$-plane for the reference case (I). This figure not only provides an alternative view on the conditions for predissociation, but also highlights the 1:2 resonance of the round trip times by an Lissajous parabola for the wave packet center of mass motion on the B-state PES.

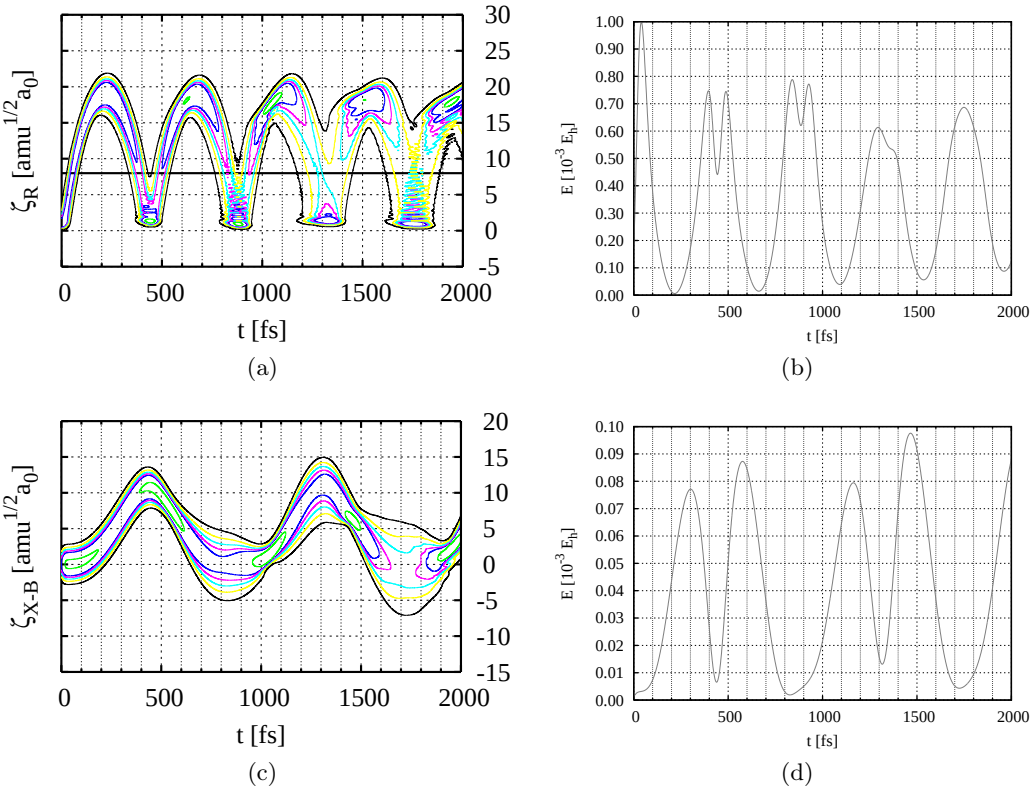

Figure 4.7: Same as Fig. 4.5, but for a resonant laser pulse excitation to the B-state starting from the vibrationally preexcited Bromine coordinate ζ_R, case (II).

Focusing on the effect of different initial conditions in Fig. 4.3, that is vibrational preexcitation in the X-state, for case (II), the preexcitation of the Bromine coordinate ζ_R, one finds that the overall population transfer during the first 2 ps is slightly reduced as compared to case (I). This behavior can be traced back to the fact, that, due to the lowered excitation energy required for fulfilling the resonance condition of the $B \leftarrow X$ transition the wave packet is located deeper in the B-state potential, which reduces the degree of matrix excitation upon reflection from the matrix wall around the outer turning point. A more detailed view on this reduced molecule-matrix interaction is provided when comparing the amplitudes of the Bromine and matrix coordinates in Fig. 4.7a and Fig. 4.7c, as well as the energy kinetic energies in Fig. 4.7b and Fig. 4.7d to the respective quantities in Fig. 4.5. Qualitatively, the double peak structure of the Bromine kinetic energy in Fig. 4.7b vanishes upon wave packet broadening at the inner turning points for $t = 1300$ fs and $t = 1750$ fs (cf. Fig. 4.7a). Further, the oscillations of the matrix kinetic energy in Fig. 4.7d appear uniform in comparison to Fig. 4.5d indicating a diminishing energy exchange between the Bromine and matrix coordinates. An overall picture of the dynamics for case (II) can be inferred from the trajectory in Fig. 4.6b. Apparently, for this excitation condition the trajectory resembles even more a 1:2 parabolic Lissajous figure, which does not fluctuate around the outer turning point, hence reflecting the reduced anharmonicity of the PES at this energy.

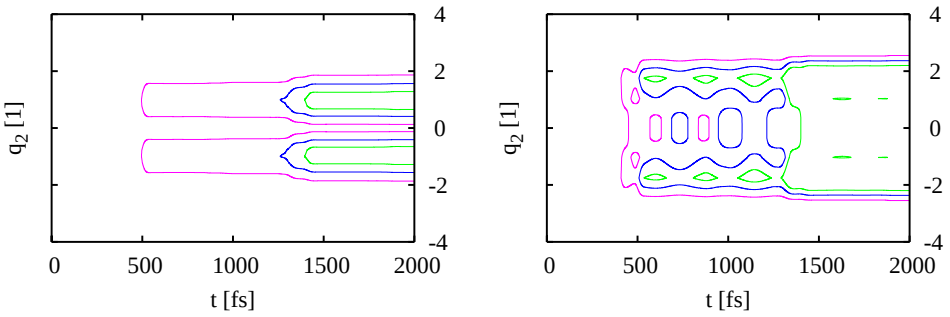

Figure 4.8: Evolution of the density (isodensity values 0.00005, 0.00010, 0.00015) along the coupling mode q_2 in the C-state for (a) case (I) and (b) case (III).

Next, when considering the case (III) in Fig. 4.3 one notices that the preexcitation of the vibronic coupling mode q_2 leads to an increase of the population transfer by a factor of about 2. Here, even without appreciable matrix coordinate elongation transfer occurs, e.g. around 1000 fs. Qualitatively this is a consequence of the linear coordinate dependence of the vibronic coupling operator. In more (semi-)quantitative terms one may think of this increase in the context of Landau-Zener theory (see, e.g. [179]). Suppose that $|m\rangle$ and $|n\rangle$ denote the sets of eigenstates of the coupling mode oscillator q_2 in the electronic B- and C-states. For the linear coupling, Eq. (4.24), the non-vanishing transition matrix elements are then given by:

$$\langle m|q|n\rangle \quad \propto \quad \sqrt{n}\langle m|n-1\rangle + \sqrt{n+1}\langle m|n+1\rangle \ ,$$

which follows as consequence of the ladder operator representation of the coordinate operator in a harmonic oscillator basis set as detailed in Sec. 5.6. Thus, starting from B_0 ($m = 0$ level in B-state) the dominant pathway is $B_0 \rightarrow C_1$, whereas upon preexcitation one has the two pathways $B_1 \rightarrow C_0$ and $B_1 \rightarrow C_2$. This circumstance is illustrated in Fig. 4.8 showing the density along the vibronic mode q_2 in the C-state. Here it is confirmed that for case (I) only the $n = 1$ vibrational eigenstate of q_2 is populated, whereas the respective wave packet in case (III) is a mixture of the $n = 0$ and $n = 2$ vibrational eigenstates.

4.4 Systematic Extension: 5D Model

In Sec. 3.2.2 it has been shown, that the matrix coordinate ζ_{X-B} already resembles the linear coupling of the tuning modes (cf. set G_1 in Eq. (3.24) of Sec. 3.1.3) in the Franck-Condon region of the B-state to a large extend. However, particularly when comparing the spectral weights of the $B \leftarrow X$ transition in Fig. 3.3a to the normal mode projection of ζ_{X-B} in Fig. 3.3b for the dominant peak at 63 cm^{-1} one notices that the effective matrix coordinate cannot completely reproduce the coupling of this specific normal mode. In order to recover that part of coupling missing in the LAC description the individual gradients of the B-state diagonal matrix elements can be mapped onto those ground state normal

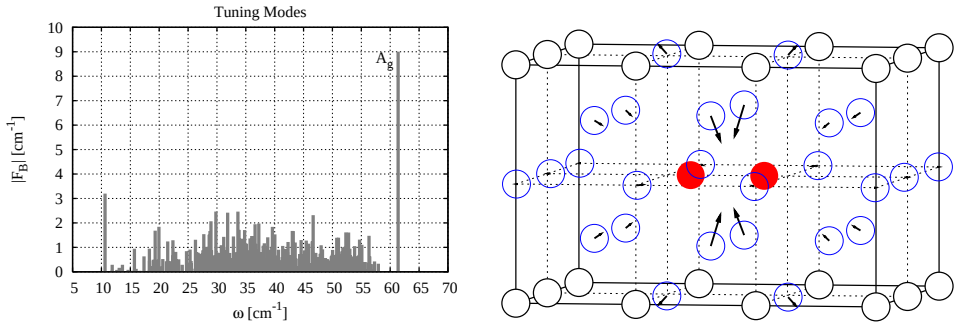

(a) (b)

Figure 4.9: (a) Coupling to the $B \leftarrow X$-transition and (b) atomic displacement vectors of the tuning mode q_3 ($\omega_3 = 61.4$ cm^{-1}) with A_g symmetry.

modes q_k with $k = 1, \ldots, 3N-5$, which are orthogonal to the reaction plane. The absolute values of the resulting linear intra-state coupling constants $f_k^{(B)}$ determined in the Franck-Condon region of the B-state PES are shown in Fig. 4.9a. Next to an almost continuous distribution of weakly coupling modes within the interval $10 \leq \omega \leq 57$ cm^{-1} one again finds a dominant contribution similar to Fig. 3.3a, which now appears at a frequency of $\omega = 61$ cm^{-1}. The respective atomic displacement vectors in Fig. 4.9b clearly identify this mode as Belt mode with A_g symmetry. This normal mode corresponds to the dominant contribution in Fig. 3.3 of Sec. 3.2.2, however, with its respective frequency ω_3 shifted due to the orthogonalization.

It is thus suggestive to add this mode q_3 to the 4D minimal model from Sec. 4.3. For this purpose, next to the linear coupling $f_3^{(B)}$ of this tuning mode within Franck-Condon region of the B-state PES also its dependence $f_3^{(B)}(\zeta_R, \zeta_{X-B})$ along the Bromine and matrix coordinates is required. Rather than explicitly evaluating this force at each grid point of the reaction surface its dependence can be approximated by means of the second derivatives $k_{3,R}^{(B)}$ and $k_{3,X-B}^{(B)}$ of the B-state potential with respect to q_3, ζ_R and ζ_{X-B}:

$$f_3^{(B)}(\zeta_R, \zeta_{X-B}) \approx k_{3,R}^{(B)} \cdot \zeta_R + k_{3,X-B}^{(B)} \cdot \zeta_{X-B} \, . \tag{4.31}$$

In turn, these mixed second derivatives, which may be abbreviated as $k_{3,s}^{(B)}$ with $s = R, X-B$, can be obtained from mass-weighted Hessian matrix elements $\tilde{k}_{ij}^{(B)}$ via the following bilinear transform:

$$k_{3,s}^{(B)} = \sum_{i=1}^{3N} \sum_{j=1}^{3N} l_{3i} \tilde{k}_{ij}^{(B)} u_{js} \, , \tag{4.32}$$

with the coefficients l_{3i} and u_{js} defining the respective normal mode and LAC representations, see Eq. (3.7) and Eq. (3.11). Focusing on the dependence of the population transfer efficiency on different initial conditions there adds a 4th case to three scenarios discussed in Sec. 4.3, which corresponds to:

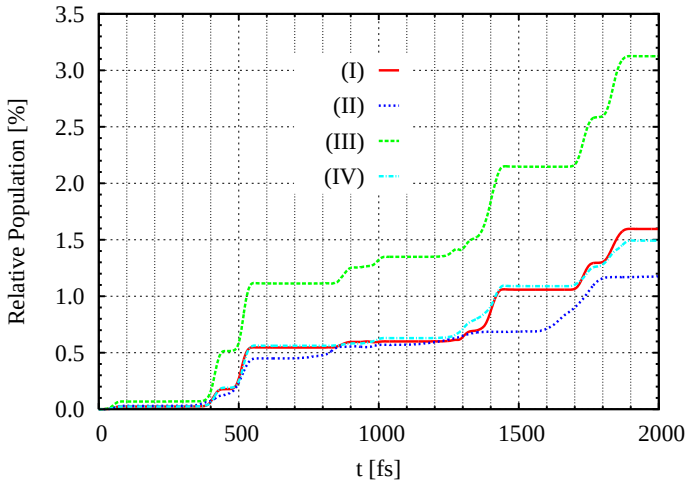

Figure 4.10: Population dynamics (relative C-state population, Eq. (4.29), 5D model) for (I) a Franck-Condon vertical transition, (II) a vibrational preexcitation of the Bromine coordinate ζ_R, (III) a vibrational preexcitation of the B_{2g}-mode q_2 and (IV) a vibrational preexcitation of the A_g-mode q_3. For comparison see Fig. 4.3.

(IV) a resonant excitation starting from the first vibrationally excited state of the tuning mode q_3.

Comparing the population dynamics for the cases shown in Fig. 4.10 to those of Fig. 4.3 one again finds a similar step-wise population transfer with plateaus in between. Qualitatively, there appears a new rise interval between $t = 1700$ and $t = 1900$ fs, which particularly dominates in case (III) for the reasons discussed in Sec. 4.3. Quantitatively, this rise interval leads to an increase of the overall population transfer efficiency, which amounts to 1.5-3.0% in total. In order to explain this new rise interval it is instructive to first consider the time-evolution of the reduced 2D density for case (I) in Fig. 4.11. Analog to Fig. 4.4 again the wave packet describes a parabolic motion on the B-state surface for the first round trip along the Bromine coordinate and stays compact until the end of the propagation time. However, when following the wave packet center of mass motion for case (I) in Fig. 4.12a over the total time interval, it immediately becomes clear, that its trajectory does not form a simple Lissajous parabola, unlike in Fig. 4.6a. This deviation from the initial 1:2 ratio of the periods for the Bromine and matrix motions can be attributed to the coupling of both motions to the tuning mode q_3.
A more detailed view on this coupling is provided when analyzing Fig. 4.13 for case (I). For instance, comparing the reduced 1D densities in Fig. 4.13c and Fig. 4.13e it is seen, that the time-evolution of the matrix coordinate clearly carries the signature of the tuning mode oscillation. In particular, this signature is seen for the out-of-phase motion at $t = 800$ and $t = 1800$, where the matrix motion is decelerated by the tuning mode. This deceleration is accompanied by respective minimum values of the kinetic energy in Fig. 4.13d. For the in-phase motion, in turn, the matrix coordinate is accelerated and reaches its maximum kinetic energy in the time interval between 1200 and 1300 fs. Concerning the coupling and the energy exchange between the tuning mode and the Bromine coordinate, one sees

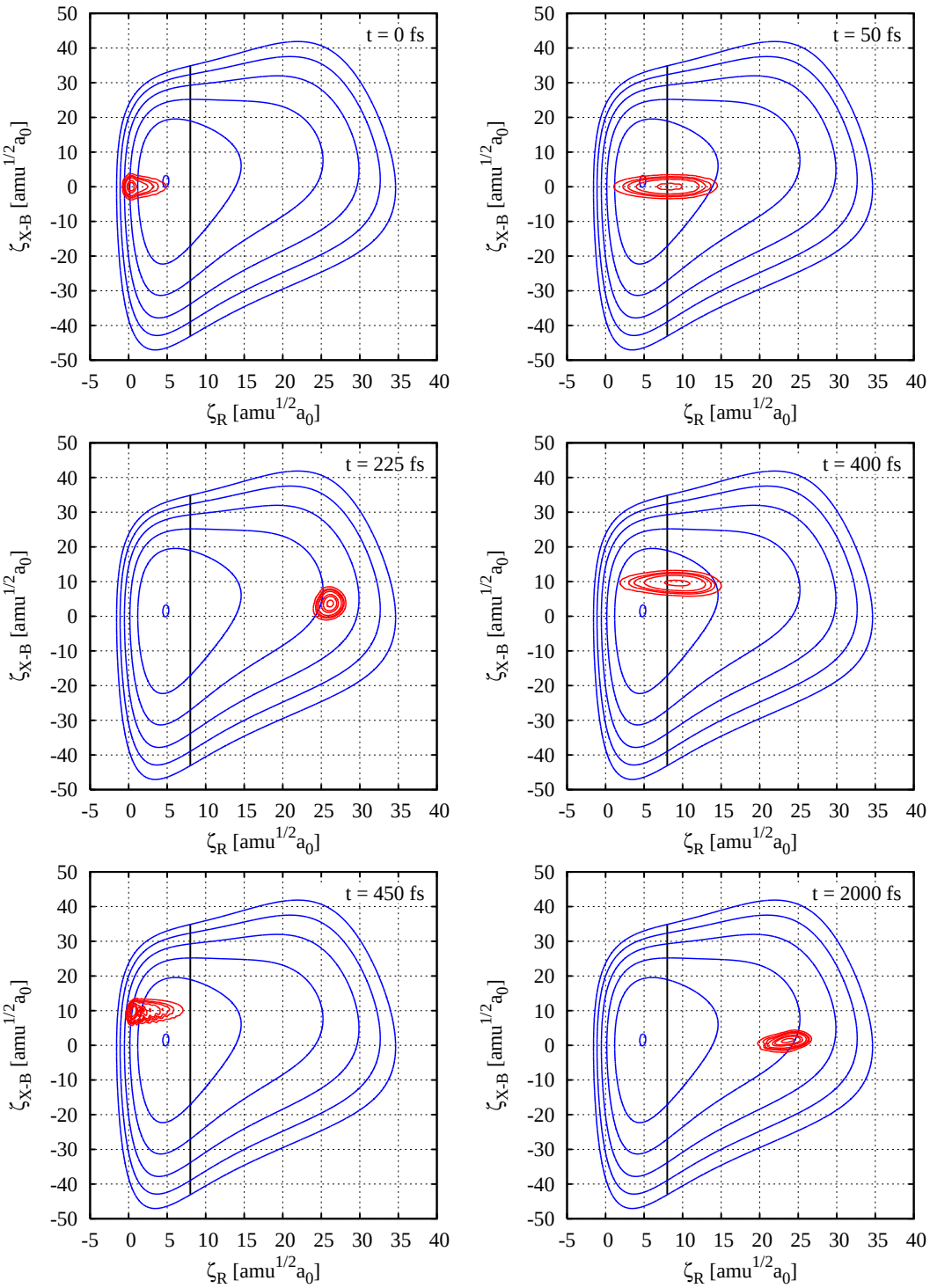

Figure 4.11: Snapshots showing the time-evolution of the 2D reduced density $\rho_B(\zeta_R, \zeta_{X-B})$ (isodensity values 0.0001, 0.0003, 0.0005, 0.001, 0.003, 0.005, 0.01, 0.03) on the diabatic B-state surface (contour levels 0.069, 0.08, 0.09, 0.10, 0.11, 0.12 E_h) after Franck-Condon excitation, case (I), within the 5D model. The position of the crossing seam (cf. Fig. 3.5a) is indicated by a vertical line.

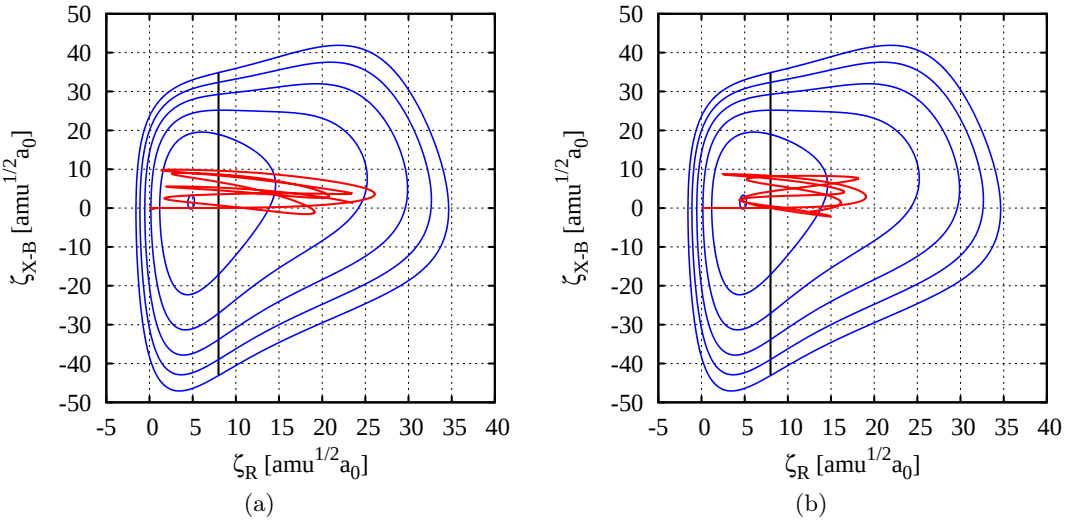

Figure 4.12: Trajectories $(\langle\zeta_R\rangle, \langle\zeta_{X-B}\rangle)$ for the wave packet center of mass motion on the diabatic B-state surface within the 5D model following (a) a Franck-Condon vertical excitation without prior vibrational preexcitation, case (I) (cf. Fig. 4.4), and (b) a resonant excitation of the vibrationally preexcited Bromine coordinate ζ_R, case (II). Potential contours are the same as in Fig. 4.11.

that the change of the amplitude of ζ_R, Fig. 4.13a, as well as the loss of its kinetic energy, Fig. 4.13b, approximately corresponds to a rise of the kinetic energy of q_3 in Fig. 4.13f. When correlating these results to the population transfer dynamics in Fig. 4.10 it is seen further, that the rise interval between $t = 1700$ and $t = 1900$ fs exactly coincides with the out-of-phase motion between the matrix and tuning mode oscillations. Thus, next to the specific constellation of the two large amplitude coordinates at the inner and outer turning points found in Sec. 4.3 the coupling of the tuning mode q_3 to ζ_{X-B} adds as a 3rd condition promoting the population transfer between the B- and C-states. The mechanistic details of the coupling can be inferred from Fig. 4.14 in terms of an energy gap modulation between the B- and C-state surfaces. When contrasting the time-evolution of the potential energy expectation values between the 4D and 5D models, the B- and C-states surfaces only cross one another two times within the region of interest in Fig. 4.14a, whereas they remain degenerate running parallel in Fig. 4.14b. In that sense, the tuning mode supports the population transfer by forcing the degeneracy in the crossing region.
Focusing on the effect of different initial conditions in Fig. 4.10 resulting from vibrational preexcitation of the coordinates in the electronic ground state, one again finds that the overall population transfer for case (II) is reduced as compared to case (I). According to the argumentation of Fig. 4.3 and Fig. 4.7 in Sec. 4.3 the reason can be found in the excitation of the wave packet at lower energies in the B-state PES, which directly can be seen from a comparison of the amplitudes for case (I) in Fig. 4.12a and case (II) in Fig. 4.12b. In particular, the overall reduced molecule-matrix interaction is reflected by the reduced amplitude and kinetic energy of the Bromine motion when comparing Fig. 4.15a and Fig. 4.15b to Fig. 4.13a and Fig. 4.13b. Comparing the motions of the

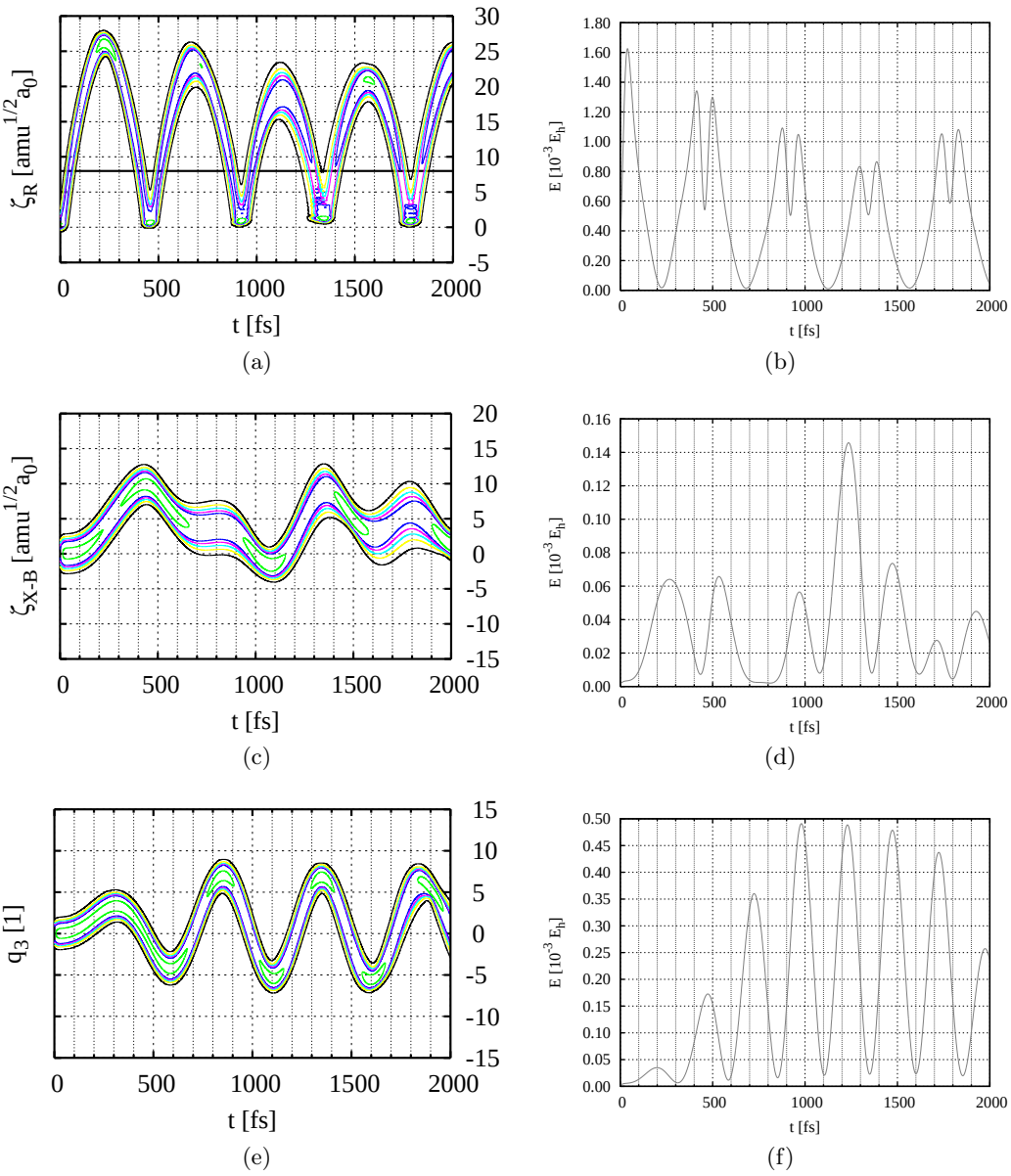

Figure 4.13: Franck-Condon excitation, case (I), 5D model: Time-dependent reduced 1D B-state densities for (a) the Bromine coordinate $\rho^{(B)}(\zeta_R, t)$ (isodensity values 0.001, 0.003, 0.005, 0.007, 0.01, 0.03), (c) the matrix coordinate $\rho^{(B)}(\zeta_{X-B}, t)$ (isodensity values 0.002, 0.004, 0.006, 0.008, 0.01, 0.02) and (e) the tuning mode $\rho^{(B)}(q_3, t)$ (isodensity values 0.001, 0.003, 0.005, 0.007, 0.01, 0.03) together with the respective expectation values of (b) the Bromine kinetic energy, (d) the matrix kinetic energy and (f) the kinetic energy of the tuning mode. The position of the crossing seam is indicated by a horizontal line in (a).

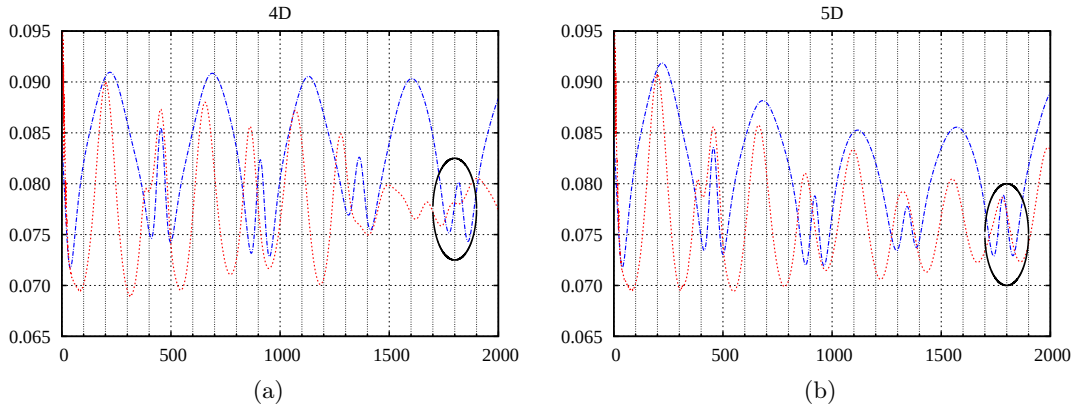

Figure 4.14: Temporal evolution of potential energy expectation values showing the modulation of the energy gap between the B- (dashed) and C-state (dotted) PES (cf. Fig. 3.4). The encircled region contrasts the energy gap in the time-interval of interest ($1700 \leq t \leq 1900$ fs, cf. Fig. 4.3 and Fig. 4.10) for case (I) – (a) 4D model and (b) 5D model.

matrix coordinate and the tuning mode one sees that signature of the latter, Fig. 4.15e, is still present in reduced density of the Fig. 4.15c at $t = 800$ fs, but starts to disappear in the time-interval between $t = 1600$ and $t = 1700$ fs. Within about this time-interval the condition for population transfer in case (II) is matched by the positions of the Bromine and matrix coordinates in Fig. 4.13a and Fig. 4.13c. However, the respective rise interval of the C-state population in Fig. 4.10 appears rather flat as compared to case (I), which hints to a reduced interaction between the tuning mode and the Bromine and matrix coordinates. This reduced interaction can be understood in terms of Eq. (4.31) relating the coupling strength of q_3 to the amplitude of both coordinates, ζ_R and ζ_{X-B}. In turn, this reduced coupling not only reduces the overall energy exchange between the tuning mode, Fig. 4.15f, and the Bromine and matrix coordinates, Fig. 4.15b and Fig. 4.15d, when comparing the respective kinetic energies to Fig. 4.13, but also lowers the amplitude and period of the tuning mode oscillation in Fig. 4.15e as compared to Fig. 4.13e.
For the vibrational preexcitation of the tuning mode in case (IV), the coupling of the tuning mode to the Bromine and matrix coordinates is the same as in case (I), only the amplitude of the tuning mode oscillation is bigger. Further, the intervals for the population transfer coincide with case (I). Finally, as a note in caution it should be mentioned, that the validity of the above findings are of course restricted to those cases of preexcitation discussed, as well as to those domains of the B-state potential accessed.

4.5 Relaxation to an Effective Bath

Although the 4D and 5D models from Sec. 4.3 and Sec. 4.4 describe the energy transfer among the Bromine and matrix coordinates as well as their exchange with the tuning mode q_3, they do not account for the energy relaxation into other matrix degrees of freedom. Experimentally, the total vibrational relaxation rate has been estimated to about $2000 - 3000$

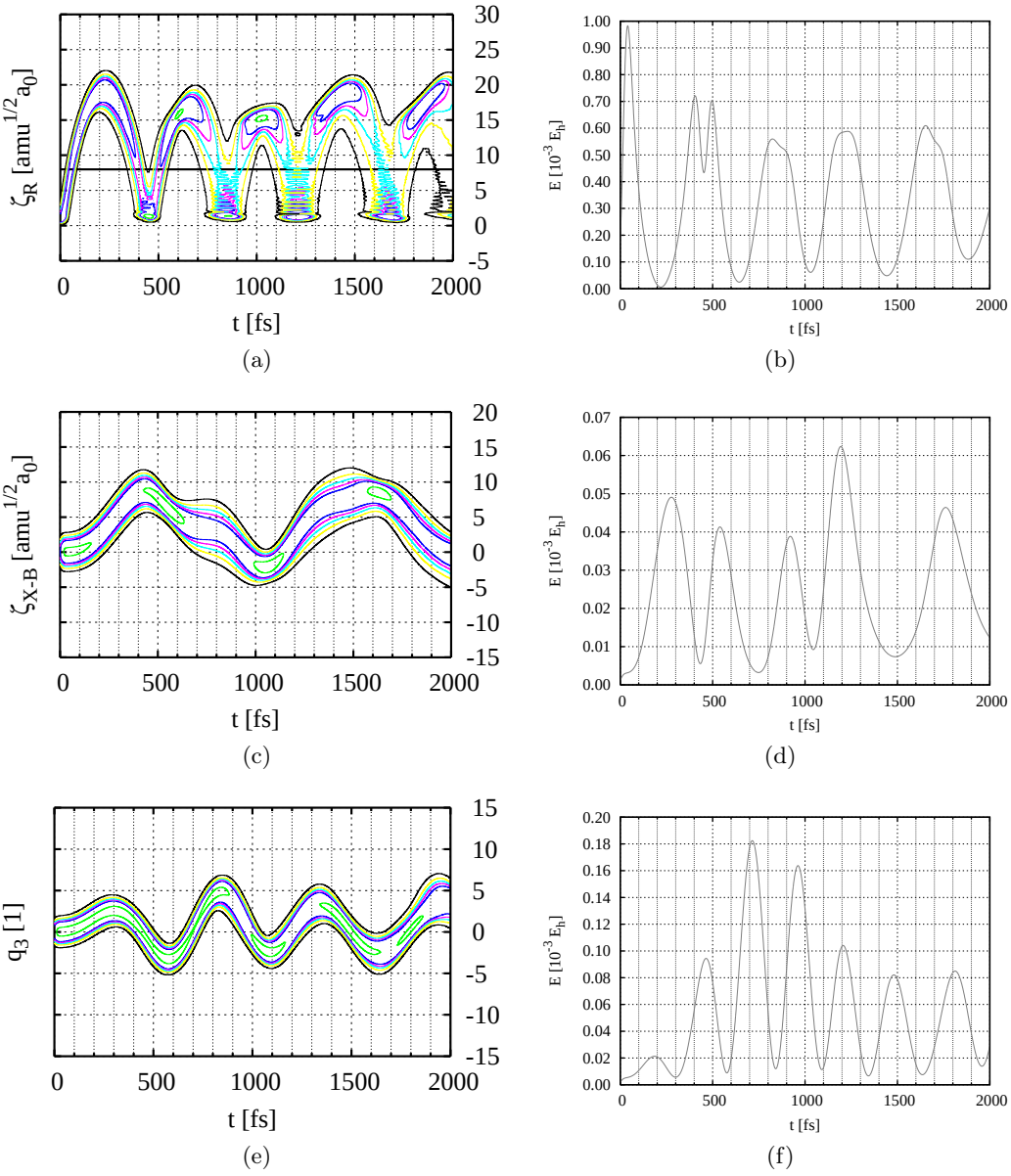

Figure 4.15: Same as Fig. 4.13, but for a resonant Laser pulse excitation to the B-state starting from the vibrationally preexcited Bromine coordinate ζ_R, case (II).

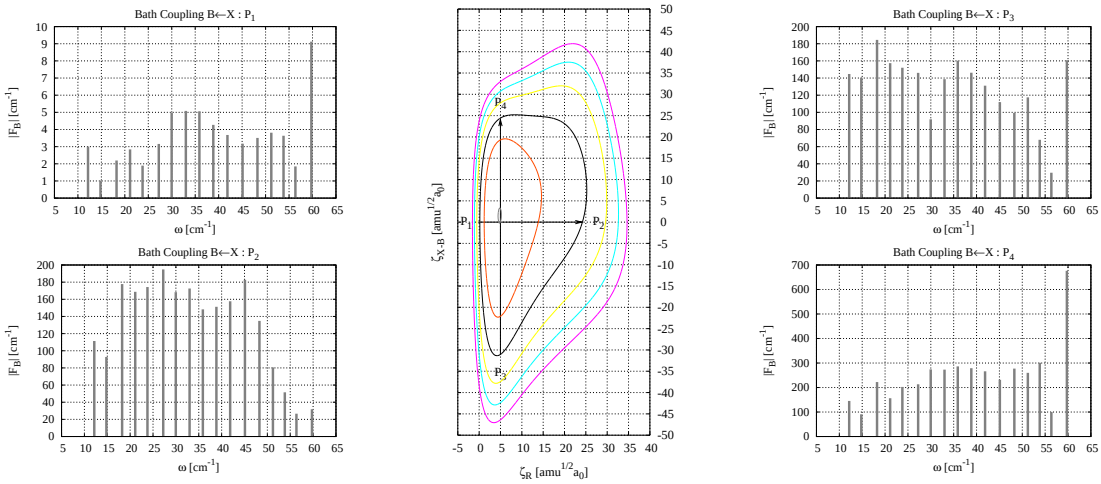

(a) (b) (c)

Figure 4.16: (a)+(c) Effective bath oscillators representing the coupling of the tuning modes orthogonal to the reaction plane at the four characteristic points of Fig. (b), each within frequency intervals of $\Delta\omega = 3$ cm^{-1}. (b) B-state PES (isopotential contour lines at 0.069, 0.080, 0.090, 0.100, 0.110 and 0.120 E_h).

cm^{-1}/ps for the B-state close to the gas phase dissociation limit [13], so that one should not attempt to compare these low-dimensional models with the experiment on time scales exceeding a few round trip times. A straightforward way to account for effects of vibrational energy relaxation within the frame of a system-bath treatment is to supplement the minimum model from Sec. 4.3 by a *finite* set of harmonic oscillators, which linearly couple to the B-state PES as it has been demonstrated exemplarily for q_3 in Eq. 4.31 of Sec. 4.4. This approach is hampered by the fact, that the $B \leftarrow X$ transition is characterized by a quasi-continuous spectral density of states (cf. Fig. 3.3a and Fig. 4.9a) rather than by a discrete spectrum of few distinct lines. Further, in Sec. 4.4 it has been shown that a proper description of the coupling requires a linear approximation of its dependence on the reaction surface. Numerically, however, it is impossible to represent the individual linear couplings of all tuning modes on the whole grid spanned by the LAC. To overcome this limitation, a finite set of effective bath oscillators has been introduced, which approximate the linear couplings of the matrix phonons to the reaction plane at four specific points of the B-state PES. Therefore, first the linear couplings of the tuning modes orthogonal to the reaction plane have been determined for the points P_1, P_2, P_3 and P_4 along the Bromine and matrix coordinates as shown in Fig. 4.16b. In a second step, these tuning mode couplings have been rediscretized by calculating the geometric mean of the forces $f_k^{(B)}$ for the arithmetic mean of the normal modes frequencies ω_k, each within a frequency interval of $\Delta\omega = 3$ cm^{-1}. The results of this rediscretization are shown in Fig. 4.16a and Fig. 4.16c. Alongside with this rediscretization technique there goes a loss of information, not only about specific normal modes, but also on the direction of the linear coupling. That is the effective bath oscillators obtained this way have no meaning deeper than just to reproduce

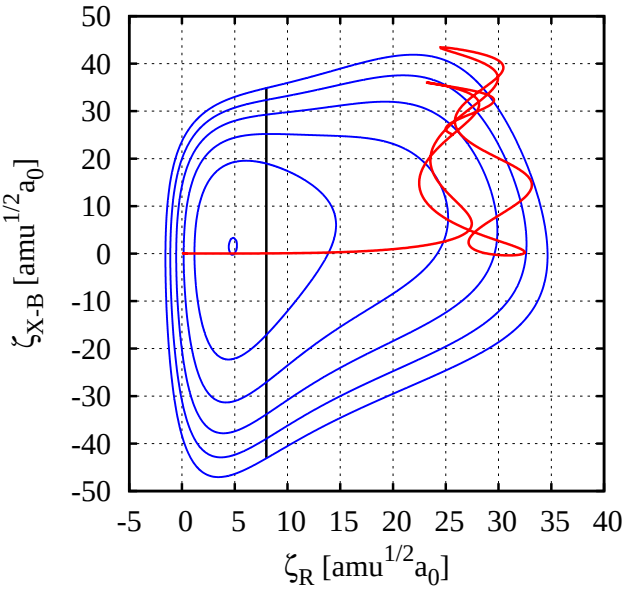

Figure 4.17: Trajectories $(\langle\zeta_R\rangle, \langle\zeta_{X-B}\rangle)$ for the wave packet center of mass motion on the diabatic B-state surface following a Franck-Condon vertical excitation (cf. Fig. 4.18). Potential contours are the same as in Fig. 4.4.

the absolute value of the coupling, not its sign. The dependence of the effective bath oscillators on the Bromine and matrix coordinates has been approximated by the differences in the linear couplings between each two opposite points on the reaction surface. Hence, this approximation differs from the one given in Eq. (4.31) of Sec. 4.4. It has been used, since a rediscretization of the second order coupling quantities from Eq. (4.32) cannot be accomplished in a systematic way.

Inspecting the linear couplings in Fig. 4.16 it can be seen, that their magnitude predicts high vibrational excitations of the bath oscillators, particularly at the points P_2 and P_4. These high vibrational excitations can be inferred from Tab. 4.1, where they correlate to the numbers of DVR functions required to avoid artificial reflection effects at the end points of the oscillator grid. In consequence, the rather large bath couplings lead to a strong distortion of the wave packet trajectory along the matrix coordinate as shown in Fig. 4.17.

A more detailed view on this scenario describing a trapping of the Bromine atoms in the matrix cage is provided by Fig. 4.18. Focusing on the reduced densities in Fig. 4.18 it is clear that the separation of the Bromine atoms, Fig. 4.18a, is accompanied by large amplitude breathing motions of the matrix coordinate, Fig. 4.18c. Only at the very end of the simulation the onset of a damping of the latter motion becomes visible. Concerning the energy exchange between the reaction coordinates and the oscillator bath it is seen that the kinetic energy of the Bromine motion, Fig. 4.18b, is absorbed by the bath and partially redistributed into the motion of the matrix coordinate, Fig. 4.18d.

As a note in caution one should mention, that the present bath model treats the energy flow between the effective oscillators only indirectly via coupling to both reaction coordinates, that is a direct exchange via bilinear bath couplings is not contained. Even in case

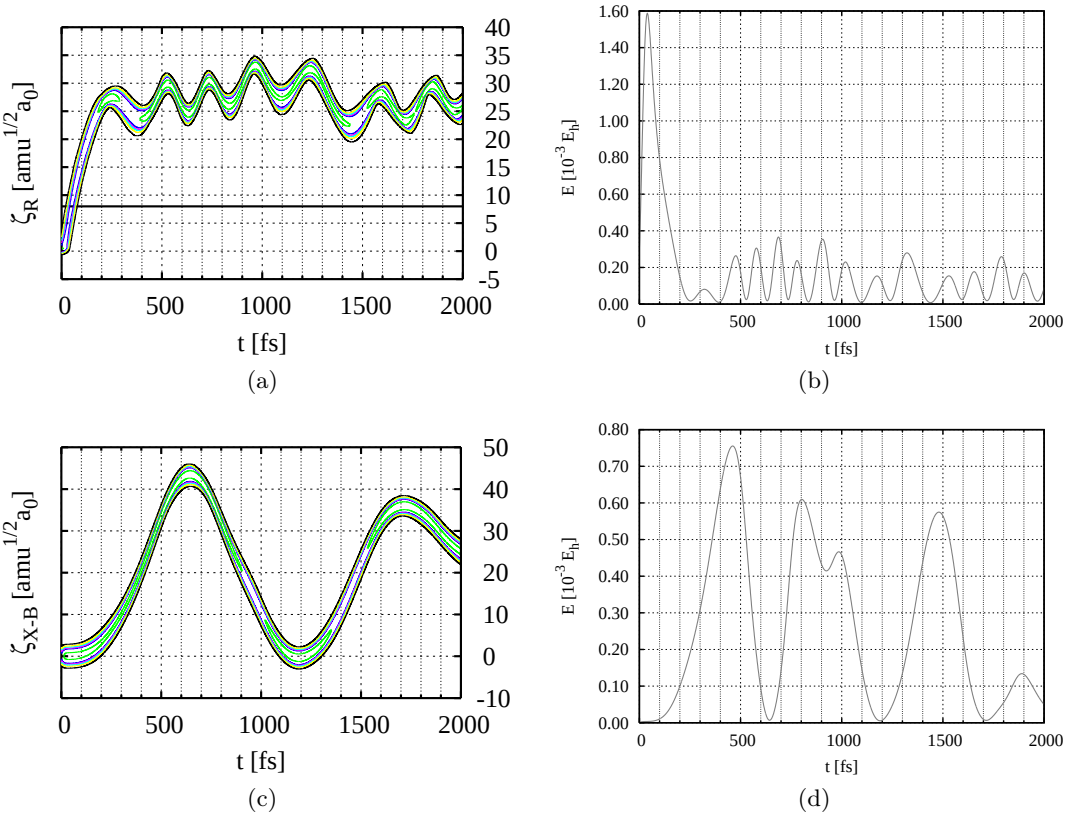

Figure 4.18: Franck-Condon excitation, 21D model: Time-dependent reduced 1D B-state densities for (a) the Bromine coordinate $\rho^{(B)}(\zeta_R, t)$ (isodensity values 0.001, 0.003, 0.005, 0.007, 0.01, 0.03) and (c) the matrix coordinate $\rho^{(B)}(\zeta_{X-B}, t)$ (isodensity values 0.002, 0.004, 0.006, 0.008, 0.01, 0.02) together with the respective expectation values of (b) the Bromine kinetic energy and (d) the matrix kinetic energy. The position of the crossing seam is indicated by a horizontal line in (a).

of the 17 effective oscillators considered here such attempt would lead to 136 additional couplings, which again explicitly depend on the reaction surface.
Technically, the representation of the 17-dimensional wave function for the oscillator bath can only be handled in Hartree approximation using one SPF per bath degree of freedom $\tilde{q}$ as it is indicated in Tab. 4.1. Strictly speaking such Hartree approximation is justified in case of *weak* couplings only, if one can assume correlation effects to be small. Further, for the high vibrational excitations predicted, which are accompanied by high vibrational amplitudes, the harmonic approximation becomes inadmissible for the bath.
In view of these drawbacks the effective bath approach, which is likely to overestimate the vibrational relaxation rate in the B-state, has to be considered with caution, since in addition the Bromine molecule is trapped in a region of the PES, where the energy gap to other electronic states not included into the model becomes small, such that subsequent electronic relaxation processes have to be expected. Despite of these drawbacks, however, the trapping scenario found could explain the persistence of probe signals without significant modulation as observed for some probe windows in respective pump-probe spectra of matrix-isolated Cl_2 [180] and Br_2 [181], especially in case of high energy excitations with short pump wavelengths below a certain threshold.

4.6 Spectral Information - The B-state Absorption Spectrum

The reduced dimensionality models of the former sections, Sec. 4.3-Sec. 4.5, have been designed to specifically describe the short-time aspect of wave packet dynamics. This dynamics is characterized by a rather broad energy distribution of the nuclear wave packet in the B-state triggered by excitation of the respective ground state wave packet via an ultrashort laser pulse. Next to this wave packet simulations, it would be desirable to also calculate some time-independent spectroscopic properties of matrix-isolated Br_2 for a direct comparison with recent experimental data provided by the Schwentner group [84].
In principle such spectral information can be obtained on the basis of wave packet propagations via the Fourier transform of the dipole-dipole autocorrelation function [145,182–184]. When applying a discrete Fourier transform with a frequency resolution $\Delta\omega = {}^{2\pi}/_{N\Delta t}$ inversely proportional to the sampling time $N\Delta t$ such an approach would require the propagation of wave packets on time scales of about 10 ps in order to resolve individual B-state vibrational levels. However, on this time scale the reaction surface based models of the former sections reach their limit of applicability for two reasons: First, the excited state wave function loses its compactness in time, that is the number of single-particle functions required for its proper representation rapidly increases and converges towards the number of grid points as in case of a numerically exact calculation. Second, the weak molecule-matrix couplings neglected in these models are likely to become important on a longer time scale and one cannot expect the reduced models to hold over this period of time.
Hence, it would be advantageous to have a simple model, which not only takes into account the full dimensionality of the system, but which is also able to reproduce its main spec-

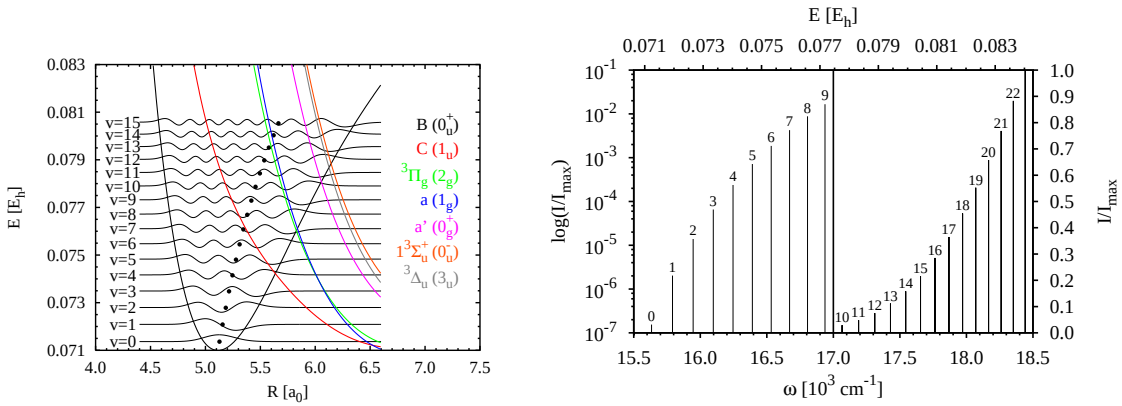

(a) (b)

Figure 4.19: (a) Vibrational eigenfunctions of the B-state potential with position expectation values (dots) of the Br-Br bond distance in the frozen matrix. Additionally, the potential energy curves of those states leading to the B-state predissociation are drawn. (b) Transition amplitudes $|\langle v''=0|v'\rangle|^2$ of the $B \leftarrow X$ transitions to the vibrational levels of (a). Note, that the intensities have been normalized to the strongest transition at $v'=23$. The 1st half of the picture shows the relative intensities for $v'=0,\ldots,9$ on a logarithmic scale.

troscopic features such as zero-phonon lines (ZPL) and phonon sidebands (PSB) [83, 84]. Neglecting non-adiabatic couplings these features can be described in terms of the standard Huang-Rhys model (for details see Sec. 5.7 of the Appendix). For this model a closed expression of the dipole-dipole autocorrelation function in Condon-approximation exists (see Ref. [145]). However, this model needs to be extended such as to describe the experimentally observed anharmonicity of the ZPL, as well as the dependence of the PSB contributions on the Br_2 vibrational quantum number [84].
Therefore, the following expression for the optical absorption coefficient has been applied to the calculation of the B-state absorption spectrum:

$$\sigma(\omega) \quad \sim \quad \sum_{v'} |\langle v''=0|v'\rangle|^2 \cdot e^{-G_{v'}(t=0)} \int_{t=0}^{t\to\infty} e^{-i\omega_{0v'}t} \cdot e^{G_{v'}(t)} \cdot e^{i\omega t} dt \ , \qquad (4.33)$$

where, when adapting the terminology of Ref. [84], the sum runs over the Br_2 vibrational levels v' in the B-state with $v''=0$ being the zero level of the X-state. The squared Franck-Condon factors $|\langle v''=0|v'\rangle|^2$ between the respective eigenfunctions in Eq. (4.33) reflect the intensities of the $B \leftarrow X$ zero-phonon transitions with the associated frequencies $\omega_{0v'} = {}^{E_{v'}-E_{v''=0}}/_{\hbar}$. These transition frequencies and intensities are depicted in Fig. 4.19b. The necessary eigenenergies and eigenfunctions have been obtained from 1D potential energy curves as function the Br-Br bond-distance R in the frozen Ar matrix using the Fourier grid Hamiltonian (FGH) method [173, 174]. Fig. 4.19a shows these quantities for the B-state potential of the chromophore. It should be mentioned, that the transition probabilities from the $v''=0$ level to the lower vibrational levels v' of the B-state (cf.

Fig. 4.19a) are comparatively small. As indicated by the logarithmic scale in the 1st half of Fig. 4.19b this can be attributed to rather weak Franck-Condon factors, which immediately can be rationalized by means of the distinct equilibrium distances $R_e^{(X)} = 4.35$ a$_0$ and $R_e^{(B)} = 5.12$ a$_0$ of the X- and B-state potentials, taking into account, that the ground state wave packet in the X-state (not shown) is only about half that wide than that in the B-state.

The time-dependent function $G_v(t)$ appearing in the exponent of the integrand in Eq. (4.33) carries the complete information about the coupling of the individual lattice normal modes q_k to the $B \leftarrow X$-transition, including the dependence of this coupling on the quantum number v' of the Bromine molecule. Explicitly, $G_{v'}(t)$ has been calculated according to the following formula (see Ref. [145]):

$$G_{v'}(t) \quad = \quad \sum_k S_{v',k} e^{-i\omega_k t} \; . \tag{4.34}$$

At time $t = 0$ Eq. (4.34) is given by the sum of the individual Huang-Rhys factors $S_{v',k}$. According to Sec. 5.7 the integral prefactor $e^{-G_{v'}(t=0)}$ in Eq. (4.33) weights each ZPL by the fraction of intensity entering into its corresponding PSB. $G_{v'}(t)$ itself sums the time-dependent modulation of the Huang-Rhys factors $S_{v',k}$ by the normal mode frequencies ω_k, so that the Fourier transform of this function leads to the spectral density of states defined in Eq. (3.32) of Sec. 3.2.2. In analogy to Sec. 3.2.2 and Sec. 5.7 the Huang-Rhys factors in Eq. (4.34) have been calculated from the forces $f_{v',k}^{(B)}$ acting on the ground state normal modes q_k in the B-state using dimensionless oscillator coordinates:

$$S_{v',k} \quad = \quad \frac{1}{2} \left[\frac{f_{v',k}^{(B)}}{\hbar \omega_k} \right]^2 \; , \tag{4.35}$$

with the modification, that these forces have been determined in dependence on the individual bond expectation values $\langle v'|R|v' \rangle$ of the Bromine molecule:

$$f_{v',k}^{(B)} \quad = \quad \left. \frac{\partial V_B}{\partial q_k} \right|_{\langle v'|R|v' \rangle} \; . \tag{4.36}$$

These bond expectation values are indicated by black dots in Fig. 4.19a. Once the functions $G_{v'}(t)$, Eq. (4.34), as well as the individual transition amplitudes $|\langle v'' = 0|v' \rangle|^2$ and frequencies $\omega_{0v'}$ are known, the complete B-state absorption spectrum can be calculated according to the Fourier transform given by Eq. (4.33).

Fig. 4.20 contrasts the resulting absorption spectrum versus the experimentally measured B-state excitation spectrum [84]. Compared are the zero-phonon lines (ZPL) and phonon sideband (PSB) contributions. Inspecting the vibrational progression of the zero-phonon lines within the observed interval $2 \leq v' \leq 20$ in Fig. 4.20a one immediately recognizes irregularities in the intensities of the ZPL for $v' = 4, 5$ and $v' = 7 - 9$. These irregularities hint to population transfer events via the B-state predissociative channels depicted in

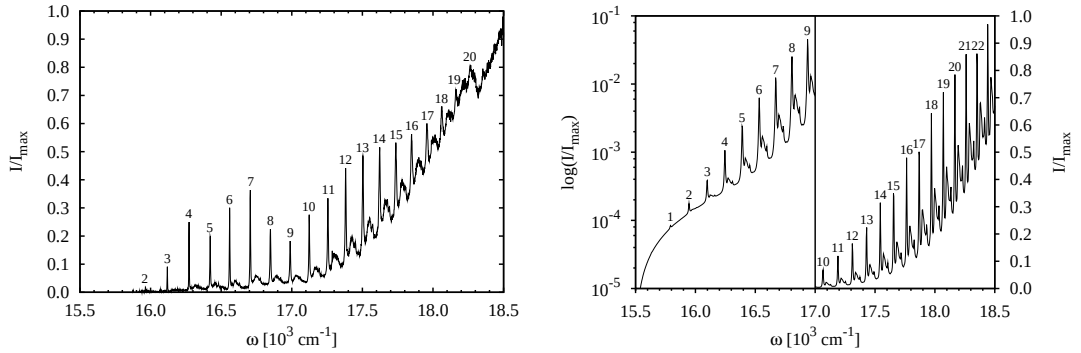

(a) (b)

Figure 4.20: (a) Experimental B-state excitation spectrum [84] showing the vibrational progression of the zero-phonon lines (ZPL) for Br_2 in matrix Ar from $v' = 2$ up to $v' = 19, 20$ with corresponding phonon sideband (PSB) contributions. (b) Calculated B-state absorption spectrum (cf. Fig. 4.19b).

Fig. 4.19a. Notice, that the curve crossings predicted on the basis of the 1D effective DIM potential from Fig. 4.19a approximately coincide with the respective positions observed in the experiment, Fig. 4.20a. However, the effect of predissociation has not been taken into account in the present simple model.

Further, when comparing the level spacings of the ZPL between Fig. 4.20a and Fig. 4.20b one notices a different anharmonicity, particularly for higher vibrational levels v', which can be attributed to the deviation of the calculated 1D B-state potential in the frozen Ar matrix from the true potential containing the average effect of matrix motions.

Concerning the relative intensities of the individual ZPL in Fig. 4.20a one should keep in mind, that the measured excitation spectrum reflects that fraction of B-state population emitting from the B-state upon resonant absorption only *after* the various predissociative channels from Fig. 4.19a have been passed. That is, when adding those parts of B-state population lost by predissociation, which experimentally have been verified in the emission signals of the lower-lying A- and A'-states [84], it should be possible to at least approximately recover the "pure" absorption spectrum from Fig. 4.20b.

Next, when focusing on the phonon sideband (PSB) contributions in Fig. 4.20 one notices a qualitative agreement of the PSB structures between the measured and calculated spectra. In both cases one finds a double peaked PSB structure, which, for instance, can be seen for the sidebands to $v' = 12$ and $v' = 13$. Further, one notices a dependence of the PSB contributions on the vibrational quantum number of the Br_2 molecule, specifically from $v' = 10$ up to higher vibrational levels. Particularly, the rising intensity of the PSB contributions is a clear indication for a stronger molecule-matrix coupling with increasing Br_2 vibrational amplitude.

Experimentally, the individual PSB contributions from Fig. 4.20a have been quantified in terms of cumulative Huang-Rhys coupling constants $S_{v'}$. These constants are shown by filled squares in Fig. 4.21a and may directly be compared to the respective calculated quantities shown by filled circles, which correspond to $G_{v'}(t = 0)$. Notice, that both, the

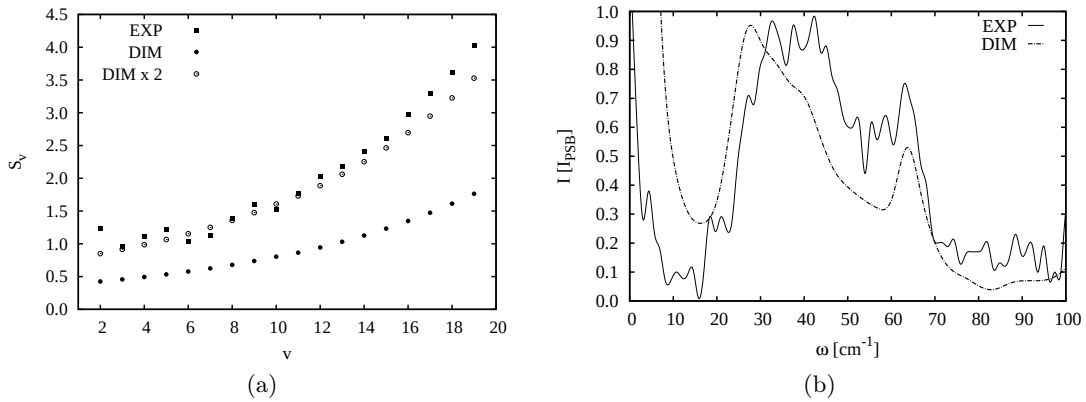

(a) (b)

Figure 4.21: (a) Huang-Rhys factors (experimental values [84] depicted by squares, calculated values by circles). (b) Phonon sideband (PSB) to $v' = 12$, see Fig. 4.20 (experimental PSB drawn as solid curve, calculated PSB as dash-dotted curve). Notice, that the approach given by Eq. (4.35) and Eq. (4.36) is essential for obtaining Fig. (a) and Fig. (b).

experimental and calculated values, follow the same trend of a nonlinear increase with the vibrational quantum number v'. This increase is even more evident when scaling the DIM-based values have by a factor of 2. Based on this comparison one could argue that the DIM model underestimates the forces $f^{(B)}_{v',k}$ by a factor of $\sqrt{2}$ as they enter into Eq. (4.36) quadratically. In particular, this factor may be traced back to the Br-Ar potential, Sec. 2.4.1. However, in this context one should also mention, that the coupling constants obtained from experiment in terms of the relative intensity and line-width measurements are necessarily afflicted with some error, too.

On the other hand, when considering Fig. 4.21b, which shows close-up views of the PSB to $v' = 12$ from Fig. 4.20, one not only finds a qualitative, but also a semiquantitative agreement, so that the difference between experiment and theory vanishes. This agreement facilitates the resolution of the double peaked PSB structure in terms of the individual contributions $S_{v',k}$. Fig. 4.22a shows the corresponding spectrum of the PSB from Fig. 4.21b.

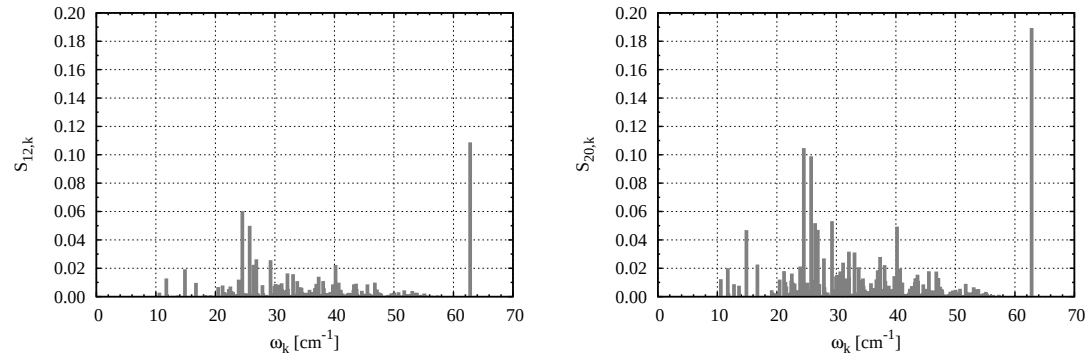

(a) (b)

Figure 4.22: Mode resolved PSB contributions to (a) $v' = 12$ (cf. Fig. 4.21b) and (b) $v' = 20$.

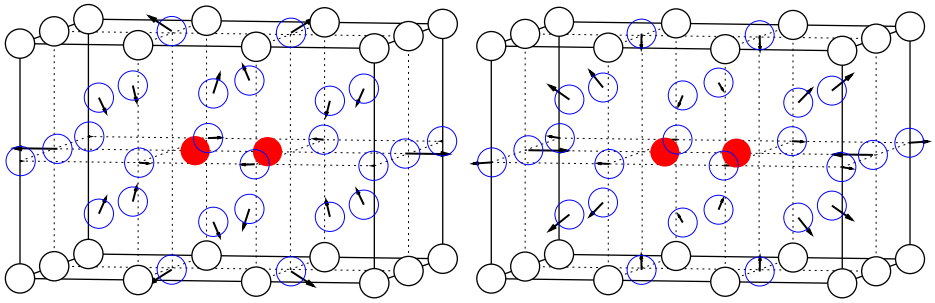

Figure 4.23: Displacement vectors for two modes of A_g symmetry contributing to the PSB (cf. Fig. 4.21b and Fig. 4.22) with the harmonic frequencies $\omega = 24.5$ cm^{-1} (left) and $\omega = 25.8$ cm^{-1} (right).

Inspecting this figure one can clearly identify two main peaks at the normal mode frequencies $\omega = 24.5$ cm^{-1} and $\omega = 25.8$ cm^{-1} and another dominant peak at 62.8 cm^{-1}. Still, it has to be checked, whether this mode spectrum of the PSB changes when going to higher vibrational quantum numbers, for instance to $v' = 20$ as shown in Fig. 4.22b. It can be seen, that, except for higher $S_{v',k}$ values, all modes substantially contributing to Fig. 4.22a also dominate in this case.
Analyzing these normal modes in detail it was found, that the high-frequency peak in Fig. 4.22 corresponds to the tuning mode q_3 discussed in Sec. 4.4. The respective displacements vectors of the other two lower-frequency modes are shown in Fig. 4.23. According to the opposite sign of the displacement vectors as well as the nearby frequencies it can be concluded that both modes are quasi-degenerate, which also could explain their higher intensity contributions in Fig. 4.21b as compared to q_3 . It should be mentioned, that in contrast to the localized Belt mode q_3 from Fig. 4.9b both modes in Fig. 4.23 extend deeper into the crystal than depicted here for the purpose of a better visibility. In other words, they are less localized at the chromophore, which also explains their lower frequency as compared to the Belt mode. Altogether, with the aid of these three normal modes the double peak structure of the phonon sideband can be explained.

5 Summary and Conclusion

The major investigations and results of the thesis may be summarized as follows:
The Diatomics-in-Molecules method has been implemented for the system Br_2 in solid Ar as detailed in Chap. 2. In Sec. 2.4.2 a specific simulation box containing 700 atoms has been defined in terms of an extended Ar lattice cut-out along the crystallographic $\langle 110 \rangle$ direction using cut-off radii of pair potentials and nearest neighbor separations for determining its particular extension. On the basis of this simulation box the ground state equilibrium geometries of the system in the electronic X- and B-states have been calculated using a classical thermostating method. The calculated relaxation effects of the nearest neighbor Ar atoms in the vicinity of the chromophore are in accordance with the findings of related MD simulations for Cl_2 [17] and Br_2 [127, 128] molecules in Ar matrices. In addition, the flexibility and rotational barriers of the Bromine molecule has been investigated for its double substitutional lattice site in Sec. 2.4.3 leading to a similar angular confinement as reported for Cl_2 in Xe matrices [37].
In Sec. 2.4.4 an approach for reducing the complexity of the DIM Hamiltonian matrix towards application to specific problems in the context of laser spectroscopy has been proposed. Within this approach the separability of the DIM Hamiltonian matrix has been explored in terms of a particular block-mask scheme. By imposing the block-diagonal structure of the molecular Hamiltonian onto the total Hamiltonian the disturbance of its individual Hund's case c symmetry blocks by the matrix could be grouped into intra-symmetric or inter-symmetric couplings. The separate role of both coupling types has been investigated using a two-step diagonalization procedure. Here a certain separability of symmetry blocks was found to be preserved for the three different molecular dissociation limits. Specifically, it was found that the Hund's case c symmetries of the isolated molecule approximately retain their meaning within a well-ordered rare gas environment. This finding verifies the empirical usage of gas phase selection rules in the spectroscopy of matrix-isolated dihalogens. Furthermore, this separability facilitated the determination of a relevant subset of potential energy curves for the description of B-state predissociation with subsequent electronic relaxation in Sec. 2.4.5. Taking into account the Franck-Condon target energy interval for a resonant $B \leftarrow X$ transition it was found that a model Hamiltonian of reduced complexity can be approximated by 17 instead of all 36 valence states. This model Hamiltonian was shown to reproduce the eigenvalue spectrum of the complete DIM-Hamiltonian within the energy interval given. Moreover, focusing on the regime of B-state crossings relevant for photo-dissociation it was shown in Sec. 2.4.5 that the reduced and complete DIM-Hamiltonians reasonably agree in the composition of their eigenvectors. The present approach to problem-adapted model Hamiltonians shall be particularly useful

for avoiding the numerical overhead in conventional semi-classical as well as in perspective "quantum on-the-fly" applications of the DIM method.

In Chap. 3 a reduced but multi-dimensional quantum model for describing the predissociation of Br_2 molecules in Ar has been developed in the frame of a combined CRS and VCH approach. Therefore, first the theoretical fundamentals of these approaches have been introduced in Sec. 3.1. Applying the CRS concept to the electronic $B \leftarrow X$ transition two anharmonic large amplitude coordinates have been defined in Sec. 3.2.2. Whereas the first coordinate describes a linear Br-Br motion, the second coordinate describes a collective rearrangement of the matrix atoms when going from the equilibrium geometry of the system in the X-state to its equilibrium geometry in the B-state. Specifically, this matrix coordinate has been defined by interpolating between both mass-weighted equilibrium geometries and applying subsequent Gram-Schmidt orthonormalization to the Bromine coordinate. Analyzing the matrix coordinate in terms of its normal mode projections, it was shown, that this coordinate not only resembles the symmetric part of the linear coupling modes in the Franck-Condon region but also covers an essential part of the whole phonon spectrum. Further, the calculated phonon spectrum used for comparison was found to agree well with literature data for pure Ar crystals [7]. In Sec. 3.2.2 the potential energy surfaces spanned by the two large amplitudes coordinates have been shown to provide a compact description of the anharmonicity and coupling of the Bromine and matrix motions. Specifically, this PES was found to mimic the collective effect of those individual, prototypic cage fragment displacements, which have been analyzed in Sec. 3.2.1 using Belt, Phonon, Window and Collision atoms. As another important feature it was shown in Sec. 3.3 that the potential energy surfaces of the B- and C-states exhibit a crossing seam rather than a conical intersection, since both large amplitude coordinates describe totally symmetric motions. Applying vibronic coupling theory to the manifold of harmonic normal modes orthogonal to the PES defined by the large amplitude coordinates two dominant linear vibronic coupling modes of B_{2g} and B_{3_g} symmetry have been identified. For these two symmetry-breaking normal modes the dependence of the vibronic coupling on the crossing seam was found to be substantial. Further, the mapping of the potential energy as a function of the symmetric Bromine coordinate versus the vibronic coupling mode of B_{2g} symmetry was confirmed to give a conical intersection in adiabatic representation. In essence, by combining both large amplitude coordinates and both vibronic coupling modes a four-dimensional Cartesian reaction surface - vibronic coupling Hamiltonian containing four electronic states has been constructed for describing the B-state predissociation of Br_2 in Ar via C-state channel.

In Chap. 4 quantum dynamics simulations have been performed in the framework of the multi-configuration time-dependent Hartree (MCTDH) method using the above Hamiltonian as a minimal model for further extensions. A brief account of this method was given in Sec. 4.1, followed by details on the grid representation of the reaction surfaces required in Sec. 4.2. In order to investigate the wave packet dynamics in the B-state, as well as to unravel mechanistic aspects related to the B- to C-state predissociation, quantum prop-

agations of this 4D model have been carried out in Sec. 4.3. For these purposes various ground state wave packets composed of different initial vibrational levels have been excited to the B-sate using realistic laser pulses. The results of the wave packet propagation have have been analyzed in terms of reduced densities and kinetic energy expectation values of the Bromine and matrix large amplitude coordinates. Monitoring the non-adiabatic transitions in terms of fractions of the B-state population, which is transfered to the degenerate C-states, a stepwise population transfer was observed. Analyzing the nuclear dynamics in the B-state potential a parabolic motion of the wave packet with an approximate 1:2 ratio between the periods of the Bromine and matrix motions was found. By correlating both results it was shown that even though the B-state wave packet passes the B-to C-state crossing seam two times on each round-trip of the Bromine coordinate, a transition occurs only once. Specifically, it was found that the transition occurs only in that moment when the matrix coordinate is maximally elongated. This result has been explained by the strong increase of the linear vibronic couplings with matrix deformation. Concerning the mechanistic details of the predissociation it was thus shown, that for being efficient it not only requires symmetry-breaking linear vibronic coupling modes which generate a conical intersection, but also a symmetry-preserving cage deformation.
Further, the wave packet dynamics has been studied in a different Franck-Condon region of the B-state potential using vibrational preexcitation of the Bromine coordinate in the X-state as a means for lowering the resonance condition of the $B \leftarrow X$ transition as compared to the case of no excitation. Here, an overall reduced elongation of the matrix coordinate was observed leading to weaker predissociation in consequence. As another important modification of initial conditions the vibrational preexcitation of the linear vibronic coupling mode of B_{2g} symmetry has been considered. In this case an enhancement of the predissociation yield by a factor of two, even without appreciable excitation of the matrix coordinate, was found. Specifically, this finding could be explained in terms of the doubling of the number of transfer channels as compared to the case of no excitation. This principle of manipulating the efficiency of the B-state predissociation was recently confirmed by spectroscopic experiments of the Schwentner group (unpublished) using shaped laser pulses, which activate vibronic coupling modes.
The systematic extension of the minimum model was addressed in Sec. 4.4. Here a specific part of linear couplings not covered by the large amplitude coordinate model was found to persist in the B-state spectral density of the normal modes orthogonal to the reaction plane. Analyzing the latter a representative tuning mode of A_g symmetry with Belt atom character has been identified and added to the model. It was found that the linear coupling of this specific normal mode depends on the large amplitude coordinates and cannot be approximated by its value at the vertical Franck-Condon transition geometry exclusively. Repeating the investigations of Sec. 4.3 for this 5D model and contrasting the results to the former model it was further found, that the coupling of this tuning mode not only disturbs the approximate 1:2 ratio between the Bromine and matrix motions, but also increases the probability of predissociation within a certain interval. Comparing the expectation values

of the potential energy between both models it was explicitly shown, that the tuning mode supports the population transfer by reducing the energy gap between the B- and C-state surfaces. Hence, such an energy gap modulation provides another means for manipulating predissociation.

In order to specifically account for the effect of vibrational relaxation and energy dissipation into the matrix the 4D minimal model from Sec. 4.3 was further extended in Sec. 4.5 by the linear coupling of set of 17 harmonic bath oscillators. For this purpose, effective bath oscillators have been generated from the projected ground state normal modes by rediscretizing the manifold of tuning mode couplings. The dependence of the latter on the reaction coordinates has been approximated in terms of the differences between the values of the linear coupling constants calculated for each two opposite points of the reaction surface at the Franck-Condon energy. As a result of the wave packet propagation a trapping of the Bromine atoms in the matrix cage accompanied by large amplitude matrix motions was found and no population transfer was observed. Due to the rediscretization of the tuning mode couplings, as well as due to their linear approximation to the reaction surface this model, however, was found to overestimate the effect of vibrational relaxation in the B-state.

Extending the simulations to the long-time domain, for which a quantum description in terms of low-dimensional models becomes inaccurate, a simple, but full-dimensional model containing 2097 nuclear degrees of freedom has been introduced in Sec. 4.6 to calculate the B-state absorption spectrum. Specifically, this model has been designed as an extension of the Huang-Rhys model to account for the anharmonicity of the Br-Br potential as well as to account for the dependence of the linear coupling of the matrix normal modes on the vibrational excitation of the Br_2 molecule. The zero-phonon lines (ZPL) and phonon sideband (PSB) contributions of the absorption spectrum calculated have been compared to the excitation spectrum measured [84] finding an overall agreement for both features. Qualitatively, an approximate double peak structure was found for the PSB contributions in both cases. Quantitatively, Huang-Rhys coupling constants have been calculated for the PSB contributions and compared to experimentally determined values. Here it was found, that the calculated coupling constants not only follow the same trend of a non-linear increase with the quantum number of the ZPL, but also obey the same order of magnitude. Moreover, the double peak structure of the PSB contributions could be resolved in terms of individual normal mode contributions. Explicitly, next to the tuning mode discussed in Sec. 4.4 two other dominant normal modes of A_g symmetry with lower energy have been identified.

On the technical side, three major improvements related to the calculation of DIM matrix elements have been made in this work: The first improvement concerns the efficient summation of fragment Hamiltonians at earliest transformation stage in the laboratory frame as shown in Sec. 2.3.1. The second and the third improvements concern the analytic calculation of 1st and 2nd order Hamiltonian matrix derivatives as it has been detailed in Sec. 5.5, that is the calculation of forces, Sec. 5.5.1, and Hessian matrix elements, Sec. 5.5.2.

Throughout the work, both quantities have been applied extensively to calculate normal modes, vibrational and spectral densities of states, as well as vibronic coupling constants, permitting the technical realization of the CRS and VCH concepts this way.
The present study calls for extensions into several directions. One natural extension concerns the control of nuclear wave packets via the external electric field. The laser pulses applied in this work have just been means for preparing nuclear wave packets in the Franck-Condon region of the B-state state. In order to manipulate the yield of the predissociation one could thus try to localize these wave packets in the region of the B- to C-state crossing using optimal control theory.
Another possible extension concerns the improved treatment of tuning and coupling modes. For instance, one could include second order couplings or anharmonicity effects. The Morse parameter β required to account for anharmonicity effects in the matrix modes could be estimated from the Lennard-Jones parameters of the Ar-Ar potential, that is $\beta = {}^{6}\!/_{2^{1/6}\sigma}$.
Also on the methodical side there is plenty of room for future improvements. For instance, one could apply an effective mode approach to the vibronic coupling problem as recently proposed for the description of conical intersections in macro-systems [185–187].
In order to circumvent some of the problems arising from an explicit quantum treatment of the bath (cf. Sec. 4.5) one could couple the present reaction surface model to a classical bath via time-dependent mean-fields using the Ehrenfest theorem [188]. Such hybrid quantum/classical approach has already been successfully applied to a primitive model of I_2 in rare gas matrices [189–191]. In specific application to non-adiabatic transitions such quantum/classical approach may be combined with the Hellmann-Feynman theorem [192, 193] within a multi-configurational framework using the time-dependent self-consistent field (Q/C MCTDSCF) approximation [194]. Both approaches offer the on-the-fly calculation of trajectories for the bath degrees of freedom as a promising alternative. Another two promising approaches for treating non-adiabatic dynamics in multi-dimensional systems are the quantum-dressed classical mechanics method [195–198] as well as the variational multi-configuration Gaussian wave packet (vMCG) method [199–202]. The first method employs a discrete variable representation of the nuclear wave function in a Gauss-Hermite basis set, where the grid points follow a classical trajectory in space, the second one employs a basis set of frozen Gaussian functions within an MCTDH ansatz for the nuclear wave function. As a major advantage over the conventional quantum approach both method permit a direct calculation of the PES, that is on-the-fly and in local harmonic approximation, respectively. Given the possibility of efficiently generating gradients and Hessian the present DIM approach would be suited for a fusion with these new concepts. Here again Br_2 in solid Ar could serve as prototypic test system, which shows non-adiabatic behavior due to excited state crossings on one side, as well as classical behavior due to heavy atomic masses on the other.

Appendix

5.1 Eulerian Angles

The rotation of a rigid body in the Euclidean space is uniquely defined by three Eulerian angles α, β and γ and can be understood as a sequence of three consecutive rotations about two out of three orthogonal body-fixed axes [203, 204]. This sequence is illustrated in Fig. 5.1 assuming a right-handed coordinate system with a positive sign for the counter-clockwise rotation.

The first rotation α ($0 \leq \alpha < 2\pi$) about the z-axis of the initial frame (x, y, z), represented by the operator $\mathbf{R}_z(\alpha)$, transfers the coordinates x, y, z into their new positions x', y', z':

$$\begin{pmatrix} x' \\ y' \\ z' \end{pmatrix} = \mathbf{R}_z(\alpha) \begin{pmatrix} x \\ y \\ z \end{pmatrix} = \begin{pmatrix} \cos\alpha & \sin\alpha & 0 \\ -\sin\alpha & \cos\alpha & 0 \\ 0 & 0 & 1 \end{pmatrix} \begin{pmatrix} x \\ y \\ z \end{pmatrix}.$$

The next rotation β ($0 \leq \beta < \pi$) about the y'-axis of the new frame (x', y', z'), represented by the operator $\mathbf{R}_{y'}(\beta)$, carries the coordinates x', y', z' into another positions x'', y'', z'':

$$\begin{pmatrix} x'' \\ y'' \\ z'' \end{pmatrix} = \mathbf{R}_{y'}(\beta) \begin{pmatrix} x' \\ y' \\ z' \end{pmatrix} = \begin{pmatrix} \cos\beta & 0 & -\sin\beta \\ 0 & 1 & 0 \\ \sin\beta & 0 & \cos\beta \end{pmatrix} \begin{pmatrix} x' \\ y' \\ z' \end{pmatrix}.$$

Finally, the third rotation γ ($0 \leq \gamma < 2\pi$) about the z''-axis of the intermediate frame (x'', y'', z''), represented by the operator $\mathbf{R}_{z''}(\gamma)$, transfers the coordinates x'', y'', z'' into

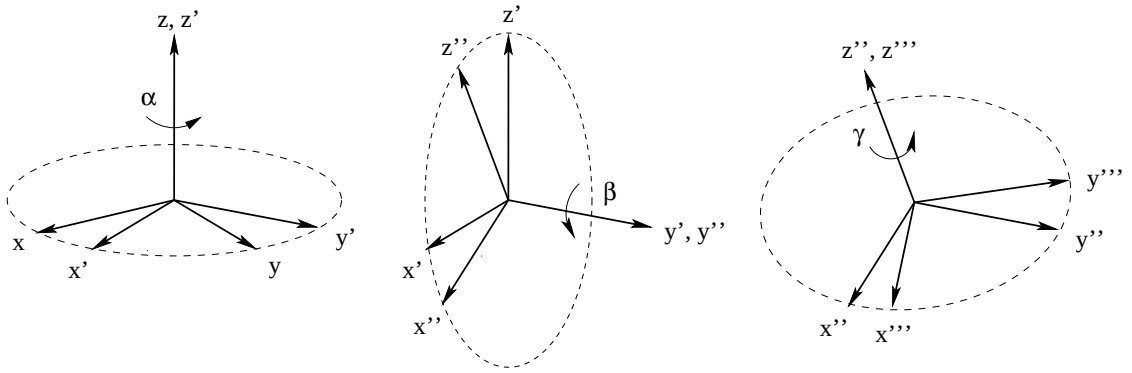

Figure 5.1: Three successive rotations $\mathbf{R}_z(\alpha)$, $\mathbf{R}_{y'}(\beta)$ and $\mathbf{R}_{z''}(\gamma)$ transforming the initial frame (x, y, z) to the final frame (x''', y''', z''').

their final positions x'''', y'''', z'''':

$$\begin{pmatrix} x'''' \\ y'''' \\ z'''' \end{pmatrix} = \mathbf{R}_{z''}(\gamma) \begin{pmatrix} x'' \\ y'' \\ z'' \end{pmatrix} = \begin{pmatrix} \cos\gamma & \sin\gamma & 0 \\ -\sin\gamma & \cos\gamma & 0 \\ 0 & 0 & 1 \end{pmatrix} \begin{pmatrix} x'' \\ y'' \\ z'' \end{pmatrix}.$$

These final positions can be linked directly to the initial ones by direct multiplication of the single rotations in the order from right to left:

$$\mathbf{R}_{z''}(\gamma)\mathbf{R}_{y'}(\beta)\mathbf{R}_{z}(\alpha), \tag{5.1}$$

where the explicit transformation is given by the matrix:

$$\begin{pmatrix} \cos\gamma\cos\beta\cos\alpha - \sin\gamma\sin\alpha & \cos\gamma\cos\beta\sin\alpha + \sin\gamma\cos\alpha & -\cos\gamma\sin\beta \\ -\sin\gamma\cos\beta\cos\alpha - \cos\gamma\sin\alpha & -\sin\gamma\cos\beta\sin\alpha + \cos\gamma\cos\alpha & \sin\gamma\sin\beta \\ \sin\beta\cos\alpha & \sin\beta\sin\alpha & \cos\beta \end{pmatrix}. \tag{5.2}$$

Inserting the following substitutions for the single rotation operators:

$$\begin{aligned} \mathbf{R}_{y'}(\beta) &= \mathbf{R}_{z}(\alpha)\mathbf{R}_{y}(\beta)\mathbf{R}_{z}(-\alpha) \\ \mathbf{R}_{z''}(\gamma) &= \mathbf{R}_{y'}(\beta)\mathbf{R}_{z'}(\gamma)\mathbf{R}_{y'}(-\beta) \\ \mathbf{R}_{z'}(\gamma) &= \mathbf{R}_{z}(\alpha)\mathbf{R}_{z}(\gamma)\mathbf{R}_{z}(-\alpha) \end{aligned}$$

into Eq. (5.1), the equivalence relation $\mathbf{R}_{z''}(\gamma)\mathbf{R}_{y'}(\beta)\mathbf{R}_{z}(\alpha) = \mathbf{R}_{z}(\alpha)\mathbf{R}_{y}(\beta)\mathbf{R}_{z}(\gamma)$ is obtained. Thus, the three rotations can be carried out in the *same* coordinate frame *if* the *order* of rotations is *reversed*. Since the Eulerian angle γ then parameterizes just one out of two rotations about the same z-axis, its particular value is arbitrary. For the choice $\gamma = 0$ the transformation matrix Eq. (5.2) simplifies to:

$$\begin{pmatrix} \cos\beta\cos\alpha & \cos\beta\sin\alpha & -\sin\beta \\ -\sin\alpha & \cos\alpha & 0 \\ \sin\beta\cos\alpha & \sin\beta\sin\alpha & \cos\beta \end{pmatrix}. \tag{5.3}$$

5.2 Supplementary DIM Matrices

The transformation matrix $\mathbf{T}_{D,m_l}$ in Eq. (2.12) of Sec. 2.3.2 is given by the linear transformation $|m_l\rangle = \mathbf{T}_{D,m_l}|p_D\rangle$ between the real and complex basis sets $|p_D\rangle = \{|p_\pi\rangle, |p_{\bar{\pi}}\rangle, |p_\sigma\rangle\}$ and $|m_l\rangle = \{|\ \ 1\rangle, |\ \ 0\rangle, |-1\rangle\}$, respectively. In matrix notation this transformation is thus given by the following expression:

$$\begin{pmatrix} |\ \ 1\rangle \\ |\ \ 0\rangle \\ |-1\rangle \end{pmatrix} = \begin{pmatrix} 1/\sqrt{2} & i/\sqrt{2} & 0 \\ 0 & 0 & 1 \\ 1/\sqrt{2} & -i/\sqrt{2} & 0 \end{pmatrix} \begin{pmatrix} |p_\pi\rangle \\ |p_{\bar{\pi}}\rangle \\ |p_\sigma\rangle \end{pmatrix}.$$

Denoting the individual matrix elements of Eq. (2.12) by H_{ij} with the indices $i, j = 1, 2, 3$, the outer product expansion in Eq. (2.13) is given by the following matrix:

$$\begin{pmatrix} H_{11} & 0 & H_{12} & 0 & H_{13} & 0 \\ 0 & H_{11} & 0 & H_{12} & 0 & H_{13} \\ H_{21} & 0 & H_{22} & 0 & H_{23} & 0 \\ 0 & H_{21} & 0 & H_{22} & 0 & H_{23} \\ H_{31} & 0 & H_{32} & 0 & H_{33} & 0 \\ 0 & H_{31} & 0 & H_{32} & 0 & H_{33} \end{pmatrix} .$$

According to Eq. (2.14) the transformation of this uncoupled Hamiltonian to the spin-coupled representation $|J, M\rangle$ is determined by the Clebsh-Cordon matrix $\mathbf{T}_{m_l m_s, JM}$ with the definition:

$$\begin{pmatrix} |\frac{3}{2}, \quad \frac{3}{2}\rangle \\ |\frac{3}{2}, \quad \frac{1}{2}\rangle \\ |\frac{3}{2}, -\frac{1}{2}\rangle \\ |\frac{3}{2}, -\frac{3}{2}\rangle \\ |\frac{1}{2}, \quad \frac{1}{2}\rangle \\ |\frac{1}{2}, -\frac{1}{2}\rangle \end{pmatrix} = \begin{pmatrix} 1 & 0 & 0 & 0 & 0 & 0 \\ 0 & \sqrt{1/3} & \sqrt{2/3} & 0 & 0 & 0 \\ 0 & 0 & 0 & \sqrt{2/3} & \sqrt{1/3} & 0 \\ 0 & 0 & 0 & 0 & 0 & 1 \\ 0 & \sqrt{2/3} & -\sqrt{1/3} & 0 & 0 & 0 \\ 0 & 0 & 0 & \sqrt{1/3} & -\sqrt{2/3} & 0 \end{pmatrix} \begin{pmatrix} |\ 1, \quad \frac{1}{2}\rangle \\ |\ 1, -\frac{1}{2}\rangle \\ |\ 0, \quad \frac{1}{2}\rangle \\ |\ 0, -\frac{1}{2}\rangle \\ |-1, \quad \frac{1}{2}\rangle \\ |-1, -\frac{1}{2}\rangle \end{pmatrix} .$$

Within the spin-coupled representation, the diatomic Hilbert space is introduced by an outer product of the individual atomic Hilbert spaces for the halogen atoms a and b with the Hamiltonian matrix elements H^a_{ij} and H^b_{ij}, where $i, j = 1, \ldots, 6$. Hence, the different outer product expansions in Eq. (2.15) and Eq. (2.16) are given by the following matrices:

$$\begin{pmatrix} H^a_{11} & 0 & 0 & 0 & 0 & 0 & H^a_{12} & 0 & 0 & 0 & 0 & 0 & H^a_{13} & 0 & 0 & 0 & 0 & 0 & H^a_{14} & 0 & 0 & 0 & 0 & 0 & H^a_{15} & 0 & 0 & 0 & 0 & 0 & H^a_{16} & 0 & 0 & 0 & 0 & 0 \\ 0 & H^a_{11} & 0 & 0 & 0 & 0 & 0 & H^a_{12} & 0 & 0 & 0 & 0 & 0 & H^a_{13} & 0 & 0 & 0 & 0 & 0 & H^a_{14} & 0 & 0 & 0 & 0 & 0 & H^a_{15} & 0 & 0 & 0 & 0 & 0 & H^a_{16} & 0 & 0 & 0 & 0 \\ 0 & 0 & H^a_{11} & 0 & 0 & 0 & 0 & 0 & H^a_{12} & 0 & 0 & 0 & 0 & 0 & H^a_{13} & 0 & 0 & 0 & 0 & 0 & H^a_{14} & 0 & 0 & 0 & 0 & 0 & H^a_{15} & 0 & 0 & 0 & 0 & 0 & H^a_{16} & 0 & 0 & 0 \\ 0 & 0 & 0 & H^a_{11} & 0 & 0 & 0 & 0 & 0 & H^a_{12} & 0 & 0 & 0 & 0 & 0 & H^a_{13} & 0 & 0 & 0 & 0 & 0 & H^a_{14} & 0 & 0 & 0 & 0 & 0 & H^a_{15} & 0 & 0 & 0 & 0 & 0 & H^a_{16} & 0 & 0 \\ 0 & 0 & 0 & 0 & H^a_{11} & 0 & 0 & 0 & 0 & 0 & H^a_{12} & 0 & 0 & 0 & 0 & 0 & H^a_{13} & 0 & 0 & 0 & 0 & 0 & H^a_{14} & 0 & 0 & 0 & 0 & 0 & H^a_{15} & 0 & 0 & 0 & 0 & 0 & H^a_{16} & 0 \\ 0 & 0 & 0 & 0 & 0 & H^a_{11} & 0 & 0 & 0 & 0 & 0 & H^a_{12} & 0 & 0 & 0 & 0 & 0 & H^a_{13} & 0 & 0 & 0 & 0 & 0 & H^a_{14} & 0 & 0 & 0 & 0 & 0 & H^a_{15} & 0 & 0 & 0 & 0 & 0 & H^a_{16} \\ \hline H^a_{21} & 0 & 0 & 0 & 0 & 0 & H^a_{22} & 0 & 0 & 0 & 0 & 0 & H^a_{23} & 0 & 0 & 0 & 0 & 0 & H^a_{24} & 0 & 0 & 0 & 0 & 0 & H^a_{25} & 0 & 0 & 0 & 0 & 0 & H^a_{26} & 0 & 0 & 0 & 0 & 0 \\ 0 & H^a_{21} & 0 & 0 & 0 & 0 & 0 & H^a_{22} & 0 & 0 & 0 & 0 & 0 & H^a_{23} & 0 & 0 & 0 & 0 & 0 & H^a_{24} & 0 & 0 & 0 & 0 & 0 & H^a_{25} & 0 & 0 & 0 & 0 & 0 & H^a_{26} & 0 & 0 & 0 & 0 \\ 0 & 0 & H^a_{21} & 0 & 0 & 0 & 0 & 0 & H^a_{22} & 0 & 0 & 0 & 0 & 0 & H^a_{23} & 0 & 0 & 0 & 0 & 0 & H^a_{24} & 0 & 0 & 0 & 0 & 0 & H^a_{25} & 0 & 0 & 0 & 0 & 0 & H^a_{26} & 0 & 0 & 0 \\ 0 & 0 & 0 & H^a_{21} & 0 & 0 & 0 & 0 & 0 & H^a_{22} & 0 & 0 & 0 & 0 & 0 & H^a_{23} & 0 & 0 & 0 & 0 & 0 & H^a_{24} & 0 & 0 & 0 & 0 & 0 & H^a_{25} & 0 & 0 & 0 & 0 & 0 & H^a_{26} & 0 & 0 \\ 0 & 0 & 0 & 0 & H^a_{21} & 0 & 0 & 0 & 0 & 0 & H^a_{22} & 0 & 0 & 0 & 0 & 0 & H^a_{23} & 0 & 0 & 0 & 0 & 0 & H^a_{24} & 0 & 0 & 0 & 0 & 0 & H^a_{25} & 0 & 0 & 0 & 0 & 0 & H^a_{26} & 0 \\ 0 & 0 & 0 & 0 & 0 & H^a_{21} & 0 & 0 & 0 & 0 & 0 & H^a_{22} & 0 & 0 & 0 & 0 & 0 & H^a_{23} & 0 & 0 & 0 & 0 & 0 & H^a_{24} & 0 & 0 & 0 & 0 & 0 & H^a_{25} & 0 & 0 & 0 & 0 & 0 & H^a_{26} \\ \hline H^a_{31} & 0 & 0 & 0 & 0 & 0 & H^a_{32} & 0 & 0 & 0 & 0 & 0 & H^a_{33} & 0 & 0 & 0 & 0 & 0 & H^a_{34} & 0 & 0 & 0 & 0 & 0 & H^a_{35} & 0 & 0 & 0 & 0 & 0 & H^a_{36} & 0 & 0 & 0 & 0 & 0 \\ 0 & H^a_{31} & 0 & 0 & 0 & 0 & 0 & H^a_{32} & 0 & 0 & 0 & 0 & 0 & H^a_{33} & 0 & 0 & 0 & 0 & 0 & H^a_{34} & 0 & 0 & 0 & 0 & 0 & H^a_{35} & 0 & 0 & 0 & 0 & 0 & H^a_{36} & 0 & 0 & 0 & 0 \\ 0 & 0 & H^a_{31} & 0 & 0 & 0 & 0 & 0 & H^a_{32} & 0 & 0 & 0 & 0 & 0 & H^a_{33} & 0 & 0 & 0 & 0 & 0 & H^a_{34} & 0 & 0 & 0 & 0 & 0 & H^a_{35} & 0 & 0 & 0 & 0 & 0 & H^a_{36} & 0 & 0 & 0 \\ 0 & 0 & 0 & H^a_{31} & 0 & 0 & 0 & 0 & 0 & H^a_{32} & 0 & 0 & 0 & 0 & 0 & H^a_{33} & 0 & 0 & 0 & 0 & 0 & H^a_{34} & 0 & 0 & 0 & 0 & 0 & H^a_{35} & 0 & 0 & 0 & 0 & 0 & H^a_{36} & 0 & 0 \\ 0 & 0 & 0 & 0 & H^a_{31} & 0 & 0 & 0 & 0 & 0 & H^a_{32} & 0 & 0 & 0 & 0 & 0 & H^a_{33} & 0 & 0 & 0 & 0 & 0 & H^a_{34} & 0 & 0 & 0 & 0 & 0 & H^a_{35} & 0 & 0 & 0 & 0 & 0 & H^a_{36} & 0 \\ 0 & 0 & 0 & 0 & 0 & H^a_{31} & 0 & 0 & 0 & 0 & 0 & H^a_{32} & 0 & 0 & 0 & 0 & 0 & H^a_{33} & 0 & 0 & 0 & 0 & 0 & H^a_{34} & 0 & 0 & 0 & 0 & 0 & H^a_{35} & 0 & 0 & 0 & 0 & 0 & H^a_{36} \\ \hline H^a_{41} & 0 & 0 & 0 & 0 & 0 & H^a_{42} & 0 & 0 & 0 & 0 & 0 & H^a_{43} & 0 & 0 & 0 & 0 & 0 & H^a_{44} & 0 & 0 & 0 & 0 & 0 & H^a_{45} & 0 & 0 & 0 & 0 & 0 & H^a_{46} & 0 & 0 & 0 & 0 & 0 \\ 0 & H^a_{41} & 0 & 0 & 0 & 0 & 0 & H^a_{42} & 0 & 0 & 0 & 0 & 0 & H^a_{43} & 0 & 0 & 0 & 0 & 0 & H^a_{44} & 0 & 0 & 0 & 0 & 0 & H^a_{45} & 0 & 0 & 0 & 0 & 0 & H^a_{46} & 0 & 0 & 0 & 0 \\ 0 & 0 & H^a_{41} & 0 & 0 & 0 & 0 & 0 & H^a_{42} & 0 & 0 & 0 & 0 & 0 & H^a_{43} & 0 & 0 & 0 & 0 & 0 & H^a_{44} & 0 & 0 & 0 & 0 & 0 & H^a_{45} & 0 & 0 & 0 & 0 & 0 & H^a_{46} & 0 & 0 & 0 \\ 0 & 0 & 0 & H^a_{41} & 0 & 0 & 0 & 0 & 0 & H^a_{42} & 0 & 0 & 0 & 0 & 0 & H^a_{43} & 0 & 0 & 0 & 0 & 0 & H^a_{44} & 0 & 0 & 0 & 0 & 0 & H^a_{45} & 0 & 0 & 0 & 0 & 0 & H^a_{46} & 0 & 0 \\ 0 & 0 & 0 & 0 & H^a_{41} & 0 & 0 & 0 & 0 & 0 & H^a_{42} & 0 & 0 & 0 & 0 & 0 & H^a_{43} & 0 & 0 & 0 & 0 & 0 & H^a_{44} & 0 & 0 & 0 & 0 & 0 & H^a_{45} & 0 & 0 & 0 & 0 & 0 & H^a_{46} & 0 \\ 0 & 0 & 0 & 0 & 0 & H^a_{41} & 0 & 0 & 0 & 0 & 0 & H^a_{42} & 0 & 0 & 0 & 0 & 0 & H^a_{43} & 0 & 0 & 0 & 0 & 0 & H^a_{44} & 0 & 0 & 0 & 0 & 0 & H^a_{45} & 0 & 0 & 0 & 0 & 0 & H^a_{46} \\ \hline H^a_{51} & 0 & 0 & 0 & 0 & 0 & H^a_{52} & 0 & 0 & 0 & 0 & 0 & H^a_{53} & 0 & 0 & 0 & 0 & 0 & H^a_{54} & 0 & 0 & 0 & 0 & 0 & H^a_{55} & 0 & 0 & 0 & 0 & 0 & H^a_{56} & 0 & 0 & 0 & 0 & 0 \\ 0 & H^a_{51} & 0 & 0 & 0 & 0 & 0 & H^a_{52} & 0 & 0 & 0 & 0 & 0 & H^a_{53} & 0 & 0 & 0 & 0 & 0 & H^a_{54} & 0 & 0 & 0 & 0 & 0 & H^a_{55} & 0 & 0 & 0 & 0 & 0 & H^a_{56} & 0 & 0 & 0 & 0 \\ 0 & 0 & H^a_{51} & 0 & 0 & 0 & 0 & 0 & H^a_{52} & 0 & 0 & 0 & 0 & 0 & H^a_{53} & 0 & 0 & 0 & 0 & 0 & H^a_{54} & 0 & 0 & 0 & 0 & 0 & H^a_{55} & 0 & 0 & 0 & 0 & 0 & H^a_{56} & 0 & 0 & 0 \\ 0 & 0 & 0 & H^a_{51} & 0 & 0 & 0 & 0 & 0 & H^a_{52} & 0 & 0 & 0 & 0 & 0 & H^a_{53} & 0 & 0 & 0 & 0 & 0 & H^a_{54} & 0 & 0 & 0 & 0 & 0 & H^a_{55} & 0 & 0 & 0 & 0 & 0 & H^a_{56} & 0 & 0 \\ 0 & 0 & 0 & 0 & H^a_{51} & 0 & 0 & 0 & 0 & 0 & H^a_{52} & 0 & 0 & 0 & 0 & 0 & H^a_{53} & 0 & 0 & 0 & 0 & 0 & H^a_{54} & 0 & 0 & 0 & 0 & 0 & H^a_{55} & 0 & 0 & 0 & 0 & 0 & H^a_{56} & 0 \\ 0 & 0 & 0 & 0 & 0 & H^a_{51} & 0 & 0 & 0 & 0 & 0 & H^a_{52} & 0 & 0 & 0 & 0 & 0 & H^a_{53} & 0 & 0 & 0 & 0 & 0 & H^a_{54} & 0 & 0 & 0 & 0 & 0 & H^a_{55} & 0 & 0 & 0 & 0 & 0 & H^a_{56} \\ \hline H^a_{61} & 0 & 0 & 0 & 0 & 0 & H^a_{62} & 0 & 0 & 0 & 0 & 0 & H^a_{63} & 0 & 0 & 0 & 0 & 0 & H^a_{64} & 0 & 0 & 0 & 0 & 0 & H^a_{65} & 0 & 0 & 0 & 0 & 0 & H^a_{66} & 0 & 0 & 0 & 0 & 0 \\ 0 & H^a_{61} & 0 & 0 & 0 & 0 & 0 & H^a_{62} & 0 & 0 & 0 & 0 & 0 & H^a_{63} & 0 & 0 & 0 & 0 & 0 & H^a_{64} & 0 & 0 & 0 & 0 & 0 & H^a_{65} & 0 & 0 & 0 & 0 & 0 & H^a_{66} & 0 & 0 & 0 & 0 \\ 0 & 0 & H^a_{61} & 0 & 0 & 0 & 0 & 0 & H^a_{62} & 0 & 0 & 0 & 0 & 0 & H^a_{63} & 0 & 0 & 0 & 0 & 0 & H^a_{64} & 0 & 0 & 0 & 0 & 0 & H^a_{65} & 0 & 0 & 0 & 0 & 0 & H^a_{66} & 0 & 0 & 0 \\ 0 & 0 & 0 & H^a_{61} & 0 & 0 & 0 & 0 & 0 & H^a_{62} & 0 & 0 & 0 & 0 & 0 & H^a_{63} & 0 & 0 & 0 & 0 & 0 & H^a_{64} & 0 & 0 & 0 & 0 & 0 & H^a_{65} & 0 & 0 & 0 & 0 & 0 & H^a_{66} & 0 & 0 \\ 0 & 0 & 0 & 0 & H^a_{61} & 0 & 0 & 0 & 0 & 0 & H^a_{62} & 0 & 0 & 0 & 0 & 0 & H^a_{63} & 0 & 0 & 0 & 0 & 0 & H^a_{64} & 0 & 0 & 0 & 0 & 0 & H^a_{65} & 0 & 0 & 0 & 0 & 0 & H^a_{66} & 0 \\ 0 & 0 & 0 & 0 & 0 & H^a_{61} & 0 & 0 & 0 & 0 & 0 & H^a_{62} & 0 & 0 & 0 & 0 & 0 & H^a_{63} & 0 & 0 & 0 & 0 & 0 & H^a_{64} & 0 & 0 & 0 & 0 & 0 & H^a_{65} & 0 & 0 & 0 & 0 & 0 & H^a_{66} \end{pmatrix} , \tag{5.4}$$

$$
\begin{pmatrix}
H^b_{11}H^b_{12}H^b_{13}H^b_{14}H^b_{15}H^b_{16} & 0\,0\,0\,0\,0\,0 & 0\,0\,0\,0\,0\,0 & 0\,0\,0\,0\,0\,0 & 0\,0\,0\,0\,0\,0 & 0\,0\,0\,0\,0\,0 \\
H^b_{21}H^b_{22}H^b_{23}H^b_{24}H^b_{25}H^b_{26} & 0\,0\,0\,0\,0\,0 & 0\,0\,0\,0\,0\,0 & 0\,0\,0\,0\,0\,0 & 0\,0\,0\,0\,0\,0 & 0\,0\,0\,0\,0\,0 \\
H^b_{31}H^b_{32}H^b_{33}H^b_{34}H^b_{35}H^b_{36} & 0\,0\,0\,0\,0\,0 & 0\,0\,0\,0\,0\,0 & 0\,0\,0\,0\,0\,0 & 0\,0\,0\,0\,0\,0 & 0\,0\,0\,0\,0\,0 \\
H^b_{41}H^b_{42}H^b_{43}H^b_{44}H^b_{45}H^b_{46} & 0\,0\,0\,0\,0\,0 & 0\,0\,0\,0\,0\,0 & 0\,0\,0\,0\,0\,0 & 0\,0\,0\,0\,0\,0 & 0\,0\,0\,0\,0\,0 \\
H^b_{51}H^b_{52}H^b_{53}H^b_{54}H^b_{55}H^b_{56} & 0\,0\,0\,0\,0\,0 & 0\,0\,0\,0\,0\,0 & 0\,0\,0\,0\,0\,0 & 0\,0\,0\,0\,0\,0 & 0\,0\,0\,0\,0\,0 \\
H^b_{61}H^b_{62}H^b_{63}H^b_{64}H^b_{65}H^b_{66} & 0\,0\,0\,0\,0\,0 & 0\,0\,0\,0\,0\,0 & 0\,0\,0\,0\,0\,0 & 0\,0\,0\,0\,0\,0 & 0\,0\,0\,0\,0\,0 \\
\hline
0\,0\,0\,0\,0\,0 & H^b_{11}H^b_{12}H^b_{13}H^b_{14}H^b_{15}H^b_{16} & 0\,0\,0\,0\,0\,0 & 0\,0\,0\,0\,0\,0 & 0\,0\,0\,0\,0\,0 & 0\,0\,0\,0\,0\,0 \\
0\,0\,0\,0\,0\,0 & H^b_{21}H^b_{22}H^b_{23}H^b_{24}H^b_{25}H^b_{26} & 0\,0\,0\,0\,0\,0 & 0\,0\,0\,0\,0\,0 & 0\,0\,0\,0\,0\,0 & 0\,0\,0\,0\,0\,0 \\
0\,0\,0\,0\,0\,0 & H^b_{31}H^b_{32}H^b_{33}H^b_{34}H^b_{35}H^b_{36} & 0\,0\,0\,0\,0\,0 & 0\,0\,0\,0\,0\,0 & 0\,0\,0\,0\,0\,0 & 0\,0\,0\,0\,0\,0 \\
0\,0\,0\,0\,0\,0 & H^b_{41}H^b_{42}H^b_{43}H^b_{44}H^b_{45}H^b_{46} & 0\,0\,0\,0\,0\,0 & 0\,0\,0\,0\,0\,0 & 0\,0\,0\,0\,0\,0 & 0\,0\,0\,0\,0\,0 \\
0\,0\,0\,0\,0\,0 & H^b_{51}H^b_{52}H^b_{53}H^b_{54}H^b_{55}H^b_{56} & 0\,0\,0\,0\,0\,0 & 0\,0\,0\,0\,0\,0 & 0\,0\,0\,0\,0\,0 & 0\,0\,0\,0\,0\,0 \\
0\,0\,0\,0\,0\,0 & H^b_{61}H^b_{62}H^b_{63}H^b_{64}H^b_{65}H^b_{66} & 0\,0\,0\,0\,0\,0 & 0\,0\,0\,0\,0\,0 & 0\,0\,0\,0\,0\,0 & 0\,0\,0\,0\,0\,0 \\
\hline
0\,0\,0\,0\,0\,0 & 0\,0\,0\,0\,0\,0 & H^b_{11}H^b_{12}H^b_{13}H^b_{14}H^b_{15}H^b_{16} & 0\,0\,0\,0\,0\,0 & 0\,0\,0\,0\,0\,0 & 0\,0\,0\,0\,0\,0 \\
0\,0\,0\,0\,0\,0 & 0\,0\,0\,0\,0\,0 & H^b_{21}H^b_{22}H^b_{23}H^b_{24}H^b_{25}H^b_{26} & 0\,0\,0\,0\,0\,0 & 0\,0\,0\,0\,0\,0 & 0\,0\,0\,0\,0\,0 \\
0\,0\,0\,0\,0\,0 & 0\,0\,0\,0\,0\,0 & H^b_{31}H^b_{32}H^b_{33}H^b_{34}H^b_{35}H^b_{36} & 0\,0\,0\,0\,0\,0 & 0\,0\,0\,0\,0\,0 & 0\,0\,0\,0\,0\,0 \\
0\,0\,0\,0\,0\,0 & 0\,0\,0\,0\,0\,0 & H^b_{41}H^b_{42}H^b_{43}H^b_{44}H^b_{45}H^b_{46} & 0\,0\,0\,0\,0\,0 & 0\,0\,0\,0\,0\,0 & 0\,0\,0\,0\,0\,0 \\
0\,0\,0\,0\,0\,0 & 0\,0\,0\,0\,0\,0 & H^b_{51}H^b_{52}H^b_{53}H^b_{54}H^b_{55}H^b_{56} & 0\,0\,0\,0\,0\,0 & 0\,0\,0\,0\,0\,0 & 0\,0\,0\,0\,0\,0 \\
0\,0\,0\,0\,0\,0 & 0\,0\,0\,0\,0\,0 & H^b_{61}H^b_{62}H^b_{63}H^b_{64}H^b_{65}H^b_{66} & 0\,0\,0\,0\,0\,0 & 0\,0\,0\,0\,0\,0 & 0\,0\,0\,0\,0\,0 \\
\hline
0\,0\,0\,0\,0\,0 & 0\,0\,0\,0\,0\,0 & 0\,0\,0\,0\,0\,0 & H^b_{11}H^b_{12}H^b_{13}H^b_{14}H^b_{15}H^b_{16} & 0\,0\,0\,0\,0\,0 & 0\,0\,0\,0\,0\,0 \\
0\,0\,0\,0\,0\,0 & 0\,0\,0\,0\,0\,0 & 0\,0\,0\,0\,0\,0 & H^b_{21}H^b_{22}H^b_{23}H^b_{24}H^b_{25}H^b_{26} & 0\,0\,0\,0\,0\,0 & 0\,0\,0\,0\,0\,0 \\
0\,0\,0\,0\,0\,0 & 0\,0\,0\,0\,0\,0 & 0\,0\,0\,0\,0\,0 & H^b_{31}H^b_{32}H^b_{33}H^b_{34}H^b_{35}H^b_{36} & 0\,0\,0\,0\,0\,0 & 0\,0\,0\,0\,0\,0 \\
0\,0\,0\,0\,0\,0 & 0\,0\,0\,0\,0\,0 & 0\,0\,0\,0\,0\,0 & H^b_{41}H^b_{42}H^b_{43}H^b_{44}H^b_{45}H^b_{46} & 0\,0\,0\,0\,0\,0 & 0\,0\,0\,0\,0\,0 \\
0\,0\,0\,0\,0\,0 & 0\,0\,0\,0\,0\,0 & 0\,0\,0\,0\,0\,0 & H^b_{51}H^b_{52}H^b_{53}H^b_{54}H^b_{55}H^b_{56} & 0\,0\,0\,0\,0\,0 & 0\,0\,0\,0\,0\,0 \\
0\,0\,0\,0\,0\,0 & 0\,0\,0\,0\,0\,0 & 0\,0\,0\,0\,0\,0 & H^b_{61}H^b_{62}H^b_{63}H^b_{64}H^b_{65}H^b_{66} & 0\,0\,0\,0\,0\,0 & 0\,0\,0\,0\,0\,0 \\
\hline
0\,0\,0\,0\,0\,0 & 0\,0\,0\,0\,0\,0 & 0\,0\,0\,0\,0\,0 & 0\,0\,0\,0\,0\,0 & H^b_{11}H^b_{12}H^b_{13}H^b_{14}H^b_{15}H^b_{16} & 0\,0\,0\,0\,0\,0 \\
0\,0\,0\,0\,0\,0 & 0\,0\,0\,0\,0\,0 & 0\,0\,0\,0\,0\,0 & 0\,0\,0\,0\,0\,0 & H^b_{21}H^b_{22}H^b_{23}H^b_{24}H^b_{25}H^b_{26} & 0\,0\,0\,0\,0\,0 \\
0\,0\,0\,0\,0\,0 & 0\,0\,0\,0\,0\,0 & 0\,0\,0\,0\,0\,0 & 0\,0\,0\,0\,0\,0 & H^b_{31}H^b_{32}H^b_{33}H^b_{34}H^b_{35}H^b_{36} & 0\,0\,0\,0\,0\,0 \\
0\,0\,0\,0\,0\,0 & 0\,0\,0\,0\,0\,0 & 0\,0\,0\,0\,0\,0 & 0\,0\,0\,0\,0\,0 & H^b_{41}H^b_{42}H^b_{43}H^b_{44}H^b_{45}H^b_{46} & 0\,0\,0\,0\,0\,0 \\
0\,0\,0\,0\,0\,0 & 0\,0\,0\,0\,0\,0 & 0\,0\,0\,0\,0\,0 & 0\,0\,0\,0\,0\,0 & H^b_{51}H^b_{52}H^b_{53}H^b_{54}H^b_{55}H^b_{56} & 0\,0\,0\,0\,0\,0 \\
0\,0\,0\,0\,0\,0 & 0\,0\,0\,0\,0\,0 & 0\,0\,0\,0\,0\,0 & 0\,0\,0\,0\,0\,0 & H^b_{61}H^b_{62}H^b_{63}H^b_{64}H^b_{65}H^b_{66} & 0\,0\,0\,0\,0\,0 \\
\hline
0\,0\,0\,0\,0\,0 & 0\,0\,0\,0\,0\,0 & 0\,0\,0\,0\,0\,0 & 0\,0\,0\,0\,0\,0 & 0\,0\,0\,0\,0\,0 & H^b_{11}H^b_{12}H^b_{13}H^b_{14}H^b_{15}H^b_{16} \\
0\,0\,0\,0\,0\,0 & 0\,0\,0\,0\,0\,0 & 0\,0\,0\,0\,0\,0 & 0\,0\,0\,0\,0\,0 & 0\,0\,0\,0\,0\,0 & H^b_{21}H^b_{22}H^b_{23}H^b_{24}H^b_{25}H^b_{26} \\
0\,0\,0\,0\,0\,0 & 0\,0\,0\,0\,0\,0 & 0\,0\,0\,0\,0\,0 & 0\,0\,0\,0\,0\,0 & 0\,0\,0\,0\,0\,0 & H^b_{31}H^b_{32}H^b_{33}H^b_{34}H^b_{35}H^b_{36} \\
0\,0\,0\,0\,0\,0 & 0\,0\,0\,0\,0\,0 & 0\,0\,0\,0\,0\,0 & 0\,0\,0\,0\,0\,0 & 0\,0\,0\,0\,0\,0 & H^b_{41}H^b_{42}H^b_{43}H^b_{44}H^b_{45}H^b_{46} \\
0\,0\,0\,0\,0\,0 & 0\,0\,0\,0\,0\,0 & 0\,0\,0\,0\,0\,0 & 0\,0\,0\,0\,0\,0 & 0\,0\,0\,0\,0\,0 & H^b_{51}H^b_{52}H^b_{53}H^b_{54}H^b_{55}H^b_{56} \\
0\,0\,0\,0\,0\,0 & 0\,0\,0\,0\,0\,0 & 0\,0\,0\,0\,0\,0 & 0\,0\,0\,0\,0\,0 & 0\,0\,0\,0\,0\,0 & H^b_{61}H^b_{62}H^b_{63}H^b_{64}H^b_{65}H^b_{66}
\end{pmatrix}, \tag{5.5}
$$

where the order of the product states to the matrix elements in Eq. (5.4) and Eq. (5.5) is defined by the state vector on the right hand side of Eq. 5.6.
The latter transformation matrix $\mathbf{T}_{JM,\Omega}$ is given by Eq. (2.3) in combination with the linear combination coefficients from Tab. 2.1 and explicitly reads to:

$$
\begin{pmatrix}
|0^+_g\rangle \\ |0^+_g\rangle \\ |0^+_g\rangle \\ |0^+_g\rangle \\ |0^-_g\rangle \\ |1_g\rangle \\ |1_g\rangle \\ |1_g\rangle \\ |1_g\rangle \\ |1_g\rangle \\ |1_g\rangle \\ |2_g\rangle \\ |2_g\rangle \\ |2_g\rangle \\ |2_g\rangle \\ |0^-_u\rangle \\ |0^-_u\rangle \\ |0^-_u\rangle \\ |0^+_u\rangle \\ |0^+_u\rangle \\ |1_u\rangle \\ |1_u\rangle \\ |1_u\rangle \\ |1_u\rangle \\ |1_u\rangle \\ |1_u\rangle \\ |1_u\rangle \\ |1_u\rangle \\ |1_u\rangle \\ |2_u\rangle \\ |2_u\rangle \\ |2_u\rangle \\ |2_u\rangle \\ |3_u\rangle \\ |3_u\rangle
\end{pmatrix}
= \frac{1}{\sqrt{2}}
\begin{pmatrix}
0\,0\,0\,0\,0\,0\,0\,0\,1\,0\,0\,0\,-1 & 0\,0\,0\,0\,0\,0\,0\,0\,0\,0\,0\,0\,0 & 0\,0\,0\,0\,0\,0\,0\,0\,0\,0\,0\,0\,0 & 0\,0\,0\,0\,0\,0\,0\,0\,0\,0\,0\,0\,0 \\
0\,0\,0\,1\,0\,0\,0\,0\,0\,0\,0\,0\,0 & 0\,0\,0\,0\,0\,0\,0\,0\,0\,0\,0\,-1 & 0\,0\,0\,0\,0\,0\,0\,0\,0\,0\,0\,0\,0 & 0\,0\,0\,0\,0\,0\,0\,0\,0\,0\,0\,0\,0 \\
0\,0\,0\,0\,0\,0\,0\,0\,0\,0\,0\,0\,0 & 0\,0\,0\,0\,0\,0\,0\,0\,0\,0\,0\,0\,0 & 0\,0\,0\,0\,0\,0\,0\,0\,0\,0\,0\,0\,0 & 0\,0\,0\,0\,0\,0\,0\,0\,0\,0\,0\,0\,0 \\
0\,0\,0\,0\,0\,0\,0\,0\,0\,0\,0\,0\,0 & 0\,0\,0\,0\,0\,0\,0\,0\,0\,0\,0\,0\,0 & 0\,0\,0\,0\,0\,0\,0\,0\,0\,0\,0\,0\,0 & 0\,0\,0\,0\,0\,0\,0\,0\,0\,0\,0\,0\,0 \\
0\,0\,0\,0\,0\,0\,0\,0\,0\,0\,0\,0\,0 & 0\,0\,0\,0\,0\,0\,0\,0\,0\,0\,0\,0\,0 & 0\,0\,0\,0\,0\,0\,0\,0\,0\,0\,0\,0\,0 & 0\,0\,0\,0\,0\,0\,0\,0\,0\,0\,0\,0\,0 \\
0\,0\,1\,0\,0\,0\,0\,0\,0\,0\,0\,0\,0 & 0\,0\,0\,0\,0\,0\,0\,0\,0\,0\,0\,0\,0 & 0\,0\,0\,0\,0\,0\,0\,0\,0\,0\,0\,0\,0 & 0\,0\,0\,0\,0\,0\,0\,0\,0\,0\,0\,0\,0 \\
0\,0\,0\,0\,0\,0\,0\,0\,0\,0\,0\,0\,0 & 0\,0\,0\,0\,0\,0\,0\,0\,0\,0\,0\,0\,0 & 0\,0\,0\,0\,0\,0\,0\,0\,0\,0\,0\,0\,0 & 0\,0\,0\,0\,0\,0\,0\,0\,0\,0\,0\,0\,0 \\
0\,0\,0\,0\,0\,0\,0\,0\,0\,0\,0\,0\,0 & 0\,0\,0\,0\,0\,0\,0\,0\,0\,0\,0\,0\,0 & 0\,0\,0\,0\,0\,0\,0\,0\,0\,0\,0\,0\,0 & 0\,0\,0\,0\,0\,0\,0\,0\,0\,0\,0\,0\,0 \\
0\,0\,0\,0\,0\,0\,0\,0\,0\,0\,0\,0\,0 & 0\,0\,0\,0\,0\,0\,0\,0\,0\,0\,0\,0\,0 & 0\,0\,0\,0\,0\,0\,0\,0\,0\,0\,0\,0\,0 & 0\,0\,0\,0\,0\,0\,0\,0\,0\,0\,0\,0\,0 \\
0\,0\,0\,0\,0\,0\,0\,0\,0\,0\,0\,0\,0 & 0\,0\,0\,0\,0\,0\,0\,0\,0\,0\,0\,0\,0 & 0\,0\,0\,0\,0\,0\,0\,0\,0\,0\,0\,0\,0 & 0\,0\,0\,0\,0\,0\,0\,0\,0\,0\,0\,0\,0 \\
0\,0\,0\,0\,0\,0\,0\,0\,0\,0\,0\,0\,0 & 0\,0\,0\,0\,0\,0\,0\,0\,0\,0\,0\,0\,0 & 0\,0\,0\,0\,0\,0\,0\,0\,0\,0\,0\,0\,0 & 0\,0\,0\,0\,0\,0\,0\,0\,0\,0\,0\,0\,0 \\
0\,0\,0\,0\,0\,0\,0\,0\,0\,0\,0\,0\,0 & 0\,0\,0\,0\,0\,0\,0\,0\,0\,0\,0\,0\,0 & 0\,0\,0\,0\,0\,0\,0\,0\,0\,0\,0\,0\,0 & 0\,0\,0\,0\,0\,0\,0\,0\,0\,0\,0\,0\,0 \\
0\,0\,0\,0\,0\,0\,0\,0\,0\,0\,0\,0\,0 & 0\,0\,0\,0\,0\,0\,0\,0\,0\,0\,0\,0\,0 & 0\,0\,0\,0\,0\,0\,0\,0\,0\,0\,0\,0\,0 & 0\,0\,0\,0\,0\,0\,0\,0\,0\,0\,0\,0\,0 \\
0\,0\,0\,0\,0\,0\,0\,0\,0\,0\,0\,0\,0 & 0\,0\,0\,0\,0\,0\,0\,0\,0\,0\,0\,0\,0 & 0\,0\,0\,0\,0\,0\,0\,0\,0\,0\,0\,0\,0 & 0\,0\,0\,0\,0\,0\,0\,0\,0\,0\,0\,0\,0 \\
0\,0\,0\,0\,0\,0\,0\,0\,0\,0\,0\,0\,0 & 0\,0\,0\,0\,0\,0\,0\,0\,0\,0\,0\,0\,0 & 0\,0\,0\,0\,0\,0\,0\,0\,0\,0\,0\,0\,0 & 0\,0\,0\,0\,0\,0\,0\,0\,0\,0\,0\,0\,0 \\
0\,0\,0\,0\,0\,0\,0\,0\,0\,0\,0\,0\,0 & 0\,0\,0\,0\,0\,0\,0\,0\,0\,0\,0\,0\,0 & 0\,0\,0\,0\,0\,0\,0\,0\,0\,0\,0\,0\,0 & 0\,0\,0\,0\,0\,0\,0\,0\,0\,0\,0\,0\,0 \\
0\,0\,0\,0\,0\,0\,0\,0\,0\,0\,0\,0\,0 & 0\,0\,0\,0\,0\,0\,0\,0\,0\,0\,0\,0\,0 & 0\,0\,0\,0\,0\,0\,0\,0\,0\,0\,0\,0\,0 & 0\,0\,0\,0\,0\,0\,0\,0\,0\,0\,0\,0\,0 \\
0\,0\,0\,0\,0\,0\,0\,0\,0\,0\,0\,0\,0 & 0\,0\,0\,0\,0\,0\,0\,0\,0\,0\,0\,0\,0 & 0\,0\,0\,0\,0\,0\,0\,0\,0\,0\,0\,0\,0 & 0\,0\,0\,0\,0\,0\,0\,0\,0\,0\,0\,0\,0 \\
0\,0\,0\,0\,0\,0\,0\,0\,0\,0\,0\,0\,0 & 0\,0\,0\,0\,0\,0\,0\,0\,0\,0\,0\,0\,0 & 0\,0\,0\,0\,0\,0\,0\,0\,0\,0\,0\,0\,0 & 0\,0\,0\,0\,0\,0\,0\,0\,0\,0\,0\,0\,0 \\
0\,0\,0\,0\,0\,0\,0\,0\,0\,0\,0\,0\,0 & 0\,0\,0\,0\,0\,0\,0\,0\,0\,0\,0\,0\,0 & 0\,0\,0\,0\,0\,0\,0\,0\,0\,0\,0\,0\,0 & 0\,0\,0\,0\,0\,0\,0\,0\,0\,0\,0\,0\,0 \\
0\,0\,0\,0\,0\,0\,0\,0\,0\,0\,0\,0\,0 & 0\,0\,0\,0\,0\,0\,0\,0\,0\,0\,0\,0\,0 & 0\,0\,0\,0\,0\,0\,0\,0\,0\,0\,0\,0\,0 & 0\,0\,0\,0\,0\,0\,0\,0\,0\,0\,0\,0\,0 \\
0\,0\,0\,0\,0\,0\,0\,0\,0\,0\,0\,0\,0 & 0\,0\,0\,0\,0\,0\,0\,0\,0\,0\,0\,0\,0 & 0\,0\,0\,0\,0\,0\,0\,0\,0\,0\,0\,0\,0 & 0\,0\,0\,0\,0\,0\,0\,0\,0\,0\,0\,0\,0 \\
0\,0\,0\,0\,0\,0\,0\,0\,0\,0\,0\,0\,0 & 0\,0\,0\,0\,0\,0\,0\,0\,0\,0\,0\,0\,0 & 0\,0\,0\,0\,0\,0\,0\,0\,0\,0\,0\,0\,0 & 0\,0\,0\,0\,0\,0\,0\,0\,0\,0\,0\,0\,0 \\
0\,0\,0\,0\,0\,0\,0\,0\,0\,0\,0\,0\,0 & 0\,0\,0\,0\,0\,0\,0\,0\,0\,0\,0\,0\,0 & 0\,0\,0\,0\,0\,0\,0\,0\,0\,0\,0\,0\,0 & 0\,0\,0\,0\,0\,0\,0\,0\,0\,0\,0\,0\,0 \\
\sqrt{2}\,0\,0\,0\,0\,0\,0\,0\,0\,0\,0\,0\,0 & 0\,0\,0\,0\,0\,0\,0\,0\,0\,0\,0\,0\,0 & 0\,0\,0\,0\,0\,0\,0\,0\,0\,0\,0\,0\,0 & 0\,0\,0\,0\,0\,0\,0\,0\,0\,0\,0\,0\,0 \\
0\,0\,0\,0\,0\,0\,0\,0\,0\,0\,0\,0\,0 & 0\,0\,0\,0\,0\,0\,0\,0\,0\,0\,0\,0\sqrt{2} & 0\,0\,0\,0\,0\,0\,0\,0\,0\,0\,0\,0\,0 & 0\,0\,0\,0\,0\,0\,0\,0\,0\,0\,0\,0\,0
\end{pmatrix}
\begin{pmatrix}
|\frac{3}{2},\frac{3}{2})a|\frac{3}{2},\frac{3}{2})b \\ |\frac{3}{2},\frac{3}{2})a|\frac{3}{2},\frac{1}{2})b \\ |\frac{3}{2},\frac{3}{2})a|\frac{3}{2},-\frac{1}{2})b \\ |\frac{3}{2},\frac{3}{2})a|\frac{3}{2},-\frac{3}{2})b \\ |\frac{3}{2},\frac{3}{2})a|\frac{1}{2},\frac{1}{2})b \\ |\frac{3}{2},\frac{3}{2})a|\frac{1}{2},-\frac{1}{2})b \\ |\frac{3}{2},\frac{1}{2})a|\frac{3}{2},\frac{3}{2})b \\ |\frac{3}{2},\frac{1}{2})a|\frac{3}{2},\frac{1}{2})b \\ |\frac{3}{2},\frac{1}{2})a|\frac{3}{2},-\frac{1}{2})b \\ |\frac{3}{2},\frac{1}{2})a|\frac{3}{2},-\frac{3}{2})b \\ |\frac{3}{2},\frac{1}{2})a|\frac{1}{2},\frac{1}{2})b \\ |\frac{3}{2},\frac{1}{2})a|\frac{1}{2},-\frac{1}{2})b \\ |\frac{3}{2},-\frac{1}{2})a|\frac{3}{2},\frac{3}{2})b \\ |\frac{3}{2},-\frac{1}{2})a|\frac{3}{2},\frac{1}{2})b \\ |\frac{3}{2},-\frac{1}{2})a|\frac{3}{2},-\frac{1}{2})b \\ |\frac{3}{2},-\frac{1}{2})a|\frac{3}{2},-\frac{3}{2})b \\ |\frac{3}{2},-\frac{1}{2})a|\frac{1}{2},\frac{1}{2})b \\ |\frac{3}{2},-\frac{1}{2})a|\frac{1}{2},-\frac{1}{2})b \\ |\frac{1}{2},\frac{3}{2})a|\frac{3}{2},\frac{3}{2})b \\ |\frac{1}{2},\frac{3}{2})a|\frac{3}{2},\frac{1}{2})b \\ |\frac{1}{2},\frac{3}{2})a|\frac{3}{2},-\frac{1}{2})b \\ |\frac{1}{2},\frac{3}{2})a|\frac{3}{2},-\frac{3}{2})b \\ |\frac{1}{2},\frac{3}{2})a|\frac{1}{2},\frac{1}{2})b \\ |\frac{1}{2},\frac{3}{2})a|\frac{1}{2},-\frac{1}{2})b \\ |\frac{1}{2},\frac{1}{2})a|\frac{3}{2},\frac{3}{2})b \\ |\frac{1}{2},\frac{1}{2})a|\frac{3}{2},\frac{1}{2})b \\ |\frac{1}{2},\frac{1}{2})a|\frac{3}{2},-\frac{1}{2})b \\ |\frac{1}{2},\frac{1}{2})a|\frac{3}{2},-\frac{3}{2})b \\ |\frac{1}{2},\frac{1}{2})a|\frac{1}{2},\frac{1}{2})b \\ |\frac{1}{2},\frac{1}{2})a|\frac{1}{2},-\frac{1}{2})b
\end{pmatrix} \tag{5.6}
$$

5.3 The Nosé-Hoover Thermostat

The Nosé-Hoover (NH) thermostat [130, 131, 205, 206] is a molecular dynamics method for calculating the equilibrium phase-space distribution of a canonical ensemble at a specific temperature T. It is based on the extended system (ES) approach by Nosé, in which an

external heat bath, represented by an additional degree of freedom with the coordinate s, the *mass-like* parameter M of dimension [Et^2], and the momentum p_s, is coupled to a subsystem of N particles with the masses m_i and $3N$ coordinates x_i with momenta p_i. Its Hamiltonian [205,206] has been postulated on the basis of the *virtual* (scaled) momenta p'_i, p'_s and times t':

$$\begin{aligned} H(x_1,\ldots,x_{3N};p'_1,\ldots,p'_{3N};s,p'_s) &= \sum_{i=1}^{3N}\frac{p_i'^2}{2m_i s^2} + V(x_1,\ldots,x_{3N}) \\ &\quad + \frac{p_s'^2}{2M} + 3Nk_BT\ln s \ , \end{aligned} \tag{5.7}$$

which are connected to the *real* variables via the following relations:

$$p'_i = s\cdot p_i, \quad p'_s = s\cdot p_s, \quad dt' = s\cdot dt \ . \tag{5.8}$$

Applying Hamilton's formalism to Eq. (5.7) the following set of canonical equations of motion for the virtual variables can be obtained:

$$\frac{dx_i}{dt'} = \frac{\partial H}{\partial p'_i} = \frac{p'_i}{m_i s^2} \tag{5.9}$$

$$\frac{ds}{dt'} = \frac{\partial H}{\partial p'_s} = \frac{p'_s}{M} \tag{5.10}$$

$$\frac{dp'_i}{dt'} = -\frac{\partial H}{\partial x_i} = f_i \tag{5.11}$$

$$\frac{dp'_s}{dt'} = -\frac{\partial H}{\partial s} = \sum_{i=1}^{3N}\frac{p_i'^2}{m_i s^3} - \frac{3Nk_BT}{s} \ . \tag{5.12}$$

Using the chain rule of differentiation together with Eq. (5.8), the Eqs. (5.9)-(5.12) can be transformed into the respective equations for the real variables:

$$\frac{dx_i}{dt} = s\frac{dx_i}{dt'} = \frac{p_i}{m_i} \tag{5.13}$$

$$\frac{ds}{dt} = s\frac{ds}{dt'} = s^2\frac{p_s}{M} \tag{5.14}$$

$$\frac{dp_i}{dt} = s\frac{dp'_i/s}{dt'} = \frac{dp'_i}{dt'} - \frac{p'_i}{s}\frac{ds}{dt'} = f_i - p_i\cdot s\frac{p_s}{M} \tag{5.15}$$

$$\frac{dp_s}{dt} = s\frac{dp'_s/s}{dt'} = \frac{dp_s}{dt'} - \frac{p_s}{s}\frac{ds}{dt'} = \sum_{i=1}^{3N}\frac{p_i^2}{m_i s} - \frac{3Nk_BT}{s} - s\frac{p_s^2}{M} \ . \tag{5.16}$$

Due to additional force terms, Eq. (5.15) and Eq. (5.16) are no longer canonical. Introducing a *thermodynamic friction coefficient* with the definition $\xi \equiv s\frac{p_s}{M}$, the following second order differential equations for the coordinates x_i, and first order differential equa-

tion for the friction coefficient ξ, can be derived from Eqs. (5.15) and (5.16), respectively:

$$\frac{d^2x_i}{dt^2} = \frac{1}{m_i}\frac{dp_i}{dt} = \frac{f_i}{m_i} - \xi\frac{dx_i}{dt} \tag{5.17}$$

$$\frac{d\xi}{dt} = \frac{p_s}{M}\frac{ds}{dt} + \frac{s}{M}\frac{dp_s}{dt} = \frac{\sum_{i=1}^{3N}\frac{p_i^2}{m_i} - 3Nk_BT}{M}\ . \tag{5.18}$$

5.4 Generic Three State Model

The effect of couplings on the curve crossing problem between the electronic B-state and the doubly degenerate C-states can be understood in terms of a simple 1D three state model (see Fig. 5.2) making advantage of its closed analytic formulation. Within this model, the 3×3 matrix representation of the stationary Schrödinger equation with the energy eigenvalues λ and the associated eigenvector coefficients $c_{\lambda,1}, \ldots, c_{\lambda,3}$ may look as follows:

$$\begin{pmatrix} \varepsilon_1 & v & v \\ v & \varepsilon_2 & 0 \\ v & 0 & \varepsilon_2 \end{pmatrix} \begin{pmatrix} c_{\lambda,1} \\ c_{\lambda,2} \\ c_{\lambda,3} \end{pmatrix} = \lambda \begin{pmatrix} c_{\lambda,1} \\ c_{\lambda,2} \\ c_{\lambda,3} \end{pmatrix}\ . \tag{5.19}$$

The off-diagonal matrix element v in Eq. (5.19) is chosen as a real valued parameter for modelling a constant matrix-induced coupling between the bound B- and the dissociative C-states, which are represented by the diagonal matrix elements ε_1 and ε_2, respectively. The characteristic dependence of these matrix elements on the nuclear coordinate x can be modelled using a Morse function and its repulsive term with unity parameterization:

$$\varepsilon_1 = \exp(2(1-x)) - 2\exp(1-x) + 1 \tag{5.20}$$

$$\varepsilon_2 = \exp(2(1-x))\ . \tag{5.21}$$

When giving the energy scale in units of the dissociation energy $[D_e]$ as well as the coordinate scale in units of the Morse parameter times the equilibrium distance $[\beta x_e]$, this model requires no further parameter and the coupling strength v can directly be expressed in fractions of the B-state dissociation energy, which is about equal to Bromine spin-orbit coupling constant Δ.
In order to obtain the solutions λ of the eigenvalue problem Eq.(5.19), the characteristic polynomial for its vanishing secular determinant has to be solved:

$$\begin{vmatrix} \varepsilon_1 - \lambda & v & v \\ v & \varepsilon_2 - \lambda & 0 \\ v & 0 & \varepsilon_2 - \lambda \end{vmatrix} = (\varepsilon_2 - \lambda)\left[(\varepsilon_2 - \lambda)(\varepsilon_1 - \lambda) - 2v^2\right] = 0\ . \tag{5.22}$$

Its roots are given by the following expressions:

$$\lambda_1 = \frac{1}{2}\left[\varepsilon_1 + \varepsilon_2 - \sqrt{(\varepsilon_1 - \varepsilon_2)^2 + 8v^2}\right] \tag{5.23}$$

$$\lambda_2 = \varepsilon_2 \tag{5.24}$$

$$\lambda_3 = \frac{1}{2}\left[\varepsilon_1 + \varepsilon_2 + \sqrt{(\varepsilon_1 - \varepsilon_2)^2 + 8v^2}\right] , \tag{5.25}$$

where $\lambda_2 = e_2$ directly results from $(\varepsilon_2 - \lambda) = 0$.
The eigenvector, or adiabatic state, to a particular eigenvalue λ can be expressed by a linear combination of the diabatic states $|\varphi_1\rangle, \ldots, |\varphi_3\rangle$ with the respective expansion coefficients $c_{\lambda,1}, \ldots, c_{\lambda,3}$:

$$|\psi_\lambda\rangle = c_{\lambda,1}|\varphi_1\rangle + c_{\lambda,2}|\varphi_2\rangle + c_{\lambda,3}|\varphi_3\rangle \ . \tag{5.26}$$

Inserting the eigenvalues from the Eqs. (5.23)-(5.25) into the matrix eigenvalue problem Eq. (5.19) and applying the normalization condition $|c_{\lambda,1}|^2 + |c_{\lambda,2}|^2 + |c_{\lambda,2}|^3 = 1$, the following expressions for the expansion coefficients of the orthonormalized eigenvectors can be obtained:

$$\lambda_1, \lambda_3: \quad c_{\lambda,1} = \frac{\lambda - \varepsilon_2}{\sqrt{(\lambda - \varepsilon_2)^2 + 2v^2}} \qquad \lambda_2: \quad c_{\lambda,1} = 0 \tag{5.27}$$

$$c_{\lambda,2} = \frac{v}{\sqrt{(\lambda - \varepsilon_2)^2 + 2v^2}} \qquad c_{\lambda,2} = \frac{1}{\sqrt{2}} \tag{5.28}$$

$$c_{\lambda,3} = c_{\lambda,2} \qquad c_{\lambda,3} = -c_{\lambda,2} \ . \tag{5.29}$$

Since the diabatic basis functions in Eq. (5.26) are assumed to vary only smoothly with the nuclear coordinate, the gradients of the eigenvectors are determined by the gradients of the coefficients:

$$\nabla|\psi_\lambda\rangle = \nabla c_{\lambda,1}|\varphi_1\rangle + \nabla c_{\lambda,2}|\varphi_2\rangle + \nabla c_{\lambda,3}|\varphi_3\rangle \ . \tag{5.30}$$

These gradients can be calculated from Eq. (5.27)-(5.29) using recursive definitions:

$$\lambda_1, \lambda_3: \quad \nabla c_{\lambda,1} = \frac{(1 - c_{\lambda,1}c_{\lambda,1})\nabla(\lambda - \varepsilon_2)}{\sqrt{(\lambda - \varepsilon_2)^2 + 2v^2}} \qquad \lambda_2: \quad \nabla c_{\lambda,1} = 0 \tag{5.31}$$

$$\nabla c_{\lambda,2} = \frac{-c_{\lambda,2}c_{\lambda,1}\nabla(\lambda - \varepsilon_2)}{\sqrt{(\lambda - \varepsilon_2)^2 + 2v^2}} \qquad \nabla c_{\lambda,2} = 0 \tag{5.32}$$

$$\nabla c_{\lambda,3} = \nabla c_{\lambda,2} \qquad \nabla c_{\lambda,3} = 0 \ . \tag{5.33}$$

After some algebra, the only non-vanishing derivative coupling elements can be found between the adiabatic states $|\psi_1\rangle$ and $|\psi_3\rangle$. Their coupling is given by the following expressions:

$$\langle\psi_3|\nabla|\psi_1\rangle = \frac{\lambda_3 - \varepsilon_2}{\sqrt{(\lambda_3 - \varepsilon_2)^2 + 2v^2}} \cdot \frac{\nabla(\lambda_1 - \varepsilon_2)}{\sqrt{(\lambda_1 - \varepsilon_2)^2 + 2v^2}} \tag{5.34}$$

$$\langle\psi_1|\nabla|\psi_3\rangle = -\langle\psi_3|\nabla|\psi_1\rangle \ , \tag{5.35}$$

where Eq. (5.35) can be obtained by exchanging λ_1 and λ_3 in Eq. (5.34). At the crossing point with the coordinates $x_c = 1 + \ln 2$ and $\varepsilon_1 = \varepsilon_2 = \frac{1}{4}$ the absolute value of these derivative couplings amounts to $|\frac{1}{\sqrt{32}v}|$ and approaches infinity for v going to zero.
The parametric dependence of the energy eigenvalues (Eqs. (5.23)-(5.25)) and eigenvectors coefficients (Eqs. (5.27)-(5.29)) to λ_1 and λ_3, as well as of the kinetic coupling element (Eq. (5.34)) on the coupling constant is shown in Fig. 5.2 for the three different coupling strength $v = 0.2\ \%\ \Delta, 1\ \%\ \Delta$ and $5\ \%\ \Delta$. Next to the energy separation, also the curvature of the lowest and highest adiabatic potential curves changes characteristically with increasing coupling constant. In addition, one of both degenerate diabatic potential energy curve becomes visible as second solution, Eq. (5.24), of the eigenvalue problem. When analyzing the composition of the lowest and highest adiabatic states in terms of the individual diabatic populations, the transition among the diabatic states varies from abrupt over steep to gradual. This circumstance is reflected by the typical Lorentzian profile of the derivative coupling element, which decreases in amplitude, but increases in width.
From these model study the magnitude of the effective BC coupling element in rare gas environment can be estimated to $10 \leq v \leq 40$ cm^{-1} by a phenomenological comparison of the first two panels in Fig.5.2 with the weak splitting of the numerical potential curves from Fig. 2.15 of Sec. 2.4.5.

5.5 Cartesian Derivatives of DIM Matrix Elements

In the present case, where the X_2 molecular frame is fixed within the Rg matrix (see Sec. 2.3.1 in Chap. 2), the Cartesian derivatives of the DIM-Hamiltonian matrix defined in Eq. (2.18) of Sec. 2.3.3, that is the intra- and interstate forces and force constants as required in Sec. 2.4.3 and Chap. 3, can be calculated analytically.

5.5.1 Forces

Since the matrix elements of the diagonal Hamilton matrices for the X_2 and the Rg-Rg interaction, irrespective of any electronic state labels or pair indices, can be considered as generalized pair potentials $V = V(R)$, which depend on the relative distance $R = \sqrt{x^2 + y^2 + z^2}$ only, the analytic calculation of the gradients:

$$\begin{aligned} \frac{\partial}{\partial x}V &= \frac{\partial V}{\partial R}\frac{\partial R}{\partial x} = \frac{\partial V}{\partial R}e_x \\ \frac{\partial}{\partial y}V &= \frac{\partial V}{\partial R}\frac{\partial R}{\partial y} = \frac{\partial V}{\partial R}e_y \\ \frac{\partial}{\partial z}V &= \frac{\partial V}{\partial R}\frac{\partial R}{\partial z} = \frac{\partial V}{\partial R}e_z \end{aligned} \tag{5.36}$$

is straightforward. On recalling the explicit pair indices again, e.g. i and j with:

$$R_{ij} \;=\; \sqrt{(x_j - x_i)^2 + (y_j - y_i)^2 + (z_j - z_i)^2}\ ,$$

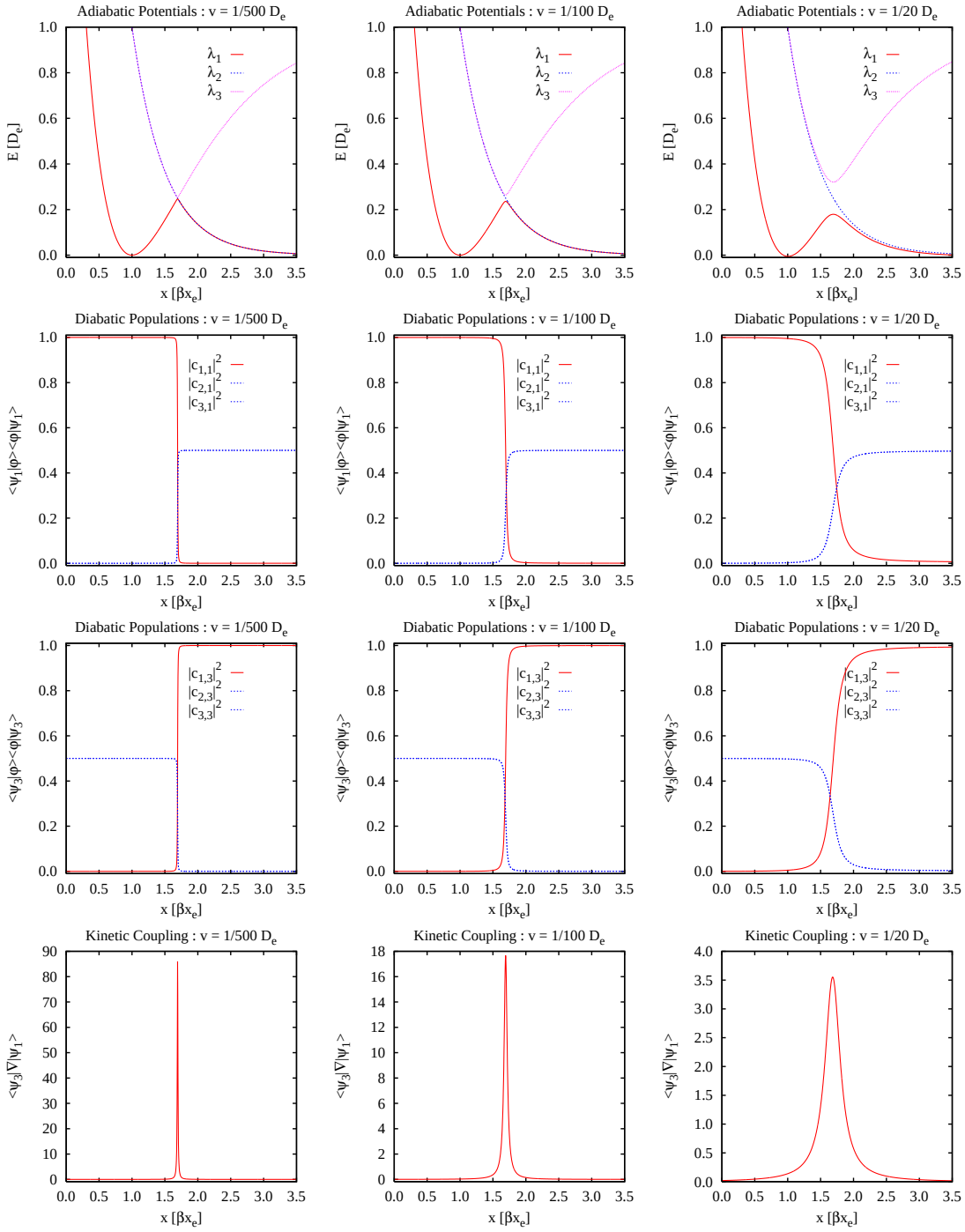

Figure 5.2: Adiabatic potential curves (1st row) and diabatic populations for the lowermost (2nd row) and the uppermost adiabatic state (3rd row) as well as their non-adiabatic couplings (4th row) for three different coupling parameters $v = 0.2$ % D_e (1st column), 1 % D_e (2nd column) and 5 % D_e (3rd column) in the order from top to bottom and left to right.

the directional signs $+1$ and -1 of the force components for the respective atoms j and i can be readily recovered.

Evaluating the gradients of the X_2-Rg Hamiltonian, on the other hand, is demanding since the individual X-Rg fragments composing this Hamiltonian also depend on the spatial orientation of the interaction.

At the lowest transformation level of the X-Rg fragment Hamiltonian, which is given by Eq. (2.9) in Sec. 2.3.1, the gradients of the respective matrix elements thus involve the following derivatives of unit vectors:

$$\begin{aligned}
&\frac{\partial}{\partial x}e_x = \frac{1-e_x^2}{R} && \frac{\partial}{\partial x}e_y = -\frac{e_x e_y}{R} && \frac{\partial}{\partial x}e_z = -\frac{e_x e_z}{R} \\
&\frac{\partial}{\partial y}e_x = \frac{\partial}{\partial x}e_y && \frac{\partial}{\partial y}e_y = \frac{1-e_y^2}{R} && \frac{\partial}{\partial y}e_z = -\frac{e_y e_z}{R} \\
&\frac{\partial}{\partial z}e_x = \frac{\partial}{\partial x}e_z && \frac{\partial}{\partial z}e_y = \frac{\partial}{\partial y}e_z && \frac{\partial}{\partial z}e_z = \frac{1-e_z^2}{R}\ .
\end{aligned} \tag{5.37}$$

Specifically, the calculation of the gradient of Eq. (2.9) involves the derivatives of unit vector products. These can be obtained from Eq. (5.37) by applying the chain rule of differentiation in combination with the unity relation $e_x^2 + e_y^2 + e_z^2 = 1$:

$$\begin{aligned}
&\frac{\partial}{\partial x}e_x e_x = \frac{(2-2e_x^2)e_x}{R} && \frac{\partial}{\partial x}e_x e_y = \frac{(1-2e_x^2)e_y}{R} && \frac{\partial}{\partial x}e_x e_z = \frac{(1-2e_x^2)e_z}{R} \\
&\frac{\partial}{\partial y}e_x e_x = -\frac{2e_x^2 e_y}{R} && \frac{\partial}{\partial y}e_x e_y = \frac{(1-2e_y^2)e_x}{R} && \frac{\partial}{\partial y}e_x e_z = -\frac{2e_x e_y e_z}{R} \\
&\frac{\partial}{\partial z}e_x e_x = -\frac{2e_x^2 e_z}{R} && \frac{\partial}{\partial z}e_x e_y = -\frac{2e_x e_y e_z}{R} && \frac{\partial}{\partial z}e_x e_z = \frac{(1-2e_z^2)e_x}{R}
\end{aligned} \tag{5.38a}$$

$$\begin{aligned}
&\frac{\partial}{\partial x}e_y e_x = \frac{\partial}{\partial x}e_x e_y && \frac{\partial}{\partial x}e_y e_y = -\frac{2e_y^2 e_x}{R} && \frac{\partial}{\partial x}e_y e_z = -\frac{2e_x e_y e_z}{R} \\
&\frac{\partial}{\partial y}e_y e_x = \frac{\partial}{\partial y}e_x e_y && \frac{\partial}{\partial y}e_y e_y = \frac{(2-2e_y^2)e_y}{R} && \frac{\partial}{\partial y}e_y e_z = \frac{(1-2e_y^2)e_z}{R} \\
&\frac{\partial}{\partial z}e_y e_x = \frac{\partial}{\partial z}e_x e_y && \frac{\partial}{\partial z}e_y e_y = -\frac{2e_y^2 e_z}{R} && \frac{\partial}{\partial z}e_y e_z = \frac{(1-2e_z^2)e_y}{R}
\end{aligned} \tag{5.38b}$$

$$\begin{aligned}
&\frac{\partial}{\partial x}e_z e_x = \frac{\partial}{\partial x}e_x e_z && \frac{\partial}{\partial x}e_z e_y = \frac{\partial}{\partial x}e_y e_z && \frac{\partial}{\partial x}e_z e_z = -\frac{2e_z^2 e_x}{R} \\
&\frac{\partial}{\partial y}e_z e_x = \frac{\partial}{\partial y}e_x e_z && \frac{\partial}{\partial y}e_z e_y = \frac{\partial}{\partial y}e_y e_z && \frac{\partial}{\partial y}e_z e_z = -\frac{2e_z^2 e_y}{R} \\
&\frac{\partial}{\partial z}e_z e_x = \frac{\partial}{\partial z}e_x e_z && \frac{\partial}{\partial z}e_z e_y = \frac{\partial}{\partial z}e_y e_z && \frac{\partial}{\partial z}e_z e_z = \frac{(2-2e_z^2)e_z}{R}\ .
\end{aligned} \tag{5.38c}$$

Introducing the following short hand notation for the symmetric X-Rg fragment Hamiltonian matrix from Eq. (2.9):

$$\mathbf{V} \;=\; \begin{pmatrix} V_{11} & \cdots & \cdots \\ V_{21} & V_{22} & \cdots \\ V_{31} & V_{32} & V_{33} \end{pmatrix} \tag{5.39}$$

and applying the relations from Eq. (5.36) to V_Σ and V_Π, together with Eq. (5.38a)-Eq. (5.38c), the gradients of Eq. (5.39), that is the force matrices $\mathbf{F}_x, \mathbf{F}_y$ and $\mathbf{F}_z$, are given by the following matrix elements:

$$\mathbf{F}_x \;:\; \begin{cases} \frac{\partial}{\partial x}V_{11} = \left[\frac{\partial V_\Pi}{\partial R} + 2\frac{V_\Sigma - V_\Pi}{R} + \left(\frac{\partial V_\Sigma}{\partial R} - \frac{\partial V_\Pi}{\partial R} - 2\frac{V_\Sigma - V_\Pi}{R}\right)e_x^2\right] e_x \\ \frac{\partial}{\partial x}V_{21} = \left[\frac{V_\Sigma - V_\Pi}{R} + \left(\frac{\partial V_\Sigma}{\partial R} - \frac{\partial V_\Pi}{\partial R} - 2\frac{V_\Sigma - V_\Pi}{R}\right)e_x^2\right] e_y \\ \frac{\partial}{\partial x}V_{31} = \left[\frac{V_\Sigma - V_\Pi}{R} + \left(\frac{\partial V_\Sigma}{\partial R} - \frac{\partial V_\Pi}{\partial R} - 2\frac{V_\Sigma - V_\Pi}{R}\right)e_x^2\right] e_z \\ \frac{\partial}{\partial x}V_{22} = \left[\frac{\partial V_\Pi}{\partial R} + \left(\frac{\partial V_\Sigma}{\partial R} - \frac{\partial V_\Pi}{\partial R} - 2\frac{V_\Sigma - V_\Pi}{R}\right)e_y^2\right] e_x \\ \frac{\partial}{\partial x}V_{32} = \left(\frac{\partial V_\Sigma}{\partial R} - \frac{\partial V_\Pi}{\partial R} - 2\frac{V_\Sigma - V_\Pi}{R}\right) e_x e_y e_z \\ \frac{\partial}{\partial x}V_{33} = \left[\frac{\partial V_\Pi}{\partial R} + \left(\frac{\partial V_\Sigma}{\partial R} - \frac{\partial V_\Pi}{\partial R} - 2\frac{V_\Sigma - V_\Pi}{R}\right)e_z^2\right] e_x \;, \end{cases} \tag{5.40a}$$

$$\mathbf{F}_y \;:\; \begin{cases} \frac{\partial}{\partial y}V_{11} = \left[\frac{\partial V_\Pi}{\partial R} + \left(\frac{\partial V_\Sigma}{\partial R} - \frac{\partial V_\Pi}{\partial R} - 2\frac{V_\Sigma - V_\Pi}{R}\right)e_x^2\right] e_y \\ \frac{\partial}{\partial y}V_{21} = \left[\frac{V_\Sigma - V_\Pi}{R} + \left(\frac{\partial V_\Sigma}{\partial R} - \frac{\partial V_\Pi}{\partial R} - 2\frac{V_\Sigma - V_\Pi}{R}\right)e_y^2\right] e_x \\ \frac{\partial}{\partial y}V_{31} = \left(\frac{\partial V_\Sigma}{\partial R} - \frac{\partial V_\Pi}{\partial R} - 2\frac{V_\Sigma - V_\Pi}{R}\right) e_x e_y e_z \\ \frac{\partial}{\partial y}V_{22} = \left[\frac{\partial V_\Pi}{\partial R} + 2\frac{V_\Sigma - V_\Pi}{R} + \left(\frac{\partial V_\Sigma}{\partial R} - \frac{\partial V_\Pi}{\partial R} - 2\frac{V_\Sigma - V_\Pi}{R}\right)e_y^2\right] e_y \\ \frac{\partial}{\partial y}V_{32} = \left[\frac{V_\Sigma - V_\Pi}{R} + \left(\frac{\partial V_\Sigma}{\partial R} - \frac{\partial V_\Pi}{\partial R} - 2\frac{V_\Sigma - V_\Pi}{R}\right)e_y^2\right] e_z \\ \frac{\partial}{\partial y}V_{33} = \left[\frac{\partial V_\Pi}{\partial R} + \left(\frac{\partial V_\Sigma}{\partial R} - \frac{\partial V_\Pi}{\partial R} - 2\frac{V_\Sigma - V_\Pi}{R}\right)e_z^2\right] e_y \;, \end{cases} \tag{5.40b}$$

$$\mathbf{F}_z \;:\; \begin{cases} \frac{\partial}{\partial z}V_{11} = \left[\frac{\partial V_\Pi}{\partial R} + \left(\frac{\partial V_\Sigma}{\partial R} - \frac{\partial V_\Pi}{\partial R} - 2\frac{V_\Sigma - V_\Pi}{R}\right)e_x^2\right] e_z \\ \frac{\partial}{\partial z}V_{21} = \left(\frac{\partial V_\Sigma}{\partial R} - \frac{\partial V_\Pi}{\partial R} - 2\frac{V_\Sigma - V_\Pi}{R}\right) e_x e_y e_z \\ \frac{\partial}{\partial z}V_{31} = \left[\frac{V_\Sigma - V_\Pi}{R} + \left(\frac{\partial V_\Sigma}{\partial R} - \frac{\partial V_\Pi}{\partial R} - 2\frac{V_\Sigma - V_\Pi}{R}\right)e_z^2\right] e_x \\ \frac{\partial}{\partial z}V_{22} = \left[\frac{\partial V_\Pi}{\partial R} + \left(\frac{\partial V_\Sigma}{\partial R} - \frac{\partial V_\Pi}{\partial R} - 2\frac{V_\Sigma - V_\Pi}{R}\right)e_y^2\right] e_z \\ \frac{\partial}{\partial z}V_{32} = \left[\frac{V_\Sigma - V_\Pi}{R} + \left(\frac{\partial V_\Sigma}{\partial R} - \frac{\partial V_\Pi}{\partial R} - 2\frac{V_\Sigma - V_\Pi}{R}\right)e_z^2\right] e_y \\ \frac{\partial}{\partial z}V_{33} = \left[\frac{\partial V_\Pi}{\partial R} + 2\frac{V_\Sigma - V_\Pi}{R} + \left(\frac{\partial V_\Sigma}{\partial R} - \frac{\partial V_\Pi}{\partial R} - 2\frac{V_\Sigma - V_\Pi}{R}\right)e_z^2\right] e_z \;. \end{cases} \tag{5.40c}$$

In order to transform the force matrices Eq. (5.40a)-Eq. (5.40c) from the p-orbital representation to the X_2 molecular state representation the various basis set transformation and expansion steps Eq. (2.12), Eq. (2.13), Eq. (2.14) (cf. Sec. 2.3.2), as well as Eq. (2.15), Eq. (2.16) and Eq. (2.17) (cf. Sec. 2.3.3) have to be applied to each matrix $\mathbf{F}_x, \mathbf{F}_y$ and $\mathbf{F}_z$

and each X-Rg interaction pair separately. This way, the matrices Eq. (5.40a)-Eq. (5.40c) of dimension 3×3 are transformed into respective matrices of dimension 36×36. Now, individual matrix elements, that is intra-state or inter-state components of particular electronic states, can be picked out and summed up properly. This double loop summation over atomic pairs can be simplified when taking into account, that the forces acting between each pair are of equal magnitude, but opposite sign.

5.5.2 Hessian

For calculating the Hessian, the second derivatives of Eq. (5.39), that is the first derivatives of Eq. (5.40a), (5.40b) and (5.40c), are required. Inspecting the above force matrices $\mathbf{F}_x, \mathbf{F}_y$ and $\mathbf{F}_z$ one notices the recurrence of the following forces and force combinations, which, for short hand notation, may be abbreviated as:

$$\begin{aligned} f_1 &= \frac{\partial V_\Sigma}{\partial R} \\ f_2 &= \frac{\partial V_\Pi}{\partial R} \\ f_3 &= \frac{V_\Sigma - V_\Pi}{R} \\ f_4 &= \frac{\partial V_\Pi}{\partial R} + 2\frac{V_\Sigma - V_\Pi}{R} = f_2 + 2f_3 \\ f_5 &= \frac{\partial V_\Sigma}{\partial R} - \frac{\partial V_\Pi}{\partial R} - 2\frac{V_\Sigma - V_\Pi}{R} = f_1 - f_4 \ . \end{aligned} \tag{5.41}$$

When applying the chain rule of differentiation to Eq. (5.40a),(5.40b) and (5.40c), one notices, that next to the derivatives of unit vectors, Eq. (5.37), and unit vectors products, Eq. (5.38a)-Eq. (5.38c), also the following derivatives of respective triple unit vectors products are required:

$$\frac{\partial e_x e_y e_z}{\partial x} = \frac{(1-3e_x^2)e_y e_z}{R} \quad \frac{\partial e_x e_y e_z}{\partial y} = \frac{(1-3e_y^2)e_x e_z}{R} \quad \frac{\partial e_x e_y e_z}{\partial z} = \frac{(1-3e_z^2)e_x e_y}{R} \ . \tag{5.42}$$

Further, one requires the derivatives of the quantities introduced in Eq. (5.41), that is:

$$\begin{aligned} k_1 &= \frac{\partial^2 V_\Sigma}{\partial R^2} \\ k_2 &= \frac{\partial^2 V_\Pi}{\partial R^2} \\ k_3 &= \frac{1}{R}\left(\frac{\partial V_\Sigma}{\partial R} - \frac{\partial V_\Pi}{\partial R} - \frac{V_\Sigma - V_\Pi}{R}\right) = \frac{f_1 - f_2 - f_3}{R} \\ k_4 &= \frac{\partial^2 V_\Pi}{\partial R^2} + \frac{2}{R}\left(\frac{\partial V_\Sigma}{\partial R} - \frac{\partial V_\Pi}{\partial R} - \frac{V_\Sigma - V_\Pi}{R}\right) = k_2 + 2k_3 \\ k_5 &= \frac{\partial^2 V_\Sigma}{\partial R^2} - \frac{\partial^2 V_\Pi}{\partial R^2} - \frac{2}{R}\left(\frac{\partial V_\Sigma}{\partial R} - \frac{\partial V_\Pi}{\partial R} - \frac{V_\Sigma - V_\Pi}{R}\right) = k_1 - k_4 \ . \end{aligned} \tag{5.43}$$

Then, applying Eq. (5.43) and Eq. (5.41), together with the relations from Eq. (5.37), Eq. (5.38a)-Eq. (5.38c) and Eq. (5.42), one obtains the following matrices for the second

derivatives of Eq. (5.39):

$$\mathbf{K}_{xx} \quad : \quad \begin{cases} \frac{\partial^2}{\partial x \partial x} V_{11} = \left[k_4 e_x + k_5 e_x e_x^2 + f_5 \frac{\partial}{\partial x} e_x^2\right] e_x + \left(f_4 + f_5 e_x^2\right) \frac{\partial}{\partial x} e_x \\ \frac{\partial^2}{\partial x \partial x} V_{21} = \left[k_3 e_x + k_5 e_x e_x^2 + f_5 \frac{\partial}{\partial x} e_x^2\right] e_y + \left(f_3 + f_5 e_x^2\right) \frac{\partial}{\partial x} e_y \\ \frac{\partial^2}{\partial x \partial x} V_{31} = \left[k_3 e_x + k_5 e_x e_x^2 + f_5 \frac{\partial}{\partial x} e_x^2\right] e_z + \left(f_3 + f_5 e_x^2\right) \frac{\partial}{\partial x} e_z \\ \frac{\partial^2}{\partial x \partial x} V_{22} = \left[k_2 e_x + k_5 e_x e_y^2 + f_5 \frac{\partial}{\partial x} e_y^2\right] e_x + \left(f_2 + f_5 e_y^2\right) \frac{\partial}{\partial x} e_x \\ \frac{\partial^2}{\partial x \partial x} V_{32} = \left(k_5 e_x^2 e_y e_z + f_5\right) \frac{\partial}{\partial x} e_x e_y e_z \\ \frac{\partial^2}{\partial x \partial x} V_{33} = \left[k_2 e_x + k_5 e_x e_z^2 + f_5 \frac{\partial}{\partial x} e_z^2\right] e_x + \left(f_2 + f_5 e_z^2\right) \frac{\partial}{\partial x} e_x \end{cases} \tag{5.44a}$$

$$\mathbf{K}_{xy} \quad : \quad \begin{cases} \frac{\partial^2}{\partial x \partial y} V_{11} = \left[k_4 e_y + k_5 e_y e_x^2 + f_5 \frac{\partial}{\partial y} e_x^2\right] e_x + \left(f_4 + f_5 e_x^2\right) \frac{\partial}{\partial y} e_x \\ \frac{\partial^2}{\partial x \partial y} V_{21} = \left[k_3 e_y + k_5 e_y e_x^2 + f_5 \frac{\partial}{\partial y} e_x^2\right] e_y + \left(f_3 + f_5 e_x^2\right) \frac{\partial}{\partial y} e_y \\ \frac{\partial^2}{\partial x \partial y} V_{31} = \left[k_3 e_y + k_5 e_y e_x^2 + f_5 \frac{\partial}{\partial y} e_x^2\right] e_z + \left(f_3 + f_5 e_x^2\right) \frac{\partial}{\partial y} e_z \\ \frac{\partial^2}{\partial x \partial y} V_{22} = \left[k_2 e_y + k_5 e_y e_y^2 + f_5 \frac{\partial}{\partial y} e_y^2\right] e_x + \left(f_2 + f_5 e_y^2\right) \frac{\partial}{\partial y} e_x \\ \frac{\partial^2}{\partial x \partial y} V_{32} = \left(k_5 e_y^2 e_x e_z + f_5\right) \frac{\partial}{\partial y} e_x e_y e_z \\ \frac{\partial^2}{\partial x \partial y} V_{33} = \left[k_2 e_y + k_5 e_y e_z^2 + f_5 \frac{\partial}{\partial y} e_z^2\right] e_x + \left(f_2 + f_5 e_z^2\right) \frac{\partial}{\partial y} e_x \end{cases} \tag{5.44b}$$

$$\mathbf{K}_{xz} \quad : \quad \begin{cases} \frac{\partial^2}{\partial x \partial z} V_{11} = \left[k_4 e_z + k_5 e_z e_x^2 + f_5 \frac{\partial}{\partial z} e_x^2\right] e_x + \left(f_4 + f_5 e_x^2\right) \frac{\partial}{\partial z} e_x \\ \frac{\partial^2}{\partial x \partial z} V_{21} = \left[k_3 e_z + k_5 e_z e_x^2 + f_5 \frac{\partial}{\partial z} e_x^2\right] e_y + \left(f_3 + f_5 e_x^2\right) \frac{\partial}{\partial z} e_y \\ \frac{\partial^2}{\partial x \partial z} V_{31} = \left[k_3 e_z + k_5 e_z e_x^2 + f_5 \frac{\partial}{\partial z} e_x^2\right] e_z + \left(f_3 + f_5 e_x^2\right) \frac{\partial}{\partial z} e_z \\ \frac{\partial^2}{\partial x \partial z} V_{22} = \left[k_2 e_z + k_5 e_z e_y^2 + f_5 \frac{\partial}{\partial z} e_y^2\right] e_x + \left(f_2 + f_5 e_y^2\right) \frac{\partial}{\partial z} e_x \\ \frac{\partial^2}{\partial x \partial z} V_{32} = \left(k_5 e_z^2 e_x e_y + f_5\right) \frac{\partial}{\partial z} e_x e_y e_z \\ \frac{\partial^2}{\partial x \partial z} V_{33} = \left[k_2 e_z + k_5 e_z e_z^2 + f_5 \frac{\partial}{\partial z} e_z^2\right] e_x + \left(f_2 + f_5 e_z^2\right) \frac{\partial}{\partial z} e_x \end{cases} \tag{5.44c}$$

$$\mathbf{K}_{yx} \quad : \quad \begin{cases} \frac{\partial^2}{\partial y \partial x} V_{11} = \left[k_2 e_x + k_5 e_x e_x^2 + f_5 \frac{\partial}{\partial x} e_x^2\right] e_y + \left(f_2 + f_5 e_x^2\right) \frac{\partial}{\partial x} e_y \\ \frac{\partial^2}{\partial y \partial x} V_{21} = \left[k_3 e_x + k_5 e_x e_y^2 + f_5 \frac{\partial}{\partial x} e_y^2\right] e_x + \left(f_3 + f_5 e_y^2\right) \frac{\partial}{\partial x} e_x \\ \frac{\partial^2}{\partial y \partial x} V_{31} = \left(k_5 e_x^2 e_y e_z + f_5\right) \frac{\partial}{\partial x} e_x e_y e_z \\ \frac{\partial^2}{\partial y \partial x} V_{22} = \left[k_4 e_x + k_5 e_x e_y^2 + f_5 \frac{\partial}{\partial x} e_y^2\right] e_y + \left(f_4 + f_5 e_y^2\right) \frac{\partial}{\partial x} e_y \\ \frac{\partial^2}{\partial y \partial x} V_{32} = \left[k_3 e_x + k_5 e_x e_y^2 + f_5 \frac{\partial}{\partial x} e_y^2\right] e_z + \left(f_3 + f_5 e_y^2\right) \frac{\partial}{\partial x} e_z \\ \frac{\partial^2}{\partial y \partial x} V_{33} = \left[k_2 e_x + k_5 e_x e_z^2 + f_5 \frac{\partial}{\partial x} e_z^2\right] e_y + \left(f_2 + f_5 e_z^2\right) \frac{\partial}{\partial x} e_y \end{cases} \tag{5.44d}$$

$$\mathbf{K}_{yy} \quad : \quad \begin{cases} \frac{\partial^2}{\partial y \partial y} V_{11} = \left[k_2 e_y + k_5 e_y e_x^2 + f_5 \frac{\partial}{\partial y} e_x^2\right] e_y + \left(f_2 + f_5 e_x^2\right) \frac{\partial}{\partial y} e_y \\ \frac{\partial^2}{\partial y \partial y} V_{21} = \left[k_3 e_y + k_5 e_y e_y^2 + f_5 \frac{\partial}{\partial y} e_y^2\right] e_x + \left(f_3 + f_5 e_y^2\right) \frac{\partial}{\partial y} e_x \\ \frac{\partial^2}{\partial y \partial y} V_{31} = \left(k_5 e_y^2 e_x e_z + f_5\right) \frac{\partial}{\partial y} e_x e_y e_z \\ \frac{\partial^2}{\partial y \partial y} V_{22} = \left[k_4 e_y + k_5 e_y e_y^2 + f_5 \frac{\partial}{\partial y} e_y^2\right] e_y + \left(f_4 + f_5 e_y^2\right) \frac{\partial}{\partial y} e_y \\ \frac{\partial^2}{\partial y \partial y} V_{32} = \left[k_3 e_y + k_5 e_y e_y^2 + f_5 \frac{\partial}{\partial y} e_y^2\right] e_z + \left(f_3 + f_5 e_y^2\right) \frac{\partial}{\partial y} e_z \\ \frac{\partial^2}{\partial y \partial y} V_{33} = \left[k_2 e_y + k_5 e_y e_z^2 + f_5 \frac{\partial}{\partial y} e_z^2\right] e_y + \left(f_2 + f_5 e_z^2\right) \frac{\partial}{\partial y} e_y \end{cases} \tag{5.44e}$$

$$\mathbf{K}_{yz} \quad : \quad \begin{cases} \frac{\partial^2}{\partial y \partial z} V_{11} = \left[k_2 e_z + k_5 e_z e_x^2 + f_5 \frac{\partial}{\partial z} e_x^2\right] e_y + \left(f_2 + f_5 e_x^2\right) \frac{\partial}{\partial z} e_y \\ \frac{\partial^2}{\partial y \partial z} V_{21} = \left[k_3 e_z + k_5 e_z e_y^2 + f_5 \frac{\partial}{\partial z} e_y^2\right] e_x + \left(f_3 + f_5 e_y^2\right) \frac{\partial}{\partial z} e_x \\ \frac{\partial^2}{\partial y \partial z} V_{31} = \left(k_5 e_z^2 e_x e_y + f_5\right) \frac{\partial}{\partial z} e_x e_y e_z \\ \frac{\partial^2}{\partial y \partial z} V_{22} = \left[k_4 e_z + k_5 e_z e_y^2 + f_5 \frac{\partial}{\partial z} e_y^2\right] e_y + \left(f_4 + f_5 e_y^2\right) \frac{\partial}{\partial z} e_y \\ \frac{\partial^2}{\partial y \partial z} V_{32} = \left[k_3 e_z + k_5 e_z e_y^2 + f_5 \frac{\partial}{\partial z} e_y^2\right] e_z + \left(f_3 + f_5 e_y^2\right) \frac{\partial}{\partial z} e_z \\ \frac{\partial^2}{\partial y \partial z} V_{33} = \left[k_2 e_z + k_5 e_z e_z^2 + f_5 \frac{\partial}{\partial z} e_z^2\right] e_y + \left(f_2 + f_5 e_z^2\right) \frac{\partial}{\partial z} e_y \end{cases} \tag{5.44f}$$

$$\mathbf{K}_{zx} \quad : \quad \begin{cases} \frac{\partial^2}{\partial z \partial x} V_{11} = \left[k_2 e_x + k_5 e_x e_x^2 + f_5 \frac{\partial}{\partial x} e_x^2\right] e_z + \left(f_2 + f_5 e_x^2\right) \frac{\partial}{\partial x} e_z \\ \frac{\partial^2}{\partial z \partial x} V_{21} = \left(k_5 e_x^2 e_y e_z + f_5\right) \frac{\partial}{\partial x} e_x e_y e_z \\ \frac{\partial^2}{\partial z \partial x} V_{31} = \left[k_3 e_x + k_5 e_x e_z^2 + f_5 \frac{\partial}{\partial x} e_z^2\right] e_x + \left(f_3 + f_5 e_z^2\right) \frac{\partial}{\partial x} e_x \\ \frac{\partial^2}{\partial z \partial x} V_{22} = \left[k_2 e_x + k_5 e_x e_y^2 + f_5 \frac{\partial}{\partial x} e_y^2\right] e_z + \left(f_2 + f_5 e_y^2\right) \frac{\partial}{\partial x} e_z \\ \frac{\partial^2}{\partial z \partial x} V_{32} = \left[k_3 e_x + k_5 e_x e_z^2 + f_5 \frac{\partial}{\partial x} e_z^2\right] e_y + \left(f_3 + f_5 e_z^2\right) \frac{\partial}{\partial x} e_y \\ \frac{\partial^2}{\partial z \partial x} V_{33} = \left[k_4 e_x + k_5 e_x e_z^2 + f_5 \frac{\partial}{\partial x} e_z^2\right] e_z + \left(f_4 + f_5 e_z^2\right) \frac{\partial}{\partial x} e_z \end{cases} \tag{5.44g}$$

$$\mathbf{K}_{zy} \quad : \quad \begin{cases} \frac{\partial^2}{\partial z \partial y} V_{11} = \left[k_2 e_y + k_5 e_y e_x^2 + f_5 \frac{\partial}{\partial y} e_x^2\right] e_z + \left(f_2 + f_5 e_x^2\right) \frac{\partial}{\partial y} e_z \\ \frac{\partial^2}{\partial z \partial y} V_{21} = \left(k_5 e_y^2 e_x e_z + f_5\right) \frac{\partial}{\partial y} e_x e_y e_z \\ \frac{\partial^2}{\partial z \partial y} V_{31} = \left[k_3 e_y + k_5 e_y e_z^2 + f_5 \frac{\partial}{\partial y} e_z^2\right] e_x + \left(f_3 + f_5 e_z^2\right) \frac{\partial}{\partial y} e_x \\ \frac{\partial^2}{\partial z \partial y} V_{22} = \left[k_2 e_y + k_5 e_y e_y^2 + f_5 \frac{\partial}{\partial y} e_y^2\right] e_z + \left(f_2 + f_5 e_y^2\right) \frac{\partial}{\partial y} e_z \\ \frac{\partial^2}{\partial z \partial y} V_{32} = \left[k_3 e_y + k_5 e_y e_z^2 + f_5 \frac{\partial}{\partial y} e_z^2\right] e_y + \left(f_3 + f_5 e_z^2\right) \frac{\partial}{\partial y} e_y \\ \frac{\partial^2}{\partial z \partial y} V_{33} = \left[k_4 e_y + k_5 e_y e_z^2 + f_5 \frac{\partial}{\partial y} e_z^2\right] e_z + \left(f_4 + f_5 e_z^2\right) \frac{\partial}{\partial y} e_z \end{cases} \tag{5.44h}$$

$$\mathbf{K}_{zz} \quad : \quad \begin{cases} \frac{\partial^2}{\partial z \partial z} V_{11} = \left[k_2 e_z + k_5 e_z e_x^2 + f_5 \frac{\partial}{\partial z} e_x^2\right] e_z + \left(f_2 + f_5 e_x^2\right) \frac{\partial}{\partial z} e_z \\ \frac{\partial^2}{\partial z \partial z} V_{21} = \left(k_5 e_z^2 e_x e_y + f_5\right) \frac{\partial}{\partial z} e_x e_y e_z \\ \frac{\partial^2}{\partial z \partial z} V_{31} = \left[k_3 e_z + k_5 e_z e_z^2 + f_5 \frac{\partial}{\partial z} e_z^2\right] e_x + \left(f_3 + f_5 e_z^2\right) \frac{\partial}{\partial z} e_x \\ \frac{\partial^2}{\partial z \partial z} V_{22} = \left[k_2 e_z + k_5 e_z e_y^2 + f_5 \frac{\partial}{\partial z} e_y^2\right] e_z + \left(f_2 + f_5 e_y^2\right) \frac{\partial}{\partial z} e_z \\ \frac{\partial^2}{\partial z \partial z} V_{32} = \left[k_3 e_z + k_5 e_z e_z^2 + f_5 \frac{\partial}{\partial z} e_z^2\right] e_y + \left(f_3 + f_5 e_z^2\right) \frac{\partial}{\partial z} e_y \\ \frac{\partial^2}{\partial z \partial z} V_{33} = \left[k_4 e_z + k_5 e_z e_z^2 + f_5 \frac{\partial}{\partial z} e_z^2\right] e_z + \left(f_4 + f_5 e_z^2\right) \frac{\partial}{\partial z} e_z \ . \end{cases} \tag{5.44i}$$

After having calculated this 3×3 representations of second derivatives in laboratory frame all subsequent transformation steps from Sec. 5.5.1 have to be repeated analogously. Then, the respective derivatives of Hamiltonian matrix elements to a given molecular electronic state can be summed up properly to give the final Hessian matrix of dimension $3N \times 3N$.

5.6 The Ladder Operator Approach to the Harmonic Oscillator

In this section the ladder operator approach to the harmonic oscillator [207, 208] is introduced as a basic method for calculating the discrete variable representation (DVR) of potential energy operators in a harmonic oscillator basis set. It has been applied to represent the DIM-based reaction surfaces from Sec. 4.2 in the form required by the MCTDH package.
Starting from the Hamiltonian of the simple harmonic oscillator:

$$H \quad = \quad \frac{p_x^2}{2m} + \frac{m\omega^2}{2} x^2 \tag{5.45}$$

at first the dimensionless oscillator coordinate q and its conjugated momentum p_q are introduced:

$$q = \sqrt{\frac{m\omega}{\hbar}} x \ , \qquad\qquad p_q = \frac{p_x}{\sqrt{\hbar m \omega}} \ . \tag{5.46}$$

With the aid of these scaled variables the above Hamiltonian, Eq. (5.45), can be simplified:

$$H \quad = \quad \frac{\hbar\omega}{2} \left(p_q^2 + q^2\right) \ . \tag{5.47}$$

Next, the squared momentum and coordinate operators in Eq. (5.47) can be factorize, taking into account, however, that the operator product of both complex roots results in the following expression:

$$(q - i p_q)(q + i p_q) \quad = \quad q^2 - 1 + p_q^2 \ . \tag{5.48}$$

Using this factorization and inserting Eq. (5.48) into Eq. (5.47) the harmonic oscillator Hamiltonian can be rewritten again:

$$H = \frac{\hbar\omega}{2}\Big((q - ip_q)(q + ip_q) + 1\Big) \ . \tag{5.49}$$

Further, when introducing the so-called raising (creation) and lowering (annihilation) operators $a^\dagger$ and a, as well as their product, the number operator $\hat{N}$, with the definitions:

$$a^\dagger = \frac{q - ip_q}{\sqrt{2}} \ , \qquad a = \frac{q + ip_q}{\sqrt{2}} \ , \qquad \hat{N} = a^\dagger a \ , \tag{5.50}$$

the factorized Hamiltonian from Eq. (5.49) can be reformulated equivalently:

$$H = \hbar\omega\left(a^\dagger a + \frac{1}{2}\right) = \hbar\omega\left(\hat{N} + \frac{1}{2}\right) \ . \tag{5.51}$$

This Hamiltonian closely resembles the eigenvalue formula of the harmonic oscillator:

$$E_v = \hbar\omega\left(v + \frac{1}{2}\right) \ , \tag{5.52}$$

so that the vibrational quantum number v in Eq. (5.52) can be seen as eigenvalue of the number operator $\hat{N}$ to the vibrational eigenfunction $|v\rangle$:

$$\hat{N}|v\rangle = v|v\rangle \ . \tag{5.53}$$

In order to understand the meaning of the individual operators $a^\dagger$ and a it is instructive to evaluate the commutators between both ladder operators first, and then to check their individual commutation relations with the number operator $\hat{N}$. Whereas the former relations:

$$[a^\dagger, a] = a^\dagger a - aa^\dagger = iqp_q - ip_q q = i[q, p_q] = -1 \qquad [a, a^\dagger] = -[a^\dagger, a] = 1 \ ,$$

reveal the $\pm$ operator identity, which has already been implied for the factorization in Eq. (5.48), the latter relations:

$$[\hat{N}, a^\dagger] = \hat{N}a^\dagger - a^\dagger\hat{N} = a^\dagger[a, a^\dagger] = a^\dagger \tag{5.54}$$

$$[\hat{N}, a] = \hat{N}a - a\hat{N} = [a^\dagger, a]a = -a \tag{5.55}$$

show, that $a^\dagger|v\rangle$ and $a|v\rangle$ are both, eigenfunctions of $\hat{N}$ *and* the respective operators $a^\dagger$ and a. Using the relations from Eq. (5.54) and Eq. (5.55) in combination with Eq. (5.53) it can be shown further:

$$\hat{N}a^\dagger|v\rangle = a^\dagger\hat{N}|v\rangle + a^\dagger|v\rangle = (v + 1)a^\dagger|v\rangle \tag{5.56}$$

$$\hat{N}a|v\rangle = a\hat{N}|v\rangle - a|v\rangle = (v - 1)a|v\rangle \tag{5.57}$$

that $a^\dagger|v\rangle$ and $a|v\rangle$ are indeed eigenfunctions of the number operator $\hat{N}$ with the eigenvalues $v+1$ and $v-1$, respectively.
From Eq. (5.56) it becomes clear, that the successive application of the raising operator $a^\dagger$ results in a sequential creation of each one quantum of energy, in other words $a^\dagger$ "climbs" up an infinite ladder of eigenfunctions. According to Eq. (5.57) the lowering operator a, in turn, steps this ladder down by annihilating each one quantum of energy. Its repetitive application, however, cannot be continued indefinitely since eigenvalue formula Eq. (5.52) cannot have negative values.
Additionally, since the norm squared of $a|v\rangle$, that is $|a|v\rangle|^2 = \langle v|a^\dagger a|v\rangle = \langle v|\hat{N}|v\rangle = v\langle v|v\rangle$, where $\langle v|v\rangle > 0$ for any $|v\rangle$, it follows that there must exist a lowest eigenfunction with the vibrational quantum number $v = 0$, which satisfies the equation $a|v\rangle = 0$. This requirement leads to the following differential equation for harmonic oscillator ground state wave function $\psi_0(q)$:

$$\left(q + \frac{\partial}{\partial q}\right)\psi_0(q) = 0 \qquad \longrightarrow \qquad d\ln\psi_0(q) = -q dq \ .$$

Its solution $\psi_0(q) = c_0 \exp(-\frac{q^2}{2})$ is straightforward, the respective normalization constant c_0 can be obtained from the normalization constraint:

$$|c_0|^2 \int_{-\infty}^{\infty} e^{-q^2} dq = |c_0|^2\sqrt{\pi} = 1 \ .$$

Putting emphasis on the *normalization* of the harmonic oscillator eigenstates in Hilbert space the vibrational index v may be replaced by n in the following, where $\langle n|n\rangle = 1$ is assumed. Once the lowest eigenstate $|0\rangle$ with $n = 0$ is known, all other eigenstates $|n\rangle$ can be created, or annihilated, algebraically by means of the ladder operators:

$$a^\dagger|n\rangle = c_n^{(+)}|n+1\rangle \ , \quad |c_n^{(+)}|^2 = \langle n|aa^\dagger|n\rangle = n+1 \quad \rightarrow \quad a^\dagger|n\rangle = \sqrt{n+1}|n+1\rangle \tag{5.58}$$

$$a|n\rangle = c_n^{(-)}|n-1\rangle \ , \quad |c_n^{(-)}|^2 = \langle n|a^\dagger a|n\rangle = n \quad \rightarrow \quad a|n\rangle = \sqrt{n}|n-1\rangle \ . \tag{5.59}$$

Here, the expansion coefficients $c_n^{(+)}$ in Eq. (5.58) and $c_n^{(-)}$ in Eq. (5.59) have been found by multiplying the respective *ket* with their complementary *bra* vectors. Within the orthonormal basis of harmonic oscillator eigenstates the non-vanishing matrix elements are given by $\langle n+1|a^\dagger|n\rangle = \sqrt{n+1}$ in case of the creation operator, and by $\langle n-1|a|n\rangle = \sqrt{n}$ in case of its adjoint operator, the annihilation operator. Thus, the representation of the ladder operators within the Hilbert space spanned by the eigenstates $|n\rangle$ is given by the

following matrices:

$$a^\dagger = \begin{pmatrix} 0 & 0 & 0 & 0 & \cdots \\ \sqrt{1} & 0 & 0 & 0 & \cdots \\ 0 & \sqrt{2} & 0 & 0 & \cdots \\ 0 & 0 & \sqrt{3} & 0 & \cdots \\ \vdots & \vdots & \vdots & \vdots & \ddots \end{pmatrix} , \qquad a = \begin{pmatrix} 0 & \sqrt{1} & 0 & 0 & \cdots \\ 0 & 0 & \sqrt{2} & 0 & \cdots \\ 0 & 0 & 0 & \sqrt{3} & \cdots \\ 0 & 0 & 0 & 0 & \cdots \\ \vdots & \vdots & \vdots & \vdots & \ddots \end{pmatrix} . \tag{5.60}$$

As a side remark, once the matrix elements of the creation operator are known, it is straightforward to obtain the normalized harmonic oscillator wave functions in position space by repeated operation of $a^\dagger$ onto the ground state wave function:

$$|n\rangle = \frac{a^\dagger}{\sqrt{n}}|n-1\rangle = \ldots = \frac{(a^\dagger)^n}{\sqrt{n!}}|0\rangle \qquad \longrightarrow \qquad \psi_n(q) = \frac{1}{\sqrt{2^n n!}}\left(q - \frac{\partial}{\partial q}\right)^n \psi_0(q) \ .$$

The strength of the ladder operator approach, however, is the convenient matrix representation of the position and momentum operators, which can be expressed as linear combinations of the raising and lowering operators by reversal of Eq. (5.50):

$$q = \frac{a^\dagger + a}{\sqrt{2}} , \qquad\qquad p_q = i\frac{a^\dagger - a}{\sqrt{2}} . \tag{5.61}$$

Combining the matrices from Eq. (5.60) according to Eq. (5.61) the following representations of the dimensionless coordinate and momentum operators can be obtained:

$$q = \frac{1}{\sqrt{2}} \begin{pmatrix} 0 & \sqrt{1} & 0 & 0 & \cdots \\ \sqrt{1} & 0 & \sqrt{2} & 0 & \cdots \\ 0 & \sqrt{2} & 0 & \sqrt{3} & \cdots \\ 0 & 0 & \sqrt{3} & 0 & \cdots \\ \vdots & \vdots & \vdots & \vdots & \ddots \end{pmatrix} , \quad p_q = \frac{i}{\sqrt{2}} \begin{pmatrix} 0 & -\sqrt{1} & 0 & 0 & \cdots \\ \sqrt{1} & 0 & -\sqrt{2} & 0 & \cdots \\ 0 & \sqrt{2} & 0 & -\sqrt{3} & \cdots \\ 0 & 0 & \sqrt{3} & 0 & \cdots \\ \vdots & \vdots & \vdots & \vdots & \ddots \end{pmatrix} \tag{5.62}$$

resulting in a symmetric matrix for q, and a hermitian matrix for p_q, respectively.
For practical applications, however, the matrices given by Eq. (5.62) have to be finite, which leads to a finite basis representation (FBR) of the respective operators. Upon diagonalizing the matrix representation of these operators their discrete variable representation (DVR) in terms of position and momentum eigenvalues can be obtained, where the respective eigenvectors provide the transformation between both equivalent representations.
In order to express arbitrary (1D) potential energy operators in a (finite) harmonic oscillator basis set the latter operators can be expressed by their discrete values determined at the respective position eigenvalues (grid points) of the harmonic oscillator.

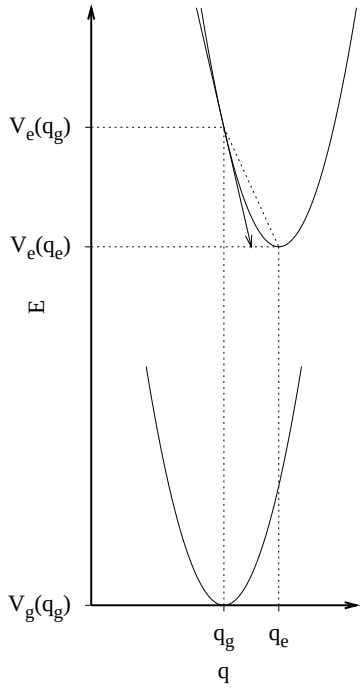

Figure 5.3: Linear shift of the harmonic oscillator ground and excited state potentials $V_g(q)$ and $V_e(q)$ along the oscillator coordinate q with the respective equilibrium geometries q_g and q_e upon $e \leftarrow g$ excitation.

5.7 Shifted Harmonic Oscillator Potential

Together with the Franck-Condon principle [169] the shifted harmonic oscillator potential [145] (cf. Fig. 5.3) forms the theoretical basis of the Huang-Rhys model [10]. This model provides a microscopic and qualitative description of the photo-absorption spectra of chromophores in optically transparent solids. Particularly, it explains the band shape and line profiles of the corresponding spectra in terms of zero-phonon line (ZPL) and phonon sideband (PSB) contributions (cf. Fig. 5.4). Within this model it is assumed that the vibrational modes of the lattice in the immediate vicinity of the chromophore linearly respond to its electronic excitation. Further, it is assumed, that these local modes (LM) can be described by specific or effective harmonic oscillators [9]. In case of a single oscillator mode q_k with the frequency ω_k the Huang-Rhys model is known as configuration coordinate (CC) model. Dropping the explicit mode index k and using dimensionless oscillator coordinates (cf. Eq. (5.46) in Sec. 5.6) the electronic ground state potential $V_g(q)$ of the harmonic oscillator q with the equilibrium geometry q_g is given by:

$$V_g(q) = \frac{\hbar\omega}{2}(q - q_g)^2 \ . \tag{5.63}$$

Following the Franck-Condon principle of a vertical electronic transition the potential energy $V_e(q)$ of the harmonic oscillator q in the electronically excited state may be expanded

into a Taylor series around q_g:

$$V_e(q) \approx V_e(q_g) + \left.\frac{\partial V_e}{\partial q}\right|_{q_g} (q - q_g) + \frac{1}{2} \left.\frac{\partial^2 V_e}{\partial q^2}\right|_{q_g} (q - q_g)^2 , \tag{5.64}$$

where the constant expansion term $V_e(q_g)$ corresponds to the Franck-Condon excitation energy of the chromophore. Further, assuming that the curvature of the harmonic oscillator in the electronically excited state is the same as in the ground state, Eq. (5.64) is just determined by the force f_e acting onto the oscillator upon excitation of the chromophore:

$$V_e(q) = V_e(q_g) - f_e(q - q_g) + \frac{\hbar\omega}{2}(q - q_g)^2 . \tag{5.65}$$

Note, that when working in dimensionless oscillator coordinates this force has the unit of an energy. From Fig. 5.3 it is seen, that, when introducing a new equilibrium geometry q_e, the excited state potential from Eq. (5.65) can be brought into the following form:

$$V_e(q) = V_e(q_e) + \frac{\hbar\omega}{2}(q - q_e)^2 . \tag{5.66}$$

Then, except for the constant energy as well as coordinate shifts $\Delta E = V_e(q_e) - V_g(q_g)$ and $\Delta q = q_e - q_g$, Eq. (5.66) resembles Eq. (5.63). In order to find the minimum position of the oscillator potential in the excited state the first derivative of Eq. (5.65) with respect to q has to vanish, that is $0 = -f_e + \hbar\omega(q - q_g)$, from which follows:

$$\Delta q = q_e - q_g = \frac{f_e}{\hbar\omega} . \tag{5.67}$$

Substituting this expression into Eq. (5.66) one obtains:

$$V_e(q) = V_e(q_e) + \frac{1}{2}\frac{f_e^2}{\hbar\omega} - f_e(q - q_g) + \frac{\hbar\omega}{2}(q - q_g)^2 , \tag{5.68}$$

which is equivalent to Eq. (5.65); the quantity $\frac{1}{2}\frac{f_e^2}{\hbar\omega} = \Delta E$ is called *reorganization* or *readjustment* energy. Dividing this reorganization energy by the energy quantum $\hbar\omega$ of the harmonic oscillator one obtains the dimensionless Huang-Rhys coupling constant S:

$$S = \frac{\Delta E}{\hbar\omega} = \frac{1}{2}\Delta q^2 , \tag{5.69}$$

which serves a measures for the coupling strength of the harmonic oscillator to the electronic transition of chromophore. Its particular value reflects the average number of quanta absorbed by the oscillator to compensate its shift in the excited state.

Fig. 5.4 shows a model absorption spectrum for a single mode q_k coupling to a given optical transition of a chromophore with the frequency ω' for different coupling parameters $S_k = 0, 1, 2, 3, 4$ and 5. Starting with limiting case of zero coupling $S_k = 0$ there is only one peak for the resonant light absorption of the chromophore at ω'. This peak corresponds to the so-called *zero-phonon line* (ZPL) since no vibrational quantum is excited in the

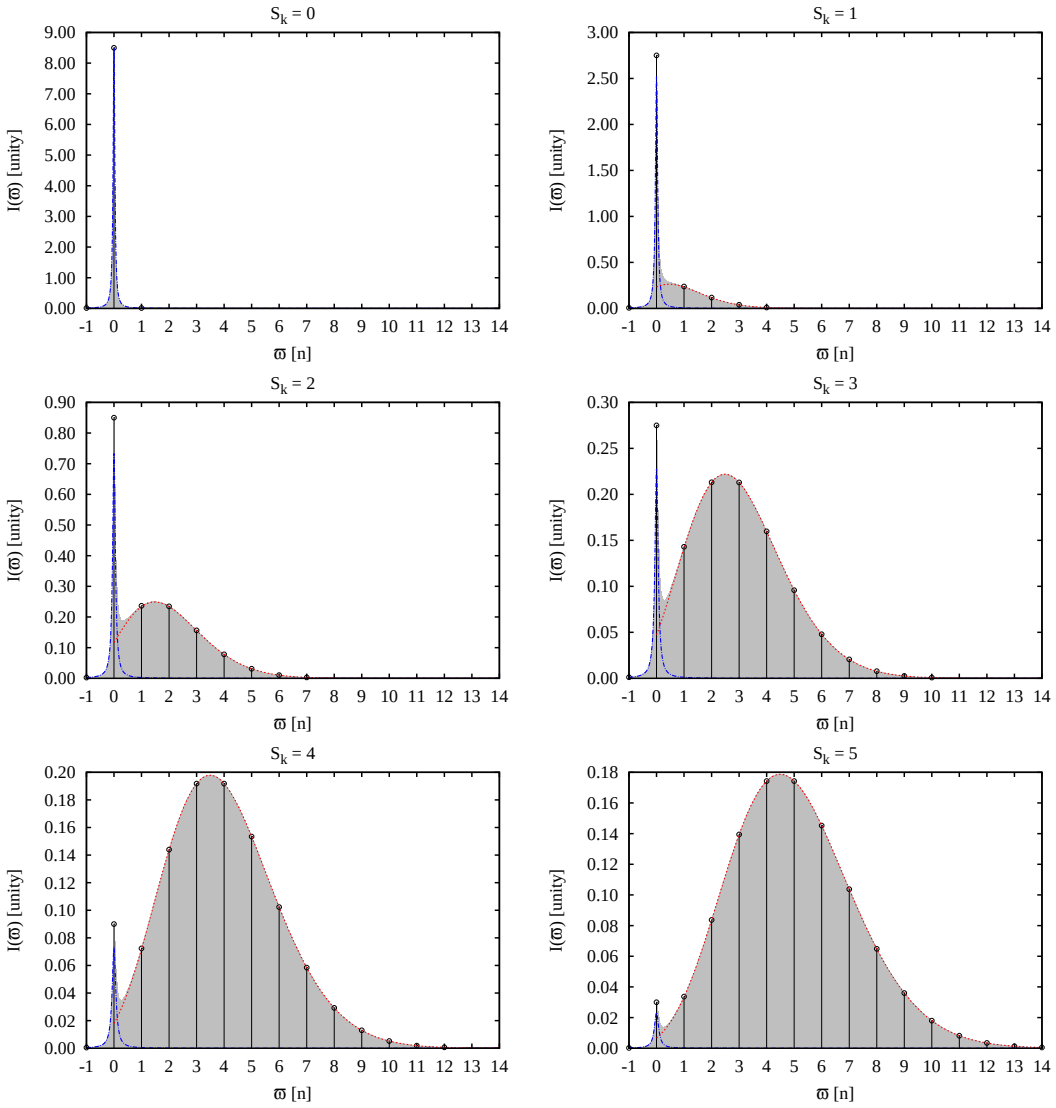

Figure 5.4: Model absorption spectrum showing the intensity weights of zero-phonon line (ZPL) peak (dash-dotted curve, Eq. (5.70)) and its phonon sideband (PSB) contributions (discrete lines with dashed envelope, Eq. (5.71)) for different Huang-Rhys coupling parameters $S_k = 0, 1, 2, 3, 4, 5$ in the order from left to right and top to bottom.

oscillator upon electronic transition, that is the respective harmonic potential curves from Fig. 5.3 are not shifted with respect to one another. The line profile of the ZPL peak follows a Lorentzian curve $f_L(\tilde{\omega})$ [8]:

$$f_L(\tilde{\omega}) \quad = \quad \frac{1}{\pi}\frac{\gamma/2}{\tilde{\omega}^2+\gamma^2/4}, \tag{5.70}$$

which is characterized by the full-width at half maximum (FWHM) parameter γ. With increasing coupling strength $S_k = 1, 2, 3$ the intensity of this ZPL successively decreases in favor of a rapidly growing *phonon sideband* (PSB) with a Poisson distribution $f_P(\tilde{\omega})$ [9]:

$$f_P(\tilde{\omega}) \quad = \quad e^{-S_k}\sum_{n=0}^{\infty}\frac{S_k^n}{n!}\delta(\tilde{\omega}-n)\ , \tag{5.71}$$

where the index n counts the vibrational quanta $\hbar\omega_k$ in excited state of q_k. Note, that the argument $\tilde{\omega}$ in Eq. (5.70) and Eq. (5.71) has been defined in terms of a shifted frequency $\omega - \omega'$, normalized by ω_k:

$$\tilde{\omega} \quad \equiv \quad \frac{\omega-\omega'}{\omega_k}$$

such that its integer values correspond to n. The maximum intensity of the PSB lies between $n = S_k - 1$ and $n = S_k$, so that the Huang-Rhys constant S_k reflects the *mean* number of quanta excited in the oscillator coordinate. In case of a rather strong coupling $S_k = 4, 5$ the oscillator's PSB contributions finally dominate the chromophore's ZPL in the maximum intensity and the respective Poisson distribution gradually turns into Gaussian. Accordingly, the total line-shape $I(\tilde{\omega})$ of the spectrum can be seen as a normalized superposition of $f_L(\tilde{\omega})$ and $f_P(\tilde{\omega})$ [8]:

$$I(\tilde{\omega}) = \alpha f_L(\tilde{\omega}) + (1-\alpha) f_P(\tilde{\omega})\ , \tag{5.72}$$

where the normalization constant $\alpha = \exp(-S_k)$ is characterized by the relative intensities of the ZPL and PSB contributions in fractions of the total area under both curves.
Of course the above consideration can be generalized to the situation, where many harmonic oscillators q_k with distinct Huang-Rhys factors S_k couple to the chromophore. In this case the total coupling strength is determined by the sum of the individual coupling constants:

$$S \quad = \quad \sum_k S_k\ . \tag{5.73}$$

Acronyms

BS	Bulirsch-Stoer
CC	Configuration Coordinate
CMF	Constant Mean-Field
CRS	Cartesian Reaction Surface
DIM	Diatomics-in-Molecules
DOF	Degree of Freedom
DVR	Discrete Variable Representation
EOM	Equation of Motion
FBR	Finite Basis Representation
FFT	Fast Fourier Transform
FGH	Fourier Grid Hamiltonian
FWHM	Full Width at Half Maximum
HFDID	Hartree-Fock Dispersion Individually Damped
IRP	Intrinsic Reaction Path
LAC	Large Amplitude Coordinate
LCAO	Linear Combination of Atomic Orbitals
LJ	Lennard-Jones
LM	Local Mode
MCTDH	Multi-Configuration Time-Dependent Hartree
MO	Molecular Orbital
NH	Nosé-Hoover
PES	Potential Energy Surface
PSB	Phonon Sideband
SAD	Small Amplitude Displacement
SIL	Short Iterative Lanczos
SOC	Spin-Orbit Coupling
SOCI	Spin-Orbit-Coupled Configuration Interaction
SPF	Single Particle Function
TDSE	Time-Dependent Schrödinger Equation
VB	Valence Bond
VCH	Vibronic Coupling Hamiltonian
VMF	Variable Mean-Field
ZPL	Zero-Phonon Line

Bibliography

[1] G. Herzberg, *Molecular Spectra and Molecular Structure. I. Spectra of Diatomic Molecules*, Van Nostrand Reinhold, New York, 1950.

[2] K. P. Huber and G. Herzberg, *Molecular Spectra and Molecular Structure. IV. Constants of Diatomic Molecules*, Van Nostrand Reinhold, New York, 1979.

[3] H. Lefebvre-Brion and R. W. Field, *The Spectra and Dynamics of Diatomic Molecules*, Elsevier Academic Press, San Diego, 2004.

[4] G. Gilat and L. J. Raubenheimer, "Accurate mumerical method for calculating frequency-distribution functions in solids," *Phys. Rev.* **144**, p. 390, 1966.

[5] J. A. Barker, M. L. Klein, and M. V. Bobetic, "Elastic constants and phonon dispersion curves for solid argon near 0° K," *Phys. Rev. B* **2**, p. 4176, 1970.

[6] L. Verlet and J.-J. Weis, "Equilibrium theory of simple liquids," *Phys. Rev. A* **5**, p. 939, 1972.

[7] Y. Fujii, N. A. Lurie, R. Pynn, and G. Shirane, "Inelastic neutron scattering from solid ^{36}Ar," *Phys. Rev. B* **10**, p. 3647, 1974.

[8] J. Friedrich and D. Haarer, "Photochemical hole burning: A spectroscopic study of relaxation processes in polymers and glasses," *Angew. Chem. Int. Ed.* **23**, p. 113, 1984.

[9] J. J. Markham, "Interaction of normal modes with electron traps," *Rev. Mod. Phys.* **31**, p. 956, 1959.

[10] K. Huang and A. Rhys, "Theory of light absorption and non-radiative transitions in F-centres," *Proc. Roy. Soc. A* **204**, p. 406, 1950.

[11] V. A. Apkarian and N. Schwentner, "Molecular photodynamics in rare gas solids," *Chem. Rev.* **99**, p. 1481, 1999.

[12] M. Bargheer, A. Borowski, A. Cohen, M. Fushitani, R. B. Gerber, M. Gühr, P. Hamm, H. Ibrahim, T. Kiljunen, M. V. Korolkov, O. Kühn, J. Manz, B. Schmidt, M. Schröder, and N. Schwentner, "Coherence and control of molecular dynamics in rare gas matrices," in *Analysis and Control of Ultrafast Photoinduced Reactions*, O. Kühn and Ludger Wöste, ed., *Springer Series in Chemical Physics Vol. 87*, p. 257, Springer, (Heidelberg), 2007.

[13] M. Gühr, M. Bargheer, M. Fushitani, T. Kiljunen, and N. Schwentner, "Ultrafast dynamics of halogens in rare gas solids," *Phys. Chem. Chem. Phys.* **9**, p. 779, 2007.

[14] M. Bargheer, M. Y. Niv, R. B. Gerber, and N. Schwentner, "Ultrafast solvent-induced spin-flip and nonadiabatic coupling: ClF in argon solids," *Phys. Rev. Lett.* **89**, p. 108301, 2002.

[15] M. Bargheer, R. B. Gerber, M. V. Korolkov, O. Kühn, J. Manz, M. Schröder, and N. Schwentner, "Subpicosecond spin-flip induced by the photodissociation dynamics of ClF in an Ar matrix," *Phys. Chem. Chem. Phys.* **4**, p. 5554, 2002.

[16] M. Bargheer, A. Cohen, R. B. Gerber, M. Gühr, M. V. Korolkov, J. Manz, M. Y. Niv, M. Schröder, and N. Schwentner, "Dynamics of electronic states and spin-flip for photodissociation of dihalogens in matrices: Experiment and semiclassical surface-hopping and quantum model simulations for F_2 and ClF in solid Ar," *J. Phys. Chem. A* **111**, p. 9573, 2007.

[17] M. Fushitani, N. Schwentner, M. Schröder, and O. Kühn, "Cage motions induced by electronic and vibrational excitations: Cl_2 in Ar," *J. Chem. Phys.* **124**, p. 024505, 2006.

[18] M. Gühr and N. Schwentner, "Effective chromophore potential, dissipative trajectories, and vibrational energy relaxation: Br_2 in Ar matrix," *J. Chem. Phys.* **123**, p. 244506, 2005.

[19] M. Bargheer, M. Gühr, and N. Schwentner, "Collisions transfer coherence," *Israel J.Chem.* **44**, p. 9, 2004.

[20] M. Gühr, M. Bargheer, and N. Schwentner, "Generation of coherent zone boundary phonons by impulsive excitation of molecules," *Phys. Rev. Lett.* **91**, p. 085504, 2003.

[21] M. Gühr and N. Schwentner, "Coherent phonon dynamics: Br_2 in solid Ar," *Phys. Chem. Chem. Phys.* **7**, p. 760, 2005.

[22] M. Karavitis, R. Zadoyan, and V. A. Apkarian, "Time resolved coherent anti-Stokes Raman scattering of I_2 isolated in matrix argon: Vibrational dynamics on the ground electronic state," *J. Chem. Phys.* **114**, p. 4131, 2001.

[23] Z. Bihary, M. Karavitis, R. B. Gerber, and V. A. Apkarian, "Spectral inhomogeneity induced by vacancies and thermal phonons and associated observables in time- and frequency-domain nonlinear spectroscopy: I_2 isolated in matrix argon," *J. Chem. Phys.* **115**, p. 8006, 2001.

[24] Z. Bihary, R. Zadoyan, M. Karavitis, and V. A. Apkarian, "Dynamics and the breaking of a driven cage: I_2 in solid Ar," *J. Chem. Phys.* **120**, p. 7576, 2004.

[25] R. Zadoyan, J. Almy, and V. A. Apkarian, "Lattice dynamics from the 'eyes' of the chromophore: Real-time studies of I_2 isolated in rare gas matrices," *Faraday Discuss.* **108**, p. 255, 1997.

[26] M. Karavitis and V. A. Apkarian, "Vibrational coherence of I_2 in solid Kr," *J. Chem. Phys.* **120**, p. 292, 2004.

[27] D. Segale, M. Karavitis, E. Fredj, and V. A. Apkarian, "Quantum coherent dissipation: A glimpse of the "cat"," *J. Chem. Phys.* **122**, p. 111104, 2005.

[28] M. Gühr, H. Ibrahim, and N. Schwentner, "Controlling vibrational wave packet revivals in condensed phase: Dispersion and coherence for Br_2 in solid Ar," *Phys. Chem. Chem. Phys.* **6**, p. 5353, 2004.

[29] M. Fushitani, M. Bargheer, M. Gühr, and N. Schwentner, "Pump-probe spectroscopy with phase-locked pulses in the condensed phase: Decoherence and control of vibrational wavepackets," *Phys. Chem. Chem. Phys.* **7**, p. 3143, 2005.

[30] J. C. Tully and R. K. Preston, "Trajectory surface hopping approach to nonadiabatic molecular collisions: The reaction of H^+ with D_2," *J. Chem. Phys.* **55**, p. 562, 1971.

[31] J. C. Tully, "Molecular dynamics with electronic transitions," *J. Chem. Phys.* **93**, p. 1061, 1990.

[32] D. F. Coker, "Computer Simulation Methods for Nonadiabatic Dynamics in Condensed Phase," in *Computer Simulation in Chemical Physics*, M. P. Allen and D. J. Tildesley, eds., Kluwer Academic Publishers, (Dordrecht), 1993.

[33] F. O. Ellison, "A Method of diatomics in molecules. I. General theory and application to H_2O," *J. Am. Chem. Soc.* **85**, p. 3540, 1963.

[34] F. O. Ellison, N. T. Huff, and J. C. Patel, "A method of diatomics in molecules. II. H_3 and H_3^+," *J. Am. Chem. Soc.* **85**, p. 3544, 1963.

[35] J. C. Tully, "Diatomics-in-molecules potential energy surfaces. I. First-row triatomic hydrides," *J. Chem. Phys.* **58**, p. 1396, 1973.

[36] J. C. Tully, "Diatomics-in-molecules potential energy surfaces. II. Nonadiabatic and spin-orbit interactions," *J. Chem. Phys.* **59**, p. 5122, 1973.

[37] I. H. Gersonde and H. Gabriel, "Molecular dynamics of photodissociation in matrices including nonadiabatic processes," *J. Chem. Phys.* **98**, p. 2094, 1993.

[38] I. H. Gersonde, S. Hennig, and H. Gabriel, "Nonadiabatic transitions in the photodissociation of HCl," *J. Chem. Phys.* **101**, p. 9558, 1994.

[39] W. G. Lawrence and V. A. Apkarian, "Many-body potentials of an open shell atom: Spectroscopy of spin-orbit transitions of iodine in crystalline Xe and Kr," *J. Chem. Phys.* **101**, p. 1820, 1994.

[40] V. S. Batista and D. F. Coker, "Nonadiabatic molecular dynamics simulation of photodissociation and geminate recombination of I_2 in liquid xenon," *J. Chem. Phys.* **105**, p. 4033, 1996.

[41] V. S. Batista and D. F. Coker, "Nonadiabatic molecular dynamics simulation of ultrafast pump-probe experiments on I_2 in solid rare gases," *J. Chem. Phys.* **106**, p. 6923, 1997.

[42] V. S. Batista and D. F. Coker, "Nonadiabatic molecular dynamics simulations of the photofragmentation and geminate recombination dynamics in size-selected $I_2^-\cdot Ar_n$ cluster ions," *J. Chem. Phys.* **106**, p. 7102, 1997.

[43] A. I. Krylov and R. B. Gerber, "Photodissociation dynamics of HCl in solid Ar: Cage exit, nonadiabatic transitions, and recombination," *J. Chem. Phys.* **106**, p. 6574, 1997.

[44] M. Y. Niv, A. I. Krylov, and R. B. Gerber, "Photodissociation, electronic relaxation and recombination of HCl in Ar_n(HCl) clusters," *Faraday Discuss.* **108**, p. 243, 1997.

[45] M. Y. Niv, A. I. Krylov, and R. B. Gerber, "Photodissociation of HCl adsorbed on the surface of an Ar_{12} cluster: Nonadiabatic molecular dynamics simulations," *J. Chem. Phys.* **110**, p. 11047, 1999.

[46] R. Baumfalk, N. H. Nahler, U. Buck, M. Y. Niv, and R. B. Gerber, "Photodissociation of HBr adsorbed on the surface and embedded in large Ar_n clusters," *J. Chem. Phys.* **113**, p. 329, 2000.

[47] B. L. Grigorenko, A. V. Nemukhin, and V. A. Apkarian, "Inclusion of ion-pair states in the diatomics-in-molecules description of potential energy surfaces: Van der Waals complexes of He-Cl_2 and Ar-Cl_2," *Chem. Phys.* **219**, p. 161, 1997.

[48] B. L. Grigorenko, A. V. Nemukhin, A. A. Buchachenko, N. F. Stepanov, and S. Y. Umanskii, "Diatomics-in-molecules description of the Rg-Hal_2 rare gas-halogen van der Waals complexes with applications to He-Cl_2," *J. Chem. Phys.* **106**, p. 4575, 1997.

[49] B. L. Grigorenko, A. V. Nemukhin, and N. V. Ozhegova, "MD-DIM simulations of the $^3\Pi_g$(ion-pair) $\rightarrow$ $^3\Pi_u$(valence) red-shifted transitions of Cl_2 in neon matrices," *Chem. Phys. Lett.* **296**, p. 84, 1998.

[50] A. A. Buchachenko and N. F. Stepanov, "Ar-I_2 interactions: The models based on the diatomics-in-molecule approach," *J. Chem. Phys.* **104**, p. 9913, 1996.

[51] A. A. Buchachenko and N. F. Stepanov, "Structure and interaction energies of the Ar...Cl_2 complex. Application of first-order intermolecular potentials," *Chem. Phys. Lett.* **261**, p. 591, 1996.

[52] A. A. Buchachenko, "Predissociation of the Rg$\cdots$I$_2$(B) (Rg=Ne, Ar, Kr) complexes: Simulations based on the first-order diatomics-in-molecule perturbation theory," *Chem. Phys. Lett.* **292**, p. 273, 1998.

[53] M. P. de Lara-Castells, A. A. Buchachenko, G. Delgado-Barrio, and P. Villarreal, "The open-shell interaction of He with the B $^3\Pi_u(0^+)$ state of Br_2: An *ab initio* study and its comparison with a diatomics-in-molecule perturbation model," *J. Chem. Phys.* **120**, p. 2182, 2003.

[54] C. J. Margulis, D. F. Coker, and R. M. Lynden-Bell, "Symmetry breaking of the triiodide ion in acetonitrile solution," *Chem. Phys. Lett.* **341**, p. 557, 2001.

[55] C. J. Margulis, D. F. Coker, and R. M. Lynden-Bell, "A Monte Carlo study of symmetry breaking of I_3^- in aqueous solution using a multistate diabatic Hamiltonia," *J. Chem. Phys.* **114**, p. 367, 2001.

[56] C. J. Margulis and D. F. Coker, "Modeling solvation of excited electronic states of flexible polyatomic molecules: Diatomics-in-molecules for I_3 in argon clusters," *J. Chem. Phys.* **114**, p. 6744, 2001.

[57] C. J. Margulis and D. F. Coker, "Applying diatomic-in-molecules in excited electronic state calculations for flexible polyatomic molecules. The I_3 molecule," *J. Chem. Phys.* **113**, p. 6113, 2000.

[58] A. K. Belyaev, A. S. Tiukanov, and W. Domcke, "Generalized diatomics-in-molecules method for polyatomic anions," *Phys. Rev. A* **65**, p. 012508, 2001.

[59] H. Wang and M. Thoss, "Semiclassical simulation of absorption spectra for a chromophore coupled to an anharmonic bath," *Chem. Phys.* **304**, p. 121, 2004.

[60] O. Kühn and N. Makri, "Forward-backward semiclassical calculation of spectral line shapes: I_2 in a rare gas cluster," *J. Phys. Chem. A* **103**, p. 9487, 1999.

[61] M. Ovchinnikov, V. A. Apkarian, and G. A. Voth, "Semiclassical molecular dynamics computation of spontaneous light emission in the condensed phase: Resonance Raman spectra," *J. Chem. Phys.* **114**, p. 7130, 2001.

[62] M. Ovchinnikov and V. A. Apkarian, "Mixed-order semiclassical dynamics in coherent state representation: The connection between phonon sidebands and guest–host dynamics," *J. Chem. Phys.* **108**, p. 2277, 1998.

[63] M. L. Brewer, J. S. Hulme, and D. E. Manolopoulos, "Semiclassical dynamics in up to 15 coupled vibrational degrees of freedom," *J. Chem. Phys.* **106**, p. 4832, 1997.

[64] D. Thirumalai, E. J. Bruskin, and B. J. Berne, "On the use of semiclassical dynamics in determining electronic spectra of Br_2 in an Ar matrix," *J. Chem. Phys.* **83**, p. 230, 1985.

[65] H. Wang, M. Thoss, and W. H. Miller, "Systematic convergence in the dynamical hybrid approach for complex systems: A numerically exact methodology," *J. Chem. Phys.* **115**, p. 2979, 2001.

[66] M. Thoss, H. Wang, and W. H. Miller, "Self-consistent hybrid approach for complex systems: Application to the spin-boson model with Debye spectral density," *J. Chem. Phys.* **115**, p. 2991, 2001.

[67] P. Jungwirth and R. B. Gerber, "Quantum molecular dynamics of ultrafast processes in large polyatomic systems," *Chem. Rev.* **99**, p. 1583, 1999.

[68] P. Jungwirth, E. Fredj, and R. B. Gerber, "Quantum molecular dynamics of large systems beyond separable approximation: The configuration interaction classical separable potential method," *J. Chem. Phys.* **107**, p. 8963, 1997.

[69] P. Jungwirth and R. B. Gerber, "Quantum dynamics of large polyatomic systems using a classically based separable potential method," *J. Chem. Phys.* **102**, p. 6046, 1995.

[70] H. Eshet, M. Ratner, and R. Gerber, "Selective energy and phase transfer in the photodissociation of I_2 in argon clusters: Quantum dynamics simulations," *Chem. Phys. Lett.* **431**, p. 199, 2006.

[71] R. B. Gerber, M. V. Korolkov, J. Manz, M. Y. Niv, and B. Schmidt, "A reflection principle for the control of molecular photodissociation in solids: Model simulation for F_2 in Ar," *Chem. Phys. Lett.* **327**, p. 76, 2000.

[72] G. Chaban, R. B. Gerber, M. V. Korolkov, J. Manz, M. Y. Niv, and B. Schmidt, "Photodissociation dynamics of molecular fluorine in an argon matrix induced by ultrashort laser pulses," *J. Phys. Chem. A* **105**, p. 2770, 2001.

[73] M. V. Korolkov and J. Manz, "Initial processes of laser induced diatomic molecular photodissociation in matrices: Quantum simulations for F_2 in Ar in reduced dimensionality," *Z. Phys. Chemie* **217**, p. 115, 2003.

[74] M. V. Korolkov and J. Manz, "Coherent spin control of matrix isolated molecules by IR + UV laser pulses: Quantum simulations for ClF in Ar," *J. Chem. Phys.* **120**, p. 11522, 2004.

[75] M. V. Korolkov and J. Manz, "Cage exit supported by spin-orbit coupling: Quantum model simulations for ClF in an Ar matrix," *J. Chem. Phys.* **393**, p. 44, 2004.

[76] A. B. Alekseyev, M. V. Korolkov, O. Kühn, J. Manz, and M. Schröder, "Model simulation of coherent laser control of the ultrafast spin-flip dynamics of matrix-isolated Cl_2," *J. Photochem. & Photobiol. A* **180**, p. 262, 2006.

[77] M. V. Korolkov and J. Manz, "Design of UV laser pulses for the preparation of matrix isolated homonuclear diatomic molecules in selective vibrational superposition states," *J. Chem. Phys.* **126**, p. 174306, 2007.

[78] G. Flachenecker, V. A. Ermoshin, and V. E. et al., "Photodissociation and recombination dynamics of I_2 in DDR (decadodecasil 3R): Dependence on the geometry of the host matrix monitored by femtosecond time-resolved pump probe experiments," *Phys. Chem. Chem. Phys.* **5**, p. 865, 2003.

[79] V. A. Ermoshin, G. Flachenecker, A. Materny, and V. Engel, "Caging of I_2 in decadodecasil 3R: Pump-probe experiments and molecular dynamics modeling," *J. Chem. Phys.* **114**, p. 8132, 2001.

[80] R. Zadoyan, M. Sterling, M. Ovchinnikov, and V. A. Apkarian, "Predissociation dynamics of I_2(B) in liquid CCl_4 observed through femtosecond pump-probe measurements: Electronic caging through solvent symmetry," *J. Chem. Phys.* **107**, p. 8446, 1997.

[81] N. Yu, C. J. Margulis, and D. F. Coker, "Influence of solvation environment on excited state avoided crossings and photodissociation dynamics," *J. Phys. Chem. B* **105**, p. 6728, 2001.

[82] M. C. Heaven, "Fluorescence decay dynamics of the halogens and interhalogens," *Chem. Soc. Rev.* **15**, p. 405, 1986.

[83] V. E. Bondybey and S. S. B. C. Fletcher, "Br_2 B $^3\Pi(0_u^+)$ excitation spectra and radiative lifetimes in rare gas solids," *J. Chem. Phys.* **64**, p. 5243, 1976.

[84] H. Ibrahim, M. Gühr, and N. Schwentner, "Valence transitions of Br_2 in Ar matrices: Interaction with the lattice, phonon sidebands and predissociation," *J. Chem. Phys.* **128**, p. 064504, 2008.

[85] L. D. Landau, "On the theory of transfer of energy at collisions II," *Phys. Z. Sov.* **2**, p. 46, 1932.

[86] C. Zener, "Non-adiabatic crossings of energy levels," *Proc. R. Soc. Lond. A* **137**, p. 696, 1932.

[87] N. Rosen and C. Zener, "Double Stern-Gerlach experiment and related collision phenomena," *Phys. Rev.* **40**, p. 502, 1932.

[88] W. Domcke, D. R. Yarkony, and H. Köppel, *Conical Intersections*, World Scientific, Singapore, 2004.

[89] H. Köppel, W. Domcke, and L. S. Cederbaum, "Multimode molecular dynamics beyond the Born-Oppenheimer approximation," *Adv. Chem. Phys.* **57**, p. 59, 1984.

[90] W. Domcke and G. Stock, "Theory of ultrafast nonadiabatic excited-state processes and their spectroscopic detection in real time," *Adv. Chem. Phys.* **100**, p. 1, 1997.

[91] R. Schneider, W. Domcke, and H. Köppel, "Aspects of dissipative electronic and vibrational dynamics of strongly vibronically coupled systems," *J. Chem. Phys.* **92**, p. 1045, 1990.

[92] G. Stock and W. Domcke, "Theory of femtosecond pump-probe spectroscopy of ultrafast internal conversion processes in polyatomic molecules," *J. Opt. Soc. Am. B* **7**, p. 1970, 1990.

[93] G. A. Worth, H.-D. Meyer, and L. S. Cederbaum, "Relaxation of a system with a conical intersection coupled to a bath: A benchmark 24-dimensional wave packet study treating the environment explicitly," *J. Chem. Phys.* **109**, p. 3518, 1998.

[94] S. Krempl, M. Winterstetter, H. Plöhn, and W. Domcke, "Path-integral treatment of multi-mode vibronic coupling," *J. Chem. Phys.* **100**, p. 926, 1994.

[95] A. Raab, I. Burghardt, and H.-D. Meyer, "The multiconfiguration time-dependent Hartree method generalized to the propagation of density operators," *J. Chem. Phys.* **111**, p. 8759, 1999.

[96] G. Stock and M. Thoss, "Classical description of nonadiabatic quantum dynamics," *Adv. Chem. Phys.* **131**, p. 243, 2005.

[97] W. H. Miller, N. C. Handy, and J. E. Adams, "Reaction path Hamiltonian for polyatomic molecules," *J. Chem. Phys.* **72**, p. 99, 1980.

[98] T. Carrington Jr. and W. H. Miller, "Reaction surface Hamiltonian for the dynamics of reactions in polyatomic systems," *J. Chem. Phys.* **81**, p. 3942, 1984.

[99] B. A. Ruf and W. H. Miller, "A new (Cartesian) model for reaction dynamics in polyatomic systems, with application to H-atom transfer in malonaldehyde," *J. Chem. Soc.,Faraday Trans. 2* **84**, p. 1523, 1988.

[100] W. H. Miller, B. A. Ruf, and Y. T. Chang, "A diabatic reaction path Hamiltonian," *J. Chem. Phys.* **89**, p. 6298, 1988.

[101] K. Giese, M. Petković, H. Naundorf, and O. Kühn, "Multidimensional quantum dynamics and infrared spectroscopy of hydrogen bonds," *Phys. Rep.* **430**, p. 211, 206.

[102] L. S. Cederbaum and W. Domcke, "Theoretical aspects of ionization potentials and photoelectron spectroscopy: A many-body approach," *Adv. Chem. Phys.* **36**, p. 205, 1977.

[103] L. S. Cederbaum, W. Domcke, H. Köppel, and W. von Niessen, "Strong vibronic coupling effects in ionization spectra: The mystery band of butatriene," *Chem. Phys.* **26**, p. 126, 1977.

[104] A. Raab, G. Worth, H.-D. Meyer, and L. S. Cederbaum, "Molecular dynamics of pyrazine after excitation to the S_2 electronic state using a realistic 24-mode model Hamiltonian," *J. Chem. Phys.* **110**, p. 936, 1999.

[105] S. Mahapatra, V. Vallet, C. Woywod, H. Köppel, and W. Domcke, "Multimode Jahn-Teller and pseudo-Jahn-Teller coupling effects in the photoelectron spectrum of CH_3F," *Chem. Phys.* **304**, p. 17, 2004.

[106] M. H. Beck, A. Jäckle, G. A. Worth, and H.-D. Meyer, "The multiconfiguration time-dependent Hartree method: A highly efficient algorithm for propagating wavepackets," *Phys. Rep.* **324**, p. 1, 2000.

[107] H.-D. Meyer and G. A. Worth, "Quantum molecular dynamics: Propagating wavepackets and density operators using the multiconfiguration time-dependent Hartree (MCTDH) method," *Theor. Chem. Acc.* **109**, p. 251, 2003.

[108] Y. Asano and S. Yabushita, "Theoretical study on the nonadiabatic transitions in the photodissociation of Cl_2, Br_2 and I_2," *Bull. Korean Chem. Soc* **24**, p. 703, 2003.

[109] J. A. Coxon, "Low-lying Electronic States of Diatomic Halogen Molecules," in *Molecular Spectroscopy Volume 1*, R. F. Barrow, D. A. Long, and D. J. Millen, eds., The Chemical Society, (London), 1973.

[110] F. Hund, "Zur Deutung einiger Erscheinungen in den Molekelspektren," *Zeits. f. Physik* **36**, p. 657, 1926.

[111] M. Saute and M. Aubert-Frécon, "Calculated long-range potential-energy curves for the 23 molecular states of I_2," *J. Chem. Phys.* **77**, p. 5639, 1982.

[112] T. Y. Chang, "Moderately long-range interatomic forces," *Rev. Mod. Phys.* **39**, p. 911, 1967.

[113] S. J. Umanskij and E. E. Nikitin, "Elektronenwellenfunktionen und Terme zweiatomiger Moleküle bei großen Atomabständen," *Theor. Chim. Acta* **13**, p. 91, 1969.

[114] J. L. Schreiber and P. J. Kuntz, "A criterion for the applicability of the method of diatomics-in-molecules to potential surface calculations. I. Selection of the DIM basis," *J. Chem. Phys.* **76**, p. 1872, 1982.

[115] P. J. Kuntz and J. L. Schreiber, "A systematic procedure for extracting fragment matrices for the method of diatomics-in-molecules from *ab initio* calculations on diatomics," *J. Chem. Phys.* **76**, p. 4120, 1982.

[116] S. Yabushita *private communication, unpublished results* .

[117] Y. Asano and S. Yabushita, "Theoretical study of nonadiabatic transitions in the photodissociation of Cl_2 and Br_2," *Chem. Phys. Lett.* **372**, p. 348, 2003.

[118] Y. Zhao, I. Yourshaw, G. Reiser, C. C. Arnold, and D. M. Neumark, "Study of the $ArBr^-$, ArI^-, and KrI^- anions and the corresponding neutral van der Waals complexes by anion zero electron kinetic energy spectroscopy," *J. Chem. Phys.* **101**, p. 6538, 1994.

[119] I. Yourshaw, Y. Zhao, and D. M. Neumark, "Many-body effects in weakly bound anion and neutral clusters: Zero electron kinetic energy spectroscopy and threshold photodetachment spectroscopy of Ar_nBr^- (n=2-9) and Ar_nI^- (n=2-19)," *J. Chem. Phys.* **105**, p. 351, 1996.

[120] C. H. Becker, P. Casavecchia, Y. T. Lee, R. E. Olsen, and W. E. Lester, "Coupled-channel study of halogen (^{2}P) + rare gas (^{1}S) scattering," *J. Chem. Phys.* **70**, p. 5477, 1979.

[121] J. N. Murrell, S. Carter, S. C. Farantos, P. Huxley, and A. J. C. Varandas, *Molecular Potential Energy Functions*, John Wiley & Sons, New York, 1984.

[122] R. A. Aziz, "A highly accurate interatomic potential for argon," *J. Chem. Phys.* **99**, p. 4518, 1993.

[123] R. A. Aziz, M. J. Slaman, and A. R. Janzen, "Critique of interatomic potentials obtained from neutron diffraction," *Phys. Rev. E* **49**, p. 5310, 1994.

[124] H. Kunz, J. G. McCaffrey, R. Schriever, and N. Schwentner, "Spectroscopy and photodissociation of molecular chlorine in argon matrices," *J. Chem. Phys.* **94**, p. 1039, 1991.

[125] R. Alimi, R. Gerber, J. McCaffrey, H. Kunz, and N. Schwentner, "Delayed and direct cage exit in photodissociation of Cl_2 in solid Ar," *Phys. Rev. Lett.* **69**, p. 856, 1992.

[126] J. McCaffrey, H. Kunz, and N. Schwentner, "Photodissociation of molecular chlorine in xenon matrices," *J. Chem. Phys.* **96**, p. 2825, 1992.

[127] R. Fraenkel and Y. Haas, "Molecular dynamics simulations of rare gas matrix deposition," *Chem. Phys.* **186**, p. 185, 1994.

[128] X.-J. Ning and Q.-Z. Qin, "A new molecular dynamics method for simulating trapping site structures in cryogenic matrices," *J. Chem. Phys.* **110**, p. 4920, 1999.

[129] S. Toxvaerd, "Algorithms for canonical molecular dynamics simulations," *Mol. Phys.* **72**, p. 159, 1991.

[130] M. P. Allen and D. J. Tildesley, *Computer Simulation of Liquids*, Oxford University Press, Oxford, 1987.

[131] M. Griebel, S. Knapek, G. Zumbusch, and A. Caglar, *Numerische Simulationen in der Moleküldynamik: Numerik, Algorithmen, Parallelisierung, Anwendungen*, Springer, Berlin, Heidelberg, 2004.

[132] J. Manz, P. Saalfrank, and B. Schmidt, "Quantum dynamical aspects of rotationally and vibrationally mediated photochemistry in matrices and at surfaces HCl/DCl in Ar and NH_3/ND_3 at Cu(111)," *J. Chem. Soc. Faraday Trans.* **93**, p. 957, 1997.

[133] P. Zdanska, B. Schmidt, and P. Jungwirth, "Photolysis of hydrogen chloride embedded in the first argon solvation shell: Rotational control and quantum dynamics of photofragments," *J. Chem. Phys.* **110**, p. 6246, 1999.

[134] V. Berghof, M. Martins, B. Schmidt, and N. Schwentner, "Vibrational overtones and rotational structure of HCl in rare gas matrices," *J. Chem. Phys.* **116**, p. 9364, 2002.

[135] B. Schmidt, "Quantum dynamics of HF photodissociation in icosahedral $Ar_{12}HF$ clusters: Rotational control of the hydrogen atom cage exit," *Chem. Phys. Lett.* **301**, p. 207, 1999.

[136] T. Kiljunen, M. Bargheer, M. Gühr, and N. Schwentner, "A potential energy surface and a trajectory study of photodynamics and strong-field alignment of ClF molecule in rare gas (Ar, Kr) solids," *Phys. Chem. Chem. Phys.* **6**, p. 2185, 2004.

[137] T. Kiljunen, M. Bargheer, M. Gühr, N. Schwentner, and B. Schmidt, "Photodynamics and ground state librational states of ClF molecule in solid Ar. Comparison of experiment and theory," *Phys. Chem. Chem. Phys.* **6**, p. 2932, 2004.

[138] T. Kiljunen, B. Schmidt, and N. Schwentner, "Intense-field alignment of molecules confined in octahedral fields," *Phys. Rev. Lett.* **94**, p. 123003, 2005.

[139] T. Kiljunen, B. Schmidt, and N. Schwentner, "Aligning and orienting molecules trapped in octahedral crystal fields," *Phys. Rev. A* **72**, p. 053415, 2005.

[140] T. Kiljunen, B. Schmidt, and N. Schwentner, "Time-dependent alignment of molecules trapped in octahedral crystal fields," *J. Chem. Phys.* **124**, p. 164502, 2006.

[141] S. L. Altmann and P. Herzig, *Point-Group Theory Tables*, Clarendon Press, Oxford, 1994.

[142] J. Reinhold, *Quantentheorie der Moleküle*, B. G. Teubner, Stuttgart, 1994.

[143] R. Poliák, I. Paidarová, and P. J. Kuntz, "Diatomics-in-molecules models for H_2O and H_2O^-. I. Valence bond diatomic fragment matrices," *J. Chem. Phys.* **82**, p. 2352, 1985.

[144] N. Makri and W. H. Miller, "Basis set methods for describing the quantum mechanics of a 'system' interacting with a harmonic 'bath'," *J. Chem. Phys.* **86**, p. 1451, 1987.

[145] V. May and O. Kühn, *Charge and Energy Transfer Dynamics in Molecular Systems, 2nd Revised and Enlarged Edition*, Wiley-VCH, Weinheim, 2004.

[146] E. B. Wilson Jr., "The normal modes and frequencies of vibration of the regular plane hexagon model of the benzene molecule," *Phys. Rev.* **45**, p. 706, 1934.

[147] E. B. Wilson Jr., "Some mathematical methods for the study of molecular vibrations," *J. Chem. Phys.* **9**, p. 76, 1941.

[148] H. Köppel, W. Domcke, and L. S. Cederbaum, "The Multi-Mode Vibronic-Coupling Approach," in *Conical Intersections*, W. Domcke, D. R. Yarkony, and H. Köppel, eds., p. 323, World Scientific, (Singapore), 2004.

[149] H. Köppel, "Jahn-Teller and Pseudo-Jahn-Teller Intersections: Spectroscopy and Vibronic Dynamics," in *Conical Intersections*, W. Domcke, D. R. Yarkony, and H. Köppel, eds., p. 429, World Scientific, (Singapore), 2004.

[150] G. A. Worth, H.-D. Meyer, and L. S. Cederbaum, "Multidimensional Dynamics Involving a Conical Intersection: Wavepacket Calculations Using the MCTDH Method," in *Conical Intersections*, W. Domcke, D. R. Yarkony, and H. Köppel, eds., p. 583, World Scientific, (Singapore), 2004.

[151] D. Heidrich, W. Kliesch, and W. Quapp, *Properties of chemically interesting potential energy surfaces*, Springer, New York, 1991.

[152] D. Heidrich, *The reaction path in chemistry: Current approaches and perspectives*, Kluwer Academic Publishers, Dordrecht, 1995.

[153] D. R. Yarkony, "Conical Intersections: Their Description and Consequences," in *Conical Intersections*, W. Domcke, D. R. Yarkony, and H. Köppel, eds., p. 41, World Scientific, (Singapore), 2004.

[154] N. Makri and W. H. Miller, "Time-dependent self-consistent field (TDSCF) approximation for a reaction coordinate coupled to a harmonic bath: Single and multiple configuration treatments," *J. Chem. Phys.* **87**, p. 5781, 1987.

[155] H.-D. Meyer, U. Manthe, and L. S. Cederbaum, "The multi-configurational time-dependent Hartree approach," *Chem. Phys. Lett.* **165**, p. 73, 1990.

[156] U. Manthe, H.-D. Meyer, and L. S. Cederbaum, "Wave-packet dynamics within the multiconfiguration Hartree framework: General aspects and application to NOCl," *J. Chem. Phys.* **97**, p. 3199, 1992.

[157] M. H. Beck and H.-D. Meyer, "An efficient and robust integration scheme for the equations of motion of the multiconfiguration time-dependent Hartree (MCTDH) method," *Z. Physik D: At., Mol. Clusters* **42**, p. 113, 1997.

[158] D. O. Harris, G. G. Engerholm, and W. D. Gwinn, "Calculation of matrix elements for one-dimensional quantum-mechanical problems and the application to anharmonic oscillators," *J. Chem. Phys.* **43**, p. 1515, 1965.

[159] A. S. Dickinson and P. R. Certain, "Calculation of matrix elements for one-dimensional quantum-mechanical problems," *J. Chem. Phys.* **49**, p. 4209, 1968.

[160] J. C. Light, I. P. Hamilton, and J. V. Lill, "Generalized discrete variable approximation in quantum mechanics," *J. Chem. Phys.* **82**, p. 1400, 1985.

[161] J. C. Light and T. Carrington, "Discrete-variable representations and their utilization," *Adv. Chem. Phys.* **114**, p. 263, 2000.

[162] R. Kosloff, "Time-dependent quantum-mechanical methods for molecular dynamics," *J. Phys. Chem.* **92**, p. 2087, 1988.

[163] G. A. Worth, M. H. Beck, A. Jäckle, and H.-D. Meyer. The MCTDH Package, Version 8.4, (2007). See http://www.pci.uni-heidelberg.de/tc/usr/mctdh/.

[164] A. Jäckle and H.-D. Meyer, "Product representation of potential energy surfaces," *J. Chem. Phys.* **104**, p. 7974, 1996.

[165] A. Jäckle and H.-D. Meyer, "Product representation of potential energy surfaces II," *J. Chem. Phys.* **109**, p. 3772, 1998.

[166] J.-Y. Fang and H. Guo, "Multiconfiguration time-dependent Hartree studies of the CH_3I/MgO photodissociation dynamics," *J. Chem. Phys.* **101**, p. 5831, 1994.

[167] G. A. Worth, H.-D. Meyer, and L. S. Cederbaum, "The effect of a model environment on the S_2 absorption spectrum of pyrazine: A wave packet study treating all 24 vibrational modes," *J. Chem. Phys.* **105**, p. 4412, 1996.

[168] J. Franck and E. G. Dymond, "Elementary processes of photochemical reactions," *Trans. Faraday Soc.* **21**, p. 536, 1926.

[169] E. U. Condon, "Nuclear motions associated with electron transitions in diatomic molecules," *Phys. Rev.* **32**, p. 858, 1928.

[170] M. A. A. Clyne, M. C. Heaven, and J. Tellinghuisen, "Theoretical treatment of the spontaneous predissociation of Br_2, B $^3\Pi(0_u^+)$," *J. Chem. Phys.* **76**, p. 5341, 1982.

[171] R. Schinke, *Photodissociation Dynamics - Spectroscopy and Fragmentation of Small Polyatomic Molecules*, Cambridge University Press, Cambridge, 1993.

[172] D. T. Colbert and W. H. Miller, "A novel discrete variable representation for quantum mechanical reactive scattering via the S-matrix Kohn method," *J. Chem. Phys.* **96**, p. 1982, 1992.

[173] C. C. Marston and G. G. Balint-Kurti, "The Fourier grid Hamiltonian method for bound state eigenvalues and eigenfunctions," *J. Chem. Phys.* **91**, p. 3571, 1989.

[174] J. Stare and G. G. Balint-Kurti, "Fourier grid Hamiltonian method for solving the vibrational Schrödinger equation in internal coordinates: Theory and test applications," *J. Phys. Chem. A* **107**, p. 7204, 2003.

[175] D. Kosloff and R. Kosloff, "A Fourier method solution for the time-dependent Schrödinger equation as a tool in molecular dynamics," *J. Comput. Phys.* **52**, p. 35, 1983.

[176] R. J. L. Roy, R. G. Macdonald, and G. Burns, "Diatom potential curves and transition moment functions from continuum absorption coefficients: $Br_2^{*\dagger}$," *J. Chem. Phys.* **65**, p. 1485, 1976.

[177] J. Tellinghuisen, "Transition strengths and potential curves for the valence transitions in Br_2 from a reanalysis of the ultraviolet-visible absorption at low resolution," *J. Chem. Phys.* **115**, p. 10417, 2001.

[178] J. Tellinghuisen, "Erratum: "Transition strengths and potential curves for the valence transitions in Br_2 from a reanalysis of the ultraviolet-visible absorption at low resolution"," *J. Chem. Phys.* **118**, p. 1573, 2003.

[179] A. Lami and G. Villani, "Model Studies of the Dynamics at Conical Intersections," in *Conical Intersections*, W. Domcke, D. R. Yarkony, and H. Köppel, eds., p. 369, World Scientific, (Singapore), 2004.

[180] M. Bargheer, *Ultrafast photodynamics in condensed phase: ClF, Cl_2 and I_2 in solid rare gases.* PhD thesis, Fachbereich Physik - Freie Universität Berlin, 2002.

[181] M. Gühr, *Coherent dynamics of small molecules in rare gas crystals.* PhD thesis, Fachbereich Physik - Freie Universität Berlin, 2005.

[182] G. G. Balint-Kurti, R. N. Dixon, and C. C. Marston, "Time-dependent quantum dynamics of molecular photofragmentation processes," *J. Chem. Soc. Faraday Trans.* **86**, p. 1741, 1990.

[183] E. J. Heller, "Quantum corrections to classical photodissociation models," *J. Chem. Phys.* **68**, p. 2066, 1978.

[184] E. J. Heller, "Photofragmentation of symmetric triatomic molecules: Time dependent picture," *J. Chem. Phys.* **68**, p. 3891, 1978.

[185] L. S. Cederbaum, E. Gindensperger, and I. Burghardt, "Short-time dynamics through conical intersections in macrosystems," *Phys. Rev. Lett.* **94**, p. 113003, 2005.

[186] E. Gindensperger, I. Burghardt, and L. S. Cederbaum, "Short-time dynamics through conical intersections in macrosystems. I. Theory: Effective-mode formulation," *J. Chem. Phys.* **124**, p. 144103, 2006.

[187] E. Gindensperger, I. Burghardt, and L. S. Cederbaum, "Short-time dynamics through conical intersections in macrosystems. II. Applications," *J. Chem. Phys.* **124**, p. 144104, 2006.

[188] P. Ehrenfest, "Bemerkungen über die angenäherte Gültigkeit der klassischen Mechanik innerhalb der Quantenmechanik," *Z. Phys. A* **45**, p. 455, 1927.

[189] L. Liu and H. Guo, "Quantum/classical hybrid dynamics of I_2(A) photodissociation and recombination in matrix Ar, linear chain model," *Chem. Phys. Lett.* **237**, p. 299, 1995.

[190] L. Liu and H. Guo, "A linear chain hybrid quantum/classical model for the photodissociation and recombination of I_2 (A) in rare gas matrices," *J. Chem. Phys.* **103**, p. 7851, 1995.

[191] L. Liu and H. Guo, "Validity of a hybrid quantum/classical approach in photodissociation/recombination of I_2 in rare gas matrices," *J. Chem. Phys.* **104**, p. 528, 1996.

[192] H. Hellmann, *Einführung in die Quantenchemie*, Deuticke, Leipzig, 1937.

[193] R. P. Feynman, "Forces in molecules," *Phys. Rev.* **56**, p. 340, 1939.

[194] L. Wang, "Quenching methods for chemical reaction dynamics within mixed quantum/classical approximation," *Phys. Chem. Chem. Phys.* **2**, p. 2883, 2000.

[195] C. Coletti and G. D. Billing, "Quantum dressed classical mechanics: Application to the photo-absorption of pyrazine," *Chem. Phys. Lett.* **368**, p. 289, 2003.

[196] G. D. Billing, "Quantum-dressed classical mechanics: Theory and application," *Phys. Chem. Chem. Phys.* **4**, p. 2685, 2002.

[197] G. D. Billing, "A split-Lanczos method for solving time-dependent discrete variable Gauss-Hermite dynamics," *Chem. Phys. Lett.* **339**, p. 237, 2001.

[198] G. D. Billing, "Time-dependent quantum dynamics in a Gauss-Hermite basis," *J. Chem. Phys.* **110**, p. 5526, 1999.

[199] B. Lasorne, M. A. Robb, and G. A. Worth, "Direct quantum dynamics using variational multi-configuration Gaussian wavepackets. Implementation details and test case," *Phys. Chem. Chem. Phys.* **9**, p. 3210, 2007.

[200] B. Lasorne, M. J. Bearpark, M. A. Robb, and G. A. Worth, "Direct quantum dynamics using variational multi-configuration Gaussian wavepackets," *Chem. Phys. Lett.* **432**, p. 604, 2006.

[201] G. A. Worth, M. A. Robb, and I. Burghardt, "A novel algorithm for non-adiabatic direct dynamics using variational Gaussian wavepackets," *Faraday Discuss.* **127**, p. 307, 2004.

[202] G. A. Worth and I. Burghardt, "Full quantum mechanical molecular dynamics using Gaussian wavepackets," *Chem. Phys. Lett.* **368**, p. 502, 2003.

[203] A. R. Edmonds, *Drehimpulse in der Quantenmechanik*, Bibliographisches Institut, Mannheim, 1964.

[204] R. N. Zare, *Angular Momentum: Understanding Spatial Aspects in Chemistry and Physics*, Wiley, New York, 1988.

[205] W. G. Hoover, "Canonical dynamics: Equilibrium phase-space distributions," *Phys. Rev. A* **31**, p. 1695, 1985.

[206] S. Nose, "A unified formulation of the constant temperature molecular dynamics methods," *J. Chem. Phys.* **81**, p. 511, 1984.

[207] P. W. Atkins and R. S. Friedman, *Molecular Quantum Mechanics, Third Edition*, Oxford University Press, Oxford, 2001.

[208] E. Fick, *Einführung in die Grundlagen der Quantentheorie*, Aula-Verlag, Wiesbaden, 1988.

Acknowledgments

I thank Prof. Jörn Manz for taking me into his group, providing this interesting research topic, and supporting this work. Him and the group, past and present, I want to thank for the open and friendly working atmosphere. In particular, I thank my supervisor, Prof. Oliver Kühn, for his guidance, support and interest in the work. I am grateful for his patience and the open door he had for any of my questions. Not only for sharing the office with me and teaching me science, but also for many private discussions I thank Dr. Mikhail Korolkov. Him and Dr. Guennaddi Paramonov, with whom I share a passion for cigarettes, I want to thank for the friendship. For their assistance with computer problems, mental support and amusing discussions in our coffee breaks I want to thank Dr. Holger Naundorf, Dr. Markus Oppel and Dr. Marko Schreiber. In Dr. Werner Gans and Prof. Dietrich Haase I found people to contact for good advice at any time. I don't want to forget to thank Mrs. Julija Djordjevic, who managed many things around bureaucracy and group activities. Finally, I wish my successor Antonio Accardi all the best for his future work.
Prof. Nikolaus Schwentner and his group, past and present, my experimental colleagues Dr. Markus Gühr, Heide Ibrahim and Monika Hejjas, I want to thank for their cooperation and the stimulating discussions. Within the Sfb project I also profited from the discussion with the partners from Jerusalem, Prof. Benny Gerber, Dr. Arik Cohen and Hagai Eshet, in many respects. Prof. David F. Coker and his group I am grateful for their warm hospitality during a visit to Boston in May/June 2005. I thank Prof. Satoshi Yabushita from Keio University for providing the ab-inito data of Br_2.
Finally, it is on my heart to express deep thanks to my parents, my grandparents, my sister and my brothers, my relatives and my friends for their understanding and support across the board.
For financial support I thank the Sonderforschungsbereich 450 der Deutschen Forschungsgemeinschaft.

Erklärung

Hiermit erkläre ich, dass ich die vorliegende Arbeit mit den angegebenen Hilfsmitteln selbständig angefertigt habe.

Berlin, 2008